Contribution to the study of the vulnerability of critical systems to Intentional Electromagnetic Interference (IEMI)

THÈSE N^{O} 6888 (2016)

PRÉSENTÉE LE 27 MAI 2016
À LA FACULTÉ DES SCIENCES ET TECHNIQUES DE L'INGÉNIEUR
GROUPE SCI STI FR
PROGRAMME DOCTORAL EN GÉNIE ÉLECTRIQUE

ÉCOLE POLYTECHNIQUE FÉDÉRALE DE LAUSANNE

POUR L'OBTENTION DU GRADE DE DOCTEUR ÈS SCIENCES

PAR

Nicolas MORA PARRA

acceptée sur proposition du jury:

Dr S.-R. Cherkaoui, président du jury
Prof. F. Rachidi-Haeri, Dr I. Junqua, directeurs de thèse
Prof. R. Thottappillil, rapporteur
Prof. M. Rubinstein, rapporteur
Prof. A. Skrivervik, rapporteuse

ÉCOLE POLYTECHNIQUE
FÉDÉRALE DE LAUSANNE
Suisse
2016

To Lina,

may we enjoy the fruits of all these busy years...

To my mother,

that your prayers show us the way to our victories…

To the memory of those who left and the patience of those who stayed.

Résumé

Les progrès des sources électromagnétiques de haute puissance (HPEM) au cours des années 1990 a soulevé l'inquiétude dans la communauté de la compatibilité électromagnétique (CEM) qu'elles pourraient être déployées pour interférer avec le bon fonctionnement des systèmes électroniques modernes à des fins criminelles. Il est bien établi que les champs électromagnétiques suffisamment intenses peuvent causer des troubles ou des dommages dans les systèmes électroniques et, par conséquent, peuvent affecter presque toutes les infrastructures critiques (IC) qui sont basées sur les technologies de l'information et de la communication (TIC). Ce champ d'étude a d'abord été connu comme le terrorisme électromagnétique, mais ce terme a été changé pour le terme plus englobant interférences électromagnétiques d'origine intentionnelle (IEMI en anglais).

La protection contre les menaces IEMI peut être reconnue comme une réminiscence de la période de la guerre froide et les programmes de recherche sur la protection contre les impulsions électromagnétiques de haute altitude (IEM-HA). Les sources IEMI génèrent des perturbations allant de quelques dizaines de MHz à plusieurs GHz. Ces fréquences sont significativement plus élevées que celles associées à la foudre et les IEM-HA, et par conséquent, les méthodes d'analyse et de protection traditionnels doivent être revues.

Cette thèse est une contribution aux techniques d'évaluation de la vulnérabilité des IC contre les IEMI. Afin de quantifier leur impact, l'environnement électromagnétique créé par des sources IEMI doit être caractérisé, les composants et sous-systèmes sensibles des IC doivent être identifiés, et les perturbations attendues doivent être évaluées. Les études menées dans cette thèse traitent l'amélioration des méthodes existantes pour l'évaluation générale des risques encourus par les IC, le classement des sources IEMI existantes, ainsi que l'évaluation expérimentale et numérique de la réponse de câbles commerciaux aux IEMI.

Nous présentons une méthodologie qualitative pour mener à bien l'audit IEMI d'une installation. Compte tenu de la complexité du problème, il a été décidé que la vulnérabilité d'une infrastructure doit être évaluée de façon qualitative en considérant les conséquences de l'interruption d'un service, la probabilité d'occurrence d'une attaque IEMI, et l'état de préparation des infrastructures pour résister à une attaque. L'objectif principal de cette méthode

est de permettre aux opérateurs de prendre des mesures correctives et de mitigation appropriées, d'après les résultats de l'audit IEMI.

Il est important de comprendre les capacités techniques actuelles dans le développement de sources IEMI afin de concevoir des stratégies de durcissement adéquates pour les équipements critiques. Nous présentons une analyse actualisée et une classification des sources IEMI potentielles qui ont été recueillies à partir d'un grand nombre de publications scientifiques. Les sources ont été classées en fonction de leur environnement électromagnétique, leur transportabilité, leur développement technologique, et leurs coûts. Il a été constaté que les sources conduites sont plus disponibles que les sources rayonnées. En outre, l'évaluation des sorties maximales attendues de sources HPEM est fait en regardant les limitations physiques du développement des technologies actuelles. Afin d'étudier les caractéristiques spectrales des sources, une méthode analytique est proposée pour l'évaluation du bandratio des signaux en utilisant l'indice de Blumer.

Les niveaux de perturbations attendues dues à l'illumination des systèmes de câblage à l'intérieur d'un bureau à des hyperfréquences ont été étudiés par des mesures effectuées à l'aide d'une goulotte en plastique de 2 mètres contenant plusieurs types de câbles trouvés dans les bâtiments commerciaux. La goulotte a été illuminée avec des impulsions HPEM à l'intérieur une cellule GTEM et avec des champs de faible puissance à l'intérieur d'une chambre de réverbération (CR). Les tests ont révélé qu'à des fréquences basses et intermédiaires, les câbles d'alimentation basse tension sont plus sensibles par rapport aux câbles de téléphone ou de réseaux. Aux hautes fréquences, le couplage est dominé par des ouvertures et discontinuités dans les connecteurs et charges de terminaison déséquilibrées. Comme attendu, les meilleurs résultats ont été obtenus avec l'utilisation de paires torsadées blindées. Les fonctions de transfert obtenues peuvent être utilisées pour l'obtention des niveaux de perturbation dans des analyses des risques IEMI pour les différents types de CI.

L'un des défis dans le calcul des perturbations IEMI avec l'utilisation de la théorie des lignes de transmission (LT) est la possibilité de définir un conducteur de référence pour l'évaluation des signaux de mode commun et différentiel. Les immeubles contiennent de faisceaux de câbles très longs qui sont généralement flottants à l'intérieur des goulottes ou conduits qui ne sont pas nécessairement à proximité de surfaces métalliques. L'applicabilité de la théorie LT dans l'évaluation des signaux de mode différentiel de lignes à deux fils flottant au-dessus d'un plan de masse a été étudiée grâce à des comparaisons avec des simulations avec des outils full wave. Il a été constaté que la présence du plan de masse peut être négligée dans le calcul de l'impédance caractéristique des lignes, lorsque la hauteur des fils est supérieure à environ deux fois la distance de séparation entre eux. En outre, les résultats ont montré que la validité de la théorie LT est conditionnée à une courte distance électrique entre les fils différentiels, quelles que soient les distances au-dessus du plan de masse.

La propagation des signaux IEMI le long de lignes de puissance ou communication est affectée par les effets de dispersion qui atténuent significativement les formes d'onde au-delà d'une certaine distance en raison des pertes en conduction et diélectriques. La théorie LT est utilisée pour évaluer l'effet de ces deux types de pertes dans la dispersion des signaux IEMI injectés le long de câbles de puissance et communication en fonction de la longueur de propagation. Un

modèle de LT du câblage électrique à basse tension de la goulotte en plastique a été mis au point et afin de valider les modèles, les résultats numériques ont été comparés aux mesures obtenues en utilisant des techniques de domaine fréquentiel et temporel.

Certaines installations critiques comprennent des assemblages de câbles complexes, y compris des câbles blindés individuellement, ou avec sur-blindages et connecteurs à broches multiples blindés. Le couplage électromagnétique à ces câblages est régi par l'impédance de transfert globale de l'ensemble. Des considérations générales et des lignes directrices pour l'application de la théorie LT afin d'évaluer l'impédance de transfert global de faisceaux de câbles complexes sont données. Les résultats de simulation obtenus sont en bon accord avec les données expérimentales jusqu'à des fréquences de 500 MHz. Il a été constaté que les impédances de contact entre les blindages et les connecteurs, et l'impédance d'interconnexion des connecteurs au châssis de l'équipement jouent un rôle très important. Finalement, un modèle amélioré pour estimer l'impédance de transfert d'une tresse à deux couches est également proposé et validé à l'aide de données expérimentales.

Mots-clés: Interférences électromagnétiques d'origine intentionnelle (IEMI), infrastructures critiques (IC), électromagnétisme haute puissance (HPEM), compatibilité électromagnétique (CEM), théorie des lignes de transmission (LT), l'indice de Blumer

Abstract

The progress of high power electromagnetic (HPEM) sources during the late 1990s raised the concern in the electromagnetic compatibility (EMC) community that they could be deployed for criminal purposes to interfere with the operation of modern electronic systems. It is well established that sufficiently intense electromagnetic fields can cause upset or damage in electronic systems and therefore, can affect almost every critical infrastructure (CI) that is based on information and communication technologies (ICT). This field of study was initially known as electromagnetic terrorism, but was changed to the more encompassing term of intentional electromagnetic interference (IEMI).

Protection against IEMI threats can be acknowledged as a reminiscence of the cold war period and the research programs on protection against high altitude electromagnetic pulses (HEMP). IEMI sources generate disturbances ranging from tens of MHz to several GHz, frequencies that are significantly higher than those associated with lightning and HEMP, and therefore, the traditional analysis and protection methods need to be revisited.

This thesis is a contribution to the assessment techniques of the vulnerability of CIs against IEMI. In order to quantify their impact, the electromagnetic environment created by IEMI sources needs to be characterized, the susceptible components and subsystems of the CIs should be identified, and the expected disturbances have to be evaluated. The studies undertaken in this thesis deal with the improvement of the existing methods for the general assessment of the IEMI risks encountered by CIs, the classification of existing IEMI sources, and the experimental and numerical assessment of the response of commercial cables to IEMI.

We present a methodology to carry out the so-called IEMI audit of a facility. Given the complexity of the problem, it was decided that the vulnerability of an infrastructure should be evaluated in a qualitative manner by regarding the consequences of interrupting the normal provision of a service, the probability of occurrence of an IEMI attack, and the preparedness of the infrastructure to withstand an attack. The main objective of this methodology is to enable the business continuity management operators to take appropriate corrective and mitigation measures, based on the results of the IEMI audit.

Understanding the current technical capabilities in the development of IEMI sources is important to design adequate hardening strategies for critical equipment. We present an updated survey and classification of potential IEMI sources that were collected from a large number of scientific publications. The sources have been classified according to their electromagnetic environment, their transportability, technological development, and cost level. It was found that potential IEMI conducted sources are more available than radiated sources. Also, an assessment of the maximum expected outputs of HPEM sources is made by looking at the physical limitations that constrain the development of current technologies. In order to study the spectral characteristics of the IEMI sources, an analytical method is proposed for the evaluation of the band-ratio of the signals by using the so-called Blumer index.

The expected disturbances due to a high frequency illumination of representative cabling systems inside an office were studied through measurements performed using a 2- meter long plastic raceway containing several types of cables found in commercial buildings. The raceway was illuminated with HPEM transients inside a gigahertz transverse electromagnetic (GTEM) cell and with low power fields inside a reverberation chamber (RC). The tests revealed that at low and intermediate frequencies, low voltage power cables are more susceptible compared to telephone or network cables. At high frequencies, the coupling is dominated by connector apertures and discontinuities and load unbalance. As expected, the best performance was obtained with the use of shielded twisted pairs. The obtained transfer functions can be used for bounding the disturbance levels in IEMI risk analyses for different types of CIs.

One of the challenges in the calculation of the IEMI disturbances with the use of transmission line (TL) theory is the possibility of defining a reference conductor for the evaluation of the common and differential mode signals. Office buildings contain very long cablings that are generally floating inside raceways or conduits that are not necessarily close to metallic surfaces. The applicability of the TL theory in evaluating differential mode signals in two-wire lines floating above a ground plane was studied through comparisons with full-wave simulations. It was found that the presence of the ground plane can be disregarded in the calculation of the characteristic impedance of the lines, when the height of the wires is larger than about twice the separation distance between them. Also, the results showed that the validity of the TL theory is conditioned upon an electrically short distance between the differential wires, regardless of the distances above the ground plane.

The propagation of high frequency IEMI signals along power/communications lines is affected by dispersion effects that will significantly damp the waveforms beyond a certain distance due to the conductive and dielectric losses. TL theory is used to assess the effect of both types of losses in the dispersion of injected IEMI signals along power and communication cables as a function of the propagation length. A TL model of the low voltage power cabling of the plastic raceway was developed and in order to validate the models, the numerical results were compared against measurements obtained using frequency and time domain techniques.

Some critical facilities include complicated cable assemblies including individually shielded cables, overshields, and multi-pin shielded connectors. The electromagnetic coupling to such cablings is governed by the so-called overall transfer impedance of the assembly. General considerations and guidelines for the application of the TL theory for evaluating the overall

transfer impedance of complex cable assemblies are given. The obtained simulation results were found to be in good agreement with the experimental data up to frequencies of about 500 MHz. It was found that the generally overlooked contact impedances between the cable shields and connectors, and the impedance of the connector backshell interconnection to the equipment chassis play a significant role. Finally, an improved model for estimating the transfer impedance of a two-layer braided shield is also proposed and validated using experimental data.

Keywords: Intentional electromagnetic interference (IEMI), critical infrastructures (CI), high power electromagnetics (HPEM), electromagnetic compatibility (EMC), transmission line (TL) theory, Blumer index

Acknowledgements

I have finally reached my time at the EMC laboratory of EPFL and it will certainly be very difficult to include in this acknowledgement the long list of names to whom I owe this triumph.

I have been blessed and privileged to work under the direction of Prof. Farhad Rachidi, who enabled my scientific career at international level and has always kept my back in all my commitments to improve at professional and personal extent. His support, diplomacy, patience, and accurate advice have driven my achievements during this past six years. Me and my family, we will always keep him in our hearts.

I owe also very deep gratitude to Dr. Isabelle Junqua from ONERA who followed carefully my work from Toulouse; and with whom I shared an office during a wonderful month of deep discussions about electromagnetics back in 2014. Her critical look contributed to a more profound and rigorous approaching of the matters discussed in this thesis.

My most sincere gratitude goes also to Prof. Rajeev Thottappillil from KTH, Prof. Anja Skrivervik from EPFL, and Prof. Marcos Rubinstein form the University of Applied Sciences of Western Switzerland for accepting the revision of my manuscript and acting as juries of my final dissertation. Also, to Prof. Rachid Cherkaoui from EPFL for accepting the presidency of the jury during the private defense of this thesis.

Let me thank again Prof. Marcos Rubinstein because he is also a good friend and colleague whose advice helped in the elaboration and improvement of the results of this work. He was always available for discussing the many issues encountered during the projects.

I am very grateful to my friend and colleague Prof. Felix Vega from the National University of Colombia and ancient member of the EMC laboratory of EPFL. Thanks to him I made my way to Switzerland. The many discussions and works together in the area of HPEM constitute a major input for elaborating the first part of this work.

I will never forget the moral and technical support of my friend and colleague Dr. Carlos Romero. He significantly contributed to the development of the HPEM tests performed in the GTEM cell in Bern.

Thanks are also due to my colleague Gaspard Lugrin of the EMC laboratory. We have worked together in the projects dealing with the IEMI threat to CI and we are coauthors of a big majority of the articles that support this work.

I want to thank Dr. Jean Philippe Parmantier for enabling my collaboration with ONERA and the theoretical discussions about the validity of transmission line theory for assessing IEMI in civil infrastructures. Also, to my friend Solange Bertuol from ONERA for her support during these years of collaboration and her advice in the generation of codes for manipulating CRIPTE.

I am also deeply grateful to Bertrand Daout from Montena Technology for the long discussions about the limitations of HPEM generators and the useful advices during the measurements performed in this work.

Thanks are also for Marc Sallin, Werner Hirschi and again Bertrand Daout for the support and flexibility during my first months in Montena while working in parallel in the redaction of this manuscript. Without your help, this work would not have finished on the expected delays.

My gratitude goes also to: Markus Nyffeler and Pierre Bertholet from Armasuisse, for the constant financial and experimental support received for carrying out the studies presented in this thesis; Dr. Ian Flintoft and his colleagues in the University of York for the exchanges and collaboration during the measurements with the reverberation chamber; and to Dr. Chaouki Kasmi from the ANSSI for the long discussions and his support during the experiments to validate the implementation of TL models for modeling the propagation in low voltage power network.

I was very lucky to count with the moral support of my laboratory mates who made my life easier during the tough periods of writing. Thanks to my office mates Lorenzo Reyes, Dongshuai Li, Enrica Scolari; and to the Iranian team Reza Razzaghi, Mostafa Nick, Maryam Bahrami, Mohammed Azadifar, and Mokthar Bozorg. This document would not have been possible without the silent help of Omid Alizadeh, who may be does not know, but the entire laboratory has used the format of his manuscript for writing the thesis.

Thanks to Andrée Moinat and Sophie Flynn who made my life easier in whatsoever was needed for achieving the projects. Your help and your company were highly appreciated during the stressful period while finalizing the many ongoing projects.

This achievement is also thanks to the constant support and guidance of my mother who has taught me perseverance and the forward thinking to make our and others life better. She and my aunts and uncles are the inspiration for pursuing my career.

Finally, I have an infinite indebtedness with my wife and friend Lina who has supported every year of this work and who has backed me up during the difficult periods since my arrival to this country. Her constancy and company have been my moral motor for achieving such a long journey. She also contributed with the graphic layout of several of the presented plots.

Contents

List of Acronyms

AC	Anechoic Chamber
ANSSI	Agence Nationale de la Sécurité des Systèmes d’Information
ATM	Automatic Teller Machine
BFP	Breakdown Failure Probability
BLT	Baum-Liu-Tesche
BWO	Backward Wave Oscillator
CC	Control Center
CDF	Cumulative Distribution Function
CIGRE	International Council on Large Electric Systems
CIs	Critical Infrastructures
CM	Common Mode
COTS	Commercial Off-the Shelf
CW	Continuous Wave
DM	Differential Mode
EM	Electromagnetic
EMC	Electromagnetic Compatibility
EMP	Electromagnetic Pulse

EMT	Electromagnetic Topology
FEL	Free Electron Laser
FERC	Federal Energy Regulatory Commission
FFT	Fast Fourier Transform
FO	Fiber Optic
FTA	Fault Tree Analysis
FWHM	First Width at Half Maximum
GTEM	Gigahertz Transverse Electromagnetic
HEMP	High Altitude Nuclear Electromagnetic Pulses
HIRA	Half IRA
HPEM	High Power Electromagnetic
HPM	High Power Microwaves
ICT	Information and Communications Technology
IEC	International Electrotechnical Commission
IEEE	Institute of Electrical and Electronics Engineers
IEME	Intentional Electromagnetic Interference Environment
IEMI	Intentional Electromagnetic Interference
IRA	Impulse Radiating Antenna
ITU	International Telecommunication Union
LAN	Local Area Network
LPM	Low Power Microwave
LVP	Low Voltage Power
MILO	Magnetically Insulated Line Oscillator
MPM	Matrix Pencil Method
MSE	Mean Square Error

MSC	Mode Stirred Chamber
MTL	Multiconductor Transmission Line
NEMP	Nuclear Electromagnetic Pulse
p.u.l.	per-unit-length
PC	Personal Computer
PDF	Probability Distribution Function
PE	Polyethylene
PTD	Physical Theory of Diffraction
PTFE	Polytetrafluoroethylene
PVC	Polyvinyl Chloride
PWB	Power Balance Method
RC	Reverberation Chamber
RF	Radio Frequency
RFC	Radio Frequency Coaxial
SCADA	Surveillance, Control And Data Acquisition
SOLT	Short Open Load Through
STP	Standard Temperature and Pressure
SWO	Switching Oscillator
TEL	Telephone
TEM	Transverse Electromagnetic
TL	Transmission Line
TWP	Twisted Pair
TWT	Travelling Wave Tube
UTD	Uniform Theory of Diffraction
UWB	Ultra Wide Band

VNA	Vector Network Analyzer

1 Introduction

1.1 What is IEMI and why do we study it?

IEMI or Electromagnetic Terrorism is a relatively new threat to electronic and electric systems that has attracted a great deal of attention within the EMC community during the past two decades or so. According to the IEC definition [1], IEMI is the intentional malicious generation of EM energy introducing noise or disturbances into electric and electronic systems, thus disrupting, confusing or damaging these systems for terrorist or criminal purposes. It is well established that sufficiently intense EM fields in the frequency range of 200 MHz to 5 GHz can cause upset or damage in electronic systems [2] and therefore, can affect almost every economic and social infrastructure that is based on ICT services [3]. In the past, the few key electronic systems that existed worked at higher voltage levels than today's machines and at lower frequencies, making them less sensitive to EM disruption [4]. Today, the vast majorities of CIs are or will be operated through digital control, thus, bringing devastating effects on the economy and in people's lives in the case of a successful IEMI attack [3, 5].

In order to quantify the impact of IEMI on critical systems, the EM environment created by IEMI sources needs to be characterized. In addition, critical components and subsystems of the CIs that might be the target of IEMI attacks should be identified. In this regard, ICT infrastructure is expected to be one of the key potential victims. Proper functioning of the ICT systems is becoming a major issue for reliable and secure supply of electricity since they support the power system operation, critical monitoring and control functions. It has been shown [6-14] that an IEMI attack could cause a wide range of effects on electronic components and processors, ranging from malfunction to permanent damage. A recent study has pointed out the crucial role of ICT in recent blackouts over Europe and North America [15].

Among various terrorist threats, IEMI can be attractive to potential attackers since it can be undertaken anonymously and at some distance away from physical barriers [16]. Also, unlike other means of attack, EM weapons can be used without much risk since an EM attacker can try and try again, and no one will notice until computer systems begin to fail (and the victims may not know why) [4]. Possible distances for sabotage of unprotected ICT equipment using small, suitcase-size radiating sources are estimated to be of the order of 50 meters and, up to 500 m for larger sources that might be fitted into a van [12]. Recent studies by Russian scientists [17] showed significant effects of injected pulse disturbances on power, telecommunication, or grounding circuits outside the controlled region of power substations causing upset and damage of typical power system control equipment, including a SCADA terminal.

Moreover, criminals and terrorists are already able to build EMI sources that can generate high-level transient radiated and conducted electromagnetic disturbances [8, 16]. There are several reported cases of criminal IEMI attacks that have not been fully divulged for the sake of security; but their analysis has allowed to identify the motivation and technical skills of the culprits, the characteristics of the generated IEMI environment as well as their effects on the target systems [18].

The IEMI threats can be acknowledged as a reminiscence of the HEMP era [19], in which the relatively new and transportable HPEM weapons [20] have redefined the field amplitudes and frequencies under study, and therefore, the traditional analysis and protection methods. This threat is now recognized by international organisms such as URSI [21] and IEEE [22] and, as a result, IEMI concerns have been the subject of workshops and technical sessions in recent scientific symposia (e.g. [8, 23]).

HPEM source technologies can radiate EM spectrum from tens of MHz to several GHz, frequencies that are significantly higher than those associated with lightning and HEMP. For comparison, Fig. 1.1 illustrates a rough estimation of the electric field spectra generated by different EM phenomena like lightning, HEMP, classical industrial EMI, UWB sources, and narrowband sources [1]. Notice that the spectral density of lightning and HEMP are higher than that of UWB or some of the narrowband sources. In this work, we have only considered IEMI sources that are susceptible to be transported. Therefore, neither HEMP nor heavy HPM sources have been included as possible threats within the framework of this thesis.

1.2 Response of CIs to IEMI

Although the susceptibility of individual electronic systems to IEMI sources has been the subject of many investigations during the past two decades or so (see a list of relevant references in [24]), there was little work before 2010 on the response of large and extended infrastructures, such as power systems, airports, communications facilities, etc.; and their relevant equipment [25-28]. Among the few efforts, the vulnerability of electrified railway facilities to IEMI [12, 14] and the general mitigation and assessment methodology against IEMI [28, 29] were subject of investigations in Uppsala university.

As part of another initiative started in early 2007 in Sweden, a consortium was created involving Sweden, the Netherlands, and Lithuania to assess the risks, and take measures to prevent the disabling of SCADA systems as a result of an IEMI attack [27]. The consortium also initiated a program in which brings together stakeholders of the transmission and distribution systems along with experts in IEMI to analyze the possible outcomes of an attack against the Swedish grid.

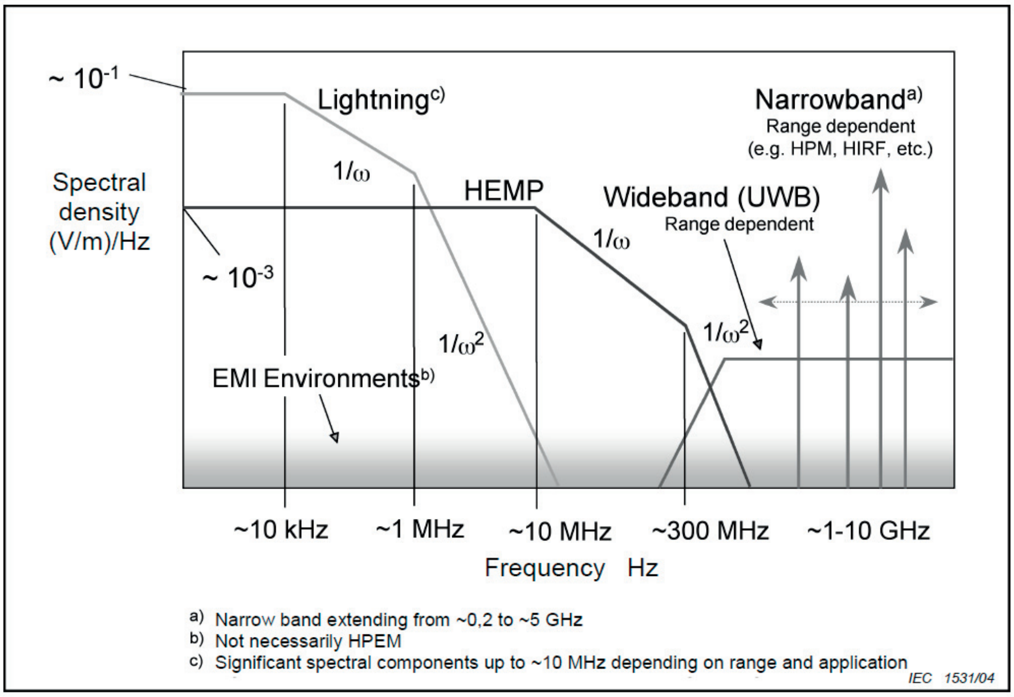

Fig. 1.1 Chart presenting the comparison of the approximate spectra generated by different EM disturbances. Taken from [1].

The commission to assess the threat to the United States from an EMP Attack has published a very comprehensive report containing a description of the potential vulnerabilities of the US critical national infrastructures to EMP threats, with emphasis on NEMP [30]. In the same study line, Metatech Corporation presented a report in which the possible impacts of IEMI in the US power grid were assessed [31]. In both documents, an outlook is presented of a test program targeted at identifying thresholds at which significant control and protective components for electrical systems would begin to fail through disruption, false data acquisition, and permanent damage. Very recently, in 2010, the US House of Representatives approved a new bill, HR-5026, known as The GRID Act. The bill enables the FERC to mandate protection of the power grid from IEMI. In [31], several vulnerable electronic devices were identified in the power generation and transmission systems. Coupling strengths that resulted in either a reboot or a reduction of the life cycle of the affected hardware were measured. The effects observed on the tested equipment included direct malfunctions of some tested control elements, loss of calibration data which required the reset of the device, loss of data transmission and, what could be worse, false measurements from the sensors. In general, the response of the tested equipment was found to be highly variable. Nevertheless, the tests performed in [30] showed that every tested SCADA system failed when exposed to the simulated NEMP environment. Many of these results can be extrapolated to the IEMI environment since the frequency ranges and amplitudes in some cases could be the same.

As a consequence, at generation facilities, the upset of protection and control systems could cause the plant to trip or trigger a controlled emergency shutdown. The operations at transmission substations are generally operated by using different communication strategies that could also be vulnerable to IEMI since the sensors, communications and power connections are generally found outdoor with either buried or overhead cabling. If communications were completely interrupted, it is still reasonably possible to continue operations. However, the restoration without some form of communication would not be possible [30].

At the distribution level, the IEMI threat appears to be less dramatic at this time since it has been found that these networks barely run with ICT equipment. It is believed that distribution networks can be significantly affected only by arcing, which in principle should not occur in the case of IEMI attacks due to the low expected amplitudes (in the range of 10kV/m or less). However, in view of the trend towards smart and distributed energy systems, it can be anticipated that distribution systems will become more vulnerable to such disturbances.

Besides studying the threat against the generation, transmission, and distribution networks themselves, it is of interest to assess the control paths at power control centers. From previous studies [30-32], it is expected that a significant fraction of all remote control systems could be easily disabled with traditional conducted IEMI weapons. They can be very effective because of their large energetic content at low frequencies. Several studies show that conducted IEMI propagates easily in buildings through LVP and/or grounding networks [17, 33-35]. It has been found that voltage levels between 0.5 to 1 kV could be enough to induce a perturbation on traditional PCs [31].

The global study of the risk of critical facilities has become necessary to quantify the need of hardening and ensure business continuity. A method for the systematic analysis of the IEMI risk of a critical facility from the view point of the system owner has been recently proposed in [36]. This method combines the IEMI source characteristics, the susceptibility data of the components, and an FTA for calculating its failure probability after running several Monte Carlo simulations. The practical implementation of such strategy has not been fully investigated and there are still open questions about the feasibility of such detailed analysis in complex scenarios.

In 2012, the European Community sponsored three FP7 research projects to ensure the security of the citizens from threats posed by IEMI [37]: STRUCTURES [38], HIPOW [39], and SECRET [40]. The projects were aimed at generating awareness in the national policy makers about the IEMI risks faced by modern CIs (STRUCTURES and HIPOW) and railway systems (SECRET), and developing improved protection strategies for mitigating their vulnerability. The STRUCTURES project was focused on the assembly of numerical tools to analyze the EM interaction of different infrastructures with the environment generated by IEMI sources [41]. To this aim, the EMT concept was used to decompose the general interaction problem into simpler sub-problems that were solved with the appropriate method. The EMT concept has also been used in the HIPOW project [42] for calculating the EM environment inside buildings with the aid of the PWB method. Further explanations about EMT and the state of the art in numerical methods for calculating the EM interaction of complex systems will follow in the next subsection.

It is important to mention that many of the findings of this thesis were obtained from the work performed by the author in the framework of the STRUCTURES project, and two national projects sponsored by the Swisselectric Research Consortium and the HPE Laboratory of the Swiss Federal Department of Defense – Armasuisse. The former project was entitled “Impact of IEMI on Electric Power Systems”. The final aim of the project was to propose guidelines for the mitigation of the risks of an IEMI attack to the Swiss power grid. The latter project was entitled “Study of the propagation of IEMI interferences along transmission lines”. This project aimed at understanding the possibility of studying the coupling and propagation of IEMI disturbances along commercial lines and buildings with the use of the TL theory.

A new project was recently initiated in Sweden aimed at maintaining the functional safety of CIs under an IEMI Attack [43]. Within this project, experimental results on the shielding effectiveness of window panes and energy saving windows were obtained [44].

1.3 Numerical analysis methods for IEMI

A general view of the state of the art of the numerical simulation tools for the study of the EM interaction with complex systems is presented in this section, which draws heavily from [41].

Due to the complexity of the CIs and the difficulty in obtaining experimental data, the use of numerical simulation tools to evaluate the effect of IEMI disturbances is desirable. Substantial efforts have been made during the last three decades to assess EM field coupling to structures and to develop protection against EMI (e.g., [45-49]). Outstanding progress in numerical EM simulation tools and computational power have made possible a more detailed and accurate modeling of complex geometries that may be encountered in the real world. With the appearance of IEMI as a new threat to society, new challenges have been posed to the community in terms of the need for methodologies to address the compatibility of facilities against radiated and conducted interferences with ranges of frequencies and amplitudes that may differ from the traditional disturbance sources (e.g. lightning, industrial noise, communications broadcasting). This has led to the trend of providing more efficient modeling strategies for analyzing the response of large complex systems such as airplanes [50], cars [51, 52], or helicopters [53]; and critical facilities such as electrified railway facilities [12], and electric power infrastructures [27, 54]. The main issues that arise when considering the analysis of large complex systems are the big amount of required memory and CPU time for handling such simulations, and the possibility of including the physical models of the generally neglected components(materials, junctions, slots) that are required to obtain accurate description of current distributions [53].

1.3.1 Electromagnetic topology

In order to perform approximate analyses of the response of complex systems, the EMT concept [55, 56] has played a key role since it permits dividing a complicated chain of EM interaction events into a number of simpler parts. Within an EMT-based analysis, the response of a system is obtained by considering independently all the interaction problems that occur; starting from the knowledge of the incident field and ending with the internal component response [46].

Civil infrastructures like office buildings or commercial infrastructures without any special EMC requirement are typically designed without an EM topological division of zones. This complicates the decomposition of CIs into topological layers since they are not very well defined. Also, many of the EM hardening concepts can be violated. Conceptually, it is easier to estimate the response at a specified location inside the CI with the aid of an EMT diagram because the interaction mechanisms that are responsible at each stage of the EM penetration can be described by separate transfer functions. The chaining of all the associated transfer functions will constitute the so-called interaction sequence diagram (for more information see, e.g., chapter 1 of [49] or [53]). The interaction sequence diagram of systems exhibiting characteristics similar to the CIs under study have already been addressed in the literature (see Fig. 1.2).

According to Fig. 1.2, in many practical cases the largest contribution to a response within the system is due to transmission lines which provide a direct propagation path from one point to another. Thus, the analysis could be carried out by evaluating only the contribution of direct connections to the volume under test.

1.3.2 Simulation techniques at low or intermediate frequencies

At low or intermediate frequencies, three different types of fully validated numerical tools can be used to solve the coupling problem [53] at each shielding level:

1.3.2.1 Three dimensional full-wave simulation codes

In 3-D full-wave numerical tools, the problem is formulated in terms of formal solutions to Maxwell's equations and the appropriate field boundary conditions. Fields are calculated in the exterior and the interior of the structures using either a time domain, or a frequency domain technique. Even though full-wave approaches can in principle be used at very high frequencies, their application to cases when the size of the system is much bigger than the wavelength might become prohibitive in terms of computation time and memory requirement.

Three main families of fully validated codes may be distinguished [53]: Volumetric codes, where the whole calculation volume is meshed into volume shells (FDTD for example); Surface codes, where only the surfaces of the diffracting object are meshed (MoM for example); and Asymptotic techniques which are based on an asymptotic formulation of Maxwell's equations (PTD and UTD for example).

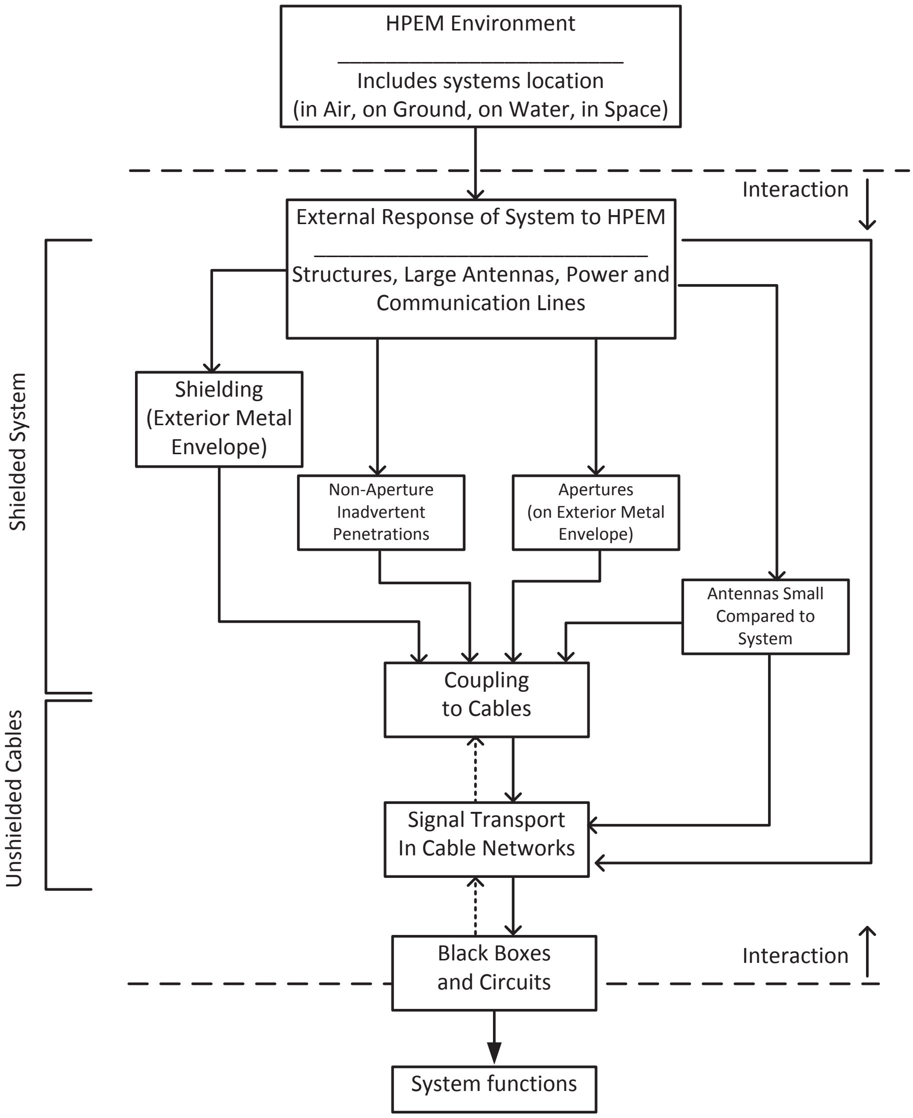

Fig. 1.2 Interaction sequence diagram for shielded systems with unshielded cables. Figure adapted from [49].

1.3.2.2 Cable network codes

Cable network codes are based on the TL theory and are used to solve the problem of electromagnetic field coupling to wires and cables, using the previously determined field distributions inside the topological shielding level. Within the TL models, several key aspects of the wiring in complex systems such as cable shield properties, frequency dependent dielectrics, or inhomogeneous propagating media, can be included independently from the cable lengths because the bundles are specified by their cross-section.

It is important to highlight that TL models do not account for radiation and assume a quasi-TEM distribution of the fields along the transmission lines. Such condition is generally observed when the MTL cross section (e.g., height over the reference plane) does not exceed a fraction of the minimum wavelength (one tenth or so) [46, 57]. Depending on the frequency, it may be desired to account for the backscattering of cables in order to identify resonant behaviors in the cavities running the wires. However, as far as the TEM mode approximation is concerned, techniques are available to handle the field emission due to cable network-induced currents with 3D codes or reciprocity-based approaches [48, 53].

The EM coupling to cables is represented in the TL model as a set of voltage and/or current generators distributed along the wires and expressed in terms of the incident electromagnetic fields, namely the fields evaluated in absence of the transmission line. The incident electromagnetic fields can be first evaluated using a full-wave approach and then imported into the cable network codes. This is how the link between 3D full-wave codes and cable network codes is made. The largest advantage of such an approach is that the calculation of the incident fields, which takes time whatever full wave technique is used, is made once for all in the absence of the cable bundles. Afterwards, the network code solving the field-to-transmission line interaction can be launched for various cable topologies, provided that the cable routes remain the same [50].

Another important advantage of working with TL models is that they can be used with an EMT formalism [58] in which the wiring network is decomposed into a set of tubes and junctions respectively representing the network branches and nodes. Currents on the branches are obtained from the frequency domain solution of the so called BLT equations describing all the interactions within the network [50]. The junctions are described in terms of any type of Z, Y, or S multiport matrices derived from analysis or measurements.

When dealing with shielded cables, the coupling between the external currents flowing in the cable screens and the internal induced voltages and currents is made through the so-called transfer impedance and admittance of the screens [48, 59]. The theoretical estimation and measurement of the transfer impedance of common cables at frequencies above 100 MHz become an issue, and poses a difficulty for implementing the MTL models.

Recent efforts to extend the cable models at higher frequencies have provided with methods to generalize the TL models to account simultaneously for the propagation and radiation effects

[57, 60-62]. These methods are still under development and have only been validated for simple geometrical setups.

1.3.2.3 Electrical circuit codes

Once the currents and voltages at the cable terminations (equipment inputs) are determined, electrical circuit codes such as SPICE can be used to solve the internal equipment response [53].

1.3.3 Simulation techniques at high frequencies

At high frequencies, where wavelengths are much smaller than the dimensions of the system, the use of the 3D codes and the circuit and TL theory for the analysis of CIs will get complicated. Facilities are not generally conceived from an EMT philosophy and some typically made assumptions in EMT analysis (e.g. good shielding approximations, or small apertures) may not be applicable. Furthermore, high-frequency responses of systems are very sensitive; i.e. very small variations in the geometry, may result in very large variations in the field distributions [53]. Since the design and the placement of components in complex systems at high frequencies are not well controlled, deterministic models are not favored to be the appropriate methodologies for estimating the response.

It has been suggested that statistical approaches may provide more appropriate tools for obtaining the EMC behavior subject to random input parameters [63]. A common approach to tackle such a problem has been for years through the well-known Monte-Carlo approach which requires a large number of trials of deterministic simulations to obtain the PDF of the output of the system [64]. In the kind of models required for EMI studies, where running a single deterministic simulation represents a major computational task, the use of the Monte Carlo approach might be prohibitive in terms of computation time. Methods like the unscented transform [63] or the stochastic collocation method [65], among others, which allow inferring the PDF, or at least some of its moments, from a small number of simulations, have shown to be promising. However, to the best of the author’s knowledge, their accuracy in modeling real system configurations have not been quantified in the literature.

In the context of IEMI, a statistical approach provides estimates of mean coupling but it does not provide any worst case scenario. Physical uncertainties (or variability) in EM quantities are generally modeled with Gaussian distributions. This implicitly restricts the analysis to the mean contributions of the observables. In security and safety contexts, this kind of restriction may reduce the analysis soundness since Gaussian approximations are known to fail in accurately modeling rare events which are the most critical in our applications [66]. The application of the extreme value theorem and more precisely the excess model has shown to be a useful tool to avoid the underestimation of the probability associated with critical extreme events [67]. In [67], the Generalized Pareto Distribution was used to extrapolate the very high level of voltages and currents that can be induced by IEMI in power distribution networks.

The PWB method [68] is another statistical macroscopic approach for the EM coupling into oversized complex systems. The PWB method is based on energy equilibrium and has been shown to provide satisfactory results at high frequencies. This approach is based on the assumption that the EM fields inside the enclosures of complex systems behave as random variables, similarly to what happens in an MSC [69]. BLT-like equations can also be derived to solve for the power densities and dissipated powers at each node; and as a consequence, the PWB method can also be described with an EMT formalism [68]. It has recently been shown that PWB can be effectively used to calculate the transfer functions between different areas of a building and the exterior of it in order to assess the EM environment in potentially critical rooms subjected to an IEMI threat [70].

1.4 IEMI standardization and recommendations

Given its importance to society, the protection of military and civil infrastructures is constantly assessed by international organizations and procurement agencies. The global risk of CIs being unclear, at the moment, there are not normative standards enforcing a safety qualification of systems against IEMI. However, important advances have been made in the last years in the generation of recommendations and standards for testing the immunity of electronic systems and designing general protection strategies. In what follows, an overview of the standards and recommendations generated by IEC, IEEE, ITU, and CIGRE is given.

1.4.1 Standards and recommendations according to IEC

The subcommittee SC77C of IEC has dedicated since 1992 lots of efforts to provide recommendations and protection guidelines for HEMP, and more recently, for HPEM and IEMI. This subcommittee is perhaps the most active committee in this field and usually other standardization committees (IEEE, ITU, CIGRE) make reference to the general guidelines, environment definitions, and specific protection and hardening strategies defined by IEC-SC77C [71].

A summary of the standards published by the SC77C of IEC is presented in Fig. 1.3. In this chart, the standards dealing with HEMP protection are presented with black lines, and the standards dealing with HPEM/IEMI environments are presented with red lines. Documents under preparation are presented with gray lines. There are six recommendations available for the study of the protection against HPEM/IEMI. Among these, three documents deal directly with the issue of protection and susceptibility evaluation for HPEM/IEMI environments.

The recommendation 61000-1-5 [32] covers the general definition of the HPEM threat and provides a general overview of the expected effects in civilian systems. This is the first document produced by IEC in which specific mention to the IEMI threat was made. A general description of the expected IEMI environments and the documented effects in the available literature are presented. Notice that the considered sources in the elaboration of this standard are up to 2004. In this thesis, we have made an effort to revisit and update the survey of existing IEMI sources.

The final chapter of this recommendation deals with a brief overview of the suggested protection methods. The document focuses in distinguishing the classical EMC measures that can be used for the mitigation of the so-called front-door coupling (deliberate penetration) and the so-called back-door penetration (inadvertent) [72]. The need of providing the system with alternative protection methods including active monitoring, system redundancy, error detection and correction is also emphasized.

The recommendation 61000-5-9 [73] presents a methodology that can be used to assess the impact of HEMP and HPEM environments on electronic systems. Since the proposed methodology is very general, some application examples are provided in the form of annexes to the main document. However, the document does not include safe operation techniques.

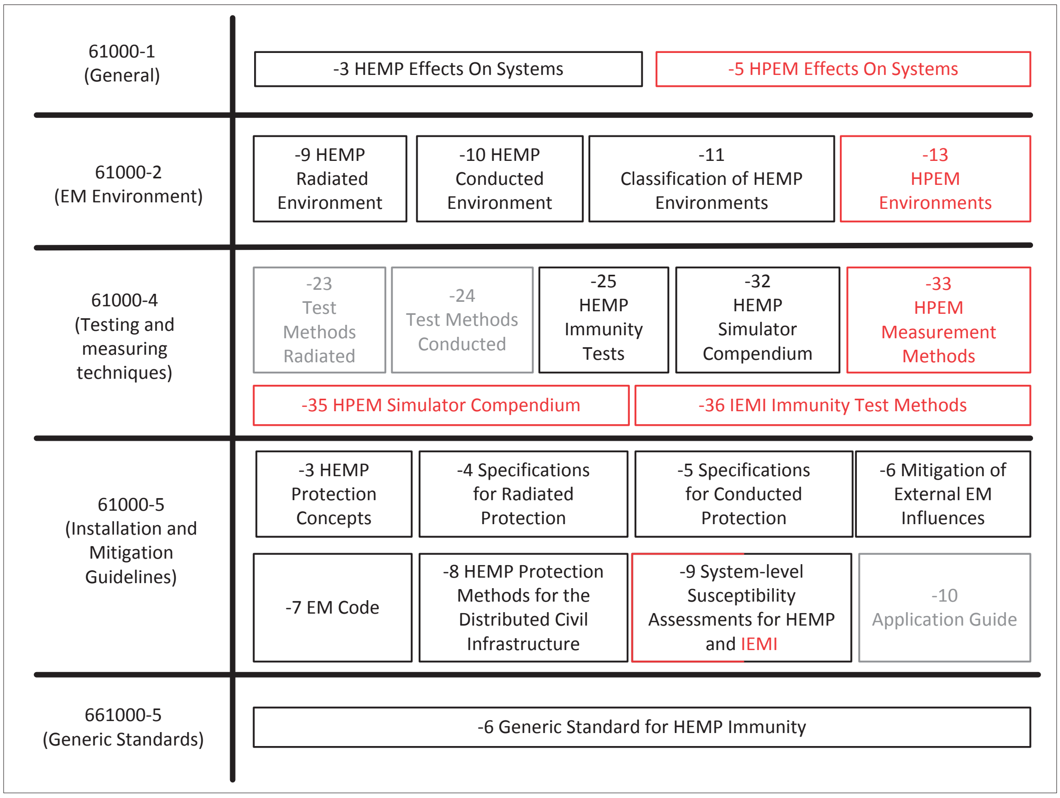

Fig. 1.3 Overview of the documents produced by the subcommittee SC77C of IEC. Image adapted from [71].

This document can be used to determine the status of a particular system (including vehicles, aircrafts, and small ships), subsystem, or equipment, with respect to hardening. The proposed method is based on low-level (transfer function) and high-level tests (to consider nonlinear failures). The techniques presented in this recommendation are very useful for the determination of the hardness of a CI as it will be shown in Chapter 2.

Similarly, the recommendation 61000-4-36 [74] can be used to define the test level conditions for the assessment of the immunity of equipment and systems. The strategy considers several sources that have been classified according to their far-voltage[1] and other criteria like the required technical preparation of the attacker, and the deployment scenarios. The existing protection level due to the location of the equipment is evaluated based on previous studies of building attenuation. Notice that the experimental campaigns presented in Chapter 4 and the calculations performed in Chapter 5 and Chapter 6 can also be considered for the analysis of the attenuation due to cable coupling and propagation along commercial lines. However, it is advised that the protection level to be calculated is based on on-site measurements.

Finally, the actual environment in the equipment surrounding is estimated by using the path loss due to the distance from the source and the equipment enclosure. The test limits are derived assuming that the victim equipment is placed inside a building that is at a certain distance from a typical IEMI source. After understanding the EM environment, the assessment options presented in Fig. 1.4 [74] can be used to decide the test method that will emulate the equipment stress under real conditions.

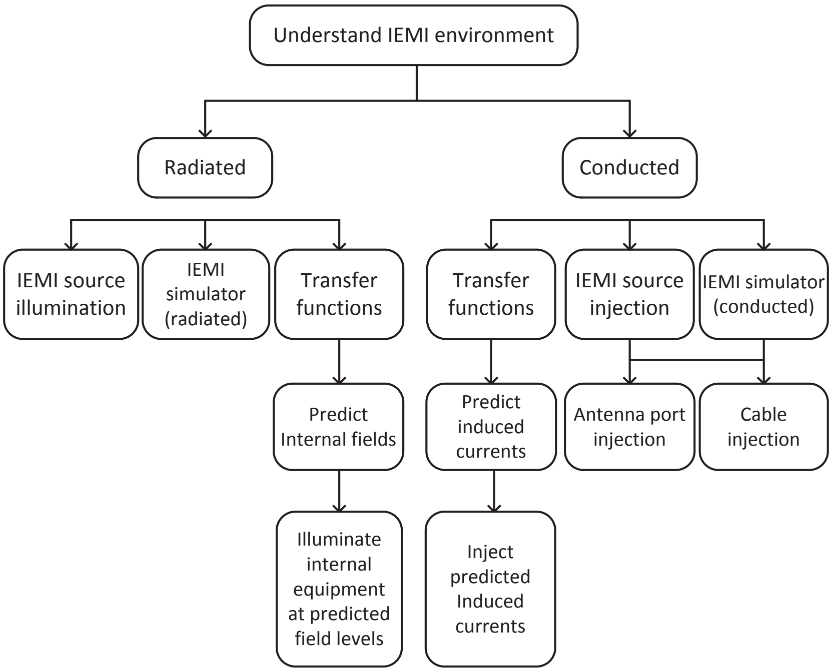

Fig. 1.4 Assessment options for immunity testing according to IEC 61000-4-36 [74].

---

[1] The far voltage is defined as the range-normalized radiated E-field (see Chapter 3).

Depending on the adopted tool, there are generic suggested test levels for radiated and conducted susceptibility for all kind of sources:

(i) Hyperband, mesoband, and hypoband illumination [2];

(ii) Damped sinusoid, CW or impulse injection.

To this end, the source inventory and characteristics presented in Chapter 3 are very useful in defining the required test levels and the source type.

1.4.2 Standards and recommendations according to ITU, IEEE and CIGRE

Other standardization committees dealing with IEMI include ITU, IEEE and CIGRE. Some recommendations have been recently published by each of these organizations and will be briefly described in what follows. As it has been already mentioned, some of these documents make reference to standards and recommendations of IEC.

ITU recommendation K81 discusses the HPEM protection of telecommunication systems. It proposes a classification scale for IEMI sources and intrusion areas. It also studies the expected field levels of several HPEM sources and derives required security levels according to the standards complied with by the equipment. Finally, suggested protection levels for data centers and similar facilities are provided.

IEEE has elaborated the standard P1642 [75] for the specific protection of publicly accessible computer systems (ATMs, cash registers, computers in stores, banks, etc.). The standard recommends protection levels based on a physical security approach and EM topological zoning, and the use of modern strategies like fault tolerant computation methods, monitoring and alarms. A similar method to that used in K81 for calculating the required protection levels for ensuring safe EM environments is also used in this standard.

CIGRE has elaborated the recommendation 600 [76] for the protection of control centers in HV substations. After several visits to HV substations and specific immunity testing of the control equipment, CIGRE recommends required protection levels by assuming a typical IEMI weapon in the surroundings of the facilities. The protection methods include cable layout, shielding, ferrite installation, SPDs installation, etc.

1.5 Objectives and original contributions of this thesis

The present thesis constitutes a contribution to the existing methods for the analysis of the vulnerability of critical systems to IEMI. Throughout the study, three main research questions guided the author in the elaboration of the research work presented in this thesis:

(i) The need of a qualitative method for the assessment of a CI: one of the difficulties of the application of the existing IEMI analysis techniques is the complexity of the CIs under study and therefore the prohibitive time required for an accurate estimate of the IEMI risk.
(ii) The need of an updated and systematic classification of the realizable IEMI sources: the correct understanding of the expected IEMI environments will define the required protection techniques.
(iii) The need of experimental and numerical methodologies to predict the response of commercial cables at frequencies representative of IEMI.

This manuscript contains the most relevant studies and achievements obtained by the author in the framework of different collaboration projects between the EMC Laboratory of EPFL and other national and international laboratories working in the field of EMC, HPEM, and protection against electromagnetic attacks. The original contributions presented in this document have resulted in publications in peer-reviewed journals and presented at international conferences. A summary of the main publications related to the work presented in this thesis is presented in Tab. 1.1.

Tab. 1.1 Summary of the publications supporting this thesis

Reference	Year	Research Area	Presented at	Chapter
[77]	2012	IEMI Risk Assessment	EUROEM 2012 Conference	2
[78]	2014	IEMI Source Analysis	System Design and Assessment Notes	3
[79]	2016	IEMI Susceptibility Assessment	IEEE Transactions on EMC	4
[42]	2015	Transmission Line Theory	Joint IEEE/EMC Europe International Symposium on EMC	5
[80]	2015	IEMI Susceptibility Assessment	ASIAEM 2015 Conference Interaction Notes	5
[81]	2013	IEMI Susceptibility Assessment	ICEAA 2013 Conference	6
[82]	2014	IEMI Susceptibility Assessment	AMEREM 2014 Conference	6
[83, 84]	2015	Transmission Line Theory	IEEE Transactions on EMC	7

1.5.1 Contributions to the area of IEMI risk analysis

Assessing the risk of a critical facility against IEMI has been one of the main subjects of study in the last decade or so, and different approaches to the problem have been published in the academic literature. The methodology that we introduce in Chapter 2 is one of the many possible approaches to the study of the probability of deliberately using electromagnetic interference to stop the normal and continuous supply of services from CIs to the society. We have tried to put together all the available tools into a single methodology to carry out the so-called IEMI audit of a facility. The main objective of this methodology is to enable the business continuity management operators to take appropriate corrective and mitigation measures, based on the results of the IEMI audit.

Given the complexity of the problem, it was decided that the vulnerability of an infrastructure should be evaluated in a qualitative manner by judging the available information with regards to the consequences of interrupting the normal provision of a service, the probability of occurrence of an IEMI attack, and the preparedness of the infrastructure to withstand an attack. All these three criteria can be evaluated by the facility or EMC experts with the aid of the tools that will be explained in Chapter 2. The primary objective of the method, rather than qualifying the risk of a facility is to be able to identify the critical equipment and coupling paths that may require EM hardening.

1.5.2 Contributions to the area of IEMI source analysis

The notable progress during the past two decades in the generation of HPEM with rather transportable sources has raised concerns about the feasibility of an EM attack against critical electronic systems. Understanding the world capabilities in the development of non-lethal EM weapons is a prerequisite to design adequate hardening strategies for critical equipment. One of the latest surveys about the HPEM generation and protection capabilities around the world was published by the IEEE Transactions on EMC in its 2004 special issue on IEMI [85]. A compendium that reports the main characteristics of the HPEM facilities of several national defense agencies has been also published in 2009 by IEC [86].

Given the many advances made in the past decade, in particular in the generation of mesoband and more compact sources, we decided to revisit the survey in Chapter 3 by including new reported sources. The available sources have been classified, for the first time in a systematic way, according to their electromagnetic environment, their transportability, technological development, and cost level. We present also an overview of the possible source limitations due to physical constraints of the implemented technologies in order to provide some figures representing the maximum expected limits of a potential IEMI source. The observed general trends in the fabrication of HPEM sources as well as their expected waveform and spectral characteristics are very useful for understanding the likelihood of a given EM attack and therefore this chapter constitutes a major contribution for the planning of mitigation strategies against IEMI.

A novel technique for an efficient evaluation of the Fourier transform of the source waveforms and the extraction of their spectral characteristics is presented in Appendix A. We also propose the use of the so-called Blumer index [87] for improving the time required for estimating the bandratio of a given spectrum.

1.5.3 Contributions to the area of IEMI susceptibility assessment

In the framework of the IEMI susceptibility evaluation of a commercial building, one is interested in the expected levels of EM coupling along typical cable types inside an office; i.e. the LVP, LAN, and TEL cabling. The evaluation of wave propagation/electromagnetic coupling along cables is customarily made using the TL theory [88] which applies to uniform transmission lines with electrically small cross-sectional dimensions, where the dominant mode of propagation is TEM. The evaluation of IEMI interferences is a challenging task for a number of reasons. First, the applicability of the TL theory to disturbance sources with higher frequency content (HPM, UWB, etc.) is a questionable topic [57] since the frequency range of the interferences are typically outside the nominal range and therefore the constitutive materials, cables' cross section and connectors are not necessarily conceived for a correct propagation of the signals. Second, the random distribution of the lines inside the cable raceways and the cable imperfections create non uniformities in the propagation that are complicated to model without any experimental verification.

In order to understand the expected disturbances due to a high frequency illumination of representative cablings inside an office, without having to model the complete setup in a full-wave or transmission line environment, we have built an experimental setup consisting of a 2-meter long plastic raceway containing several LVP, LAN, and TEL cables. The raceway has been used for two experimental campaigns reported in Chapter 4. The first campaign consisted of the illumination of the raceway with an HPEM field inside a GTEM cell. In the second campaign, the same raceway was illuminated with a CW signal in a RC. For the first time in the literature, three types of cabling were investigated using an identical experimental technique in a very broad frequency range, namely from 40 MHz to 6 GHz. The transfer functions derived in this work are useful in IEMI risk analyses for many types of CIs, bearing in mind, of course, that they are derived from particular experiments.

Notice that even though it has been mentioned that very accurate modeling with TL theory is barely possible in realistic scenarios due to the random configuration of the problem, it is important to highlight that educated decisions can still be taken with the use of approximate EM models where experiments are not allowed or difficult. This is typically the case of an IEMI audit because it is not generally allowed to perform EM testing inside critical facilities, and therefore the approximate solutions obtained with TL theory become the primary asset.

The propagation of high frequency IEMI signals along power/communications lines will be affected by dispersion effects that are generally disregarded at low frequencies. One can expect that, for a specific IEMI signal, these signals will be significantly damped beyond a certain distance due to the conductive and dielectric losses. In order to further understand the governing attenuation and dispersion mechanisms at these frequencies, in the second part of Chapter 5, we used TL theory to assess the propagation of IEMI signals along power/communication cables by considering a line that is partially illuminated by IEMI, and studying the attenuation and distortion of the traveled wave as a function of the propagation length. In Chapter 6, we present the TL modeling procedure of the propagation along the LVP network of the raceway. In order to validate the models, the numerical results were compared against measurements obtained with different frequency and time domain techniques. The contributions of these two chapters are useful for understanding the important parameters that need to be considered in the TL modeling of a realistic scenario at frequencies that are beyond the classical utilization of these networks.

1.5.4 Contributions to the area of transmission line theory

One of the challenges in the calculation of the IEMI disturbances with the use of TL theory is the possibility of defining a reference conductor for the evaluation of the CM and DM signals. We deal with very long cablings that are generally floating inside raceways or conduits that are not necessarily close to metallic surfaces. Thus, the evaluation of the conducted disturbances at the input of critical equipment connected to LVP, LAN, or TEL cables requires the calculation of the DM voltage between two wires (e.g. differential signal pairs, or twisted pairs) at a height above the ground plane which is not necessarily electrically small. Provided that the application of TL theory requires lines with electrically small cross sections, the accuracy of the DM signals becomes questionable.

The analyses presented in the first part of Chapter 5 were performed for solving some open questions that were worth solving before applying the TL models for estimating the solutions of the DM propagation:

(i) As long as the DM between the floating wires is concerned, what is the influence of being closer or farther from the ground plane on the accuracy of the solution?

(ii) If the lines are electrically far from the ground plane, but they remain electrically close to each other, are the TL solutions still valid?

We studied the DM coupling due to a plane wave illumination of a transmission line composed of two wires above a ground plane - a topic that has not been specifically addressed in the literature, to the best of the author's knowledge. The results obtained using the classical TL theory are compared with full-wave solutions.

Some critical facilities include more complicated cable assemblies including individually shielded cables, overshields, and multi-pin shielded connectors. The EM coupling in such cablings is governed by the so-called overall transfer impedance of the assembly. TL theory has been successfully applied to analyze the mutual and external coupling in shielded cables. However, to the best of the author's knowledge, it has never been systematically applied to the analysis of the transfer impedance in such complex cable assemblies. Chapter 7 presents the general considerations for the application of the TL theory for simulating the overall transfer impedance of complex cable assemblies showing very good agreement with measurements up to frequencies of 500 MHz. Some of the practical issues that occur in the modeling process of various components of cable assemblies, namely connectors, pigtails and backshell are discussed and a new formulation for the evaluation of multi-layered braided shield is proposed.

1.6 Outline of the document

This document is organized following a top-down approach. The global methodology proposed for the qualitative analysis of the IEMI risk is presented in Chapter 2. The required information about the IEMI source characteristics is presented in Chapter 3. This chapter is important for defining the expected frequencies and characteristics of the sources that are used in Chapter 4. This latter presents an experimental analysis of the expected response of commercial cables that are commonly found in CIs. If experiments are not allowed due to the complexity of the device under test, the general conditions for the correct application of the TL theory in the prediction of DM coupling and propagation are introduced in Chapter 5. Chapter 6 illustrates the application of the TL theory in the prediction of the propagation of LVP cables and the experimental verification of the models' validity. In order to estimate field-to-cable coupling of complex cable harnesses, the concept of the overall transfer impedance is studied in Chapter 7. A thorough implementation and experimental validation of the TL model applied to an over-shielded cable harness is described. Finally, conclusions and future perspectives are drawn in Chapter 8.

2 Service-Based Risk Assessment

2.1 Introduction

Several methodologies that can be used to perform the audit of a critical facility and decide whether a system is vulnerable against IEMI have been proposed in international recommendations and scientific publications [28, 36, 73, 89, 90]. These strategies assume that the facilities under study have been electromagnetically designed in a topological sense and therefore, the points of entry of disturbances are easily distinguishable; which may not be the case for civilian infrastructures. Also, the evaluation of the system vulnerability according to some of these recommendations relies on susceptibility measurements that are not necessarily feasible since the infrastructures under study are critical and not usually available for testing. Moreover, the required level of detail in methodologies as e.g. [36] may result in prohibitive efforts in terms of the time and technological resources and the obtained results may not necessarily differ to those obtained with lighter methodologies.

Despite the significant advances in electromagnetic modeling during the last decades, the prediction of a failure inside a complex infrastructure with the use of computational or analytical methods is still a complex task due to the enormous amount of information required to generate a realistic model. Therefore, it is desirable to have a method in which by visual inspection and few meetings with the facility staff, the relevant information is obtained and a general assessment that identifies the possible flaws of a given infrastructure is performed. The assessment methods should rely on feasible experiments and simple analyses made with only the relevant information in order to infer the degree of hardness of a facility and the possible improvements with a reasonable amount of resources.

Many of the available publications in the area of IEMI have dealt with methods for estimating the susceptibility of specific components or subsystems, the induced interference due to cable and aperture coupling (back-door coupling [72]), or the effects of direct coupling into a reception antenna and propagation of the interference up to the low noise amplifiers (front-door coupling [72]) (see e.g. [12, 64, 72, 91-93]). On the other hand, the application of traditional methods to evaluate the overall susceptibility of large and complex infrastructures becomes prohibitive due to the large amount of subsystems and cabling. Given the high degree of uncertainty of the coupling paths in large structures, no experiments or analyses can certify the validity of a worst case scenario evaluation [90]. In practice, the audit of existent facilities is a difficult task since many of the building information are non-existent or difficult to find. Also, on-site low-power tests are generally not acceptable if they require the interruption of the activities. For obvious reasons, on-site high-power tests are neither acceptable if there is a possible compromise of ICT equipment involved in a critical process. Thus, the risk assessment methodology must remain qualitative but objective enough to provide with guidelines and hardening strategies, if required.

In order to overcome some of the previously mentioned difficulties during the evaluation of the IEMI risk of a CI, in this chapter a qualitative method called the service-based risk assessment is proposed. The proposed methodology merges the strategies proposed in previous works [29, 36, 64, 77, 91, 94-98] to qualitatively infer the IEMI risk of the *services* provided to society by a given facility. It provides the suggested methods to obtain the required information for deriving the so-called critical equipment list, the relevant coupling paths, and identifying the possible protection strategies. This method is oriented to assess the business continuity of the utilities and therefore it concentrates only on the equipment involved in the provision of important services, and considers the threats imposed by IEMI sources that are likely to occur given the accessibility constraints of the facility and the transportability of the sources.

In this approach, rather than evaluating the electromagnetic susceptibility of a complex system integrated by several subsystems and equipment, the possibility of interrupting the provision of a given *service* due to an IEMI attack is evaluated. On the other hand, it also considers the fact that critical services can also be provided by other emergency equipment or personnel, and this reduces the risk evaluation. This is the case in small infrastructures in which highly trained personnel are able to assume emergency operations with little ICT support.

This chapter is organized as follows. The method philosophy is presented in Section 2.2. The suggested scales to evaluate the so-called consequence and likelihood of an IEMI attack and the hardness of a service are presented in Sections 2.3 to 2.5. The method for the overall calculation of the service risk is explained in Section 2.6. Finally, the assessment workflow is summarized in Section 0 and conclusions are drawn in Section 2.8.

2.2 Method philosophy

It has been already mentioned that the possibilities of performing quantitative analyses during an IEMI audit are reduced and therefore qualitative analyses are easier to implement. In the service-based assessment, an EMC expert will make use of the available tools in order to evaluate the risk of a service provision. Given the time, budgetary and technical constraints, the

EMC expert will try to provide a qualitative answer to the following questions based on the available tools:

(i) What is the impact of temporarily or permanently losing the provision of a given service?

(ii) How probable is that a service could be affected by an IEMI threat given the physical conditions of the facility?

(iii) How probable is that an IEMI source could be transported and operated nearby the facility?

In traditional susceptibility investigations, the effects of disturbances in mission related equipment are described as threat levels. The threat levels imposed by a given source can be classified as (i) having no effect, (ii) capable to cause disturbances, (iii) capable to cause mission kills, and (iv) capable to cause destruction [96]. This can be regarded as a bottom-up analysis since the final effect is evaluated after exposing the equipment to different perturbations and evaluating its consequence at a higher hierarchical level.

In a service-based assessment, the analysis is top-down: the possibility of perturbing or interrupting the provision of a given service is assessed, and then the possible reasons and the equipment involved are identified. The final output is a qualitative judgment of the *risk* according to three indicators (see Fig. 2.1): the *consequence* and *likelihood* of an IEMI attack and the *hardness* of the studied service. Each of these indicators is evaluated according to several factors that will be explained throughout this chapter.

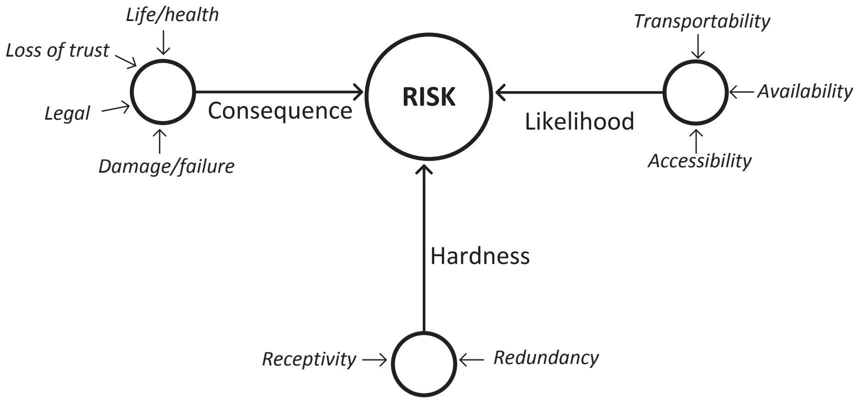

Fig. 2.1 Schematic diagram illustrating all the contributing factors for the calculation of the risk of a service against IEMI.

The risk of being able to cause an impact on the provision of a service due to an IEMI threat can be mathematically defined as the product of its consequence and its probability of occurrence [36, 94]:

$$R_i = C_i p(C_i), \tag{2.1}$$

where R_i is the risk of causing the consequence C_i, and $p(C_i)$ is the probability of occurrence of the consequence C_i.

The possibility of perturbing a service and generating consequence C_i is associated to a set of threats T_j that could induce such a failure. The probability of C_i due to all the possible threats T_j can be decomposed as the superposition of the conditional probability of C_i given that T_j exists times the probability of T_j [36, 94]:

$$p(C_i) = \sum_j p(C_i / T_j) p(T_j). \tag{2.2}$$

If many consequences are evaluated, the total risk can be calculated as:

$$R = \sum_i R_i = \sum_i C_i \sum_j p(C_i / T_j) p(T_j). \tag{2.3}$$

Thus, the risk of a service against IEMI can be understood as being:

(i) proportional to the *consequence* (impact) of losing the service temporarily or permanently (see Equation (2.1)),

(ii) proportional to the *likelihood* (probability of occurrence) of the IEMI source (see Equation (2.2)),

(iii) proportional to the probability of inducing a considerable effect given that there is an IEMI attack. In other words, the risk is inversely proportional to the system *hardness* [97]

An accurate estimation of the probabilities in (2.3) is difficult due to the many subjective criteria that have to be considered. Therefore, in what follows, the suggested scales for evaluating the *consequence*, *likelihood*, *hardness*, and *risk* of a service will be given in the form of lookup tables in which each of the contributing factors is classified according to a reduced number of levels (usually 3). These levels denote a high, low and unknown state of the factor under study. The choice of including an unknown state was previously suggested in [90] for evaluating a factor for which very little information is available during the IEMI audit. Notice that the suggested lookup tables are derived according to author's criteria and are not the result of a rigorous mathematical manipulation of the factors.

2.3 Assessing the consequences of a service loss

In order to assess the consequences of temporarily or permanently losing the provision of a service, a so-called impact analysis can be performed with the facility experts in order to decide whether the interruption of a service will:

(i) generate a *legal* sanction to the facility,

(ii) generate a *loss of trust* from the clients,

(iii) generate a *damage or failure* to a third party,

(iv) compromise the *life or health* of an individual,

(v) result in any other possible consequence.

Depending on the relevance of each consequence, an importance rating can be assigned to each of the categories and a total consequence evaluation can be derived as schematically illustrated in Fig. 2.2. While doing the impact analysis, the possibility of reestablishing the service provision in a reasonable amount of time or not being able to reestablish should be considered separately.

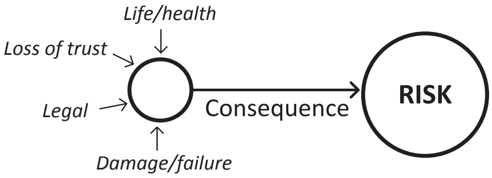

Fig. 2.2 Schematic diagram illustrating the contributing factors in the evaluation of the consequences of a service loss.

Given that the importance rating may depend on the subjective criteria of the facility experts [29], a useful strategy is to translate the consequences of a service loss into a budget percentage loss, while keeping in mind that a threat to life or health should be the most important consequence in all the possible ratings.

A suggested scale to express the total Consequence is presented in Tab. 2.1:

Tab. 2.1 Suggested consequence level scale

Consequence Level	Description
-1	Important consequence
0	Unknown
1	Less important consequence

In the above-suggested scale, unimportant consequences are deliberately omitted. Notice that the possibility of not being able to rate the consequence of a service loss is also valid in the consequence assessment and therefore the existence of an unknown level.

2.4 Assessing the likelihood of a threat

Forecasting the occurrence of an IEMI attack is a very complex task since many subjective criteria are involved. In general, the underlying assumption is that someone will deliberately attack a facility with an IEMI weapon. Therefore, in order to assign a qualitative evaluation of the likelihood of a given threat, the possibility of physically approaching the IEMI source to the facility is usually studied.

The possibility of approaching an IEMI source to a facility can be evaluated according to three factors that are schematically illustrated in Fig. 2.3:

(i) the *availability* of the source: how difficult is to build or acquire a source?

(ii) the *transportability* of the source: how difficult is it to transport and operate a source close to the facility?

(iii) the *accessibility* to the facility: how difficult is to access the facility with a source provided that the security and surveillance protocols are working?

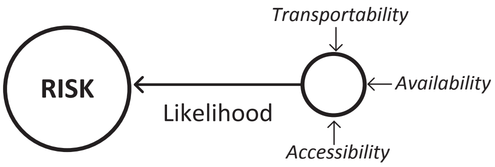

Fig. 2.3 Schematic diagram illustrating the contributing factors in the evaluation of an IEMI source likelihood.

The evaluation of these three factors are subject to the criteria of the EMC and security experts of the facility. However, some guidelines for the classification can be obtained from the available literature, as will be discussed in what follows.

2.4.1 Source availability

The source *availability* describes its attainability according to the level of sophistication of its underlying technologies. Different categorizations have been proposed in the literature to evaluate this characteristic (see a summary in [99, 100]).

2.4.1.1 Classification by Giri and Tesche (2004)

Giri and Tesche have proposed in [2] a classification of the source technology according to the following categories:

(i) Low-tech systems: characterized by a marginal performance, minimal technical capabilities, and easily assembled and deployed while hiding behind dielectric walls in trucks or similar vehicles.

(ii) Medium-tech systems: require the skills of a qualified electrical engineer and relatively more sophisticated components such as a commercially available radar system that can be modified to become a dangerous system.

(iii) High-tech systems: require specialized and sophisticated technologies and perhaps even specifically tuned to cause severe damage to a specific target.

2.4.1.2 Classification by Sabath and Garbe (2009)

In a more recent publication, Sabath and Garbe, used the term technological challenge to describe the knowledge and effort needed to design, assemble and operate a source [96]. They suggest considering the level of sophistication of the underlying technologies, the level of knowledge to design and operate the source, the availability of the components in the market, and the costs in order to classify the sources according to the following categories:

(i) Low tech systems

(ii) Medium tech systems

(iii) High tech systems

(iv) Highly sophisticated systems

Unfortunately, there is little explanation about how to decide whether a source belongs or not to each of the categories.

2.4.1.3 ITU Classification (2009)

In the same year, the term availability has been proposed in the ITU Recommendation [89] to measure both the cost and the technological sophistication of a source. The categories proposed by the ITU are:

(i) Consumer

(ii) Hobbyist

(iii) Professional

(iv) Bespoke

Unfortunately, there is no explanation about the criteria to place a source in a given category.

2.4.1.4 Classification in terms of costs

Among all the criteria that have been proposed in the literature to classify the availability of a source, the simplest measure is to use the estimated cost of a source. Sabath and Garbe have proposed some reasonable ranges for evaluating the cost category of a source in [96]:

(i) Low cost: less than 1k€

(ii) Moderate cost: between 1k€ and 100 k€

(iii) Medium cost: between 100k€ and 1M€

(iv) High cost: more than 1M€

2.4.1.5 Proposed scale

Once the method to measure the availability of the IEMI sources has been chosen by the EMC expert, the obtained results can be translated to the suggested scale presented in Tab. 2.2. Depending on the scenario, the EMC expert will try to answer the question “how difficult is to build or acquire a source?”, and the availability level should be chosen accordingly.

Tab. 2.2 Suggested availability level scale

Availability Level	Description
-1	Source easy to obtain
0	Unknown
1	Source difficult to obtain

Notice that the possibility of not being able to rate the availability of a source is also considered.

2.4.2 Source transportability

The source *transportability* evaluates its requirements in terms of size, weight, and energy supply so that it can be physically displaced close to a target. The categories for evaluating the transportability of a source are also subject to the criteria of the experts. However, there are some guidelines in recent literature that could serve as a tool for the classification (see [99, 100]).

2.4.2.1 Classification by Sabath and Garbe (2009)

Sabath and Garbe used the term *mobility* to characterize the transportability of a source in [96]. They have proposed the following categories for classifying the mobility of a source:

(i) Stationary: if the source is part of a fixed installation.

(ii) Transportable: if the source can be transported between various locations, but during operation it has to be stationary at one location.

(iii) Mobile: if the source can be integrated into a mobile platform and can operate during the motion of the platform.

(iv) Very mobile: if the source is mobile and has the ability to operate undiscovered in urban environments.

(v) Highly mobile: if the source is mobile and has the ability to operate undiscovered within a building or transportation systems.

2.4.2.2 ITU Classification (2009)

The term used by ITU to characterize the transportability of the sources is the portability level. Four portability levels were defined according to the following considerations [89]:

(i) Pocket size or body worn: applies to threat devices that can be hidden in the human body and/or in the clothing.

(ii) Brief case or back-pack sized: applies to threat devices that are too large to be hidden in the human body and/or in the clothing, but is still small enough to be carried by a person (such as in a briefcase or a back-pack).

(iii) Motor-vehicle size: applies to threat devices that are too large to be easily carried by a person, but large enough to be hidden in a typical consumer motor vehicle.

(iv) Trailer-sized: applies to threat devices that are too large to be either easily carried by a person or hidden in a typical consumer motor vehicle. Such threat devices require transportation using a commercial/industrial transportation vehicle.

2.4.2.3 Proposed scale

From an analyst point of view, the above mentioned categories do not totally answer the question “how difficult is it to transport and operate a source close to the facility?”. Therefore, the transportability levels presented in Tab. 2.3 are suggested in this work.

Tab. 2.3 Suggested transportability level scale

Transportability Level	Description
-1	Source easy to transport and operate
0	Unknown
1	Source difficult to transport and operate

The choice of the level should take into account the access ways to the facility and its surroundings. Notice that non-transportable sources cannot be categorized since they should not be part of the analysis for obvious reasons.

2.4.3 Source accessibility

The *accessibility* to a facility describes the ability of entering or approaching the critical areas where the important equipment is placed, without being recognized or identified by surveillance and /or security devices. It is a measure of the degree of protection of the implemented access restriction policies of the facility.

A similar concept was defined by Mansson et. al. in the so-called ASC (Accessibility, Susceptibility, Consequence) cube [29], in which, by using the facility EMT [49], an accessibility factor is assigned to each zone (the inner zones should be less accessible). Since typically the EMT zone boundaries are not directly related to the physical access to the facility, and considering the fact that many civilian infrastructures are not planned with an EMT approach, it is not straightforward to use these criteria for defining the accessibility.

ITU has also proposed in [89] a definition of protection zones based on the distance between the source and the facility. The definition of the protection zones is very useful to understand how transportable the source should be in order to be placed inside a zone, but it does not give insight on the likelihood of detecting the source.

2.4.3.1 Proposed scale

The accessibility of the source can be classified according to the following proposed categories:

(i) Easy: If the security restrictions may not be able to detect the presence of the source.

(ii) Unknown: if no information about the security of the facility exists.

(iii) Difficult: if rigorous security devices are installed in order to survey and to detect the presence of malicious material or personnel; e.g. material inspection at the entrance, need of passcodes, existence of surveillance cameras, metal detectors, alarms, etc.

The proposed accessibility levels are summarized in Tab. 2.4. Notice that the possibility of not being able to rate the accessibility of a source is also considered.

Tab. 2.4 Suggested accessibility level scale

Accessibility Level	Description
-1	Source easy to access
0	Unknown
1	Source difficult to access

2.4.4 Calculation of the likelihood

Once the *availability*, *transportability*, and *accessibility* levels have been defined, the EMC expert will have to judge the *likelihood* of the source. It is difficult to provide general rules for inferring the total likelihood of a source given that the presented criteria are based on propositions provided in the publications of different authors. However, the previous evaluation of the three parameters should provide with enough information to make an educated selection. The suggested scale to express the total *likelihood* of a given IEMI threat is presented in Tab. 2.5.

Tab. 2.5 Suggested likelihood level scale

Likelihood Level	Description
-1	Source likely to happen
0	Unknown
1	Source unlikely to happen

Notice that the possibility of not being able to rate the probability of a threat is also considered.

In order to calculate the total *likelihood* from the source *accessibility*, *transportability*, and *availability*, we suggest using the lookup table presented in Tab. 2.6:

Tab. 2.6 Likelihood lookup table

Case	Availability	Transportability	Accessibility	Likelihood
1	-1	-1	-1	-1
2	-1	-1	0	-1
3	-1	-1	1	1
4	-1	0	-1	0
5	-1	0	0	0
6	-1	0	1	1
7	-1	1	-1	-1
8	-1	1	0	0
9	-1	1	1	1
10	0	-1	-1	-1
11	0	-1	0	0
12	0	-1	1	1
13	0	0	-1	0
14	0	0	0	0
15	0	0	1	1
16	0	1	-1	-1
17	0	1	0	0
18	0	1	1	1
19	1	-1	-1	-1
20	1	-1	0	0
21	1	-1	1	1
22	1	0	-1	0
23	1	0	0	0
24	1	0	1	1
25	1	1	-1	1
26	1	1	0	1
27	1	1	1	1

Tab. 2.6 has been generated by assigning an important weight to the *accessibility* since it is related to the security measures, and the awareness of the facility staff. It was also assumed that the attacker will try to use sources that are not easily detected by the security network of the facility. Therefore, the detectable sources become less likely to be used. The *transportability* and *availability* of the sources have been assumed as constraints of the *likelihood* but not as determinant factors since the intention to attack the facility already exists. This means that if the source is accessible, and if the source is either difficult to obtain or to transport, the attacker will still tend to use it. On the other hand, if the source is difficult to obtain and to transport, therefore, an unlikely level is assigned.

2.5 Assessing the hardness of a service

Studying the possibility of perturbing the service provision inside a hostile IEME is perhaps the most complex task of a service-based risk assessment because it requires the competences of EMC and facility experts, but also, the use of EM computational tools or experiments. It also involves a very good knowledge of the IT equipment functional and physical connection diagrams, and if possible, their susceptibility levels. These latter are difficult to obtain because traditional off-the-shelf equipment are typically tested against only surges representative of lightning, ESD, or electromagnetic levels in the range of equipment operating in normal conditions.

The two factors proposed to calculate the hardness of a service are its *receptivity* and its *redundancy* (see Fig. 2.4). Both terms have been introduced in [29] to describe the effect of the transmitted electromagnetic energy to the supporting equipment and to consider redundancy of equipment or trained personnel that could react during a failure situation so that the service is not interrupted.

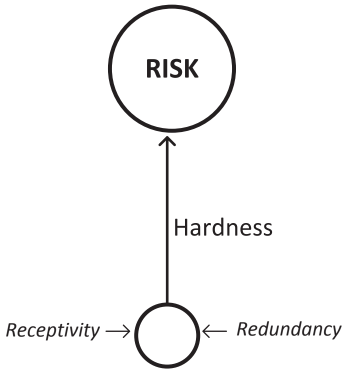

Fig. 2.4 Schematic diagram illustrating the contributing factors for the calculation of the hardness of a given service against IEMI.

In very complex infrastructures there might be several vulnerable electronic units that are vital for the provision of a service. Therefore, the receptivity of single equipment may not be enough to estimate the total hardness, and that explains the importance of knowing very well the functional connection diagrams by the facility experts. The receptivity assessment evaluates the possibility of inducing a malfunction of the equipment that supports the provision of a service given that a specific threat is acting against the infrastructure.

2.5.1 Fault tree analysis

Genender et. al. have proposed a systematic use of the FTA in [95] for identifying possible causes of a system failure and to study the breakdown of each of the separate units. The advantage of this strategy is that it is a top-down approach and therefore it helps to identify and focus only on the important equipment. In the FTA, the facility expert starts defining a top undesired event (service loss), from which the successive chain of bottom events that may have caused it are identified until the main primary causes are reached. The relations and dependencies between events are specified by using the logical AND and OR operators as schematically shown in Fig. 2.5.

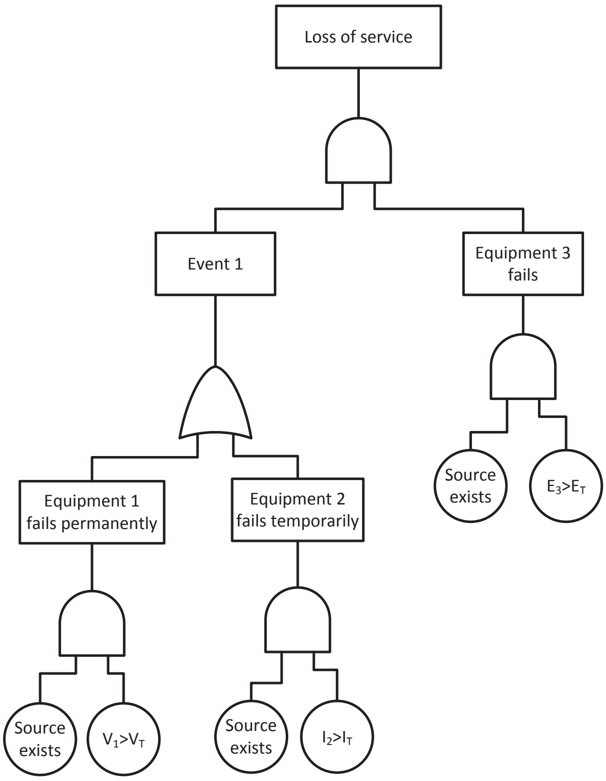

Fig. 2.5 Example illustrating the construction of an FTA.

According to the FTA of Fig. 2.5, in order to interrupt the service provision, event 1 has to occur and equipment 3 has to fail. Event 1 will happen if either equipment 1 fails permanently or equipment 2 fails temporarily. The primary causes of the equipment failure are shown with round symbols. In the case of an IEMI assessment, the primary causes are always the deliberate deployment of the source against the facility and that the induced fields, currents, or voltages at the equipment under study are higher than a failure threshold. Notice that both primary causes have to happen in order to induce a failure in equipment 1, 2, or 3. Further information about the method can be found in [36, 95].

An FTA has to be implemented for each of the services provided by the facility. The possibility of temporarily or permanently losing a service has to be analyzed separately. While doing the FTA, the experts would also notice if a service may be supplied by other redundant units or the staff. These considerations will increase the service redundancy and eventually reduce the total vulnerability of a service loss.

If the probabilities of the primary causes are considered, the probability of an equipment failure is estimated as the product (AND operator) of the probability of the existence of a source and the probability of a failure as:

$$p(X_1) = p(V_1 > V_T)\,p(T_j), \tag{2.4}$$

where X_1 is the failure of equipment 1, and T_j is the existence of source j.

Notice that this result is consistent with Equation (2.2) in which the probability of a consequence was estimated as the conditional probability of the consequence given a threat multiplied by the probability of the threat.

If the entire FTA of Fig. 2.5 is solved starting from the primary causes up to the top event, the probability of the service loss yields:

$$p(SL) = p^2(T_j)\,p(E_3 > E_T)[p(V_1 > V_2) + p(I_1 > I_2)], \tag{2.5}$$

where SL is the event of experiencing a service loss.

Notice that the terms in (2.5) depend on the choice of the events of the FTA and therefore a numerical evaluation of this expression does not guarantee that the total probability is calculated. Thus, due to time constraints and in order to simplify the analysis, if the experts consider only the main equipment, the FTA analysis provides only a reduced picture of the probability of a service loss. However, a qualitative analysis can be performed so that important equipment and important parameters causing the failure can be identified. For example, the results of (2.5) already show the importance of the magnitude of the electric field in the vicinity of equipment 3. Also, notice the importance of the *likelihood* of the source ($p(T_j)$).

2.5.2 Critical equipment list

The use of the FTA allows the identification of the critical equipment that supports the provision of a service. Once the list of critical equipment is obtained, all the possible information about equipment functions must be searched and their location inside the critical facility has to be referenced in the building plans of the facility. The critical equipment list should include the units that are considered as fundamental for the provision of a service. The equipment that appear on the top layers of the FTA and that may not have any redundancy are more likely to be included in the critical equipment list.

2.5.3 Failure thresholds of the critical equipment

The failure thresholds of the critical equipment are generally specified as current, voltage, electromagnetic field or power limits above which the equipment will experience a failure or a permanent damage. These limits can be obtained either by direct experiments [73], or by analytical calculations (see e.g. [93, 101]). Alternatively, literature research can be useful to make an educated guess by comparing with similar equipment that has already been tested against waveforms representative of IEMI (see e.g. [6, 7, 9, 11, 13, 32, 72, 102-107]).

It has been shown that failures do not always occur at the same exposure levels and therefore a probability distribution has to be defined (see e.g. [7, 93]. The use of a Weibull distribution in order to model the susceptibility threshold of equipment has been also discussed in [36, 91]. Depending on the budgetary and time constraints, multiple experiments with real equipment or computer simulations can be carried out in order to derive the failure probability distributions of the critical equipment.

2.5.4 Transfer functions between critical equipment and possible source locations

2.5.4.1 Electromagnetic topological diagram

The EMT diagram of the facility is a very useful tool that can be used to assess the expected current, voltage, field, or power level at the critical equipment inputs. It is drawn by the EMC expert by considering the paths through which the electromagnetic energy could propagate inside the facility and the nature of the shielding surfaces that may appear during the wave travel from the source up to the target. If possible, all the cable paths, lengths and cross sections should be known so that a computer simulation could be used for analytical purposes. Acquiring such detailed information is a difficult challenge not only for the EMC expert but also for the facility staff. Further illustration about the use of topological diagrams can be found elsewhere in the literature, e.g. in [53].

2.5.4.2 Critical coupling paths

The expected IEMI sources and their locations around the facility have to be chosen according to their *accessibility*, *transportability*, and *availability*. Since the positions of the critical equipment have already been obtained, the most effective coupling paths can be identified by using the topological diagram. While choosing the coupling paths, special attention has to be given to conducted penetrations and large apertures, because they constitute the main points of entry of the back-door coupling process. It is important to mention that the equipment failure is typically due to either a direct field exposure or a field-to-cable coupling into the communication ports. If a front-door coupling is expected, the analysis should address antennas and the front ends of communication equipment.

2.5.4.3 Analytical or numerical calculation of the transfer functions

After identifying the critical coupling paths, their transfer function can be estimated with the use of heavy computer analysis or simple calculations that consider the attenuation provided by building walls, metal cabinets, shielded enclosures, and cable coupling. There are many available examples of the prediction of the transfer functions between two points of a topological diagram by using either numerical calculations (e.g. [53, 98, 108-110] [70]) or approximate analytical evaluations (e.g. [76, 89, 111]). The choice between one and another depends on the expected level of accuracy. However, the possibility of estimating the correct transfer functions from analytical or numerical methods without involving experimental results remains an open challenge provided the complexity of the facilities under test.

As it happens with the failure thresholds, the transfer functions also exhibit a statistical distribution due to the uncertainty in the parameters of the coupling paths (impinging field amplitudes, wall materials, polarization angles, cable lengths, cable loading, etc.). Therefore, the transfer function calculations may include random parameters and the coupling probability distribution might be derived by using a Monte Carlo analysis [36, 64, 91]. Some examples illustrating the statistical analysis of topological diagrams can be found, e.g., in [64, 66, 67, 81, 112, 113].

2.5.4.4 Experimental determination of transfer functions

If EM tests are allowed inside the facility, the transfer functions are better characterized with experiments. Low power experiments will be useful to characterize the transfer function of systems where the presence of nonlinear components is not expected. High power tests will allow to discover any malfunctions induced due to the non-linear behavior of components [73].

However, these kinds of tests are barely allowed for security reasons. Examples and guidelines for performing such kind of measurements are also available in the literature (see [33, 73, 109, 114]). An empirical method to address the shielding effectiveness of buildings without using the time consuming two-antenna method has also been suggested in [115].

2.5.5 Failure estimation

Once the transfer functions and the failure thresholds of the critical equipment are known, the failure of the equipment can be predicted by convolution with the expected electromagnetic environment generated by the IEMI source. In general, if the induced current, voltage, field, or power is higher than the threshold, a temporal or permanent failure will appear in the equipment under test. If the thresholds or the transfer functions were obtained by considering stochastic conditions, an improved analysis can be performed to estimate the so-called breakdown failure probability [29, 91].

Assuming that the CDF of the threshold and the PDF of the transfer function are known variables, the BFP of the equipment can be calculated according to [91]:

$$BFP(E^{inc}) = p(X_c > X_T) = \int_0^\infty CDF_{X_T}(X) \cdot PDF_{X_c}(X)dX, \tag{2.6}$$

where E^{inc} is the impinging field, X_C is the coupled current, voltage, field, or power, and X_T is the threshold.

Once the BFP has been calculated, the failure probability for a given field amplitude will be obtained.

2.5.6 Service receptivity evaluation

Once the failure probabilities of all the equipment supporting the provision of a service have been calculated, the service *receptivity* can be estimated according to the possibility of interrupting or disabling the service. If the failure probabilities of the equipment have been estimated with a yes/no criteria, then the bottom-up calculation of the FTA provides the receptivity evaluation. If the service loss is feasible, there is a high receptivity to the interferences. On the other hand, if the FTA evaluation shows that there is no compromise of the service provision, the receptivity is low.

For the cases where a stochastic variation of the thresholds and the transfer functions has been considered, the probability of losing a service can be calculated by assuming a probability of occurrence of the source equals to 1, and use a similar equation to (2.5) to infer the total BFP. Of course, this is a rather complex procedure and the possibility of estimating all these functions highly depend on the available time and computational resources. The service receptivity is judged by defining a probability threshold above which the receptivity can be assumed as high or low. As an example, a BFP of 50% (or other) could be used to define the difference between high or low receptivity.

The suggested scale to estimate the service *receptivity* is presented in Tab. 2.7:

Tab. 2.7 Suggested receptivity level scale

Receptivity Level	Description
-1	High service receptivity
0	Unknown
1	Low service receptivity

2.5.7 Service redundancy evaluation

The service *redundancy* evaluates the possibility of providing the service with alternative equipment or personnel that won't be interrupted by the presence of the given IEMI source. The scale presented in Tab. 2.8 is proposed to evaluate the *service* redundancy.

Tab. 2.8 Suggested redundancy level scale

Redundancy Level	Description
-1	Not redundant service provision
0	Unknown
1	Redundant service provision

2.5.8 Service hardness evaluation

When the *receptivity* and *redundancy* of the service have been determined, the total *hardness* of the service can be evaluated according to the following categories:

(i) Weak: for systems for which no redundancy and high receptivity is expected.

(ii) Unknown: for systems for which little information about the receptivity and redundancy exist.

(iii) Strong: for systems exhibiting a low receptivity and/or redundancy.

The suggested hardness levels are summarized in Tab. 2.9.

Tab. 2.9 Suggested hardness level scale

Hardness Level	Description
-1	Weak service
0	Unknown
1	Strong service

In order to calculate the total *hardness* according to the *receptivity* and *redundancy* levels, we suggest using Tab. 2.10.

Tab. 2.10 Hardness lookup table

Case	Receptivity	Redundancy	Hardness
1	-1	-1	-1
2	-1	0	-1
3	-1	1	1
4	0	-1	0
5	0	0	0
6	0	1	1
7	1	-1	1
8	1	0	1
9	1	1	1

Notice that Tab. 2.10 has been generated by assuming that a low service receptivity or the existence of redundancy will make the service provision strong. This could constitute an optimistic perception of the hardness to the eyes of another EMC expert, and therefore the proposed level combinations can be accordingly modified.

2.6 Assessing the service risk

The final estimation of the service *risk* will use the *consequence¸ likelihood,* and *hardness* levels as inputs and according to the criteria of the EMC expert, a final qualitative evaluation is made. The risk examination is the conclusion of a thorough study in which several concepts that have been introduced in this chapter are put together in a single indicator as it was schematically illustrated in Fig. 2.1.

The final conclusion itself is perhaps less important than all the information gained in the evaluation process, namely, the identification of important services provided by the facility, the critical equipment, possible coupling paths, important physical variables, and accessibility flaws. However, in order to provide with a single evaluation of the risk of losing the provision of a service, the following categories can be used:

(i) High risk: when the service can be easily compromised with the use of IEMI and the consequences for the facility are important. These services are those to which special attention has to be paid in the business continuity management policies for allocating the resources for the required EM hardening measures.

(ii) Moderate risk: when the service does not exhibit the correct hardness and in the event of an attack with a given source, the service provision is likely to be compromised. However, the likelihood of the studied source or the consequences might not be considered as a priority in the business continuity management program.

(iii) Unknown risk: when the provided information is not enough to provide a risk evaluation.

(iv) No risk: when the service exhibits the correct hardness; or in the case of a weak hardness level, when the likelihood of the source is low and/or the consequences are insignificant.

A summary of the risk levels is presented in Tab. 2.11.

Tab. 2.11 Suggested risk level scale

Vulnerability Level	Description
-2	High risk
-1	Moderate risk
0	Unknown
1	No risk

In order to calculate the *risk* according to the *consequence*, *likelihood*, and *hardness* levels, we suggest using Tab. 2.12.

Tab. 2.12 Risk lookup table

Case	Consequence	Likelihood	Hardness	Risk
1	-1	-1	-1	-2
2	-1	-1	0	0
3	-1	-1	1	1
4	-1	0	-1	-2
5	-1	0	0	0
6	-1	0	1	1
7	-1	1	-1	-1
8	-1	1	0	0
9	-1	1	1	1
10	0	-1	-1	-2
11	0	-1	0	0
12	0	-1	1	1
13	0	0	-1	-1
14	0	0	0	0
15	0	0	1	1
16	0	1	-1	-1
17	0	1	0	1
18	0	1	1	1
19	1	-1	-1	-1
20	1	-1	0	0
21	1	-1	1	1
22	1	0	-1	-1
23	1	0	0	0
24	1	0	1	1
25	1	1	-1	1
26	1	1	0	1
27	1	1	1	1

2.7 Assessment workflow

Given the high amount of information to be retrieved and processed during the service based qualitative risk assessment methodology, it is highly convenient to perform the audit in a systematic procedure. A schematic diagram of the required steps and the necessary information for doing the assessment is presented in the flow diagram of Fig. 2.6. The highlighted icons represent the information and processes that require the presence of the EMC and facility experts, whereas for the rest, only an EMC expert is required. The arrows represent the flow of information between inputs and outputs and they provide the step-by-step procedure for performing the audit.

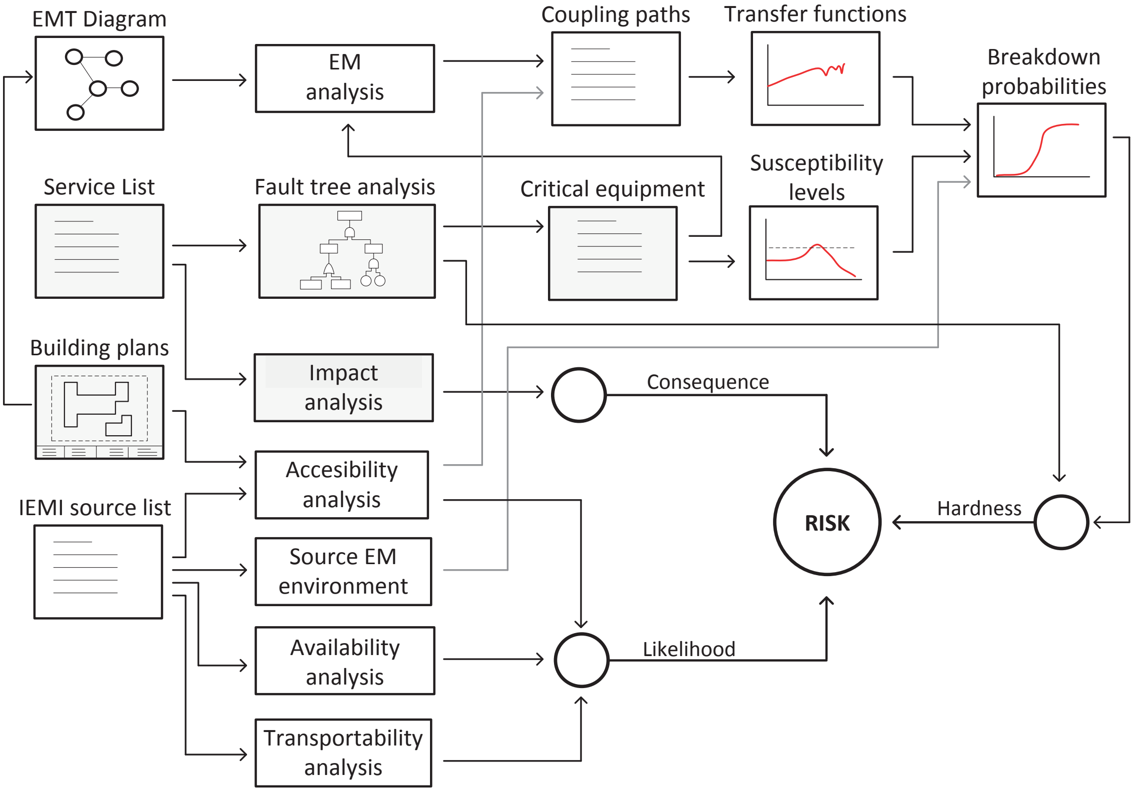

Fig. 2.6 Flow diagram of the service based qualitative assessment

According to the flow diagram Fig. 2.6, the audit starts by obtaining the services list and the building plans from the facility experts, and by deciding a plausible IEMI source list to be analyzed. For each of the services in the list and each of the sources under study, the following analysis has to be performed:

(i) With the help of the building plans and a visual inspection of the facility, the EMT diagram can be drawn and the source accessibility level can be defined.

(ii) The source availability and transportability levels are estimated, and the source likelihood is calculated.

(iii) The facility experts perform the impact analysis to decide the consequence level of a service loss.

(iv) An FTA is drawn by the facility experts in order to identify the critical equipment list and their locations inside the facility, and the possible redundancies in the service provision.

(v) The susceptibility levels of the critical equipment will be measured or obtained from the available literature.

(vi) From the EMT diagram and the critical equipment locations, an electromagnetic analysis is performed to obtain the coupling paths. Notice that this analysis has to be performed for each different position of the source (keeping in mind that the source accessibility is not modified).

(vii) The transfer functions of the coupling paths are measured, or estimated with analytical tools.

(viii) The IEME generated by the source is estimated.

(ix) The breakdown probability is estimated with the susceptibility levels, the transfer functions, and the source IEME.

(x) The service receptivity is estimated by considering the obtained breakdown probabilities.

(xi) The redundancy level is obtained from the FTA.

(xii) The service hardness level is estimated from the receptivity and redundancy.

(xiii) Finally, the service risk is estimated from the source likelihood, the service loss consequence and the service hardness.

2.8 Conclusions

In this chapter, a methodology for assessing the risk of perturbing or stopping the provision of important services by critical facilities due to IEMI was presented. The method merges some of the strategies proposed in the literature and focus on the qualitative evaluation of the risk of losing a service rather than the EMC issues of the facility itself. The need of a qualitative method for IEMI assessment has been pointed out due to the fact that numerical evaluation of the risk would require prohibitive time and resources.

Not only a qualitative assessment can be performed in shorter time periods but also it can be better understood by non-EMC experts. Thus, the method enables the intervention of the facility staff, who are the main assets of the critical infrastructures, and who should be aware of the IEMI threat.

The service-based risk assessment has been applied to study the vulnerability of a power control center in Switzerland and it was found that if the interruption of the service provision is considered, the panorama of the risk assessment evaluation may become more optimistic since there are still many processes inside critical facilities that can be run by 'non-IT' equipment or manually. According to past experiences, this panorama is more realistic and the suggested protection measures will be easier to implement in complex infrastructures that were not designed considering EMC requirements. From a business continuity point of view, the final output of a service-based risk assessment may be less important than all the information about the organizational and IT equipment weaknesses that is gained during the evaluation process.

3 Study and Classification of Potential IEMI Sources

3.1 Introduction

Prior to any analysis of the *receptivity* of a facility to an IEMI attack, a good knowledge of the expected IEME is required in order to decide the scope of the considered methodology. To do this, several questions need to be addressed, e.g. :

- What is the expected voltage waveform in the cables of the facility under study?
- What is the maximum field level expected in the vicinity of the facility under study?
- What are the frequency contents of the field spectrum that will be illuminating the facility walls?

One would expect that, given the size of hand-made electronic equipment and general purpose facilities, the majority of the sources should be built between some hundreds of MHz and some GHz (about 1 GHz according to the Baum's law [116]). There are several good surveys in the literature addressing some of these questions by making reference to the development of so-called non-lethal weapons in the US [20, 117]. In addition, useful analytical predictions of the expected field levels of sources can be found in [1, 2]. However, many advances have been made in the past few years and the survey on available sources can be revisited by including recently reported sources of different types and, in particular, mesoband sources of the past decade [118-122].

Revisiting the survey is also justified since, although general classification methods of sources according to their *transportability* and *availability* properties have been proposed [2, 89, 96], these methods have not been used in a systematic way to address available sources.

This chapter draws heavily from the Sensor and Simulation Note 41 by Mora et al. [100], in which the capabilities of publicly reported HV pulsers and HPEM radiators that could be regarded as potential IEMI sources have been assessed. This work characterized the signals generated by published IEMI sources for which relevant information and/or waveforms were made available in the documents. The studied sources were classified in terms of their transportability, technological development, and cost level in order to reveal the trends that are followed by both, conducted and radiated sources. As a product of this work, two databases including the waveforms and spectral parameters of about 39 sources, and the classification of 21 conducted sources and 55 radiated sources were presented.

This chapter is organized as follows. An overview of the previously proposed classifications of IEMI sources according to their waveform and spectral parameters, availability, and transportability is presented in Section 3.2. The analysis of the survey results is presented in Section 3.3. The expected limits for the generation of more intense or faster EM fields with hyperband, mesoband, and hypoband sources are explained in Section 3.4. Finally, some conclusions are presented in Section 3.5.

3.2 Classification of IEMI sources

3.2.1 Waveform parameters

Radiated and conducted signals can be classified by using their time-domain characteristics or their frequency spectrum. The time and frequency characterization of the sources is essential for the evaluation of the *receptivity* level.

3.2.1.1 Time domain parameters

The time domain parameters of interest are usually specified for signals following an impulse-like, damped oscillatory or CW behavior [100]. The usually-addressed parameters of impulsive, damped oscillatory, and CW waveforms are summarized respectively in Tab. 3.1,

Tab. 3.2, and Tab. 3.3. The first two columns of the tables contain the parameter name and the suggested denomination. The third column presents a brief description of the parameter.

Further explanation about the calculation method and the nature of the time-domain parameters can be found in Chapter 2 of [100].

Tab. 3.1 Single pulse waveform attributes [100]

Name	Denomination	Description
Peak amplitude	$R_{\max}$	Maximum value of the signal
Time to peak	$\Delta t_{\max}$	Time to achieve the peak amplitude
Peak derivative	$\left(\frac{dR}{dt}\right)_{\max}$	Maximum derivative of the waveform before the peak
10-90% risetime	Δt_{10-90}	Time to increase from 10% to 90% of the peak amplitude during the rise
Maximum rate of rise	$\frac{R_{\max}}{\left(\frac{dR}{dt}\right)_{\max}}$	The ratio between the peak amplitude and the peak derivative
Full-width-at-half -maximum	Δt_{50-50}	Time between the instants when the waveform reaches 50% the peak amplitude
Pulse repetition frequency	PRF	Frequency between two successive impulses

Tab. 3.2 Damped sinusoid waveform attributes [100]

Name	Denomination	Description
Peak amplitude	$R_{\max}$	Maximum value of the signal
Fall time	Δt_f	e-folding time of the signal envelope
Average period	T	Average time between two zero crossings
Average frequency	$f_0^{\text{avg}} = \frac{1}{T}$	Inverse of the average period
Average quality factor	$Q_0^{\text{avg}} = \pi \frac{\Delta t_f}{T}$	Measures the ability of delivering energy at a tuned frequency
Pulse repetition frequency	PRF	Frequency of the successive pulses

Tab. 3.3 CW waveform attributes [100]

Name	Denomination	Description
Peak amplitude	$R_{\max}$	Maximum value of the signal
Average period	T	Average time between two zero crossings
Average frequency	$f_0^{\text{avg}} = \frac{1}{T}$	Inverse of the average period
Pulse repetition frequency	PRF	Frequency between two successive bursts
Duty cycle	$D = PRF \cdot \Delta T_{on}$	Time frame during which the CW source output is active; expressed as a fraction of the burst period

3.2.1.2 Frequency domain parameters

Similarly, the frequency domain properties of the waveforms are obtained from the frequency spectrum of the signals. The frequency spectrum can be evaluated by calculating the Laplace transform along the imaginary *j* axis, or by directly calculating the Fourier transform of the time domain waveform. A summary of the usually-evaluated frequency domain parameters is presented in Tab. 3.4.

Tab. 3.4 Spectral attributes [100]

Name	Denomination	Description
Peak spectral amplitude	$R_{\max(f)}$	Maximum amplitude of the frequency spectrum of the waveform
Center frequency	f_0	Frequency at which $R_{\max(f)}$ is evaluated
Quality factor	$Q = \frac{f_0}{BW_{-3dB}}$	Ratio between the central frequency and the -3 dB bandwidth
Bandratio	$br = \frac{f_H}{f_L}$	Ratio between the 90% energy bandwidth limits.

The bandratio is a fraction that was introduced used to classify the nature of the output of a HPEM generator [2, 20, 86]. Consider the illustration of the frequency spectrum of a damped sinusoid waveform in Fig. 3.1.

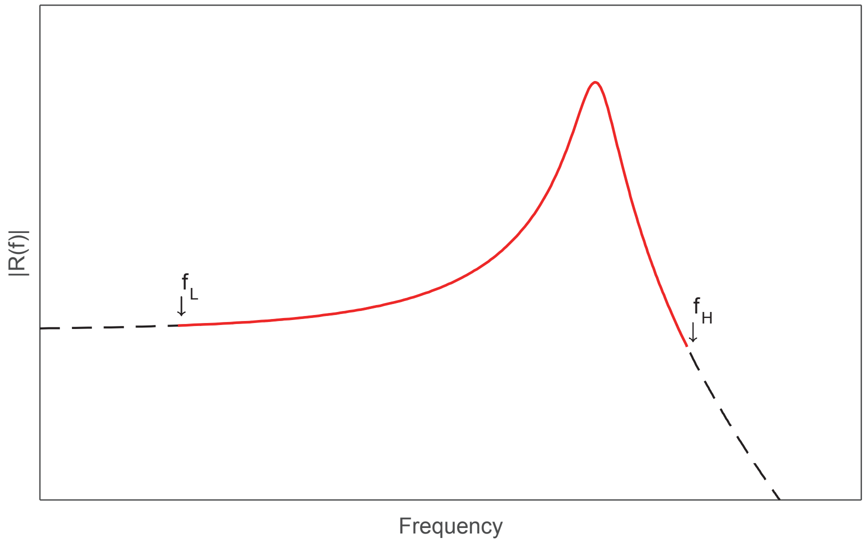

Fig. 3.1 Illustration of the frequency spectrum of a damped sinusoid waveform.

The bandratio is defined as [2, 20, 86]:

$$br = \frac{f_H}{f_L}, \tag{3.1}$$

where the low- and high- frequency limits, f_L and f_H are defined as the smallest interval in which 90% of the energy is contained [2, 86]:

$$\begin{gathered} \inf\left\{(f_H - f_L) : \{f_H, f_L\} \text{ in } A_{0.9}\right\} \\ A_{0,9} = \frac{\left\{\int\limits_{f_L}^{f_H} \left|\tilde{R}(f)\right|^2 df\right\}^{\frac{1}{2}}}{\left\{\int\limits_{0}^{\infty} \left|\tilde{R}(f)\right|^2 df\right\}^{\frac{1}{2}}} = 0.9. \end{gathered} \tag{3.2}$$

For spectra with large DC content, the lowest frequency limit is nominally defined as 1 Hz. The interval between f_L and f_H is sometimes addressed as the 90% energy bandwidth BW_{90}:

$$BW_{90} = f_H - f_L. \tag{3.3}$$

3.2.2 Spectral classification

During the past decade or so, the study of IEMI has led to different classification attempts for the fields generated by HPEM sources, also addressed as IEME. The first attempt to classify HPEM generators was developed by Giri in [123]. The proposed classification was made according to the spectrum of the generated IEME by using both, the percent bandwidth and the bandratio of the generated signals.

As it has been discussed in [2, 20], the use of the percent bandwidth to classify IEME may be inadequate in the context of UWB signals because it comes from a “communications point of view”. On the other hand, the bandratio concept was derived from a physical insight into the generated fields by the already existing HPEM sources at that time. The proposed classification was later standardized by IEC in 2005 [1]. The classification of the IEME according to the bandratio is presented in Tab. 3.5 [2, 20].

Tab. 3.5 Classification of IEME according to the bandratio

Band type	Bandratio (br)
Hypoband	≤ 1.01
Mesoband	1.010< br ≤3
Sub-hyperband	3< br ≤ 10
Hyperband	br≥10

3.2.3 E-field strength classification

Another approach for the classification of IEME generated by HPEM sources is to examine the generated E-field at a given distance from the source [2]. The main interest is to predict the possible threat imposed to electronic equipment in proximity of the IEME due to a given HPEM source. There are several publications dealing with the susceptibility of electronic IT equipment (see e.g. [6, 7, 11, 72, 104, 106, 124]). A general study summarizing different susceptibility investigations up to 2004 can be found in [32].

Regarding the possible effects induced by strong radiators on electronic equipment, Giri has proposed a 4-level consequence classification according to the order of magnitude of the generated E-field and the coupling mechanism [104]. The proposed classification is presented in

Tab. 3.6. Notice that the front-door/back-door coupling mechanism has also an impact on the required amplitudes to produce a certain consequence.

Tab. 3.6 Classification of electromagnetic effects according to E-field strength [104]

Effect	Consequence	Type of coupling	Magnitude (V/m)
Noise	Harmless	Front door	10^0
False information	Can be critical	Front door	10^1
Transient upset	System may recover	Backdoor	10^2
Permanent damage	Can be critical	Backdoor	10^3

Sabbath has also proposed a classification of the E-fields according to the so-called threat level as reported in Tab. 3.7 [125]. However, there is little information available in the literature about the rationale behind the choice of the amplitudes.

Tab. 3.7 Classification of the E-field strength according to the threat level [125]

Threat level	Description	Amplitude
XL	Extreme low	< 0.1 kV/m
L	Low	0.1-1kV/m
M	Intermediate	1-10kV/m
H	High	10-100kV/m
XH	Extreme high	>100kV/m

3.2.4 E-field range classification

Unlike HEMP environments, the IEME produced by HPEM radiators is range dependent and the amplitude of the expected fields at a given distance will depend on the technology of the source and the antenna. The radiated fields generated by any antenna in the far field region are inversely proportional to the distance and, therefore, a constant range-normalized E-field is expected. The range-normalized radiated E-field of a source is defined as its "far voltage" V_{far} [2]:

$$V_{far} = rE_f, \tag{3.4}$$

where r is the range and E_f is the far-field generated by the source.

Although this parameter is commonly addressed in the literature, to the best of the author's knowledge, no source classification has been proposed according to their far voltages. Three of the highest reported far voltages are presented in Tab. 3.8:

Tab. 3.8 Highest far voltage of reported HPEM generators

Far Voltage (MV)	Generator Name	Reference
5.3	JOLT	[126, 127]
1.4	GIMLI	[128]
1.28	Prototype IRA	[129]

The generation of HPEM fields typically requires the excitation of a given antenna with a high-voltage pulser. Another parameter of HPEM sources that has been used in the literature to compare their performance is the ratio of the far-voltage to the pulser peak-voltage V_{far}/V_0. It describes the efficiency of the source in transforming an initial pulse into a desired far field.

Notice that this ratio depends on both, the antenna, and the characteristics of the pulser (including the switching speed). For impulse radiating antennas, the far voltage amplitude is related to the derivative of the input pulse and, therefore, the risetime plays a significant role in obtaining high V_{far}/V_0 ratios. Three of the highest reported V_{far}/V_0 ratios in the literature are presented in Tab. 3.9.

3.2.5 Availability and transportability classification

The sources can also be classified according to the availability and transportability scales that were previously presented in Chapter 2. In what follows, the IEMI sources were classified according to the technological sophistication criteria proposed by Giri and Tesche in [2] and reviewed in Section 2.4.1.1, and according to their cost as proposed by Sabath and Garbe in [96] and reviewed Section 2.4.1.4 of this work. Also, the transportability of the IEMI sources was classified according to the scale proposed by the ITU in [89] and reviewed in Section 2.4.2.2 of this work.

Tab. 3.9 Highest V_{far}/V_0 ratios of reported HPEM generators

V_{far}/V_0	Generator Name	Generator Description	Reference
10.68	Prototype IRA	V_{far}=1281 kV obtained with a ±60kV/100ps pulser	[129]
5.3	JOLT	V_{far}=5.3 MV obtained with a 1MV/180ps pulser	[126, 127]
4.60	IRA II	V_{far}=690kV obtained with a ±75 kV/85ps pulser	[20]

3.3 Analysis of the potential IEMI sources characteristics

3.3.1 Survey of potential IEMI sources

In order to assess the characteristic of potential IEMI sources and their generated IEME, the relevant literature (including peer-reviewed journals, conference papers, standards, conference presentations, online catalogs and brochures, and books) containing conducted and radiated sources were analyzed. The characteristics of all the sources were extracted into a database of waveforms and sources that were used to identify some trends. The choice of the considered publications was made so that at least some basic characteristics of the sources were mentioned and measured. Only HV sources and HPEM radiators that, due to their transportability and ease of operation, would most easily be deployed against urban or rural facilities were considered as

IEMI sources. The information that could be collected about each source varied from one publication to another; therefore, not all the parameters of the sources could be retrieved.

In general, conducted sources offering pulsed outputs in the range of some hundreds of kV with moderate durations (hundreds of ns) are available on the market, and their transportability is only marginally constrained by their size and weight. High-energy sources require the use of bigger capacitors and inductors for storage, which will result in an increase of the weight of the source. The sources that are included in the survey are mainly test sources that are commonly found in EMC laboratories for ESD/lightning/NEMP testing. Low voltage sources could also be considered as potential conducted sources, and some examples have been included in the survey.

On the other hand, the choice of HPEM radiated sources was more complex since both, the HV pulser and the antenna, had to be considered. The output antennas of typical hyperband radiators are likely to have big sizes due to the lower frequency range radiation requirement (below about 200 MHz). Also, highly sophisticated radiators with increased gains due to the use of reflectors require some stability to ensure the correct focusing of the beams and, therefore, they are less likely to be operated while in movement. The radiated sources that were included in the survey were mainly obtained from peer-reviewed journal papers, conference papers, and standards. This reveals that many of the available sources are still in development phase and their commercial fabrication is not very common. HPM radiators [130] (typically present in radars and testing facilities) were not considered in the survey since they require heavy primary power for cooling and feeding the CW outputs.

The collected information has been organized into two separate databases. The first database contains the reported waveform of the source output, its frequency spectrum, and a list of various time-domain and spectral attributes. The database is available in Appendix A of [100] in the form of a collection of *wavecards* containing the waveform's parameters. The adopted procedure to digitize the source waveforms extracted from publications, and the processing steps to obtain the relevant parameters associated with each source are also presented in 8.2Appendix A of this work.

The second database generated with the survey is a spreadsheet containing a collection of all the identified potential conducted and radiated sources and their relevant characteristics. It is available in Appendix B of [100].

The information gathered in the databases has been analyzed to identify possible trends or common factors that could lead to a better understanding of the expected characteristics of IEMI sources. In what follows, the results are presented in the form of pie charts and bar plots from which general trends can be identified, providing insight into the *likelihood* of IEMI sources.

3.3.2 Characteristics of conducted sources

In general, the technologies required to produce portable HV sources have seen significant progress in the last 50 years or so, and it is quite difficult to identify trends since there are little constraints for their customized fabrication. However, the cost of test sources remains moderate, perhaps because they are still used only for research and development purposes.

3.3.2.1 Portability level

A percentage pie chart illustrating the portability level of the 21 conducted sources in the database is presented in Fig. 3.2. As it can be appreciated, almost all the sources can be transported in a briefcase, which implies that they can be operated undiscovered.

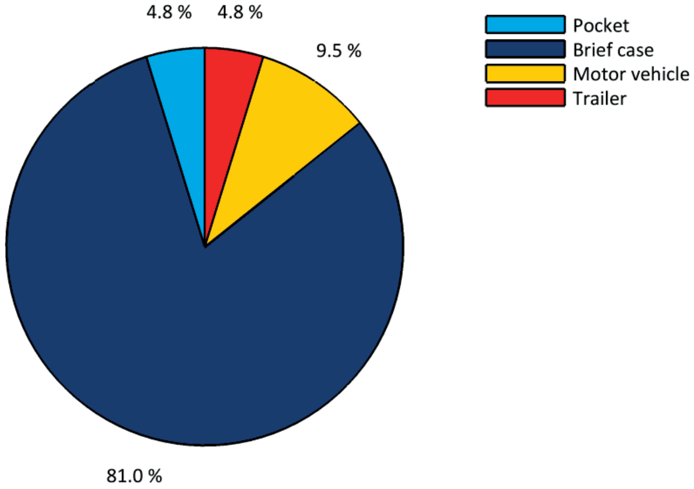

Fig. 3.2 Portability level of the conducted sources (21 sources).

3.3.2.2 Technology level

A percentage pie chart illustrating the technology level of the 21 conducted sources in the database is presented in Fig. 3.3. About half of the reported sources require high technology development for their fabrication, suggesting that half of the devices are used for very specific research and development purposes and, therefore, their availability is limited. The other sources belonging to the medium-tech and low-tech categories are more likely to be purchased from a commercial producer.

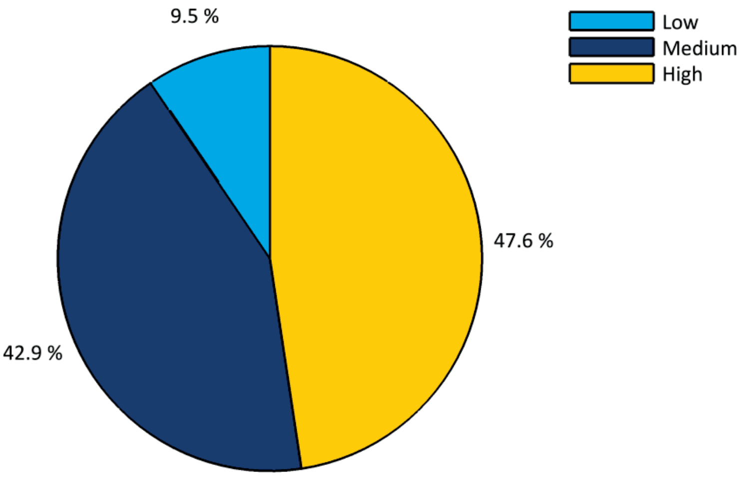

Fig. 3.3 Technology level of the conducted sources (21 sources).

3.3.2.3 Cost level

A percentage pie chart illustrating the cost level of the 21 conducted sources in the database is presented in Fig. 3.4. As expected from the previous analyses, the majority (81%) of the sources can be purchased or fabricated at a moderate cost. This could be understood as a consequence of the maturity of the required technologies and availability of the primary components.

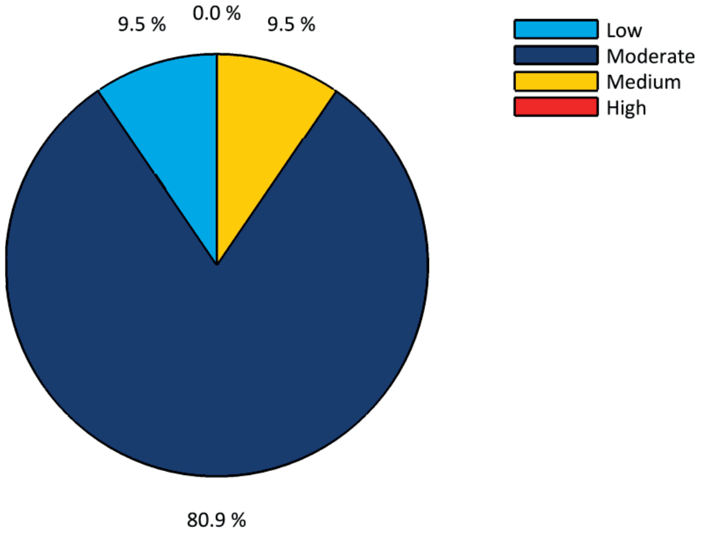

Fig. 3.4 Cost level of the conducted sources (21 sources).

3.3.2.4 Portability level vs. technology level

The portability level of the 21 sources is plotted against their technology level in the bar plot of Fig. 3.5. It can be seen that the technological level does not restrict the portability of the sources. About half of the sources that fit inside a briefcase are high-tech sources, and the other half are mainly moderate-tech and only one is low tech. Only one of the studied sources fits inside a pocket and uses low-tech technology.

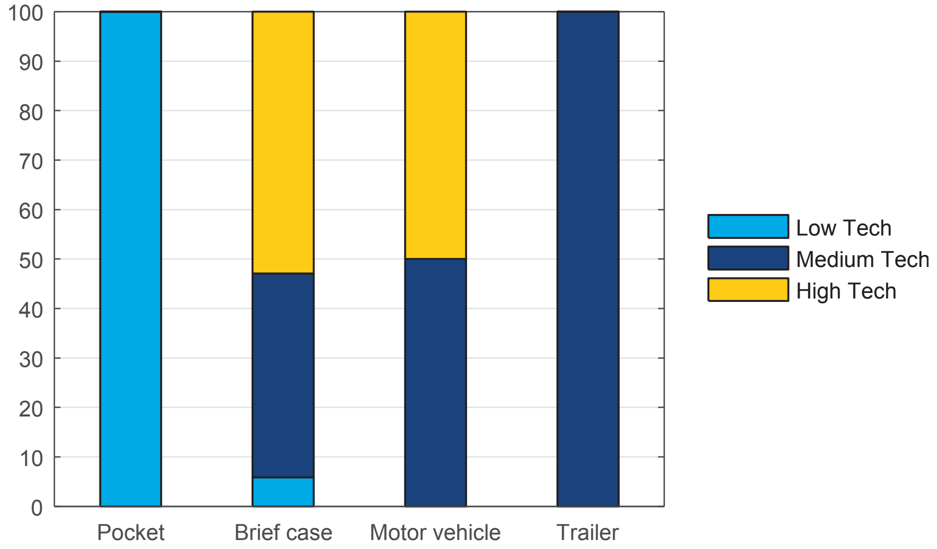

Fig. 3.5 Portability level vs. technology level of the conducted sources (21 sources).

3.3.2.5 Portability level vs. cost level

The portability level of the 21 sources is plotted against their cost level in the bar plot of Fig. 3.6. Surprisingly, the most portable sources are those exhibiting a low or moderate cost. This can be explained, at least in part, by the fact that the cost is related to the required energy storage capacity of the source, which in turn is related to its transportability level. This implies that conducted sources could be very available for a malefactor.

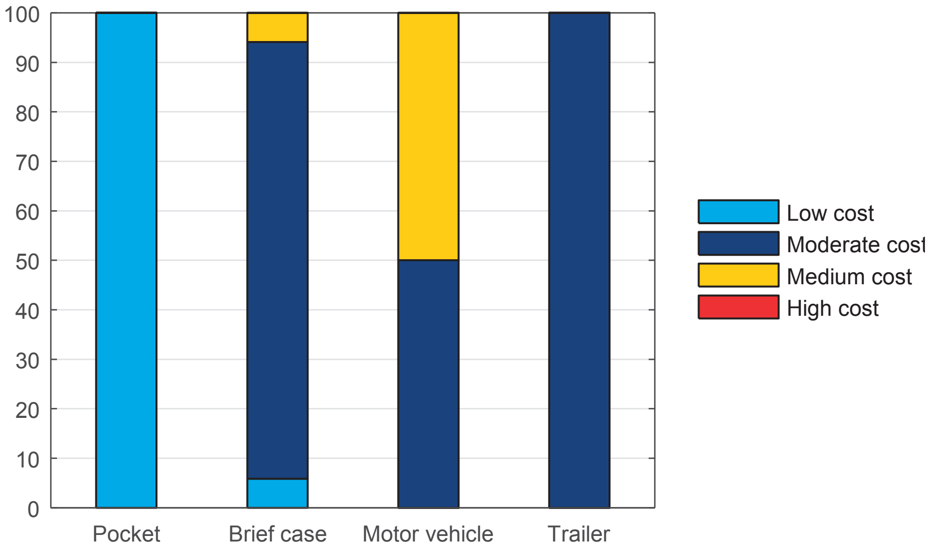

Fig. 3.6 Portability level vs. cost level of the conducted sources (21 sources).

3.3.2.6 Portability level vs. peak voltage

The portability level of the 21 sources is plotted against their peak voltage in the bar plot of Fig. 3.7. For an IEMI scenario, conducted voltage levels exceeding some kV are not likely to propagate efficiently due to insulation breakdown inside the cables. This is why a single voltage level was used to classify the sources above 10 kV. According to the bar plot, it can be concluded that sources producing peak voltages below 10 kV (the sources labeled “more than 10 kV” are of course included since they can be operated at voltages lower than their maximum rating) are available at any portability level. The main factor leading to less portability is perhaps the increase of the energy storage requirement of the source. Interestingly, the percentage of pocket-sized sources with peak voltage level lower than 1 kV is negligible in the studied dataset.

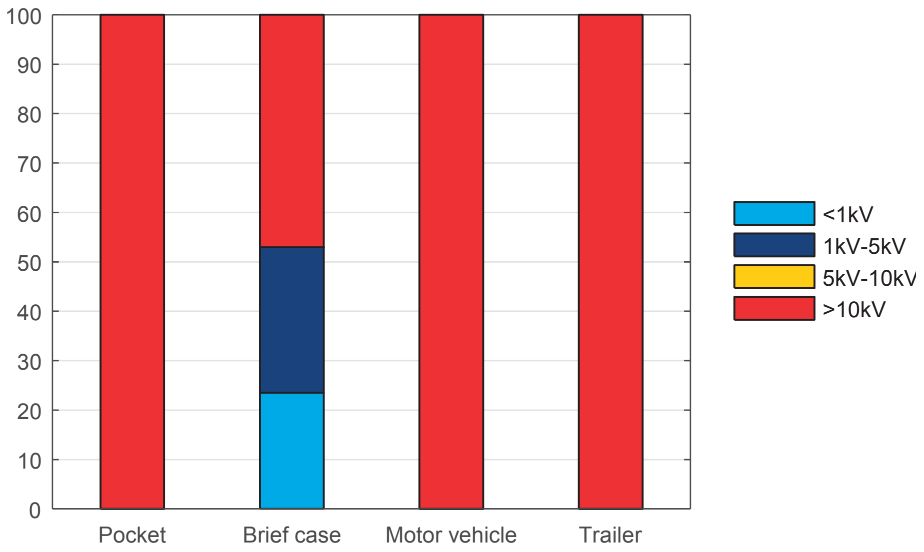

Fig. 3.7 Portability level vs. peak voltage of the conducted sources (21 sources).

3.3.3 Characteristics of radiated sources

The radiated sources that were studied were mainly published in scientific journals, and there are a few sources that can be purchased from a commercial provider. This implies that these sources still have a limited availability, perhaps due to the technological effort and test equipment required to produce them. However, due to the possibility of producing high-magntiude fields with such sources, they constitute a major threat, particularly since many of them can be easily transported. More insight about the source characteristics can be found in what follows.

3.3.3.1 Portability level

A percentage pie chart illustrating the portability level of 54 of the 55 radiated sources in the database is presented in Fig. 3.8. There is one source for which the portability level could not be inferred from the available information. According to the chart, the majority of the reported sources require a vehicle or a trailer to be transported. This is due certainly to the size of the antenna and to the weight of the primary pulser. Notice that the classification of the transportability does not consider the possibility of operating the source inside the vehicle. Thus, the question of operating it undiscovered remains open. Only a few (18%) can be transported in a briefcase, and there are no pocket sized sources reported in the literature.

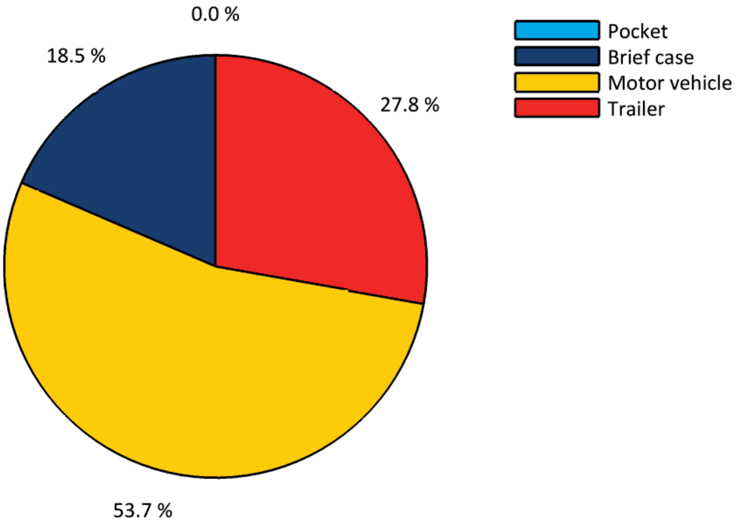

Fig. 3.8 Portability level of the radiated sources (54 sources).

3.3.3.2 Technology level

A percentage pie chart illustrating the technology level of the 55 radiated sources in the database is presented in Fig. 3.9. This figure illustrates the fact that the radiated sources are still under development and, therefore, the required technical effort is high and the availability of the required components is limited.

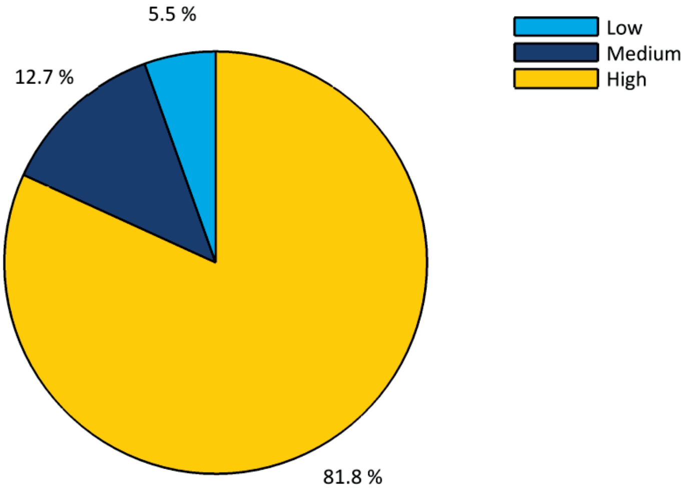

Fig. 3.9 Technology level of the radiated sources (55 sources).

3.3.3.3 Cost level

A percentage pie chart illustrating the cost level of the 55 radiated sources in the database is presented in Fig. 3.10. The majority of the sources are classified as having medium and high cost. As expected, the cost level reflects the high sophistication of some of the devices and the limited availability of the components. However, 24% of the sources can be obtained at a moderate cost, which implies that there are some already mature technologies that are available on the market.

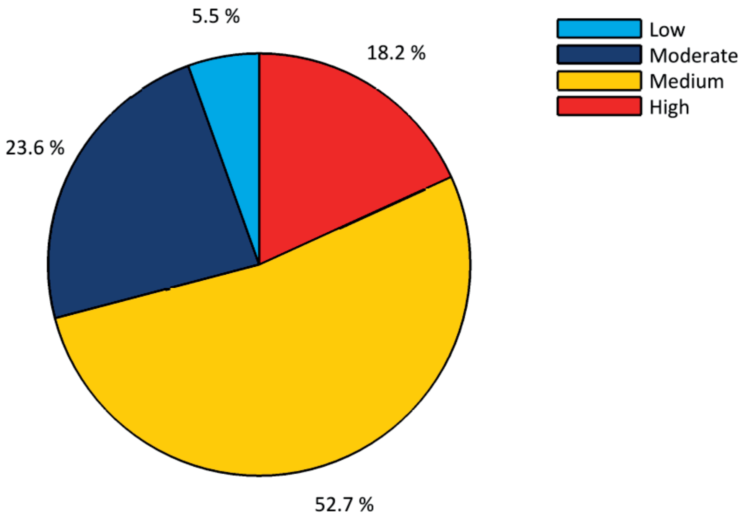

Fig. 3.10 Cost level of the radiated sources (55 sources).

3.3.3.4 Far voltage

A percentage pie chart illustrating the far voltage of 35 of the 55 radiated sources in the database is presented in Fig. 3.11. There are 20 sources for which the far voltage could not be obtained from the available information. The far voltage categories were chosen by following the considerations of the threat levels proposed in Tab. 3.6 and Tab. 3.7. According to the classification, the large majority (about 83%) of the sources produce far voltages between 10 and 1000 kV, which at a distance of 10 m would produce fields in the range of 1-100 kV/m. These levels are high enough to induce false information or transient upset in some systems and, in some cases, permanent damage. Sources producing lower levels may not imply a risk against electronics, but they remain useful for laboratory testing. A very reduced number of sources (3 sources) produce more than 1 MV of far voltage. These sources can be regarded as the most dangerous among the sources for which their far voltage is available in the literature.

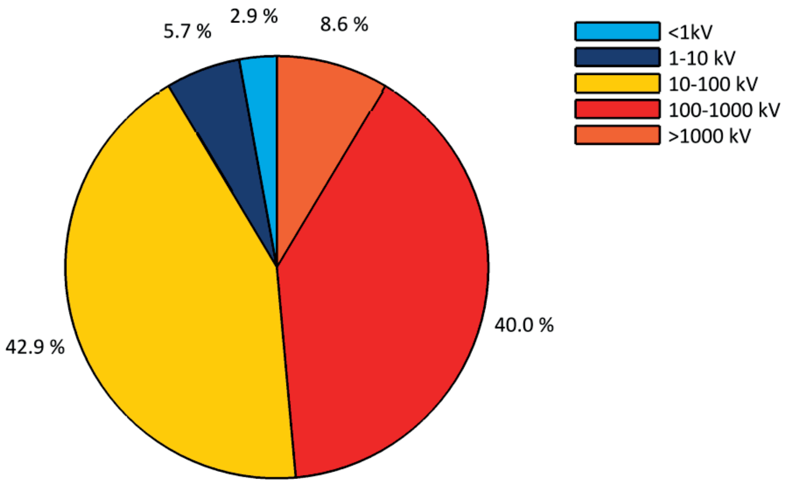

Fig. 3.11 Far voltage of the radiated sources (35 sources).

3.3.3.5 V_{far}/V_p ratio

A percentage pie chart illustrating the ratio of the far voltage to the peak pulser voltage V_{far}/V_p for 35 of the 55 radiated sources in the database is presented in Fig. 3.12. There are 20 sources for which the far voltage could not be obtained from the available information. The majority of the sources exhibit a ratio between 0.1 and 2, which gives an idea of the average conversion efficiencies available. Very few have a ratio above 5 which appears to be the conversion limit with the present technologies.

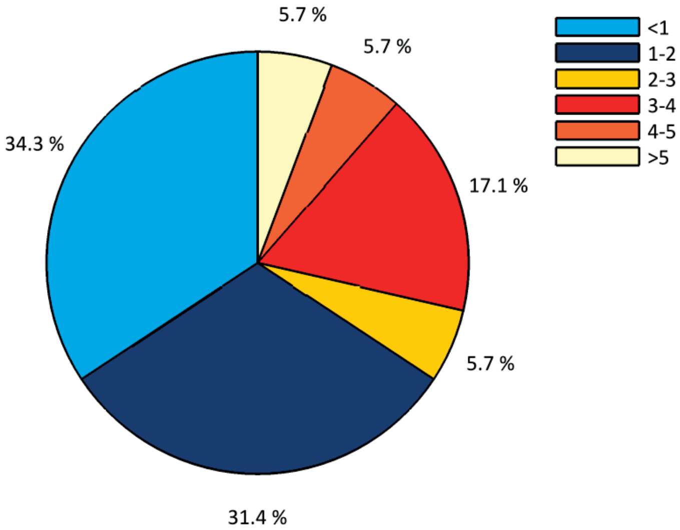

Fig. 3.12 Far voltage/ peak pulser voltage ratio of the radiated sources (35 sources).

3.3.3.6 Portability level vs. technology level

The portability level of 54 of the 55 sources is plotted against their technology level in the bar plot of Fig. 3.13. There is one source for which the portability level could not be inferred from the available information. The main conclusions that can be drawn from the plot can be summarized as follows: 1) Regardless of their technology level, none of the sources in the database can be classified into the pocket transportability level. 2) There exist low and high-tech sources that can be transported in a briefcase, motor vehicle or a trailer. 3) Only sources considered as 'Medium Tech' require at least a motor vehicle to be transported. Interestingly, high-tech sources are present at all portability levels (except in the pocket availability level).

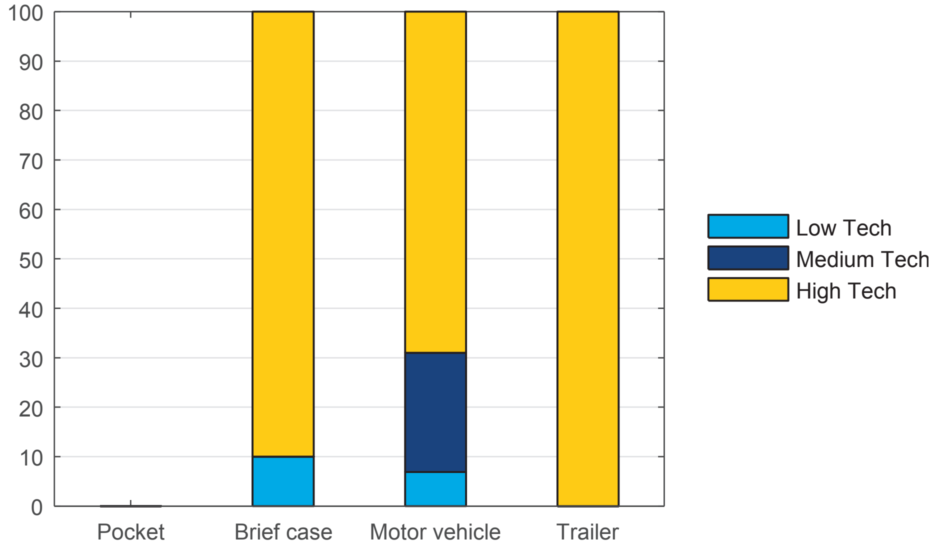

Fig. 3.13 Portability level vs. technology level of the radiated sources (54 sources).

3.3.3.7 Portability level vs. cost level

The portability level of 54 of the 55 sources is plotted against their cost level in the bar plot of Fig. 3.14. The portability level of one of the sources could not be inferred from the available information. It can be seen from this figure that the cost of the source is likely to be in the medium cost category at any transportability level. However, notice that while only about 10% of the moderate cost sources fall in the briefcase transportability bin, this percentage climbs to almost 50% for the motor vehicle sized sources. This implies that, from an availability point of view, sources are more likely to be transported in vehicles since they may exhibit a lower cost.

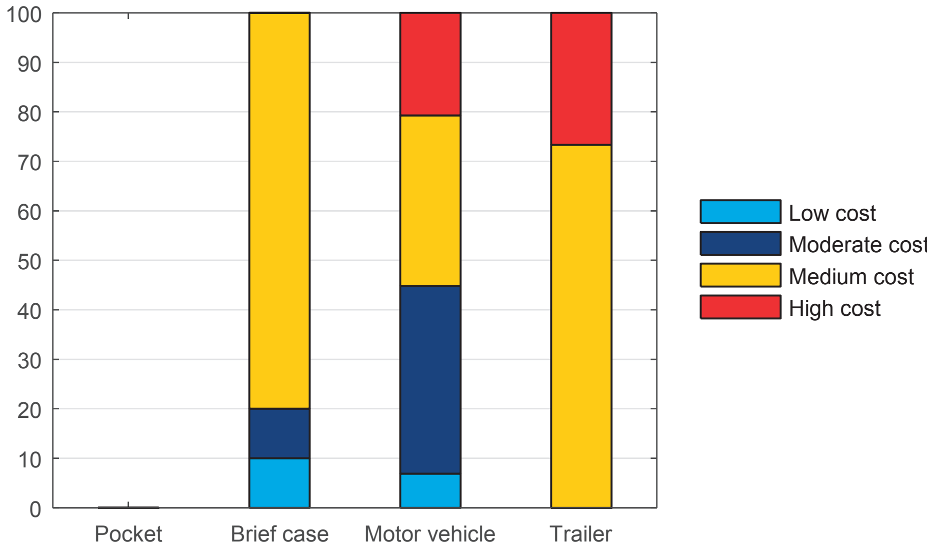

Fig. 3.14 Portability level vs. cost level of the radiated sources (54 sources).

3.3.3.8 Portability level vs. far voltage

The portability level of 35 of the 55 sources is plotted against their far voltage in the bar plot of Fig. 3.15. There are 20 sources for which the far voltage could not be obtained from the available information. From the bar plot, it can be observed that considerable far voltage levels (up to 1000 kV) can already be generated with sources fitting into suitcases. This implies a high threat level for malefactors with the available resources to acquire such a source. In general, all the far voltage levels are also available at motor vehicle sized and trailer sized sources.

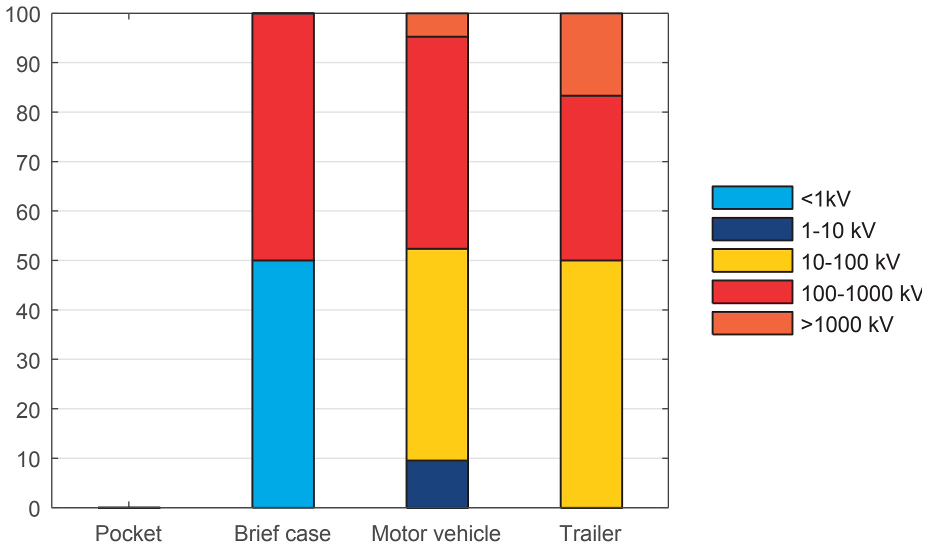

Fig. 3.15 Portability level vs. far voltage of the radiated sources (35 sources).

3.3.3.9 Band-type

The band-type of the sources was assessed in order to identify possible trends in their fabrication. A percentage pie chart illustrating the band-type of 52 of the 55 radiated sources in the database is presented in Fig. 3.16. There are 3 sources for which the band-type could not be inferred from the available information. According to the chart, similar numbers were found for mesoband, sub-hyperband and hyperband sources. Thus, it appears that from a band-type point of view, there is not a preferential kind of source.

As expected, there are a few CW sources since many of the HPM sources were not included due to the transportability and operability issues explained in Section 4. Many of the consulted references that included the use of LPM or HPM tubes were related to fixed installations and, therefore, they were not considered in the database.

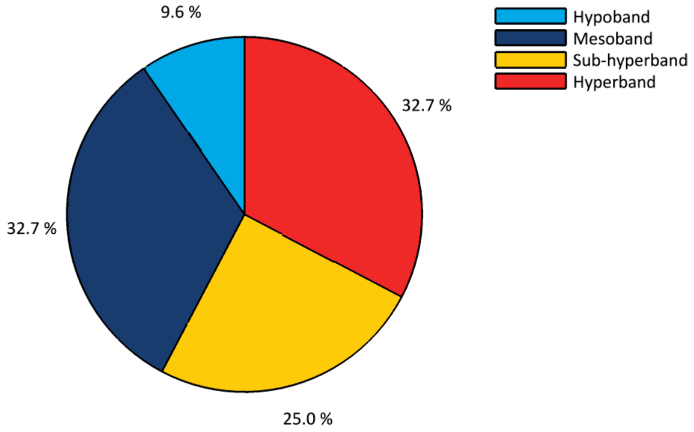

Fig. 3.16 Band-type of the radiated sources (52 sources).

3.3.3.10Year

In order to get an insight into the research and development activities performed in this area, the number of sources vs. the publication year was assessed. A bar plot illustrating the publication year of the 55 radiated sources in the database is presented in Fig. 3.17. It can be observed that there were only a handful of publications about this subject before 1995, and a few in the period ranging from 1995 to 2000. An increased activity occurred in 2000-2010, with about the same number of publications in the first 5 years of this period as in the second 5-year period. In the three-year period from 2010-2013, there is about the same number of publications than that corresponding to 2005-2010, suggesting an increase of the research and development interest.

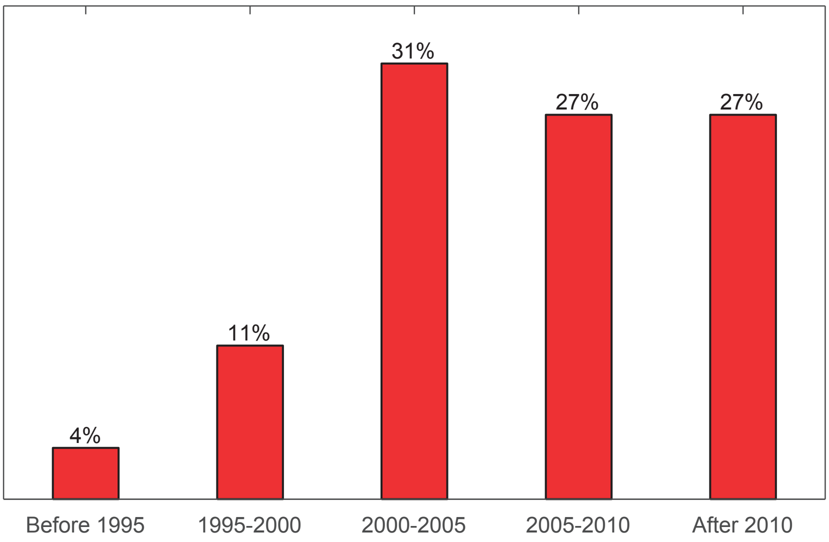

Fig. 3.17 Publication year of the radiated sources (55 sources).

3.3.3.11Year vs. band-type

Finally, the band-type vs. the publication year was also assessed to see if there is an increased interest through time for a specific kind of source. The publication year of 52 of the 55 sources is plotted against their band-type in the bar plot of Fig. 3.18. There are 3 sources for which the band-type could not be inferred from the available information. The bar plot shows a trend to produce hyperband radiators before 2000. Mesoband sources appear in 2000 and, since 2010, the majority of the reported sources belong to this category. From the waveform analysis of [100], it was found that some of the oscillating sources exhibited a very low bandratio between 3 and 4. Thus, part of the sub-hyperband sources between 2005 -2010 could be added to the mesoband sources due to their similar behaviors. Finally, as it was mentioned before, there has been considerable development on hypoband sources during the last decade or so; however, due to their increased power and low transportability, very few were considered in the database and they have not appeared in the literature since 2010.

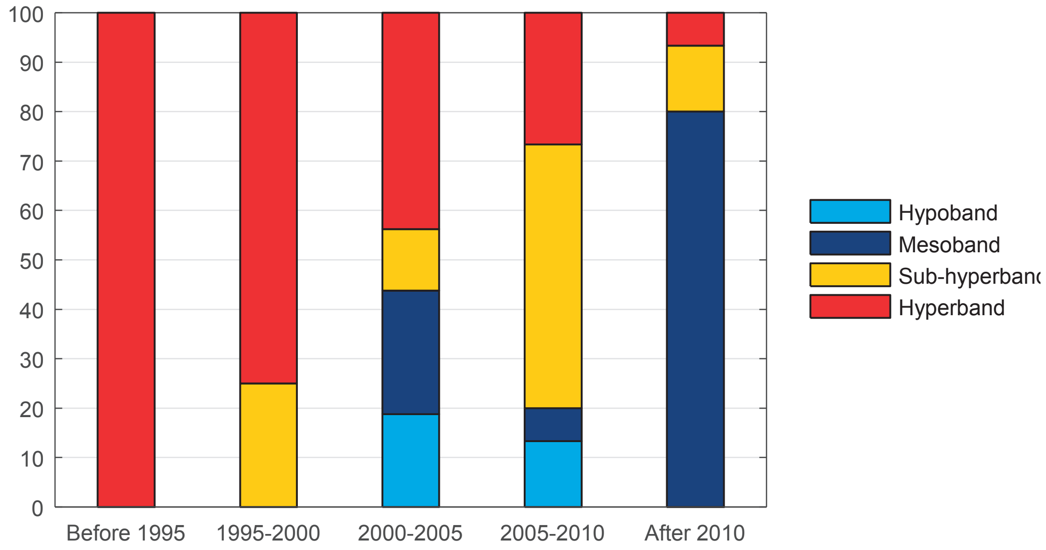

Fig. 3.18 Publication year vs. band-type of the radiated sources (52 sources).

3.4 Overview of the expected limits of potential IEMI sources and their current technologies

After studying the trends based on the collected information on sources, the types of threats that can be achievable with today's technologies and markets was also studied. These trends would certainly be modified as soon as the transportability of the sources increases or the costs are reduced due to technological improvement or market growth. The interest in generating intense fields in the range between some hundreds of MHz and some GHz can been explained by to the expected sizes of handmade electronic equipment and the so-called Baum's law [116]. However, radiated IEMI could also be generated at higher frequencies (perhaps with less impact on electronics) or at higher field levels.

The generation of HPEM fields is fundamentally limited by some physical constraints (proper to the current technologies) that are briefly overviewed in this section. When thinking about the feasibility of potential IEMI sources, the most important constraint is perhaps the physical limitation rather than the current technological limitation. However, it is quite difficult to think about the first one without the other one.

There are many schemes for generating HPEM fields. A block diagram describing a simple HPEM generation scheme is presented in Fig. 3.19 [130].

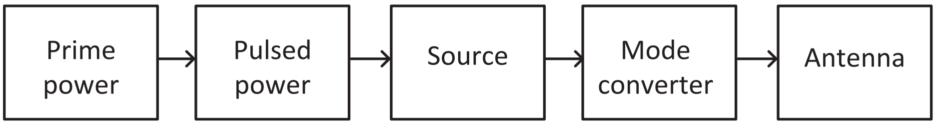

Fig. 3.19 HPEM fields generation scheme. Image adapted from [130].

One of the most common setups starts from a primary DC source that charges a capacitor bank, which in turn feeds a Marx or an inductive generator constituting the so-called primary source. The output of the primary source is injected into subsequent pulse-forming stages in which the risetime is reduced and the desired pulsed power waveform is obtained. At this point, depending on the application, the pulsed power stage can feed a microwave cavity, a HPM tube, or some form of peaking switch whose output is mode-converted and connected to an output antenna. For a conducted source, the output is directly connected to the target, or to a suitable inductive or capacitive probe that will couple to the target.

3.4.1 Technological limits

The electric field flowing in each of the stages of the HPEM generation chain is limited by the so-called gas breakdown limit for short pulses (roughly less than 1μs). For longer pulses, the key issue is the wall heating (see, e.g., page 124 of [130]). The amplitude of the electric field inside the generation chain will depend on the waveguide geometry and the primary excitation signal. When the total field propagating along a gas-filled medium is raised beyond the breakdown limit, a plasma channel is created that is able to sustain a high current value and a conduction current in the gas will short down the original field. In general, a spark develops when the accelerated electrons (due to the high intensity electric field) are capable of producing large electron avalanches. If this wave is intensive enough, the current in the intensified channel increases, becoming unstable until the total breakdown occurs [131].

The breakdown field of air and other types of gases have been extensively studied for switching applications [132-135] and for HPM generation [136]. For air at STP conditions immersed in a uniform field configuration (e.g. DC field in a parallel plate arrangement), the breakdown field is roughly 3MV/m. The study of breakdown under slowly changing non-uniform field conditions is much more complex and its analysis has to be worked out separately for each gas pressure and field configuration. There are some analytical formulas in the literature that provide the breakdown field between canonical sets of electrodes (e.g. spheres, cylinders, cylinder-plates, etc.) for different gases with a fair agreement with experiments [133, 137].

Breakdown data for various gases show higher breakdown fields for shorter duration pulses. For instance, the breakdown of air at one atmosphere pressure is a factor of 2.3 higher for a 10-ns pulse than for DC [133]. In general, the 3MV/m breakdown threshold for uniform field configurations is typically used in HPEM antenna design with a safety margin of 3 (i.e. 1MV/m at the antenna output) to account for possible enhancement points that may lead to gas breakdown [138]. If higher field values are needed, antennas are usually insulated in SF6 [122, 127] which breaks down at about 9MV/m and exhibits a similar propagation constant as air.

3.4.2 Hyperband radiators

The far electric field of hyperband HPEM radiators having aperture antennas as an output (e.g. a HIRA [20]) is governed by the slew rate of the driving voltage and the size of the aperture. The difficulty in building high voltage transient pulsers generating hundreds of kV with risetimes in the order of hundreds of picoseconds constitutes a technological limitation for the generation of such signals. High performance peaking gaps tolerate pressures up to about 100 atm and withstand E fields in the range of MV/cm. It is believed that the maximum derivative that could be expected from a gas switch is in the order of the 10^{15} V/s [20, 139]. Assuming a maximum derivative of 10×10^{15} V/s, a rough estimation of the strongest/fastest achievable pulser for hyperband radiators can be obtained. For instance, the fastest 100-kV pulser would switch at no less than 10 ps and the fastest 1-MV pulser should close at no less than 100 ps.

As already mentioned in Section 3.2, among the most powerful transient generators available in the literature is the JOLT [127]. This system is capable of delivering a radiated far field with a risetime of about 80ps, a FWHM of the order of 100ps, and a far voltage of 5.3 MV. To achieve these results, the JOLT is driven by a 1-MV pulser switching in about 200 ps ($\mathrm{d}V/\mathrm{d}t$ of about 5×10^{15} V/s). In the near field, this system could generate up to 800 kV/m [138].

3.4.3 Mesoband radiators

Mesoband generators can be built from quarter-wave switched oscillators charged with a DC voltage [120]. These systems will also be limited by the above-mentioned switching constraints. Furthermore, given the expected size of these devices, high voltage management becomes an issue. Also, if the desired oscillating frequencies of the quarter-wave oscillators exceed the GHz range, the design of the devices becomes complicated since the mechanical precision requirements for constructing metal profiles at such small dimensions are expensive and not always feasible.

One of the most powerful reported mesoband systems based on a switching oscillator is the so-called MATRIX system [117]. This system could be charged up to 150 kV and it oscillated between 180 MHz and 600MHz. The estimated far-voltage of the original MATRIX system was about 90 kV. Newer versions of the MATRIX systems include oscillators working at higher frequencies (1 and 2 GHz) but charged at lower DC voltages (50-65 kV) [140, 141] due to the above-mentioned breakdown constraints.

Another way to obtain mesoband HPEM radiated waveforms is by connecting a wire antenna to a HV impulse generator. Among the most powerful reported systems, the DIEHL suitcase generators [142] are capable of producing about 225 kV/m at 1m, oscillating at a center frequency of 350 MHz. These systems use a tunable coil antenna that is pulsed with a 600 kV Marx generator. The main technological challenge of such systems is the compaction of the Marx generator into such a small volume (100x55x82 cm^3 according to [142]).

A larger, but still transportable mesoband radiation system based on the excitation of wire antennas with a powerful Marx generator was presented in [122]. The system was capable of generating a 2 MV/300ps pulse to drive a set of helical antennas with 9 different central frequencies ranging from 200 MHz to 6 GHz. Due to breakdown issues at the generator/antenna interface, the helical antennas had to be insulated in an SF6 radome.

3.4.4 Hypoband radiators

Among the IEMI radiators, the so-called LPM sources and HPM radiators are the most dangerous since they are very energetic and may induce permanent effects due to heating of semiconductors. HPM devices are defined as those that exceed 100 MW in peak power and span the range of frequencies between 1 and 300 GHz [20, 130]. Conventional tubes may work in a continuous wave regime up to some MW of output power. If higher output power is required, HPM radiators can be tailored to emit continuous wave bursts of short duration in the hundreds of nanoseconds to some microseconds range (10^{-6} duty factors), and reach output power of some GW. Given the size and the weight of the required supply source and the cooling mechanisms of such generators, LPM and HPM sources are very difficult to transport and they are typically installed in military vehicles or big infrastructures such as airports or military bases.

In order to understand the positioning of LPM and HPM tubes, a comparison of the peak vs. average power for conventional and HPM tubes is presented in Fig. 3.21 [130]. The peak power of a device is plotted against its average power. It can be appreciated that conventional tubes span a big range in the plot while HPM tubes have not been developed to produce substantial average power levels. The straight lines are traced to identify the limits between 1, 10^{-2}, 10^{-4}, and 10^{-6} duty factors.

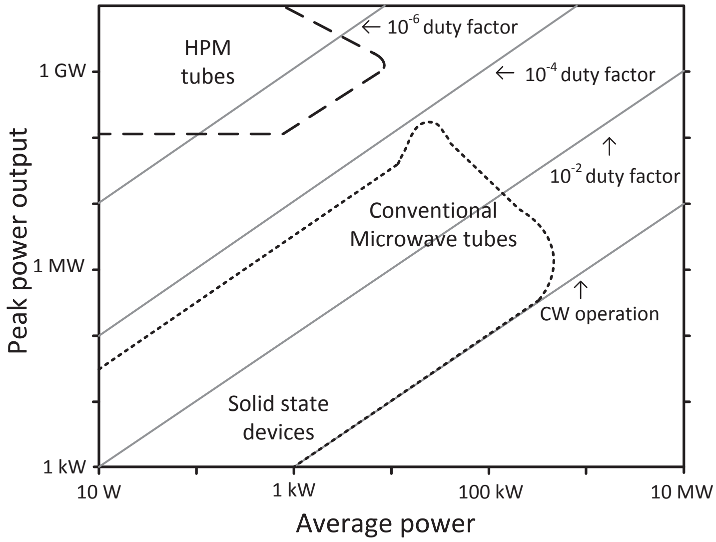

Fig. 3.20 Peak vs. average power for LPM and HPM sources. Figure adapted from [130].

Naturally, the expected peak E field of an HPM radiator is lower than that of a hyperband or mesoband radiator. It was believed in the late 90s that HPM devices were fundamentally limited above a peak power of approximately 10GW and pulse energy of 1 kJ [130, 143]. However, it is believed that with the aid of phase locking, multiple sources can conceivably increase the single device levels. For example, the output levels of a feasible multiple pulse weapon considered by Taylor and Giri in [143] was 10 GW of peak power, 100 ns pulse width, and 1 kJ of energy per pulse at a repetition rate of 1 kHz. The ultimate limits on HPM source peak power are not well known. They are set by a trade-offs between breakdown (multipactor), mode competition, and intense beam-field interactions.

Fig. 3.21 presents a plot of the peak power generated by a representative sample of high power sources adapted from [130]. It appears that the peak power of many sources falls off as Pf^2 at high frequency.

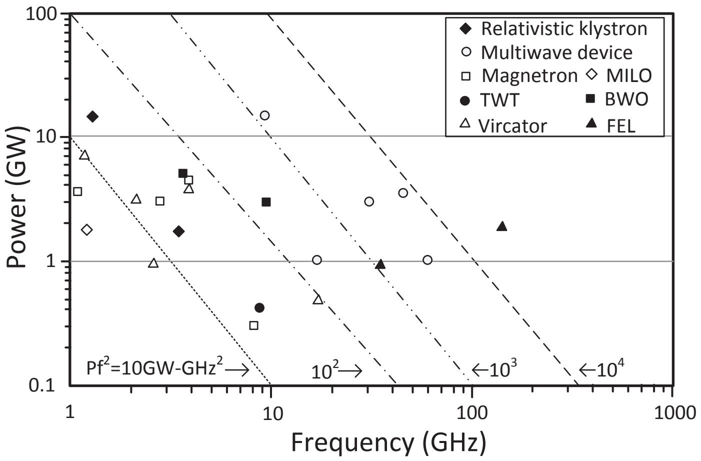

Fig. 3.21 Peak powers of HPM sources. Figure adapted from [130].

Among the most powerful and simple to build HPM sources is the virtual cathode oscillator or Vircator. The Vircator is a very attractive source for IEMI given the fact that it is a tunable CW generator in the 1-10GHz range, it does not require an applied magnetic field and it is a low impedance device (permits high power operation at low voltage). However, it is a very inefficient source (about 1-15%) and it is traditionally operated with explosives like single shot electrical generators at the input in order to reduce space.

3.5 Conclusions

In this chapter, we have presented a study and classification of potential IEMI sources that were collected from available publications. As a product of this work, two databases including a collection of *wavecards* with the waveforms and spectral parameters of about 39 sources, and a spreadsheet containing the classification of 21 conducted sources and 55 radiated sources according to the proposed criteria for assessing the strength, availability and transportability were presented. Both databases can be found in Appendices A and B of [100].

The information in the spreadsheets was used to generate pie charts and bar plots that illustrate some tendencies and characteristics of the analyzed conducted and radiated sources. It was found that potential IEMI conducted sources are more available than radiated sources. Due to the maturity of the market, and the lower frequency requirements, these sources are commercially available from various EMC test vendors. Voltage levels in the range of several kV can be achieved with sources exhibiting all of the defined portability levels (including pocket-size), and their acquisition prices remain moderate for the majority of the conducted sources. Thus, they can be regarded as likely to be deployed by an IEMI malefactor.

On the other hand, radiated sources are still in a development phase and are only available for purchase as test-sources. They require at least a vehicle to be transported and, according to the classification (made to the best of the authors' knowledge), the typical costs of such sources remain high due to the required high technology in the implementation and testing. However, there are already some prototypes that can be transported in a briefcase and whose field level outputs are capable of theoretically producing malfunctions and damages –if located close enough- to electronics. A trend to produce hyperband radiators was identified in the early 2000s. In more recent years, the survey reveals a growing activity in the development of mesoband sources.

In the last part of this chapter, the physical limitations that constrain the development of current technologies in the generation of faster and stronger HPEM sources have been reviewed in order to set up an overview of the expected worst case scenario.

4

Experimental Characterization of the Response of Commercial Cablings to IEMI

4.1 Introduction

Hardening of infrastructures against IEMI requires a prior knowledge of the *receptivity* level and the nature of the expected perturbations arriving to the protected equipment. Among the typical parameters of interest are the amplitude and frequency content of the induced current or voltage at the equipment inputs. The expected amplitudes and frequency contents of IEMI sources have been previously studied in Chapter 3.

Recent studies have shown the possibility of interrupting the normal functioning of IT networks using HPEM interferences through the LVP [11, 106] and the LAN cables [11, 106, 144]. In [11, 106], mesoband sources [2] of about 60 kV/m were used to temporarily interrupt an Ethernet switch after illuminating its LVP cable in an AC. Similar tests with hyperband fields of 44 kV/m inside a GTEM Cell [11, 106], and 6.6 kV/m in a TEM Cell [144] have been shown to slow down or permanently break the data transfer of the switch, depending on the pulse repetition frequency of the source.

Predictions of the coupled voltage and current levels at the cable terminals (input of the equipment) can be obtained with the use of the TL theory (e.g., [88] [46, 145, 146]), assuming that the cable parameters are known. The use of TL-based approximation techniques for modeling the propagation of IEMI transients in LVP networks has been studied in [81, 82] where it was shown that uncertainties in the input geometrical and electrical parameters of the exposed line may significantly impact the accuracy of simulated results. The stochastic nature of the impinging field and the wire positions can be included in the predictions (e.g., [91, 112, 147-149]). In particular, TL models of straight wire lines excited by a superposition of random plane waves have shown to provide results which are in good agreement with experimental data obtained using RC in [112, 147]. The relation between field-to-wire coupling test results obtained in a RC and AC is discussed in [150].

Electromagnetic field coupling to unshielded TWP has also been a subject of recent studies (e.g., [145, 148, 151-154]]. It has been shown that accurate predictions for the induced CM and DM voltages can be achieved as long as the considered configurations are relatively simple. On the other hand, DM voltage estimation is very sensitive to less controlled parameters like the twist pitch or a non-integer number of twists, which might lead to inaccurate predictions in realistic scenarios [11, 155]. Further insight about the challenges and modeling issues of realistic cablings at frequencies representative of IEMI interferences will be dealt in Chapters 6 and 7.

In general, the presence of non-ideal connectors, load imbalance [145, 156], line non-uniformity [157], and improper line terminations [158, 159] substantially contribute to inaccuracies in numerical/analytical predictions. Therefore, experimental results are needed to obtain correct estimates of induced DM signals in TWP cables. Similar issues occur in the prediction of field coupling to shielded cables where the overall response can be significantly affected by the presence of pigtails, or bad contact resistances between the shields and connectors (see e.g. [84]). Experimental results for shielded cables illuminated inside a RC in [160] have shown that modifications in the range of tens of dBs are obtained in the voltage response of a shielded cable due to a change of the connector type.

This Chapter is heavily drawn from [79]. It presents the results of two experimental campaigns that were carried out to study the levels of induced DM voltage and CM current in typical configurations of LVP, TEL and LAN installations inside an office, due to an external electromagnetic field illumination representative of IEMI. The first test consists of the illumination of a commercial raceway with a HPEM field inside a GTEM cell. In the second test, the same raceway was illuminated with a CW signal in a RC.

The idea of testing with these two separate methods was two-fold: (i) to estimate the expected conducted disturbances at the input of equipment connected to the cables due to a HPEM illumination, without having to model the complete setup in a full wave or transmission line environment; (ii) to be able to generalize the obtained results for the case of multiple angles of incidence and non-uniform illumination, with statistically plausible data. The first method is useful for understanding the induced levels in the time domain, whereas the second is useful to assess the general behavior of the assemblies in the frequency domain. The experiments have been performed with the intention of providing a general idea of the coupling levels and this is why representative cables and structures have been used.

This chapter is organized as follows. Section 4.2 presents the device under test, namely a typical electrical and communications raceway including several types of cables that are found in commercial buildings. Section 4.3 presents the transient HPEM illumination setup inside a GTEM cell. Section 4.4 presents the low power test setup inside a RC. The obtained results with relevant discussion are presented in Sections 4.5 to 4.7. Finally, conclusions are presented in Section 4.8.

4.2 Device under test

This section describes the electrical and communication raceway under test and the measurement interface cards that were specifically designed to access the induced signals in individual conductors.

4.2.1 Raceway description

The device under test is a 200-cm long raceway containing several LVP, LAN, and TEL cables, typical of a civilian office environment. A schematic diagram representing the cablings inside the raceway is shown in Fig. 4.1.

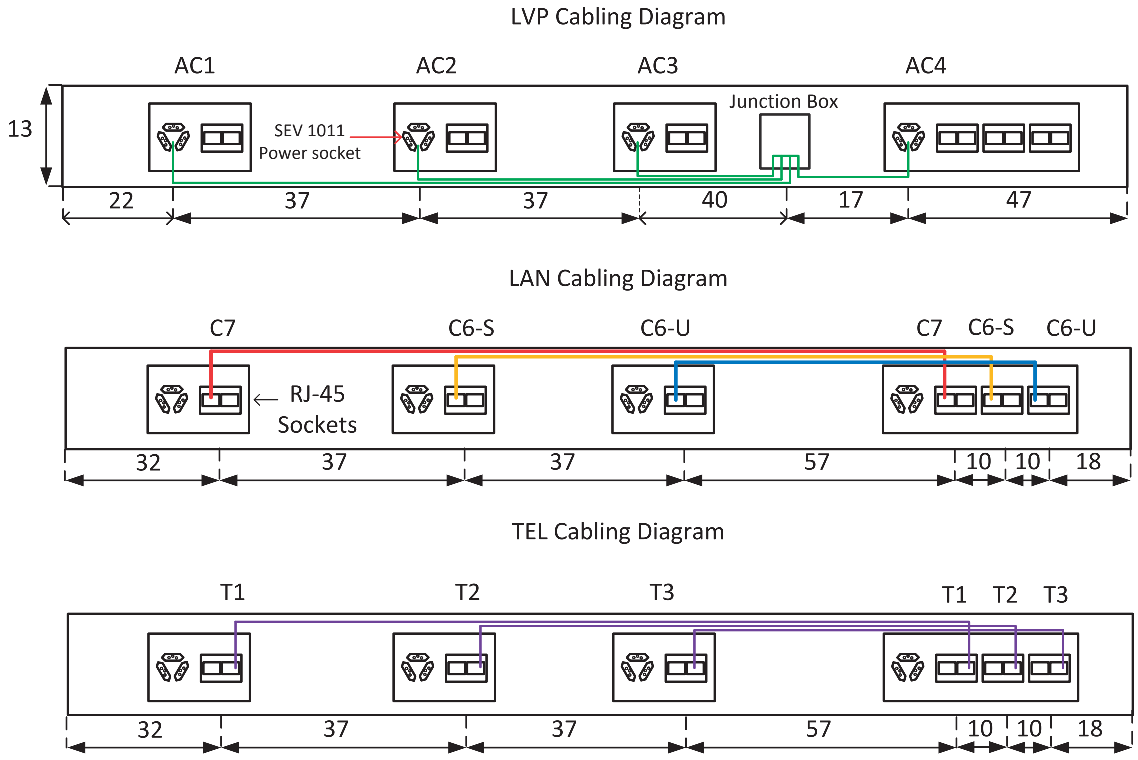

Fig. 4.1 Schematic diagram of the cablings inside the test raceway. Distances are in cm and not to scale.

4.2.1.1 Low voltage power cabling

The LVP cabling is composed of 4 TT 3 x 1.5 mm^2 cables terminated with triple-power sockets of SEV 1011 type. The LVP cables contain three coated wires corresponding to the phase, neutral, and ground conductors of the distribution network and are supposed to withstand a DM peak voltage of 1 kV before dielectric breakdown. The four power sockets were labeled from left to right as AC1, AC2, AC3, and AC4, respectively.

The power cables were connected in a star configuration with one end connected to the sockets and the other end to a junction box. The junction box can be also used to connect the test raceway to external 220V/ 50Hz power lines. Since the study did not require the test of the equipment in a powered state, the power cables were left isolated from the external power network.

4.2.1.2 Ethernet network cabling

The Ethernet network cabling is composed of 3 LAN cables terminated at both ends with RJ-45 sockets. Each LAN cable contains 4 TWPs. Each TWP is made of 2 coated copper wires that may contain a shielding screen to avoid interference with the other pairs of the bundle. The 4 TWPs are grouped into a single bundle that may be also shielded to avoid interference with the environment.

Three different LAN cable categories were used as follows:

- C7: Category 7 S/FTP cable
- C6-S: Category 6 SF/UTP cable
- C6-U: Category 6 U/UTP cable

A summary of the properties of the used LAN cables, according the manufacturer datasheets, is shown in Tab. 4.1. The RJ-45 connectors were labeled according to the LAN cable category.

Tab. 4.1 LAN cable specification

Label	Cat.	Class	Bundle shield	TWP shield	Max. Freq. (MHz)
C7	7	F	Braid	Foil	600
C6-S	6	E	Braid-foil	None	450
C6-U	6	E	None	None	300

4.2.1.3 Telephone cabling

The TEL cables were three U72 cables terminated at both ends with RJ-45 sockets. U72 are unshielded cables containing 4 twisted coated wires. According to the manufacturer’s datasheet, the maximum usable frequency for this kind of cables is 5 MHz. Notice that in practice, only 2 wires of the U72 cable are required for the telephone connections. The termination sockets of the TEL cable were labeled as T1, T2, and T3, respectively.

4.2.2 Measurement interface cards description

The current and voltage measurements performed in this work used two measurement interface cards that were specifically designed to make a transition between the different cable outputs and the 50 Ω input of a measuring oscilloscope or VNA. Additionally, the interface cards could also be used as 50 Ω or 100 Ω terminations for unused or floating wires in the cables under test.

A schematic diagram describing the measurement interface cards is shown in Fig. 4.2.

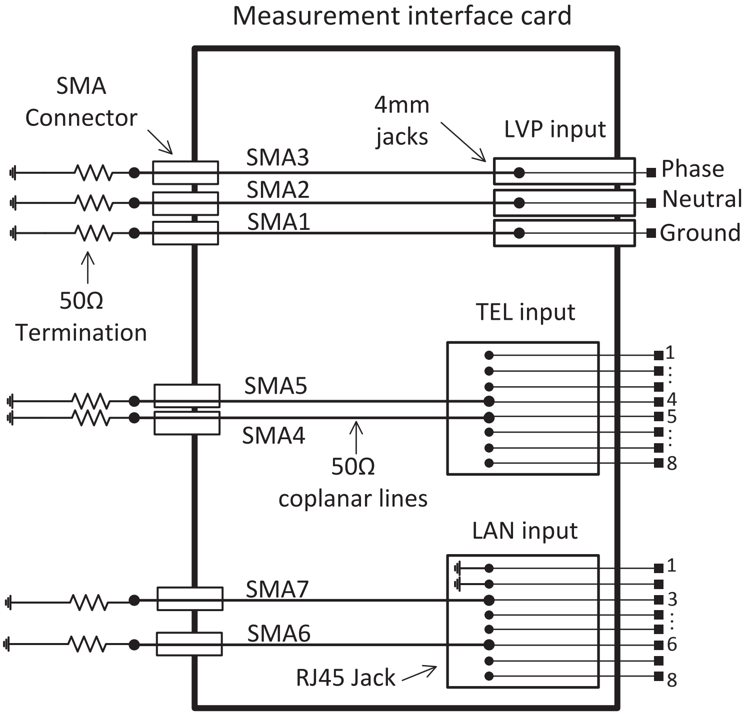

Fig. 4.2 Schematic diagram of the measurement interface cards.

The measurement card has 3 inputs, namely, the LVP input (phase, neutral, and ground wires), the TEL input (2 wires of the TEL cable connected to pins 4 and 5 of the TEL RJ 45 jack), and the LAN input (8 wires of the LAN cable connected to the LAN RJ-45 jack). The measured signals are transmitted through 50Ω coplanar lines of identical electrical length to seven SMA connectors located at the other end of the card. These connectors serve to connect the measurement channel or to terminate the lines with a 50 Ω load. The DM termination impedance between any pair of SMA connectors is 100 Ω.

Out of the 8 available wires from the LAN cable, only two (pins 3 and 6) were used for measurement. These correspond to the Rx+ and Rx- wires in classical Ethernet networks. Also pins 1 and 2 are connected to the card reference plane. These correspond to the Tx+ and Tx- wires in classical Ethernet networks.

The measurement cards were installed inside a metallic enclosure that provides better shielding than a typical COTS product. Representative RJ 45 connectors were used for the TEL and LAN inputs with additional shielding provided by a seal made up with copper tape. The effect of the additional shielding on the RJ-45s will be shown later in Fig. 4.19. A picture of one of the measurement cards (without the copper tape seal over the RJ 45s) is shown in Fig. 4.3. There are two additional SMA connectors on the top part of the picture that are connected to a through PCB line that was made for calibrating the delay between the lines due to the FR4 effective permittivity.

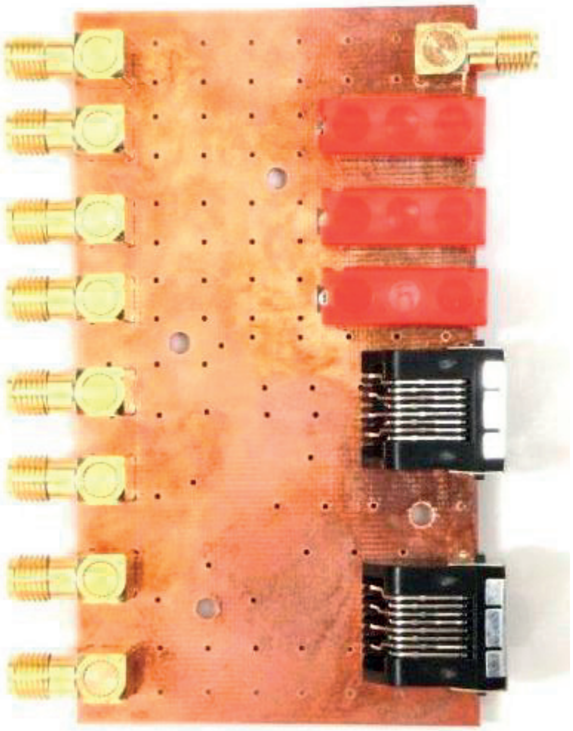

Fig. 4.3 Top view of the measurement cards without the shielding enclosure. Notice that the shield of the RJ-45 jacks is not continuous.

4.3 Transient HPEM illumination setup

In this section, the experimental setups for the high power illumination tests inside the GTEM cell are presented.

4.3.1 GTEM cell description

The illumination tests were performed in the GTEM cell of Armasuisse (Swiss Defence Procurement Agency) located in the RUAG Defense Labs in Bern. The cell reference is GTEM 3750 fabricated by EMC Baden. A schematic diagram illustrating the dimensions of the cell is presented in Fig. 4.4. The working volume was 2.5m x 2.5m x 2m.

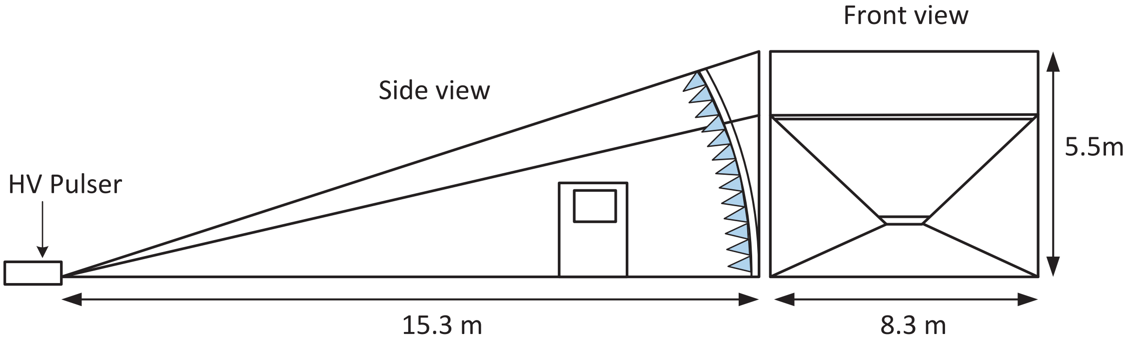

Fig. 4.4 Front and side view of the GTEM 3750 Cell of Armasuisse.

The input of the GTEM cell was connected to a bipolar 200ps/50kV peak-to-peak amplitude pulser provided by ISL [128]. The pulser was remotely operated using a computer and a FO communication link. The output of the pulser was connected to the GTEM cell input through an impedance adapter [161].

The electromagnetic field generated in the working volume was characterized using B-dot and D-dot sensors. The voltage output of the sensors was transmitted through a FO link to a digital oscilloscope. The FO transmitter was located inside the cell, and the FO receiver was installed in a shielded cabin outside the cell.

A summary of the specifications of the used equipment is given in Tab. 4.2.

Several field samples were taken at different positions inside the working volume. The measurements correspond to the average of 6 subsequent shots of the pulser. The generated field was found to be a uniform TEM wave. A plot of a typical measured vertical E-field and horizontal H-field, and their frequency spectra is presented in Fig. 4.5. In order to check the TEM validity, we have multiplied the magnetic field curve by the free space impedance $\eta = 120\pi$. We have also checked that the field components in the other directions were significantly lower.

The generated E-field is a bipolar hyperband pulse of about 40kV/m peak-to-peak amplitude. Given that the risetime of the D-dot sensor is slower than the driving source risetime (about 230ps), the risetime of the generated field is approximated to the risetime of the pulser, namely 200ps.

Tab. 4.2 GTEM cell experimental setup configuration for field mapping

Parameter	Description
D-dot max. frequency/ max. field	1.2 GHz / 1MV/m
B-dot max. frequency / max. field	1.3 GHz / 2.65kA/m
FO link max. frequency	3.2GHz
Oscilloscope sampling rate/ max. frequency	20Gs/s / 6GHz

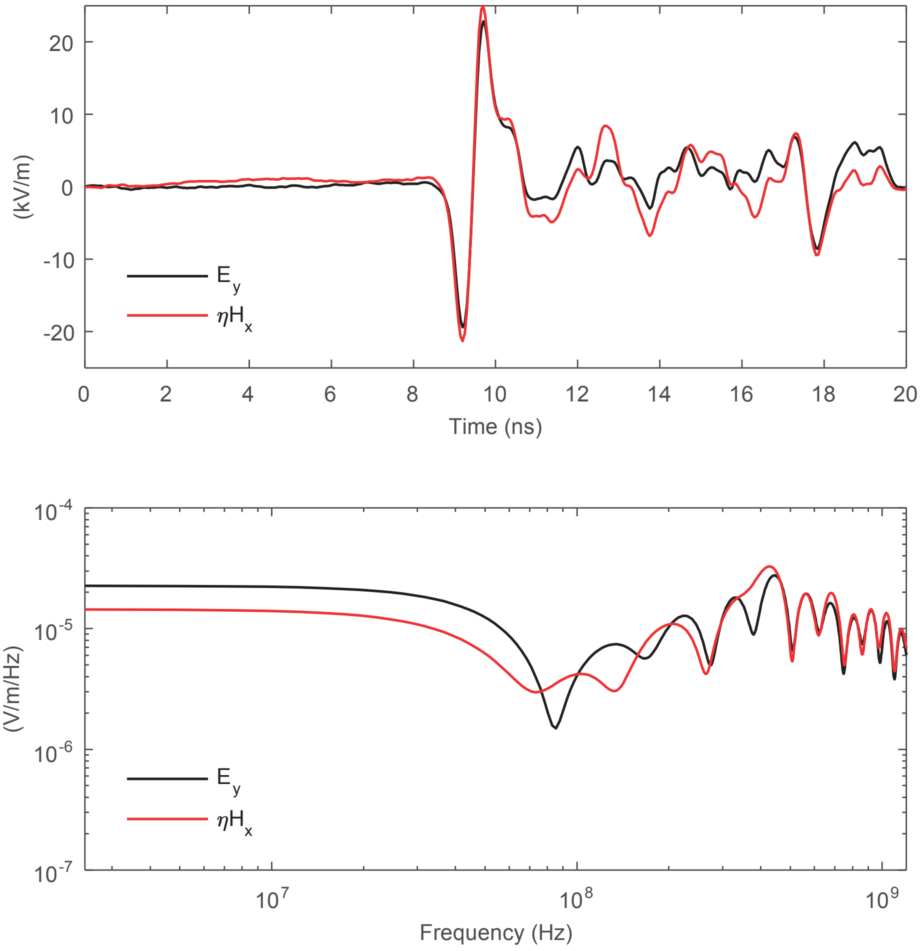

Fig. 4.5 Waveform and spectrum of the generated vertical E-field and horizontal H-field in the working volume of the GTEM cell. The DC component of the derivative sensors was removed before integration to avoid the offset-induced spurious integration ramp.

4.3.2 CM current test

A schematic diagram of the CM current measurement setup is presented in Fig. 4.6. The raceway was either vertically or horizontally positioned inside the working volume of the GTEM cell in order to test the effect of a normal and grazing incidence of the field. The induced CM current in the cable under test was measured with a current transformer (CT) connected to a digital oscilloscope through a FO transceiver. The output of the CT was attenuated in order to meet the input requirements of the FO transmitter. The oscilloscope was configured to take the average of 6 subsequent triggers.

The LVP, LAN or TEL lines were connected to the interface cards' inputs, and the CM current flowing from the output socket of the raceway was measured with the CT. All the SMA ports of the cards were terminated with 50Ω loads during this test. The connection between the cards' input and the raceway sockets was made through patch cords of the same type as the cables under test. For example, during the C7 LAN cable test, the RJ-45 jack of the interface card was connected to the raceway by using a patch cord of category 7 S/FTP.

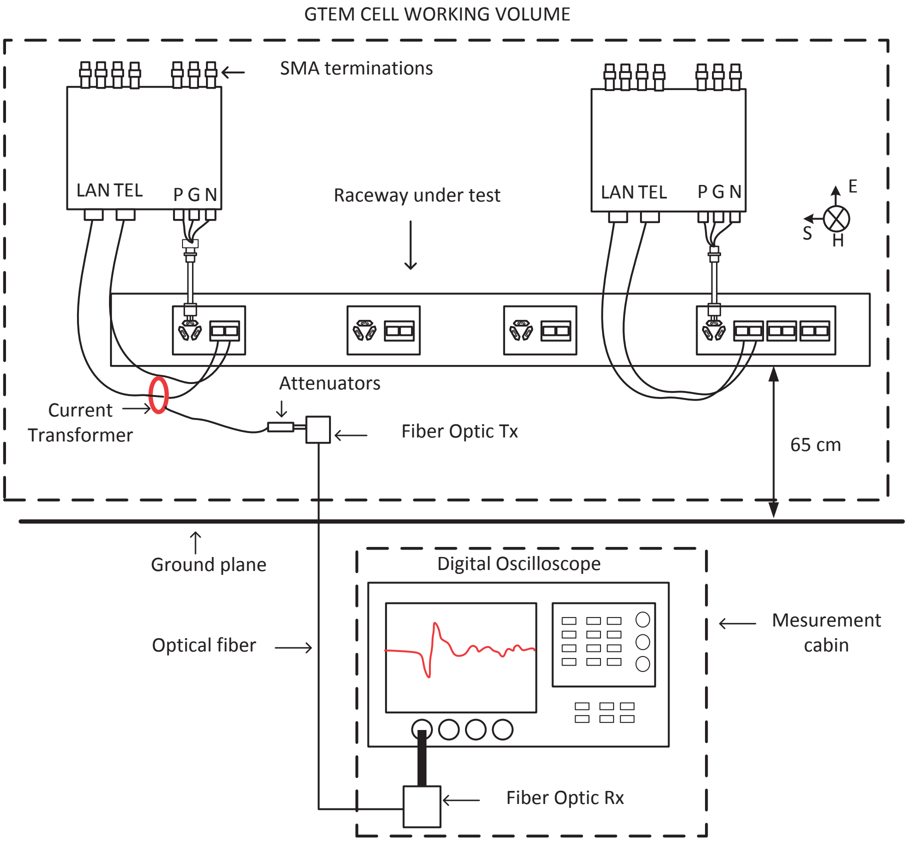

Fig. 4.6 Schematic diagram of the CM current test.

4.3.3 DM voltage test

A schematic diagram of the DM voltage measurement setup is presented in Fig. 4.7. The raceway was either vertically or horizontally positioned inside the working volume of the GTEM cell. The induced voltages in two selected wires of the cable under test were measured by connecting the interface cards' outputs to the FO transceiver. The DM voltage between the two wires was determined by calculating the difference between the signals in the two wires. The outputs of the measuring interface card were attenuated in order to meet the input requirements of the FO transmitter. As in the CM current test, the oscilloscope was configured to take the average of 6 subsequent triggers.

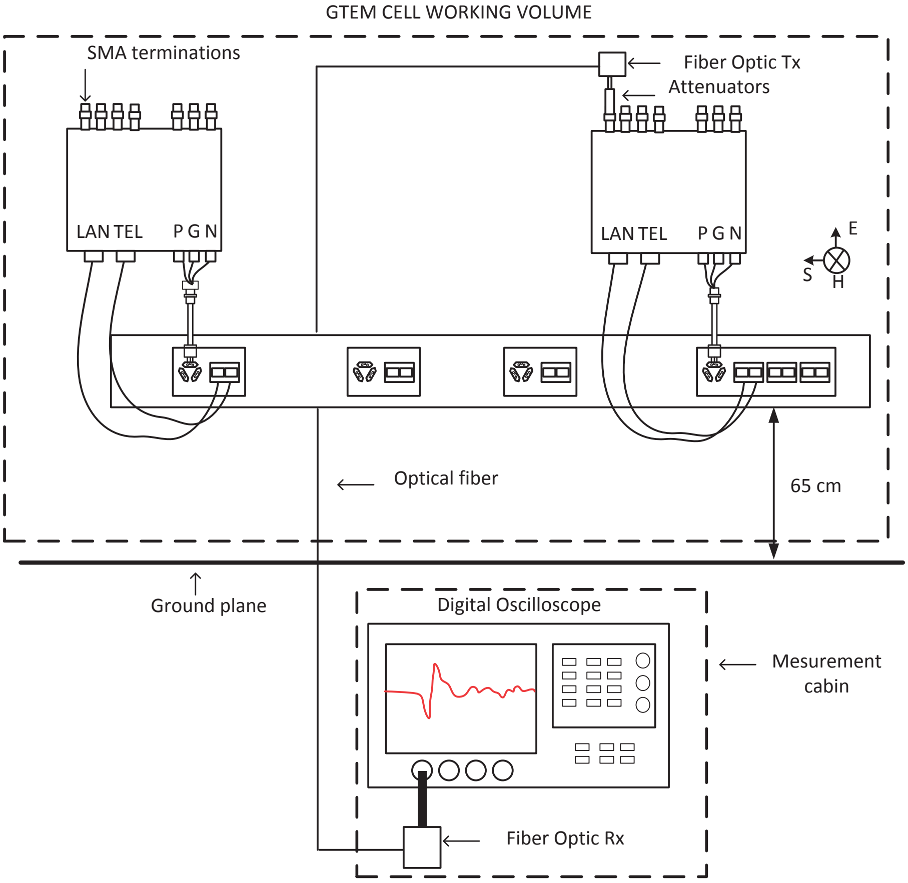

Fig. 4.7 Schematic diagram of the DM voltage test. The diagram illustrates the measurement of one of the DM lines.

The LVP, LAN or TEL lines were connected to the interface cards' inputs, and the outputs of two SMA ports were connected to the oscilloscope through the FO transceiver. The other SMA ports were terminated with 50Ω loads.

A summary of the equipment configuration for both tests is presented in Tab. 4.3.

Tab. 4.3 Experimental setup configuration for the GTEM illumination tests

Parameter	Description
CT frequency range	1 MHz-1GHz
CT max. pulse current	100A
Fiber optic link max. freq.	3.2GHz
Oscilloscope sampling rate	20Gs/s
Oscilloscope max. freq.	6GHz

4.4 Reverberation chamber setup

4.4.1 Reverberation chamber description

The RC illumination tests were performed in the chamber located in the Department of Electronics, University of York UK. The 4.70 m x 3.00 m x 2.37 m chamber has a lowest usable frequency of about 100 MHz. It is tuned using a mechanical paddle driven by a stepper motor in the chamber roof that is controlled by a PC using a serial interface. The working volume of the chamber at 1 GHz is approximately 2.3 m × 2.7 m × 2.0 m.

The measurements were conducted using a VNA controlled via a GPIB interface from a PC. The setup for the calibration and coupling measurements is shown in Fig. 4.8. The PC controlled the paddle rotation and an RF switch module located inside the chamber was used to alternate between the two signal wires being measured during each coupling experiment. The switch module has an isolation of more than 70 dB (typically 90 dB) up to 8 GHz.

All the RC measurements reported here were carried out over the frequency band 200 MHz to 6 GHz, collecting 1601 frequency samples at 100 equally spaced positions of the paddle over a full rotation. A full two-port calibration of the VNA, cables and RF switch up to the input ports of the antennas was carried out. The small amplitude and phase imbalance of the two cables from the RF switch unit to the measurement card was calibrated out by de-embedding (in post-processing) an S-parameter error block determined from a separate VNA measurement of the two cables. Hybrid “blade” antennas covering the range 200 MHz to 26 GHz were used to allow the required frequency range to be measured without switching antennas [162].

4.4.2 RC uniformity and calibration

Where appropriate the test methodology followed the IEC61000-4-21 standard [163]. The electromagnetic field generated inside of the working volume of the chamber was characterized with the raceway and any other equipment in place and the external switch shown in Fig. 4.8 set to the “power calibration” position. The transmission between the pair of blade antennas was measured and the average power density and hence the mean-square electric field, $\left\langle |\mathrm{E}^{\mathrm{inc}}|^2 \right\rangle$, within the working volume determined from

$$\langle S \rangle = \frac{\left\langle |\mathrm{E}^{\mathrm{inc}}|^2 \right\rangle}{\eta_0} = \frac{1}{\eta_2^T} \frac{8\pi}{\lambda^2} \left\langle |\mathrm{S}_{21}|^2 \right\rangle \frac{|\mathrm{V}_1^+|^2}{Z_0}. \tag{4.1}$$

Here V_1^+ is the forward voltage of the VNA, η_0 the intrinsic impedance of free-space, Z_0 the VNA port impedance and η_2^T is the total efficiency of the receiving antenna, given by

$$\eta_2^T = \eta_2^{\mathrm{rad}}(1 - |\mathrm{S}_{22}^{FS}|^2) \approx (1 - |\langle \mathrm{S}_{22} \rangle|^2), \tag{4.2}$$

where η_2^{rad} is the radiation efficiency of the antenna (due to ohmic and dielectric losses) and S_{22}^{FS} is its free-space reflection coefficient. The statistical error in the fields was about ±0.5 dB [164]. A summary of the required equipment for this test and the specifications are reported in Tab. 4.4.

Tab. 4.4 Equipment for power density calibration of RC measurements

Equipment	Description
VNA	Rhode & Schwarz ZVB 20
PC3.5 SOLT cal. kit	Rhode & Schwarz ZV-Z235
Rx/Tx antenna	UoY hybrid “Blade” antenna
RF switch	Mini-circuits MSP2TA-18, DC-18 GHz
Microwave cables	Reynolds Industries 269-0195

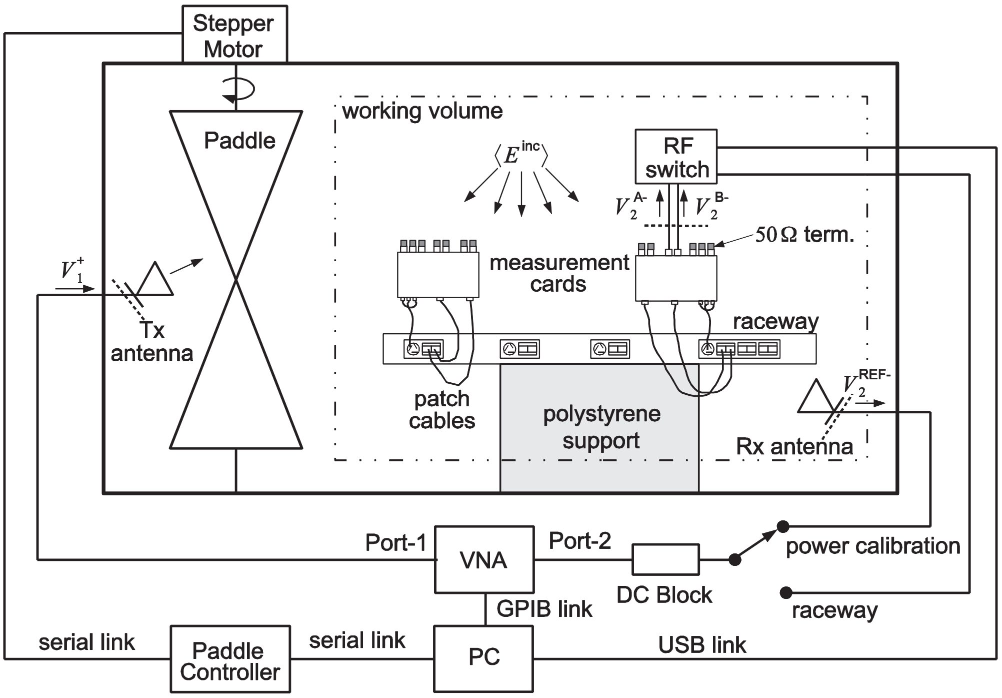

Fig. 4.8 RC Measurement setup. The dotted lines show the calibration planes of the VNA.

4.4.3 DM coupling tests

The configuration for coupling measurements was the same as in Fig. 4.8, with the external switch (after the DC block) in the “raceway” position. It was essential that the equipment was not disturbed between the power density calibration and raceway measurements in order to obtain accurate results. The RF switch unit was used to allow the measurement of the received voltage into 50 ohms on each wire in a signal pair of a cable, V_1^- and V_2^-, at each paddle angle. The mean-square DM voltage at each paddle position was calculated from

$$\left\langle |\mathrm{V_{DM}}|^2 \right\rangle = \left\langle |\mathrm{V_1^-} - \mathrm{V_2^-}|^2 \right\rangle. \tag{4.3}$$

Statistical distribution functions for $|\mathrm{V_{DM}}|$ over the different paddle positions can be also obtained. These are expected to have Rayleigh distributions [112, 147, 153, 165].

4.5 Transient HPEM illumination results

4.5.1 CM current results

CM current measurements were performed in each of the 9 cables (3 LVP, 3 TEL, and 3 LAN) while the raceway was either in the vertical or horizontal position inside the GTEM cell. Notice that in the LVP measurements, the near end measurement card was connected to AC1, AC2, or AC3, while the far end card was always connected to AC4. Depending on the cable under test, different profiles of induced current waveforms were obtained.

4.5.1.1 Typical result

An example of the CM current from a measurement performed in the C7 cable (see Fig. 4.1) is presented in the top panel of Fig. 4.9. The plot corresponds to a measurement performed while the raceway was in the vertical position. The oscillatory waveform has a peak amplitude of 6 A. The computed frequency spectrum is shown in the bottom panel of Fig. 4.9. It features several resonant frequencies with a peak at about 50 MHz, an expected behavior for line lengths of the order of meters. Similar curves exhibiting an oscillatory behavior with several resonant frequencies were obtained for the other cables.

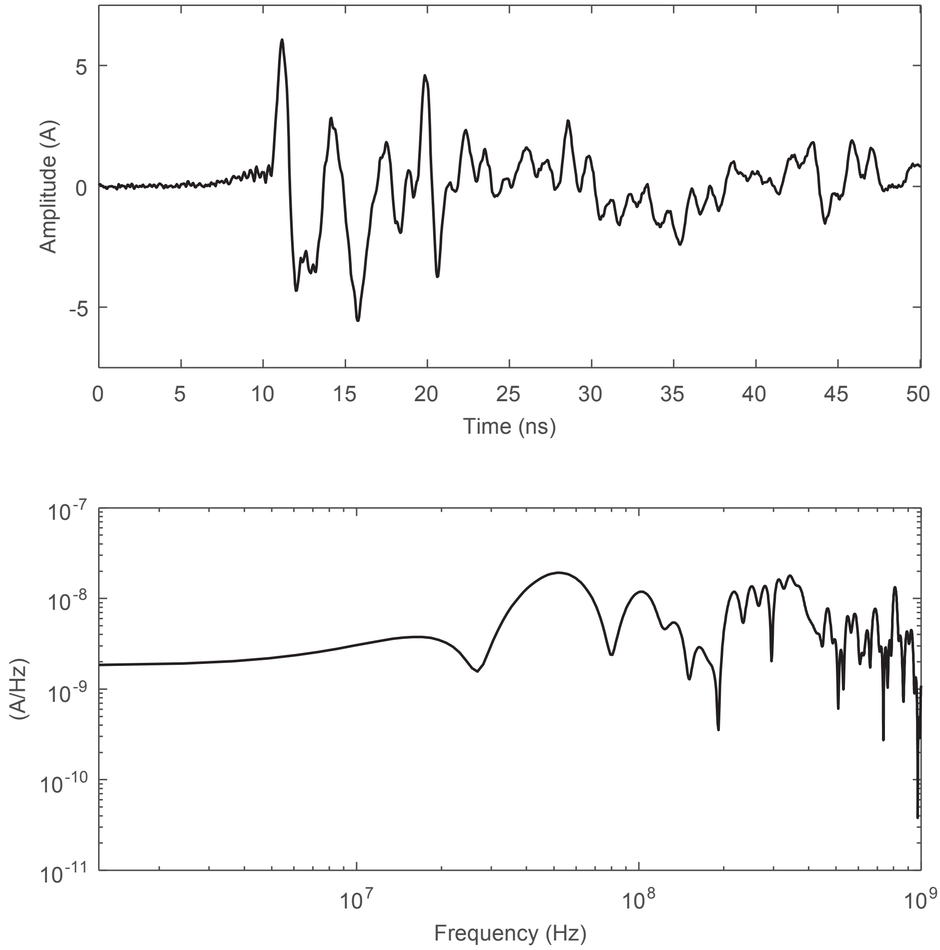

Fig. 4.9 Example of a current measurement performed in the C7 cable with the raceway in a vertical position. The incident E-field is shown in Fig. 5.

4.5.1.2 Peak amplitudes

A bar plot summarizing the peak amplitudes of the 18 measurements is presented in Fig. 4.10. The results obtained with the raceway in vertical and horizontal positions are plotted with red and blue bars, respectively. Amplitudes between 1 and 10 A were observed with higher values corresponding to the normal incidence of the field (raceway in the vertical position). Similar current levels and resonant frequencies have been reported for 44kV/m hyperband illuminations [11, 106] and 10-50 kV/m NEMP illuminations [166] of LAN cables.

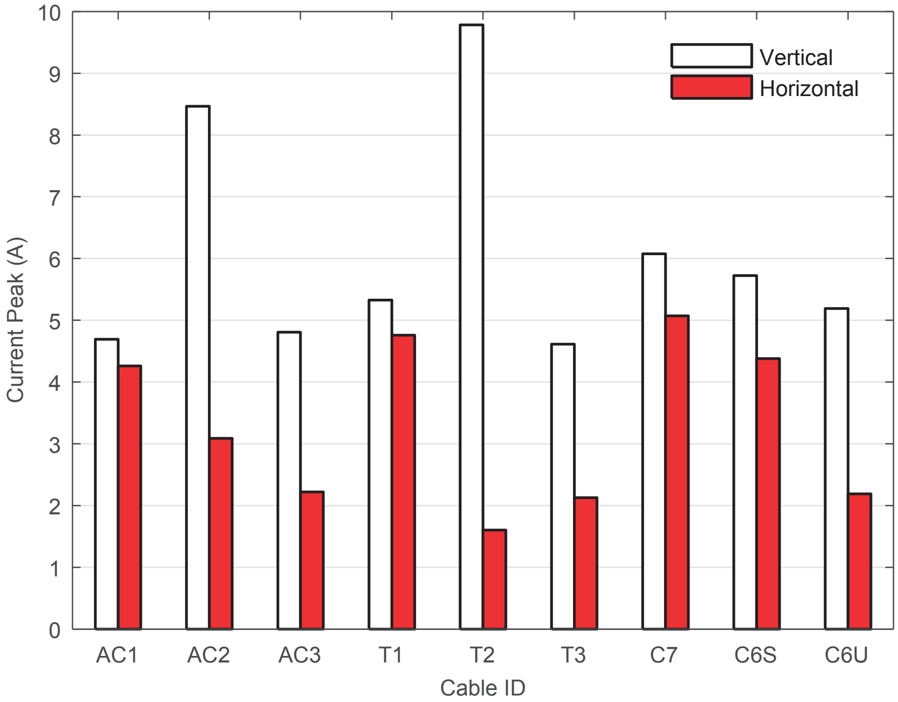

Fig. 4.10 Bar plot of the peak amplitude of the CM current measurements. The incident E-field is shown in Fig. 5.

4.5.2 DM voltage results

DM voltage tests were performed in each of the 9 cables while the raceway was either in the vertical or horizontal position. Three DM voltages were measured for each of the three LVP lines, namely, the Phase-Neutral voltage (PN), the Phase-Ground voltage (PG), and the Neutral-Ground voltage (NG). In the case of the TEL and LAN cables, the DM voltage was measured between the pins indicated in Fig. 4.2.

4.5.2.1 Typical result

Two of the DM voltages obtained in the AC3 cable while the raceway was in the vertical position are presented in Fig. 4.11. The peak amplitudes of the PN (in black) and PG (in light were 160 V and 460 V, respectively. Similar curves exhibiting an oscillatory behavior with several resonant frequencies were obtained for the other cables.

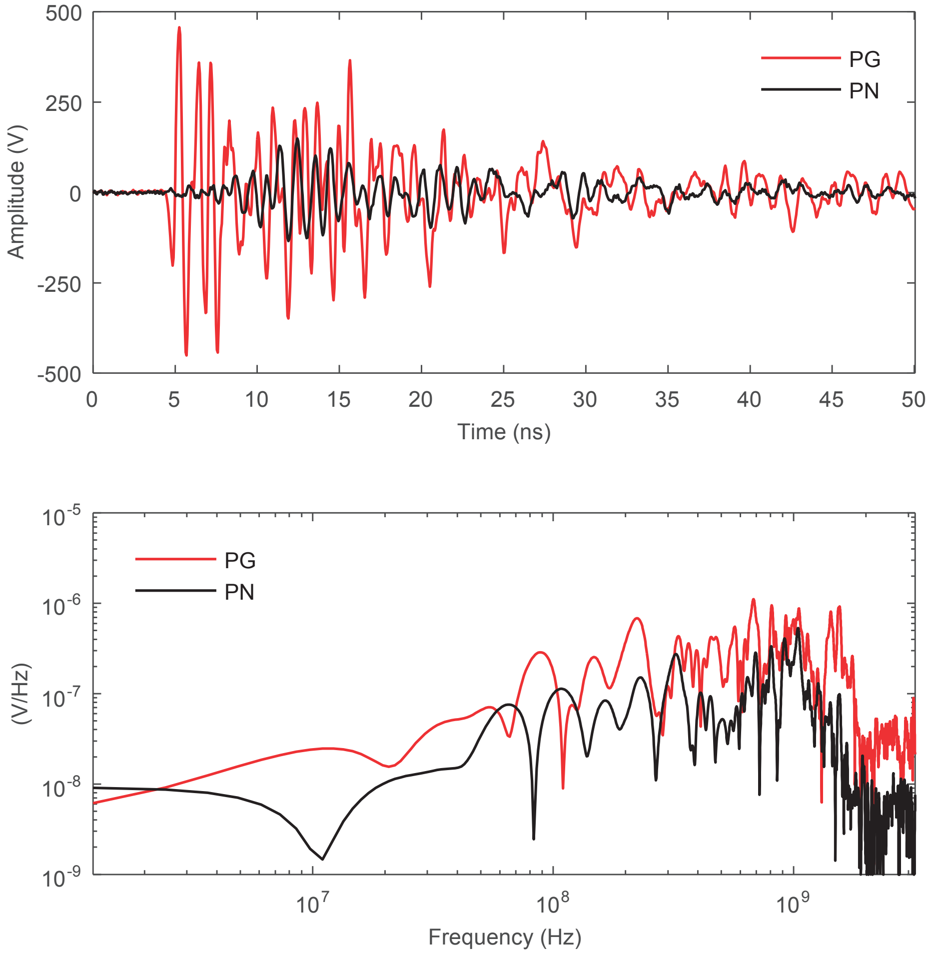

Fig. 4.11 Example of a DM voltage measurement of the AC3 cable with the raceway in a vertical position. The incident fields are shown in Fig. 4.5.

4.5.2.2 Peak amplitudes

A bar plot summarizing the peak amplitudes of the DM voltage measurements of all the cables is presented in Fig. 4.12. The three white and gray bars that are plotted in the AC categories correspond to the PN, PG, and NG voltage amplitudes respectively.

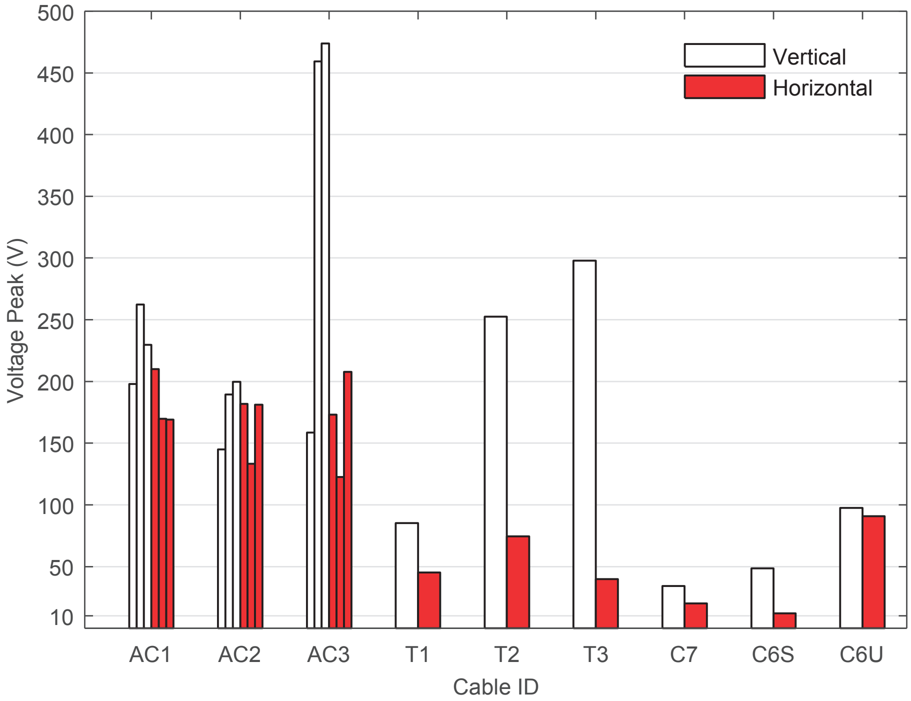

Fig. 4.12 Bar plot of the peak amplitude of the DM voltage measurements. The incident E-field is shown in Fig. 5.

It was found that almost all the induced voltages in the LVP cables remained in the range of 120-250V. Notice that there are two cases in AC3 with induced voltages of more than 450V that significantly differ from the others. Peak voltages between 40-300V were obtained for the TEL cables and between 10-100 V for the LAN cables. Similar levels were obtained for hyperband testing (at 44kV/m) of an unshielded CAT5 cable in [11].

The highest amplitudes were obtained with the raceway in the vertical position. The influence of the shielding scheme of the LAN cables can be also observed: reduced peak voltages are obtained for the shielded cables (C6S and C7).

4.6 DM voltage transfer functions

In order to address the overall shielding effectiveness of the assembly of cables, patch cords and measurement cards, the electric field to DM voltage transfer functions were calculated. Unless specified, all the transfer functions contain the overall coupling contribution from the raceway, the patch cords, and the measurement cards. The measurement cards play the role of typically found connector terminals through which EM energy can be also coupled. The obtained transfer functions give an idea of the required protection for limiting the induced voltage at the equipment terminals.

4.6.1 Transfer function definitions

4.6.1.1 Low frequency band (40MHz -200MHz)

The transfer functions between 40MHz and 200MHz were calculated by using the Fourier decomposition of the DM voltage and the illuminating field measured during the HPEM tests. The magnitude of the DM transfer functions $|H_{V_d}|$ were obtained from:

$$H_{V_d}|=\left|\frac{V_{DM}}{E^{inc}}\right|, \tag{4.4}$$

in which V_{DM} is the Fourier spectrum of the measured DM voltage between two wires of the tested cables (see Fig. 4.2) while the raceway was in the vertical position, and E^{inc} is the Fourier spectrum of the generated field inside the GTEM cell working volume. The reason for not using the horizontal measurements for the transfer function calculation is that the incident field along the raceway cannot be described with a single reference measurement (as done for the vertical case), due to the 1/r dependence of the amplitude in the longitudinal dimension of the GTEM cell. Notice that for the LVP cables, the DM voltage was measured between the phase and neutral wires. The lower frequency limit of the measurement was given by the number of samples in the time window and the sampling rate of the oscilloscope used.

4.6.1.2 High frequency band (200 MHz-6GHz)

The transfer functions between 200 MHz and 6 GHz were calculated by using the results obtained in the RC. The following definition of the transfer function was used:

$$H_{V_d}|=\sqrt{\frac{\left\langle |V_{DM}|^2\right\rangle}{\left\langle |E^{inc}|^2\right\rangle}}, \tag{4.5}$$

where $\left\langle |\mathrm{V}_{\mathrm{DM}}|^2\right\rangle$ and $\left\langle |\mathrm{E}^{\mathrm{inc}}|^2\right\rangle$ have been already defined in (4.1) and (4.3).

4.6.2 Transfer function results

Given that the nature of the transfer functions definitions is different, a priori, a consistent average transfer function value among both methods is not expected. However, according to the results of [150] the average transfer function of a plane wave illumination test should be, within a few decibels, equal to the transfer function in a reverberation chamber. As it is shown later, there is a broad consistency in the average coupling level between the low and high frequency band transfer functions. However, regarding the transition at 200 MHz, differences between 6 to 20dBs have been found.

The obtained transfer functions feature a strong variation as a function of frequency and they do not follow a common pattern. However, depending on the cable nature (untwisted, twisted, or shielded), it has been found that the transfer functions have similar behaviors as will be presented in what follows.

The magnitudes of the transfer functions of two LVP cables (AC1 and AC3), two TEL cables (T1 and T3), and two LAN cables (C7 and C6U), are plotted in Fig. 4.13, Fig. 4.14, and Fig. 4.15, respectively.

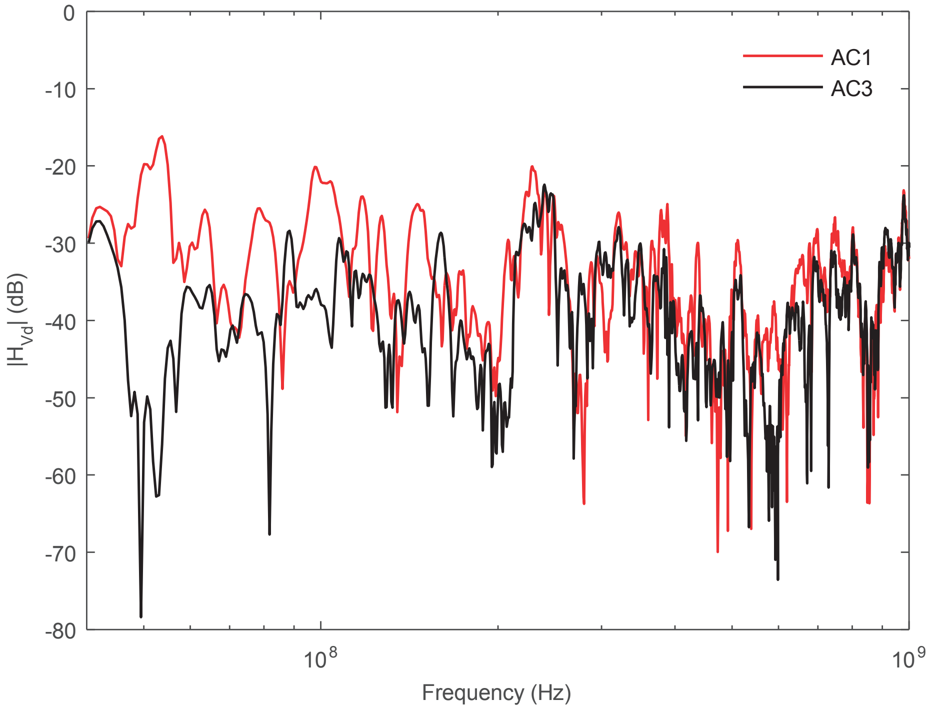

Fig. 4.13 Magnitude of the DM voltage transfer function of the AC1 and AC3 LVP cables.

The LVP cables exhibit the strongest response with the magnitude of the transfer functions reaching about -20 dB at the resonant frequencies (Fig. 4.13). Twisted cables with no overshield, like the TEL cables or the C6U cable, have an improved behavior with respect to the untwisted, with a magnitude of about -30 dB at the resonant frequencies (Fig. 4.14 and Fig. 4.15). The lowest response is obtained with the C7 cable (twisted and shielded) with nearly -40 dB at the resonant frequencies.

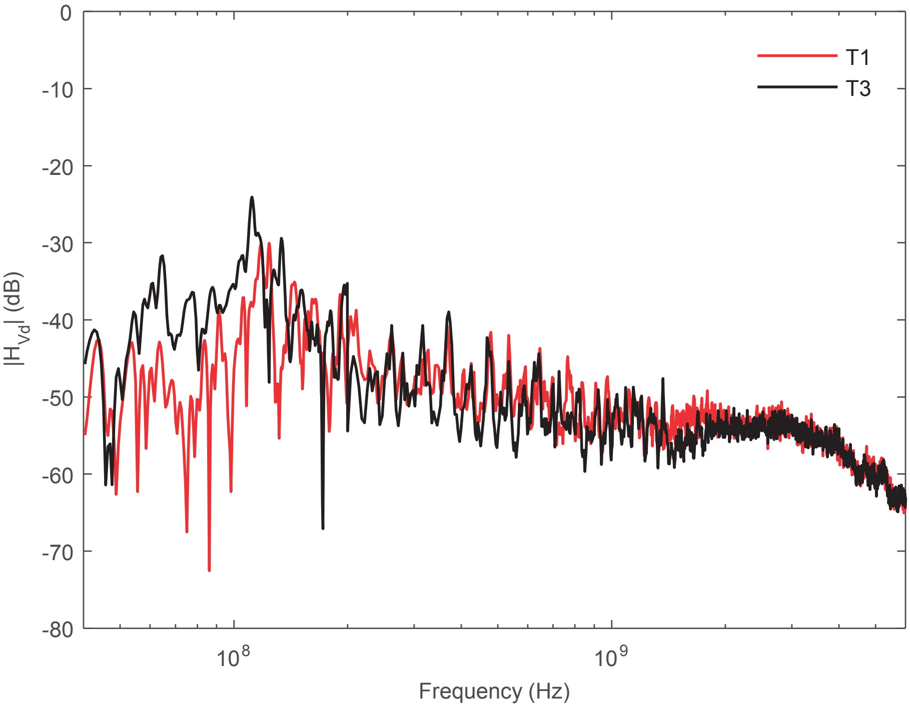

Fig. 4.14 Magnitude of the DM voltage transfer function of the T1 and T3 TEL cables.

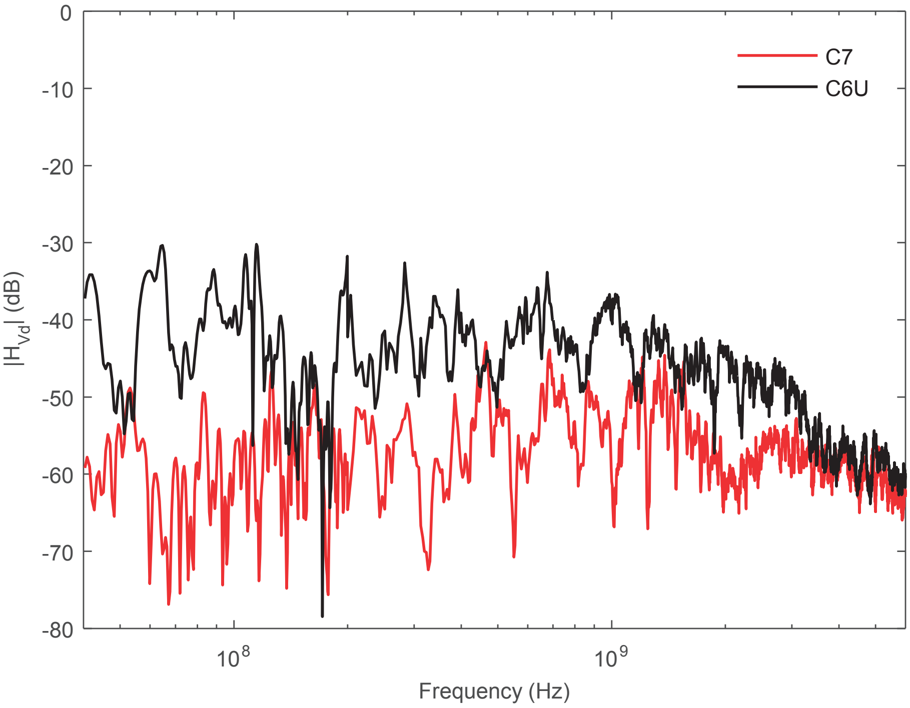

Fig. 4.15 Magnitude of the DM voltage transfer function of the C7 and C6U LAN cables.

A summary of the maximum, minimum and mean transfer functions for all the tested cables considering the whole frequency range is presented in Fig. 4.16. In this plot, the improved response of the twisted and shielded cables can be easily appreciated.

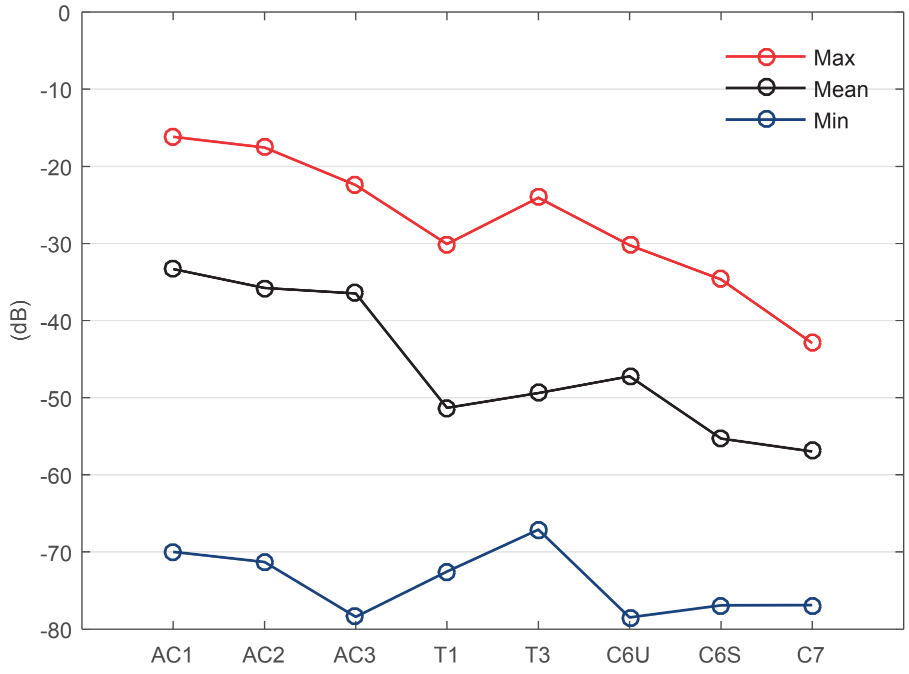

Fig. 4.16 Maximum, minimum, and mean amplitudes of the DM voltage transfer functions measured in all the cable types of the raceway

Theoretical models leading to the correct prediction of the DM mode coupling require very detailed information about the geometry and imperfections in the line terminations (see e.g. [148, 155]). Given the many uncontrolled parameters of our assembly, we have chosen to compare our results with comparable experiments reported in the literature.

Similar measurements were performed with home-made unshielded TWP of arbitrary wire separation distance by using a CW illumination in an AC in [151, 152, 155] and a RC in [154]. Contrary to our case, in these experiments a very careful termination of the wires has been made; e.g. the experiments in [154] and [155] used baluns for terminating the wires, thus reducing the CM to DM conversion.

We have tried to obtain the equivalent DM voltage transfer functions from the information provided in the cited papers. The AC results in [151, 152] and [155] exhibit levels of about -90 to -50 dB, and -80 to -40 dB, respectively. In these two examples, the TWP separation distances were around 1-2 mm and they were illuminated from particular angles of incidence. Therefore, the statistical significance of the measurements was low.

On the other hand, the RC results in [154] show transfer functions between -60 and -20 dB. In this case, the TWP separation distances were 16mm and 33.7mm, and this explains the higher coupling levels with respect to the AC examples. Also, the multiple angles of incidence imply an increased probability of exciting the TWP with illumination conditions that will be difficult to obtain with an AC test.

4.7 Governing factors in the transfer functions

In this section we present some additional measurement results that are useful for explaining the governing factors in the transfer functions. The results presented in Fig. 4.16 show that the type of cable has, in general, an appreciable effect on the obtained transfer functions; the unshielded-untwisted cables being the most susceptible, and the shielded-twisted cables the least susceptible wires (as expected). However, the difference between the transfer functions of the TEL and LAN cables becomes less significant at higher frequencies. Given that the observed transfer functions contain the joint effect of the measurement cards, the patch cords used to access the raceway, and the raceway cables, it is expected that at higher frequencies the majority of the energy penetrates through imperfections in the cable terminations or couples directly to the measurement cards. Thus, similar responses are obtained at higher frequencies.

We have performed further measurements in the RC in order to identify the governing effects in the total system response. We measured the transfer functions of the measurement cards by themselves, and with just patch cords between them (without the raceway). An example of the obtained results is presented in Fig. 4.17 which compares the magnitude of the transfer function of one measurement card alone (MC), two measurement cards with just a C7 shielded patch cord in between them (C7-PC), and the full measurement system connected to the C7 cable of the raceway (C7+C7-PC).

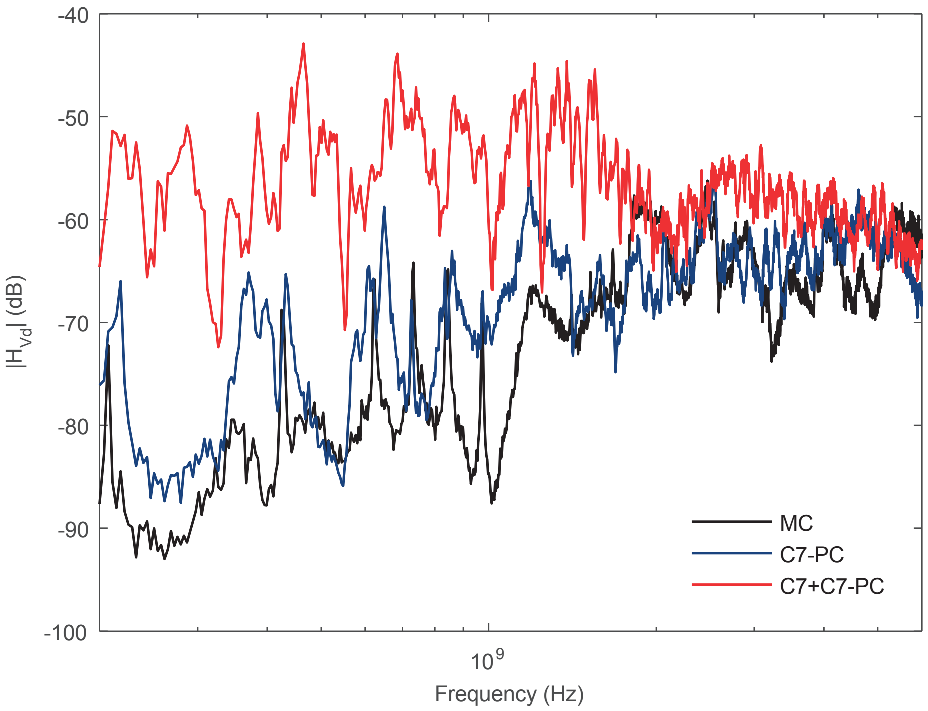

Fig. 4.17 Magnitude of the DM voltage transfer function measured in the C7 cable, the C7 patch cord, and the measurement card alone.

According to Fig. 4.17, below a frequency of about 1 GHz, the cable coupling is dominant. Beyond a frequency of about 2 GHz, direct coupling to the measurement cards become predominant. A similar behavior was observed for the other cables.

In order to separate the effect of the measurement cards and that of the connected cables, the maximum, minimum, and mean transfer functions were calculated in two separate frequency bands; namely, 0.2 to 2 GHz, and 2-6 GHz. A summary of the results is presented in Fig. 4.18, in which the transfer functions of a measurement card alone (MC) and, two measurement cards connected through patch cords (CX-PC) have been added. Notice that the statistical moments of the second band feature less variation as a function of the considered configuration compared to the first band, meaning that the coupling is independent of the cable type and is essentially governed by the measurement cards (± 5 dBs).

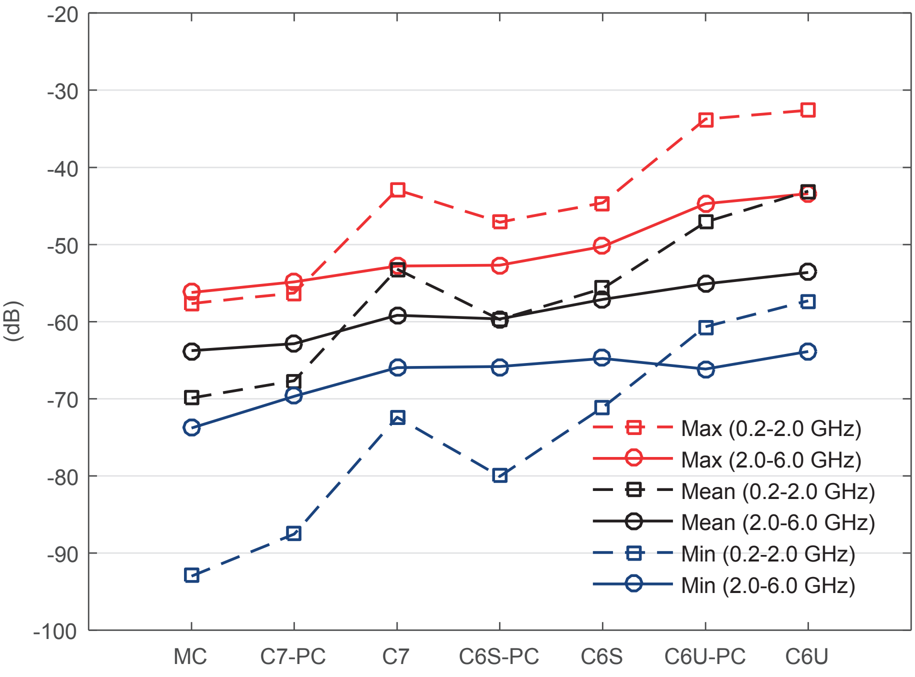

Fig. 4.18 Maximum, minimum, and mean amplitudes of the DM voltage transfer functions according to the analyzed frequency band

4.7.1 Effect of shield discontinuities

In order to assess the effect of inserting discontinuities in the shields, two tests were performed. In the first test, the transfer function of the measurement card alone without the copper seal in the RJ-45 jack was determined. A plot comparing the obtained results with the results of the former card with a continuous shield is presented in Fig. 4.19. The results with the unshielded connector card are plotted in red (MC-NS), and those with the shielded connector card are shown in black (MC). The transfer functions feature resonances which are presumably related to the PCB size and trace lengths. The observed resonance frequencies are specific to the particular MCs but it is expected that similar effects would occur in real equipment. A difference of about 15 dB is observed between the two curves.

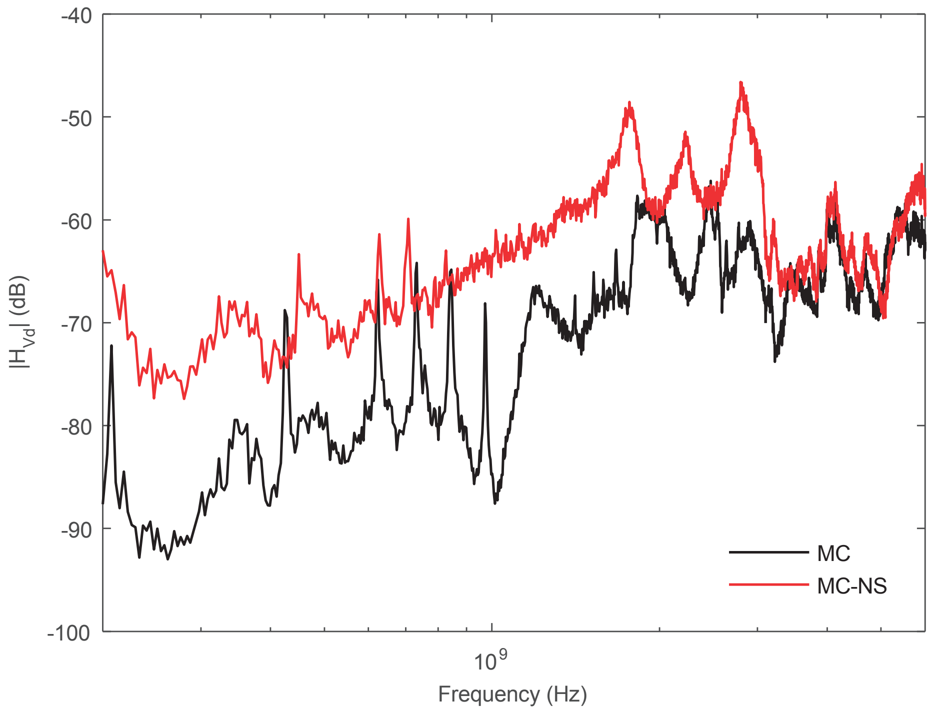

Fig. 4.19 Magnitude of the DM voltage transfer function measured in the measurement card alone with and without over shielding of the RJ-45 jack.

The second test consisted of testing the shielded cables of the raceway while connecting the measurement cards with and without shielded patch cords. The insertion of an unshielded patch cord introduced a discontinuity that degraded the performance of the entire system.

A plot comparing the response of the C7 cable of the raceway connected through shielded patch cords (C7+C7-PC), through unshielded patch cords (C7+C6U-PC), and the response of the C6U cable of the raceway connected through C6 unshielded patch cords (C6U+C6U-PC) is presented in Fig. 4.20. Notice that the presence of an unshielded patch cord degrades the response of the C7 cable so that it becomes similar to the response of an unshielded cable.

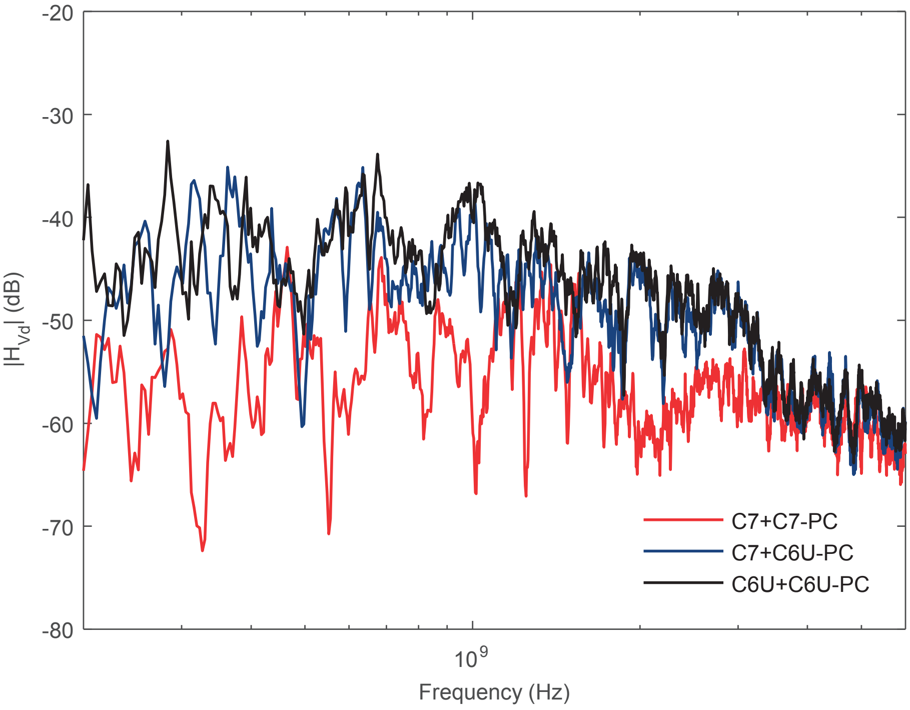

Fig. 4.20 Magnitude of the DM voltage transfer function measured in the C7 cable, the C7 cable with an unshielded patch cord, and the C6U cable.

4.8 Conclusions

In this chapter, a typical electrical and communications raceway including several types of cables found in commercial buildings was built and tested against HPEM transients inside a GTEM cell and low power fields inside a RC. In the first test, the raceway was illuminated with a fast transient bipolar E-field pulse of ± 20kV/m and 100 ps risetime, and the amplitude and frequency characteristics of the induced CM currents and DM voltages between the cable terminations were assessed.

The HPEM tests revealed that the LVP cables are the most susceptible under a hyperband illumination, compared to TEL and LAN cables.

Tab. 4.5 shows the range of the measured peak values in both tests (raceway in vertical and horizontal positions) and for each type of cabling.

In general, the amplitude of the induced CM current signals is related to the illuminated portion of the cables. On the other hand, the DM voltages are related to the illuminated portion, the presence or not of a shield, the load balance, and proper terminations of the cables. As expected, the best performance was obtained with the use of shielded twisted pairs.

Tab. 4.5 Measured range for the induced CM current and DM voltage peaks. The incident E-field is a hyperband source with a peaka-to-peak value of 20 kV/m and a risetime of 100 ps.

Cable	Current range (A)	Voltage range (V)
LVP	2.1-8.5	122-474
TEL	1.7-9.8	40-298
LAN C6U (no shield)	2.2-5.6	91-107
LAN C6S (shielded)	4.4-6.8	10-49
LAN C7 (shielded)	4-6.8	13-34

In the second test, the response of the raceway to low power swept CW stimulation was measured in a RC to determine statistical transfer functions from random incident field configurations into DM voltage in cable loads. The obtained electric field to DM voltage transfer functions were summarized in Fig. 4.18. The responses were found to be governed by the raceway under test in the lower frequencies (below 1 GHz). Between 0.2-1 GHz, the raceway gives about 10 dB higher coupling than a short patch cable. The difference is even greater at lower frequencies and for shielded cables. In the frequency band 1-3 GHz, little differences were observed between a short patch cable and full raceway, but both are still significantly higher than direct coupling to the measurement card. Beyond 3 GHz, the coupling is clearly dominated by the measurement cards.

The experiments performed in this work provide a better understanding of the expected induced voltages and currents in commercial cable systems when exposed to IEMI-like signals. For the first time in the literature, three types of cabling (plus 3 subtypes of Ethernet) were investigated using an identical experimental technique in a very broad frequency range, namely from 40 MHz to 6 GHz. The considered cabling configuration was in a representative installed environment (raceway) rather than just individual cables. The GTEM and RC test results in the cross-over region were found to be broadly consistent. The transfer functions derived in this work are therefore directly useful in IEMI risk analyses for many types of CIs, bearing in mind, of course, that they are derived from particular experiments.

5 Application of Transmission Line Theory in Evaluating Differential-Mode Signals in IEMI scenarios

5.1 Introduction

It has been previously mentioned in Chapter 4 that very accurate modeling of a CI is not always possible due to the complexity of the problem. However, it is important to highlight that educated decisions can still be taken with the use of approximate EM models where experiments are not allowed or difficult.

The estimation of the *receptivity* level of critical equipment due to an IEMI attack requires an accurate evaluation of voltages and currents at their terminals [24, 167]. IEMI stresses on a system can be applied either through conductive coupling or radiated electromagnetic coupling. In both cases, interferences will reach the sensitive devices through connected cables. Therefore, the evaluation of wave propagation/electromagnetic coupling along cables is customarily made using the TL theory [88] which applies to uniform transmission lines with electrically small cross-sectional dimensions, where the dominant mode of propagation is TEM.

The applicability of the TL theory to disturbance sources with higher frequency content (HPM, UWB, etc.) is a topic that has received increased attention during the past decade or so [57]. The accuracy of the TL theory in the evaluation of common-mode induced signals has already been addressed in the literature (e.g., [168, 169]).

The first part of this chapter is heavily based on [42]. It studies the DM coupling due to a plane wave illumination of a transmission line composed of two wires above a ground plane - a topic that has not been specifically addressed in the literature, to the best of the author’s knowledge. The differential-mode propagation existing between the two wires is evaluated by assuming that the wires are floating (i.e. no galvanic connection to ground) at a height above the ground plane which is not necessarily electrically small. The results obtained using the classical TL theory are compared with full-wave solutions obtained using the Numerical electromagnetics Code NEC-4 [170]. Provided that the above-ground height of the wires is not electrically small, the applicability of the TL theory becomes questionable (see e.g. Section 1.5 of [88]). However, the question arises whether the TL solutions for the DM coupling are still valid if the distance separating the two wires is electrically small.

The interest of studying the DM coupling with such a configuration is twofold: (i) the susceptibility thresholds of electronic equipment are typically achieved with differential mode signals (e.g. differential signal pairs inside a PVC conduit inside a building, or twisted pairs inside a cable raceway), and (ii) the influence of the wires' height above the ground plane in the accuracy of the TL solutions can be better understood.

The second part of the chapter is based on [80]. We study how the propagation of IEMI signals along power and communication lines will be affected by conductive and dielectric losses. The distorted transmission will result in the attenuation of the amplitudes and in the increase of the risetimes of the IEMI signals.

This chapter is organized as follows. In Section 5.2, a theoretical analysis is presented on the characteristic impedance of a two-wire transmission line above a ground plane, and the same two-wire line in free space. In Section 5.3, we present simulation results for the previously considered line configurations illuminated by a plane wave. Section 5.4 presents the simplified TL model for the parametric attenuation and dispersion studies and their results. Finally, the conclusions are presented in Section 5.5.

5.2 Comparison of the DM propagation along a two-wire line in free space and above a ground plane

Consider the cross sections of a two-wire lossless semi-infinite line in free space and a two-wire lossless semi-infinite line above a ground plane as shown, respectively, in the left and right panels in Fig. 5.1.

Assuming that a source is located at one end of the line (as shown in Fig. 5.1), and that one of the two wires is the reference conductor, the solutions for the current and voltage for the line in the free space case can be expressed as:

$$\begin{aligned} I(\mathrm{z}) &= \mathrm{I}_0\, e^{-jkz}, \\ \mathrm{V}(z) &= Z_c I(\mathrm{z}), \end{aligned} \tag{5.1}$$

where the current I_0 is calculated according to the boundary conditions and Z_c is the characteristic impedance of the transmission line which, for the case where $D >> r_i$ is given by [46]:

$$Z_c = \frac{\eta_0}{2\pi}\ln(\frac{D^2}{r_1 r_2}), \tag{5.2}$$

in which η_0 is the free space wave impedance.

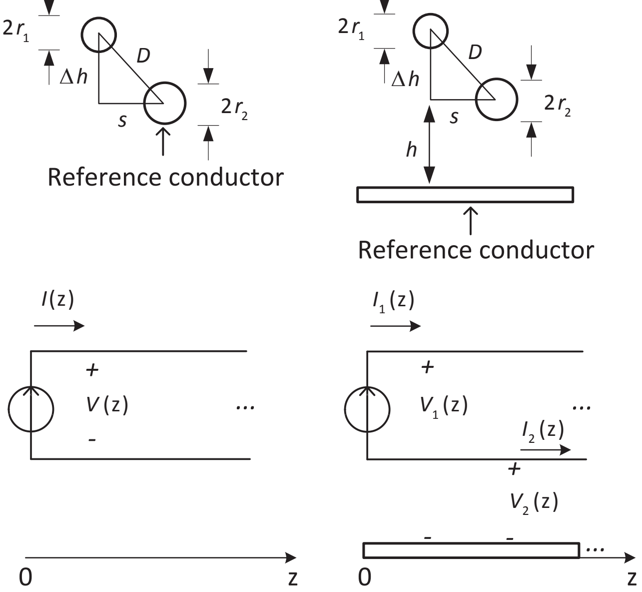

Fig. 5.1 Left: Cross section and schematic of a two-wire line in free space. Right: Cross section and schematic of a two-wire line above a ground plane.

On the other hand, if the ground plane is chosen as the reference conductor, the voltages and currents for the wires above a ground plane can be expressed as:

$$\begin{aligned}\bar{I}(\mathrm{z}) &= \begin{bmatrix} I_1(\mathrm{z}) \\ I_2(\mathrm{z}) \end{bmatrix} = \begin{bmatrix} I_{0,1}e^{-jkz} \\ I_{0,2}e^{-jkz} \end{bmatrix} = \bar{I}_0 e^{-jkz}, \\ \bar{V}(\mathrm{z}) &= \begin{bmatrix} V_1(\mathrm{z}) \\ V_2(\mathrm{z}) \end{bmatrix} = \begin{bmatrix} Z_{c1,1} & Z_{c1,2} \\ Z_{c2,1} & Z_{c2,2} \end{bmatrix} \begin{bmatrix} I_1(\mathrm{z}) \\ I_2(\mathrm{z}) \end{bmatrix} = \bar{\bar{Z}}_c \bar{I}(\mathrm{z}),\end{aligned} \tag{5.3}$$

where $\bar{I}_0$ is calculated according to the boundary conditions and $\bar{\bar{Z}}_c$ is the characteristic impedance matrix of the multi-conductor transmission line given by [46]:

$$\bar{\bar{Z}}_c = \frac{\eta_0}{2\pi}\begin{bmatrix} \ln(\frac{2h+\Delta h}{r_1}) & \ln(\frac{\sqrt{(2\mathrm{h}+\Delta \mathrm{h})^2+s^2}}{D}) \\ \ln(\frac{\sqrt{(2\mathrm{h}+\Delta \mathrm{h})^2+s^2}}{D}) & \ln(\frac{2h}{r_2}) \end{bmatrix}. \tag{5.4}$$

5.2.1 DM propagation of a two-wire line above a ground plane

The DM propagation between the two conductors assumes a current $I_1 = -I_2 = I_d$ that will produce a DM voltage V_d between the lines calculated as:

$$V_d = V_1 - V_2 = (Z_{c1,1} + Z_{c2,2} - 2Z_{c2,1})\mathrm{I}_d = Z_{c-d} I_d, \tag{5.5}$$

where the fact that $Z_{c1,2} = Z_{c2,1}$ has been used.

The DM propagation will be thus governed by the DM characteristic impedance Z_{c-d} that can be obtained from (5.4) as:

$$Z_{c-d} = Z_c + \frac{\eta_0}{2\pi} \ln\left(\frac{4h(\mathrm{h} + \Delta h)}{(2\mathrm{h} + \Delta h)^2 + s^2} \right). \tag{5.6}$$

Notice that the DM characteristic impedance will tend to the characteristic impedance of the wires in free space as the argument in the natural logarithm in (5.6) approaches unity. If a fixed distance between the wires is considered, neither Δh nor s can be modified without modifying the global geometry of the lines in free space and, therefore, the only parameter governing the above-mentioned approximation becomes the height h of the wires above the ground plane. From (5.6), it becomes obvious that for lines satisfying the condition $h >> D$ which, in turn, implies that $h >> \Delta h, s$, the characteristic impedance can be evaluated disregarding the presence of the ground plane, namely $Z_{c-d} \approx Z_c$.

5.2.2 Application example

Consider the propagation along a two-wire line characterized by the geometrical parameters in Tab. 5.1 (see Fig. 5.2):

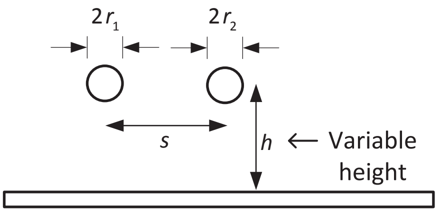

Fig. 5.2 Application example two-wire line above a ground plane cross section.

Tab. 5.1 Parameters of the application example

Parameter	variable	Value
Wires radii	r_1,r_2	1 mm
Wires horizontal separation	$s = 5r$	5 mm
Wires vertical separation	Δh	0

Fig. 5.3 presents the plot of the absolute percentage error of the approximation $Z_{c-d} \approx Z_c$ as a function of the normalized height *h/s*.

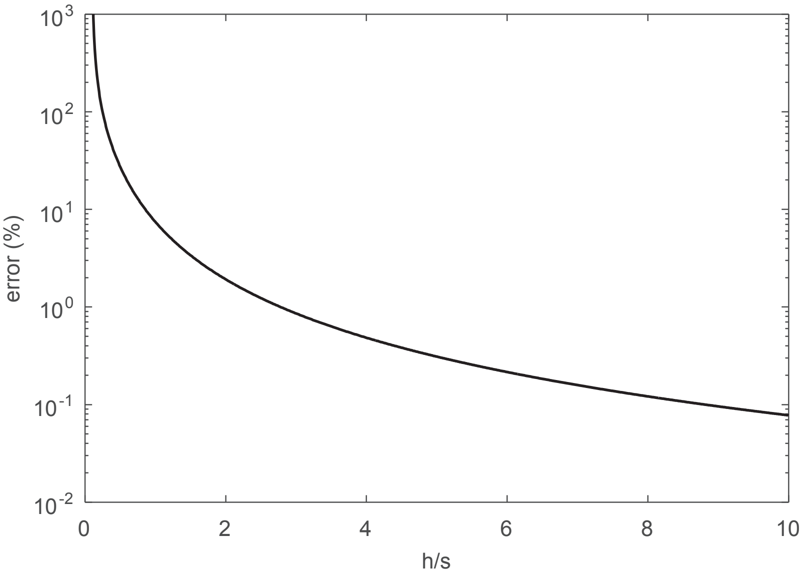

Fig. 5.3 Estimation error in the calculation of the differential-mode characteristic impedance for the case $r_1 = r_2 = r = 1$ mm, $s = 5r$, and $\Delta h = 0$.

For this particular configuration, it can be seen that the error is less than 2% when the height above ground of the wires exceeds twice their separation distance.

5.3 Plane wave illumination of a two-wire line above a ground plane

The results of the previous section imply that the differential-mode propagation becomes independent of the presence of the ground plane for lossless lines with wire heights exceeding about twice their separation distance. In this section, the accuracy of the TL theory in the prediction of the induced currents in the case of a plane wave illumination of the line when the conductors' heights are not electrically small $(h \geq \lambda)$ is assessed. We have used as reference full-wave solutions obtained using the Numerical Electromagnetics Code (NEC-4) [170].

5.3.1 Problem under study

The geometry of the problem is illustrated in Fig. 5.4. Two PEC wires of circular cross-section with a diameter *2a* and length *L* are located at heights *h* and *h+d* above a perfectly conducting ground plane. The two wires are terminated with impedances Z_1 and Z_2 that are equal to the characteristic impedance of the two-wire transmission line in free space.

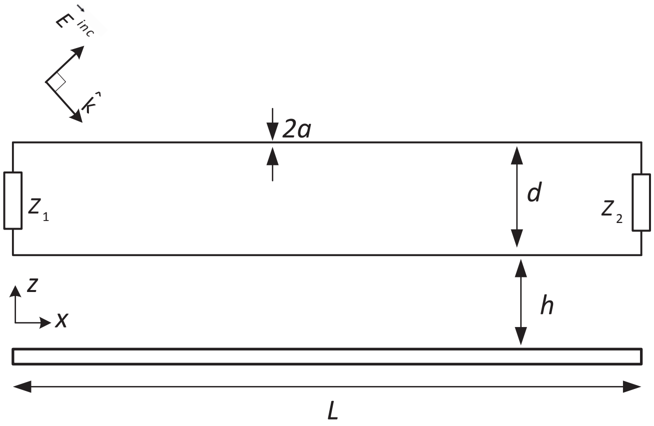

Fig. 5.4 Schematic representation of a two-wire line above a ground plane illuminated by an incident plane wave.

The wires are illuminated by a plane wave described with the polarization angles illustrated in Fig. 5.5.

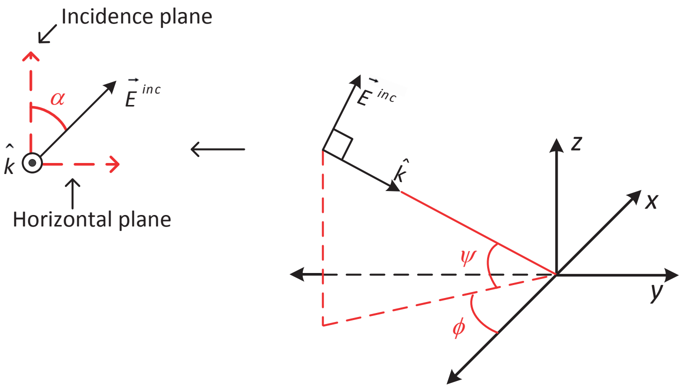

Fig. 5.5 Plane wave polarization angles adopted from chapter 7 in [46].

The induced current I_1 flowing through the impedance Z_1 is calculated using: (i) NEC-4, (ii) classical TL theory, and (iii) a simplified TL model that will be explained as follows. Given that the wires are floating above the ground plane, the current I_1 is alternatively calculated by considering that the two-wire line is located in free space (i.e. without the ground plane) and illuminated by the superposition of the impinging plane wave and its image (see Fig. 5.6).

Note that in this case, the ground plane is considered when calculating the exciting electromagnetic fields, which is the sum of the incident field and the ground-reflected field, both in absence of the two wires. On the other hand, the presence of the ground plane is disregarded when evaluating the induced signals and their propagation along the two-wire line.

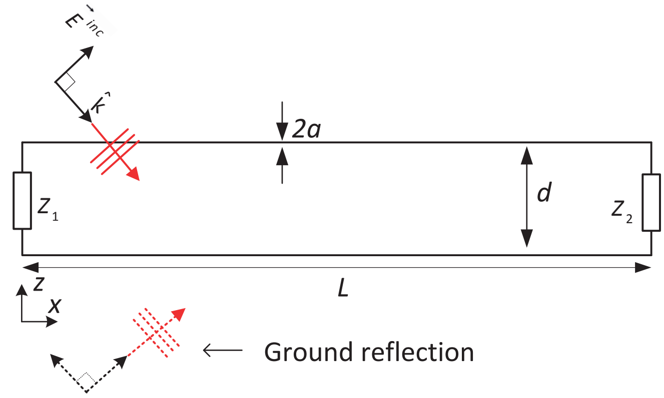

Fig. 5.6 Schematic representation of a two-wire line in free space illuminated by an incident plane wave, including the ground-reflected fields.

5.3.2 Considered line parameters

Two line configurations were tested with the above-mentioned setups. In what follows, the wavelength used for calculating the line dimensions of the configurations was evaluated in free space at a frequency of 1GHz ($\lambda = 30$ cm).

The first configuration comprises a line with $h=10\lambda$ and $d=\lambda/10$. This case is useful to assess the accuracy of the TL theory in the prediction of the DM current when the lines are far from the ground, but the distance between the lines is electrically small.

The second configuration comprises a line with $h=10\lambda$ and $d=\lambda$. This example is used to illustrate the errors obtained with the TL theory when the distance between the two conductors is no longer electrically small.

A summary of the parameters used for both configurations is presented in Tab. 5.2:

Tab. 5.2 Summary of the considered line parameters

Parameter	Variable	Value	Units
Length	L	100	cm
Radius	a	0.7	mm
Height	h	300	cm
Distance	d	3 and 30	cm
Impedance	Z_1, Z_2	450 and 727	Ω
Elevation angle	ψ	60	deg
Azimuth angle	φ	0	deg
Polarization angle	α	0	deg

5.3.3 Frequency domain results

A comparison of the magnitude of the transfer functions I_1/E^{inc} for the first configuration, obtained with NEC-4 (black), TL theory in presence of ground plane (red), and TL theory disregarding the ground plane (blue) are shown in Fig. 5.7.

It can be seen that the three curves are in excellent agreement, even at frequencies exceeding 1GHz, suggesting that for the calculation of the DM coupling, the governing factor is the electrical distance between the conductors under consideration and not the overall cross section of the line. As long as the DM of the floating wires is concerned, this latter example illustrates the possibility of using the TL theory when the electrical distance between conductors remains short, regardless of their heights above the ground plane.

A comparison of the results obtained for the second case (d= 30 cm) is presented in Fig. 5.8. The results obtained using the TL theory are in very good agreement with the full-wave simulations, for frequencies up to about 350 MHz, which corresponds to a distance $d \approx 1/3\lambda$. Beyond that frequency, as expected, the results obtained using the TL theory start to deviate with respect to full-wave simulations because the separation distance of the two-wire line is no longer electrically small. On the other hand, the TL results for the two line configurations (two-wire line in free space and two-wire line above a ground plane) are in excellent agreement in the whole frequency range. This confirms again that the differential-mode induced signal in floating wires is not significantly affected by the presence of the ground plane.

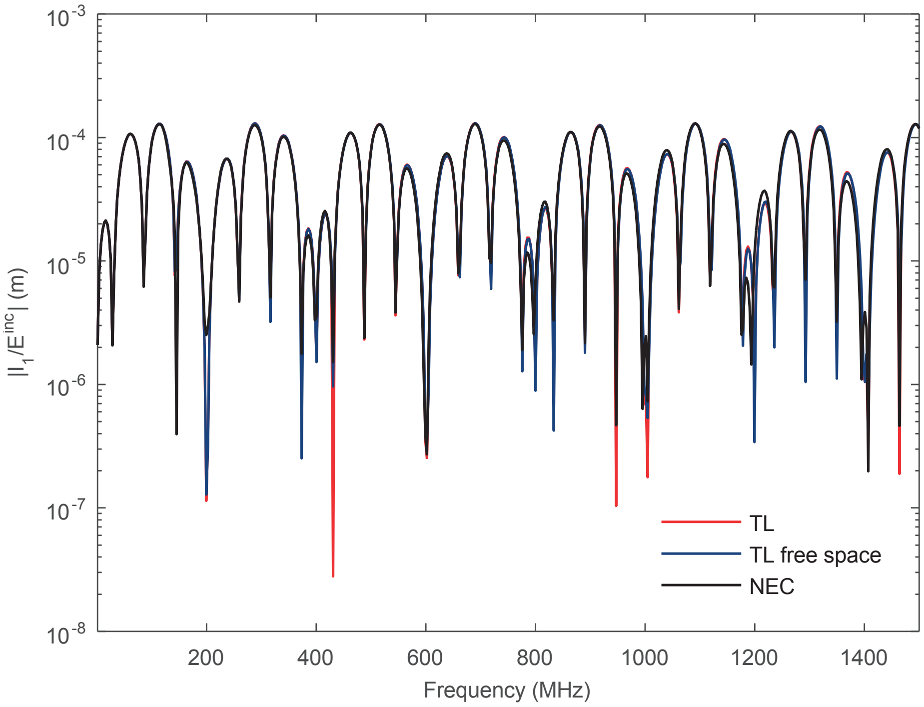

Fig. 5.7 DM current transfer function of a two-wire line above a ground plane for the case *h* = 300 cm, and *d* = 3cm.

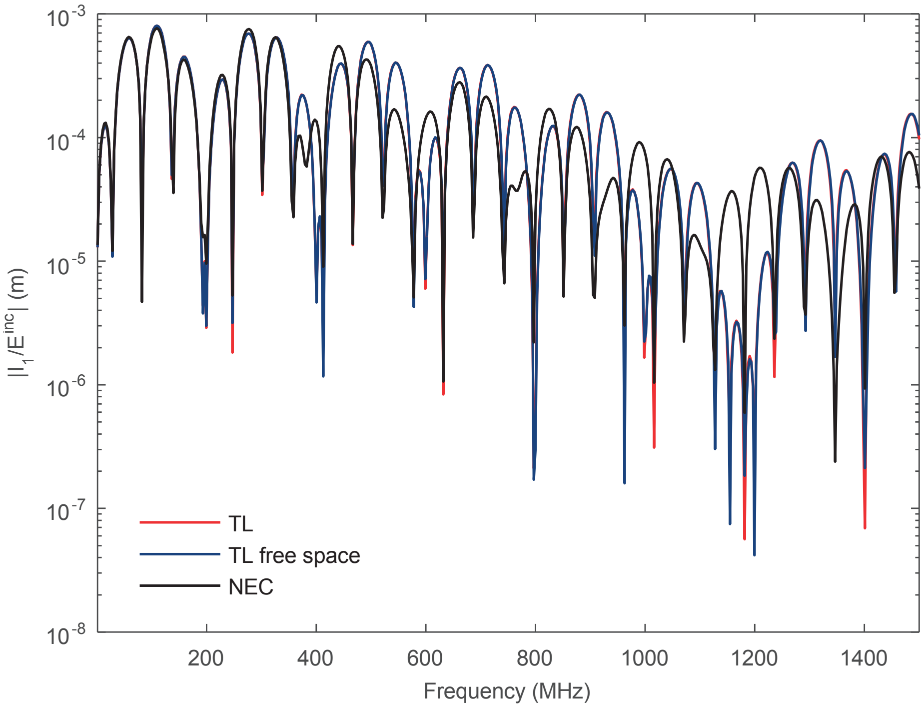

Fig. 5.8 DM current transfer function of a two-wire line above a ground plane for the case *h* = 300 cm and *d* = 30cm.

5.3.4 Time domain results

The accuracy of the time domain reconstruction of the induced current has been also tested by illuminating the lines with a set of three IEMI waveforms [100] exhibiting different bandratio. For calculating the time domain response, the transfer functions in Fig. 5.7 and Fig. 5.8 were multiplied by the incident field spectra and a classical IFFT was used to recover the current waveforms. A description of the used IEMI waveforms is presented in Tab. 5.3.

Tab. 5.3 Parameters of the IEMI waveforms used to test the time domain reconstruction accuracy

Description	Classification	Bandratio	Reference
Far field of the IRA II system	Hyperband	1.9E9	[20]
Field generated by the EPFL SWO	Mesoband	2.43	[119]
Numerically generated CW chirp	Hypoband	<1	N/A

5.3.4.1 Hyperband signal illumination

A plot of the far electric field of the IRA II system [20] is presented in Fig. 5.9. It corresponds to a fast impulse of about 60kV/m, a rise time of about 70 ps, and a FWHM of about 110 ps. The frequency spectrum of the field extends up to a significant frequency of about 5 GHz, corresponding to a minimum wavelength of 6 cm. The simulated current waveforms obtained with NEC-4 (black), TL theory in presence of ground plane (red), and TL theory disregarding the ground plane (blue) are plotted for the first configuration (*d=3* cm) in Fig. 5.10 and for the second configuration (*d=30* cm) in Fig. 5.11.

There is an excellent agreement of the waveforms obtained for the first configuration, which implies, as already mentioned, that the governing factor is the electrical distance between the conductors under consideration and not the overall cross section of the line. On the other hand, for the second configuration where the distance between the two wires is no longer electrically-small at high frequencies, a very small disagreement can be observed. Since the illuminating signal has a wide bandratio, the inverse FFT includes an important part of the low frequency spectrum in which the transfer function is correctly calculated, thus the average reconstruction exhibits amplitudes and delays that are similar to the full wave solution.

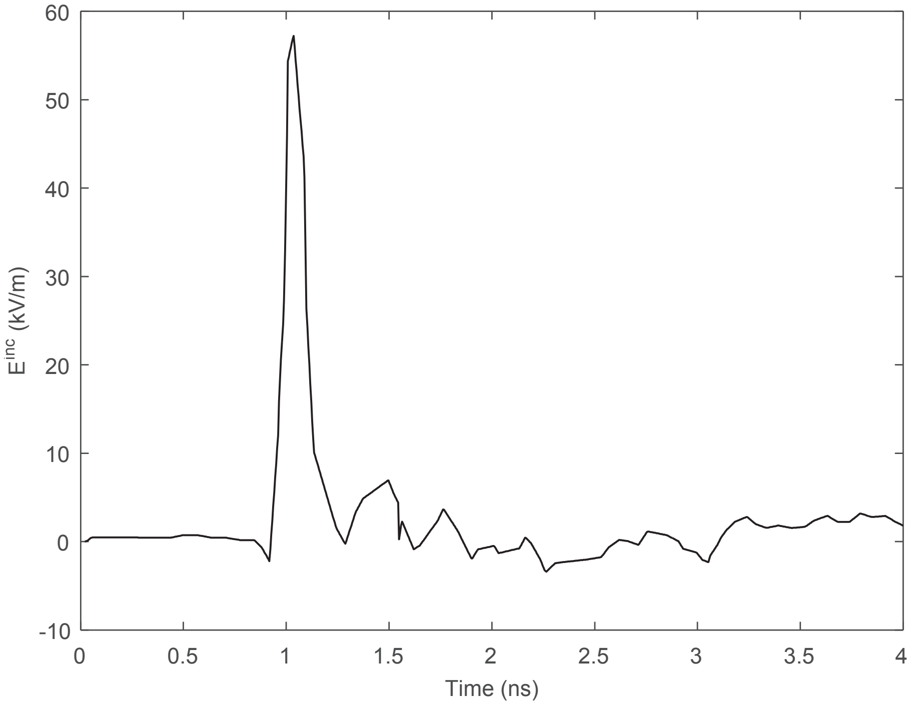

Fig. 5.9 Hyperband incident electric field: far electric field of the IRA II system [20].

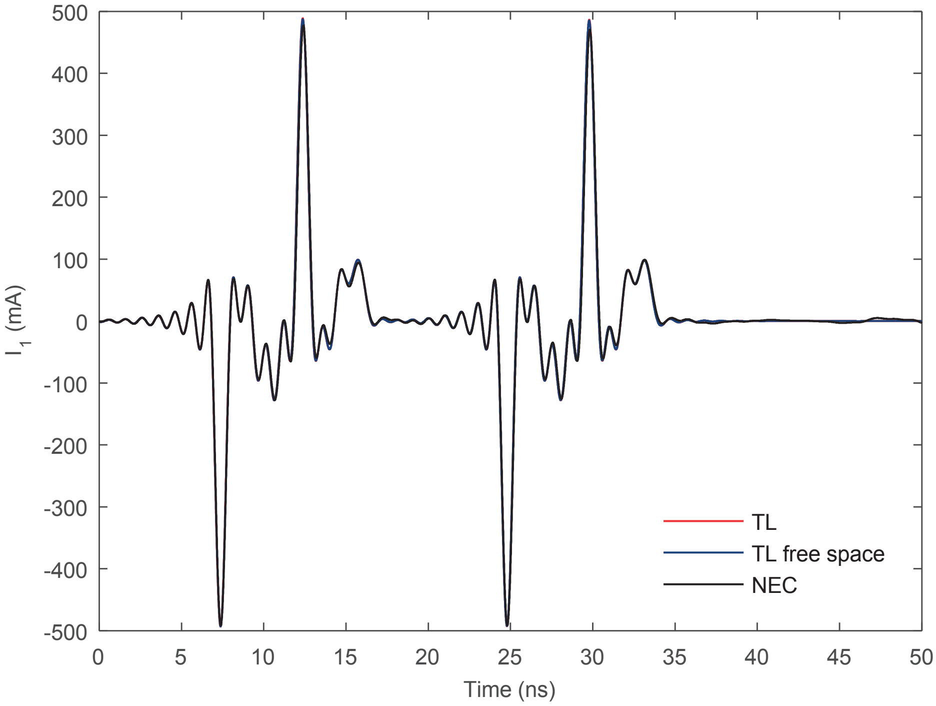

Fig. 5.10 DM current due to the hyperband illumination for the case *h* = 300 cm and *d* = 3cm.

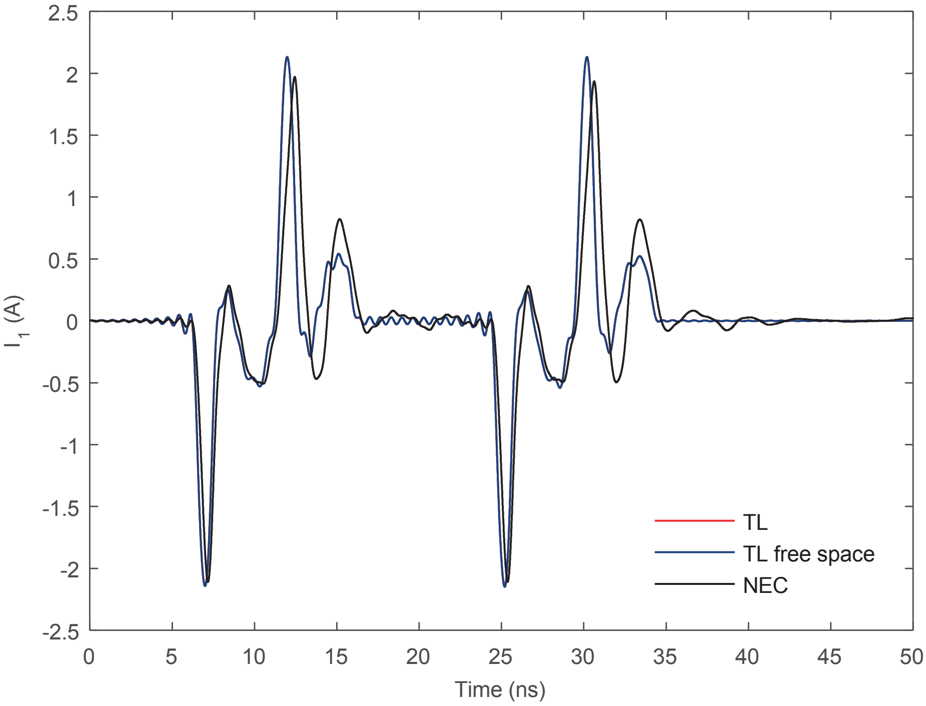

Fig. 5.11 DM current due to the hyperband illumination for the case *h* = 300 cm and *d* = 30cm.

5.3.4.2 Illumination of the line with a mesoband signal

A plot of the electric field generated by the EPFL SWO [119] is presented in Fig. 5.12. The amplitude of the signal is 6.6 kV/m, the center frequency is about 310 MHz and the quality factor is about 20. The recovered current waveforms obtained with NEC-4 (black), TL theory in presence of ground plane (red), and TL theory disregarding the ground plane (blue) are plotted for the first configuration (*d=3* cm) in Fig. 5.13 and for the second configuration (*d=30* cm) in Fig. 5.14.

Similar conclusions to those obtained for the hyperband illumination can be derived for the mesoband signal. There is an excellent agreement in the solutions obtained for the first configuration. For the second, the TL simulations are still in very good agreement with the full-wave solutions. This good agreement is consistent with the frequency domain comparison presented in Fig. 5.8, in which there is good agreement between TL and NEC results at frequencies of about 310 MHz. If the center frequency of the mesoband source is outside the validity region of the predictions for the second configuration, an over/under estimation of the amplitudes could be observed as it will be explained in what follows.

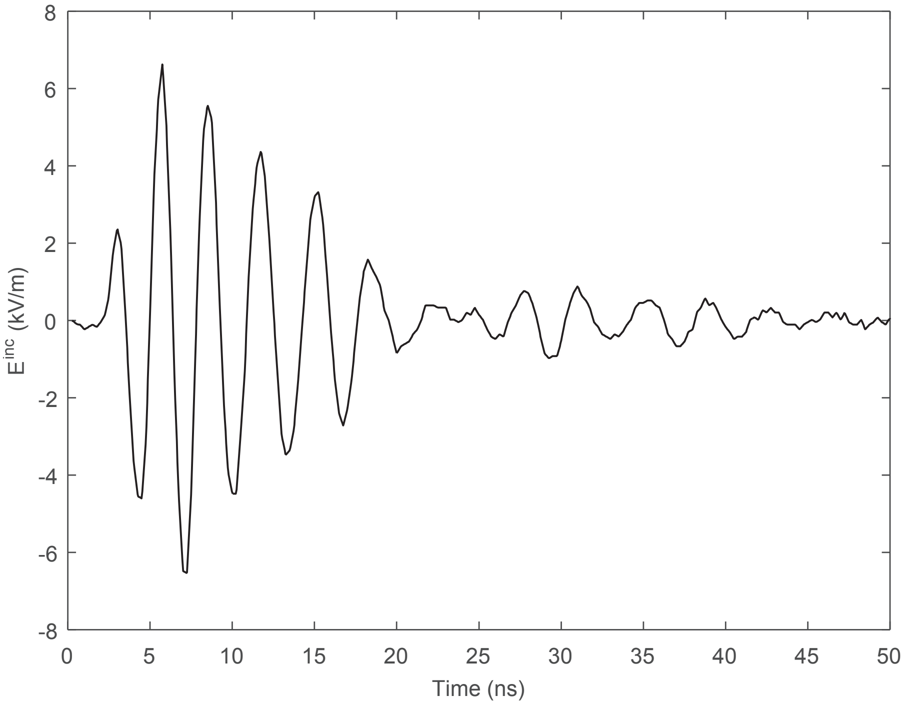

Fig. 5.12 Mesoband incident electric field: electric field generated by the EPFL SWO [119].

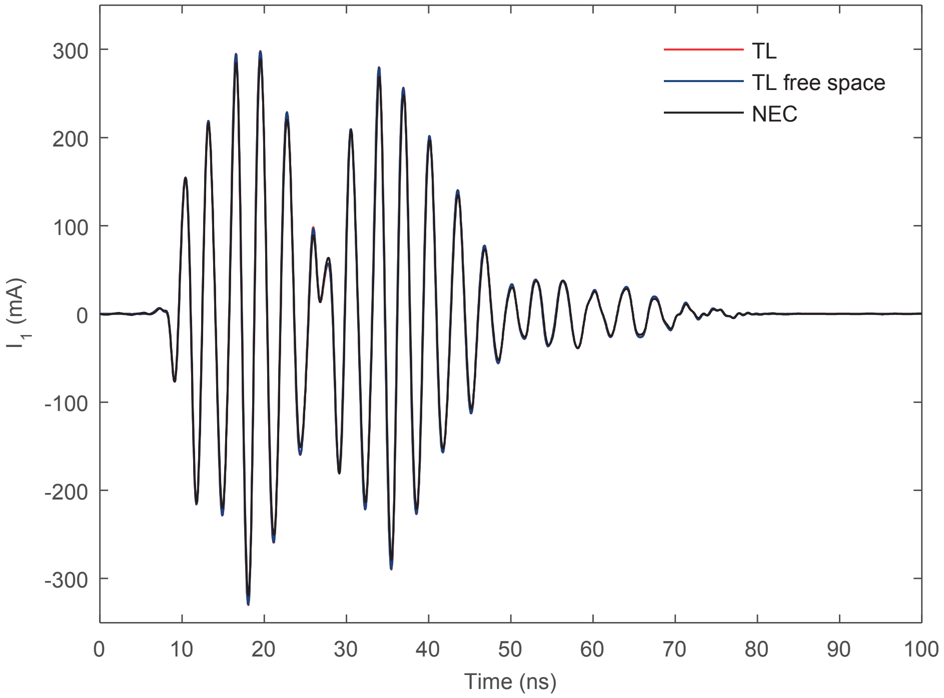

Fig. 5.13 DM current due to the mesoband illumination for the case *h* = 300 cm and *d* = 3cm.

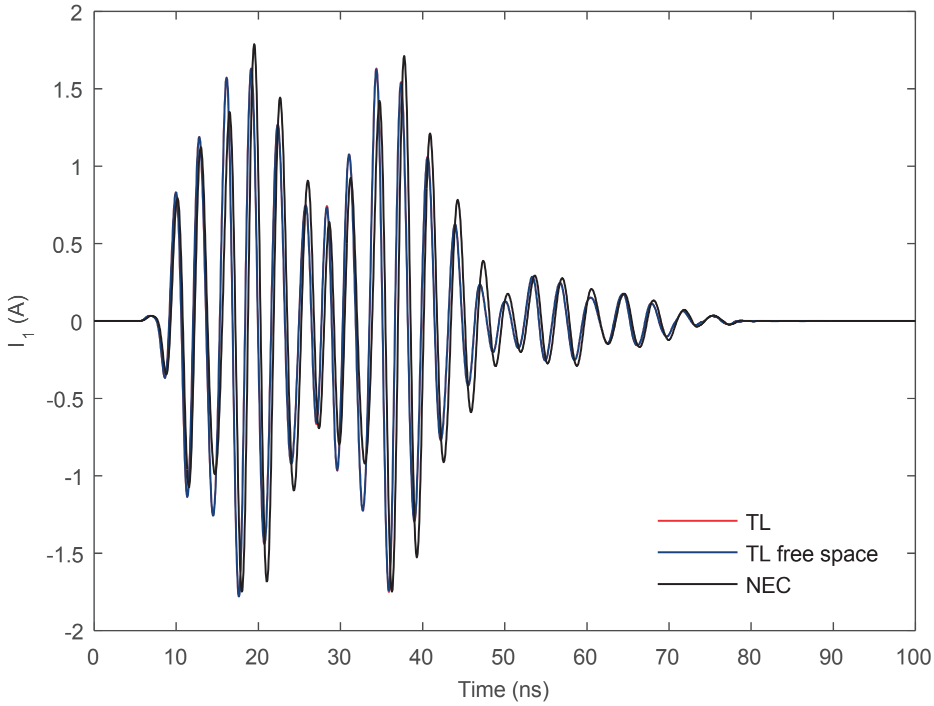

Fig. 5.14 DM current due to the mesoband illumination for the case *h* = 300 cm and *d* = 30cm.

5.3.4.3 Illumination of the line with a hypoband signal

Finally, the illumination of the lines with a CW signal of 900MHz has been considered. Fig. 5.15 plots the incident electric field that was used to excite the lines. The frequency of the signal was chosen so that the distance between the conductors satisfies the TL conditions in the first configuration, but does not in the second configuration. The simulated current waveforms obtained with NEC-4 (black), TL theory in presence of ground plane (red), and TL theory disregarding the ground plane (blue) are plotted for the first configuration (*d=3* cm) in Fig. 5.16 and for the second configuration (*d=30* cm) in Fig. 5.17.

The results of the first configuration are in perfect agreement whereas the amplitude of the induced current is overestimated by a factor of about 2 with the TL solutions in the second configuration.

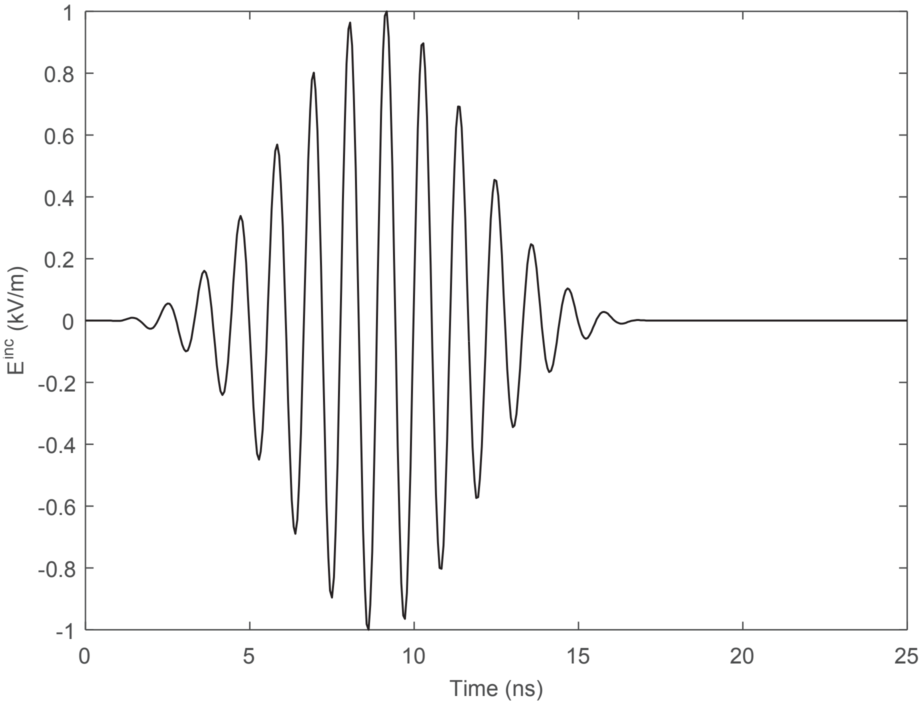

Fig. 5.15 Hypoband incident electric field: numerically generated CW chirp oscillating at 900 MHz.

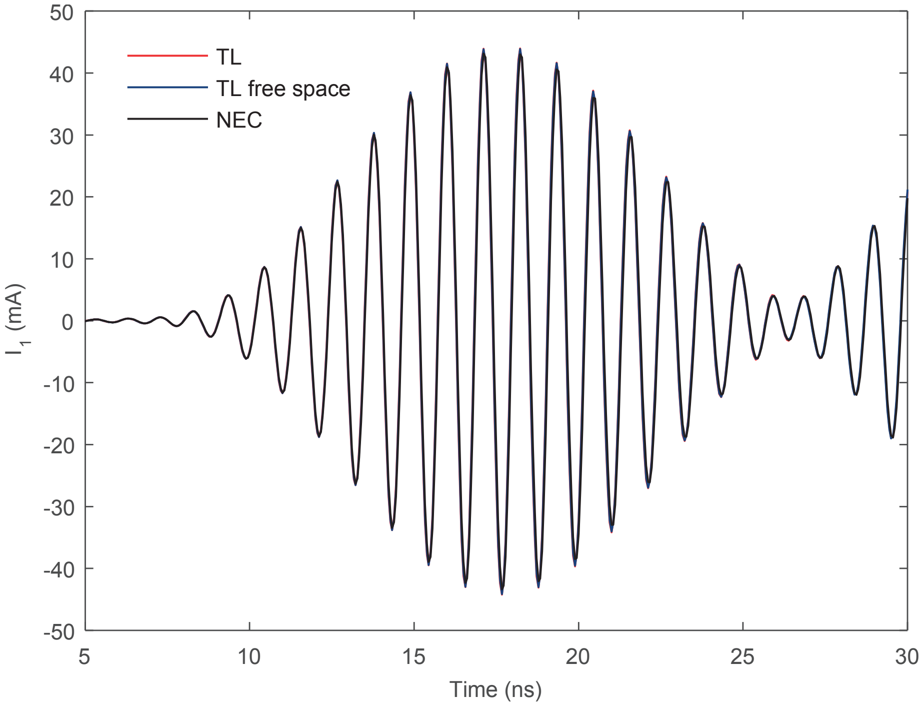

Fig. 5.16 DM current due to the hypoband illumination for the case *h* = 300 cm and *d* = 3cm.

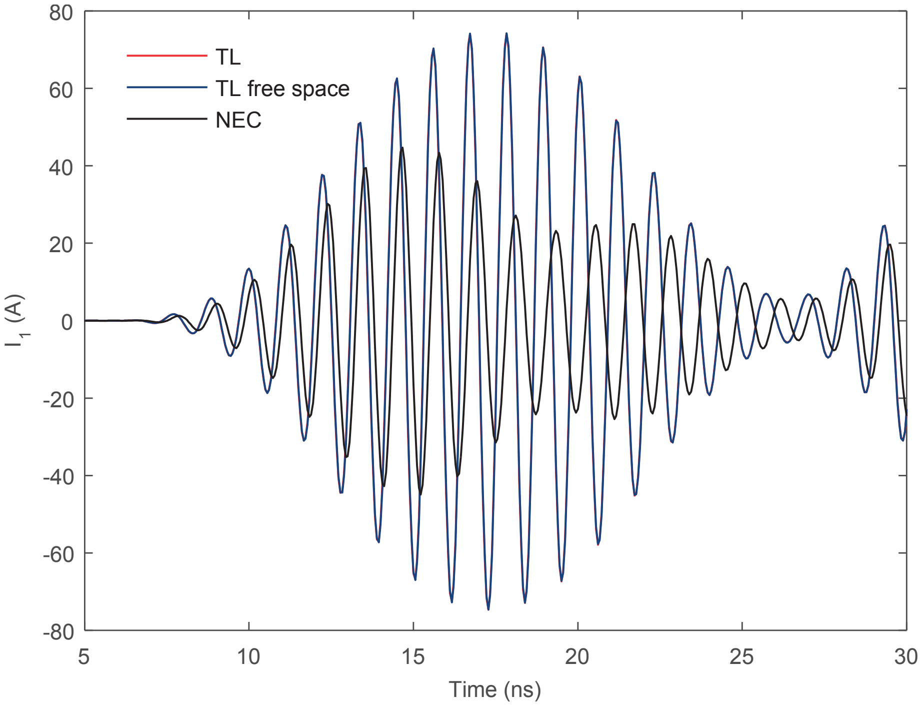

Fig. 5.17 DM current due to the hypoband illumination for the case $h = 300$ cm and $d = 30$cm.

5.3.4.4 Results analysis

The results presented in this section have illustrated the efficiency and accuracy of TL theory in the prediction of the time domain DM disturbances when dealing with sources that are outside the frequency validity limits. According to the survey of Chapter 3, a good portion of the IEMI signals exhibit a mesoband or hyperband bandratio. Therefore, a good reproduction of the time domain waveform is expected since much of the source energy remains low frequencies, where the TL solutions are correct.

The particular example used to illustrate the prediction of hypoband interferences has shown that the response may be over / underestimated by a few dBs which is acceptable for the purposes of this work. If further accuracy is required, alternative formulations of the TL equations that account for higher frequency effects like radiation in the extremities of the line due to the discontinuities can be used [62].

5.4 Study of the influence of conductive and dielectric losses in the propagation of IEMI signals along power and communication lines

The propagation of IEMI signals along power and communication lines will be affected by (i) conductive losses and dielectric losses, and (ii) radiation losses. In this section, the attenuation and distortion of selected cables is studied with a simplified TL model [3] of a two conductor line with conductive and dielectric losses. The radiation losses and reflection due to non-uniformities are not considered.

5.4.1 Modeling considerations

Consider the DM coupling of an electromagnetic disturbance onto a lossy uniform transmission line of finite length L. The electromagnetic disturbance is represented as an equivalent lumped source at a given position along the line. In order to simplify the analysis, it is assumed that the line is matched at both ends and an equivalent voltage source is used to excite the line at one end, as schematically shown in Fig. 5.18.

The transmission line is characterized by its characteristic impedance Z_0 and its complex propagation constant γ. The propagation transfer function H relating the voltages at both ends of the line can be expressed as:

$$H = \frac{V(L)}{V(0)} = e^{-\gamma L} = e^{-\alpha L} e^{-j\beta L}, \tag{5.7}$$

where the complex propagation constant γ has been decomposed into the attenuation constant α and the phase constant β.

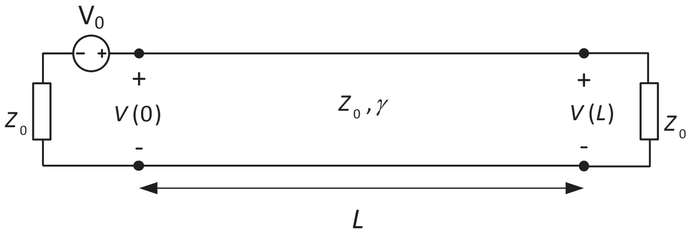

Fig. 5.18 Schematic diagram of a uniform two-wire transmission line excited by an equivalent voltage source representing the DM field-to-wire coupling from an external source.

The complex propagation constant of a transmission line can be calculated from its p.u.l. parameters as [88]:

$$\gamma = j\omega\sqrt{LC}\sqrt{(1-\frac{R'G'}{\omega^2 LC})-j(\frac{R'}{\omega L'}+\frac{G'}{\omega C'})}, \tag{5.8}$$

in which *R', L', G'* and *C'* are respectively the line P.U.L. resistance, inductance, conductance and capacitance.

5.4.1.1 DM propagation cross sections

The transfer function and the complex propagation constant of typical power and communication lines found in civilian installations, namely, (i) LVP lines, (ii) TWPs, and (iii) RFC lines were studied.

The cross sections of the LVP and TWP lines are presented in Fig. 5.19. Two wires of radii r_w and conductivity σ are coated with a dielectric insulator with a relative permittivity ε_r and a tangent loss $\tan\delta$. The outer radius of the coating is r_m.

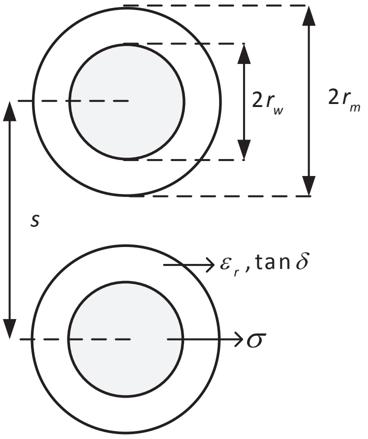

Fig. 5.19 Schematic diagram of the geometry and the constitutive materials of a lossy two-coated-wire line.

The cross section definition of the RFC line is shown in Fig. 5.20. In this figure, σ is the conductivity of the inner and outer conductors, ε_r and $\tan\delta$ are the relative permittivity and tangent loss of the dielectric insulator, *T* is the outer conductor thickness, and r_w and r_s are respectively the radii of the inner conductor and the dielectric insulator.

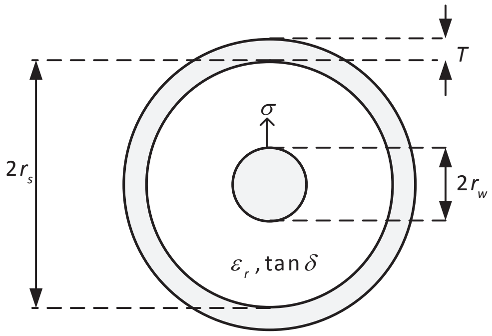

Fig. 5.20 Schematic diagram of the geometry and constitutive materials of a lossy RF coaxial line.

The P.U.L. parameters of the lines were calculated with classical analytical formulas or fast numerical procedures [88] and were used to run the parametric analyses. A summary of the formulas used to estimate the P.U.L. parameters can be found in 8.2Appendix B. The p.u.l. resistance and conductance of the lines are approximated with analytical formulas for running faster parametric analyses.

5.4.1.2 Effective complex permittivity

The constitutive parameters of the dielectrics were approximated with constant relative permittivity and tangent loss. Neglecting the conduction currents inside the dielectric, the tangent loss can be expressed as:

$$\tan\delta = \frac{\sigma_d + \omega\varepsilon''}{\omega\varepsilon'} \approx \frac{\varepsilon''}{\varepsilon'}, \tag{5.9}$$

where ε' and ε'' account respectively for the polarizability of the medium, and the loss (heat) due to the damping of the vibrating dipole moments [171].

Finally, the complex permittivity of the dielectric materials was calculated using:

$$\hat{\varepsilon} = \varepsilon_0(\varepsilon' - j\varepsilon'') = \varepsilon_0\varepsilon_r(1 - j\tan\delta). \tag{5.10}$$

5.4.1.3 Parameters of selected lines

The dimensions and the constitutive materials of several LVP, TWP, and RFC lines were used for calculating their P.U.L. parameters. The conductors of the considered lines were made of copper with conductivity $\sigma = 58$ MS/m. The dielectric insulators of the lines varied between PE, PTFE (Teflon), or PVC. The used relative permittivity and tangent loss of the dielectric insulators at a frequency of 100MHz are given in Tab. 5.4.

Tab. 5.4 Dielectric properties of constitutive materials

Dielectric	ε_r	$\tan\delta$
PVC	2.3	0.02
PE	2.1	0.8×10^{-3}
PTFE	3	0.4×10^{-3}

A summary of the parameters of each line is presented in Tab. 5.5. The first column of the table contains the usual denomination of the lines. The second and third columns present the line type and the used dielectric insulator. The approximated dimensions are contained in the third to sixth column. The approximated characteristic impedance Z_0 of the lines is given in the seventh column. The P.U.L. resistance *R'* and conductance *G'* (calculated at a frequency of 1GHz) are shown, respectively, in the eighth and ninth columns. Finally the calculated attenuation factor (in dB/100m) of the lines is shown in the last column.

In order to estimate the attenuation factor, the attenuation constant of the lines was approximated using [171]:

$$\alpha \cong \frac{1}{2}\left(\frac{\mathrm{R'}}{Z_0} + \mathrm{G'Z_0}\right). \tag{5.11}$$

Notice that the LVP lines do not necessarily have a fixed separation distance unless they are grouped inside an insulating jacket. For evaluating the parameters presented in Tab. 5.5, the separation distance was approximated to twice the radius of the dielectric. This is used only as an indication of the expected propagation characteristics.

According to Tab. 5.5, the conductive and dielectric losses of the studied lines have a considerable magnitude at 1GHz and should be included in the calculation of the propagation of a disturbance at these frequencies. The LVP lines exhibit the highest dielectric losses due to the PVC insulation. On the other hand, TWPs have the highest conductive losses due to the small cross section of the lines.

Tab. 5.5 Parameters of selected lines

Name	Type	Diel.	r_w [mm]	r_m/ r_s [mm]	s [mm]	Z_0 [Ω]	R' [Ω/m]	G' [mS/m]	Att. [dB/100m]
2X1.mm^2	LVP	PVC	0.7	1.200	2.4	90	3.6	2.56	117
2/0 AWG	LVP	PVC	6.3	8.300	16.6	70	0.42	1.94	62
Cat. 5e	TWP	PE	0.29	0.470	0.99	92	9.1	0.11	47
Cat.6	TWP	PE	0.26	0.550	1.12	105	10.1	0.15	49
Cat.7	TWP	PE	0.29	0.700	1.40	103	9.1	0.23	49
RG58	RFC	PE	0.47	1.475	N/A	50	3.7	0.56	44
RG174	RFC	PE	0.24	0.740	N/A	50	7.2	0.57	75
RG316	RFC	PTFE	0.27	0.775	N/A	50	6.6	0.28	63
RG214	RFC	PE	1.13	3.620	N/A	50	1.5	0.55	25

5.4.2 Parametric analyses and results

5.4.2.1 Numerical simulations setup

The propagation transfer function *H* was calculated with Equation (5.7) for the following lines whose parameters were previously reported in Tab. 5.5: (i) 2 x1.5mm2 (LVP), (ii) Cat 5e (TWP), and (iii) RG58 cable (RFC).

In order to compare the contribution of the conductive and dielectric losses, the transfer functions were calculated by using the parametric configurations presented in Tab. 5.6.

Tab. 5.6 Parametric loss configurations

Loss configuration	Conductivity (σ)	Tangent loss ($\tan\delta$)
None	∞	0
Only conductive	58 MS/m	0
Only dielectric	∞	According to Tab. 5.4
both	58 MS/m	According to Tab. 5.4

A hyperband signal was used as a voltage source to excite the lines at one end (see Fig. 5.18) and the transmitted voltage at the other end was calculated by convoluting the waveform with the inverse Fourier transform of the transfer function. In what follows, the transmitted voltage and the amplitude of the transfer function are presented for each of the studied lines. The total length of the lines was set to L=10 m. No approximations were made in the calculation of the complex propagation constant. Fig. 5.21 shows the injected signal, which is representative of a hyperband IEMI waveform with a risetime of 229 ps [34, 78].

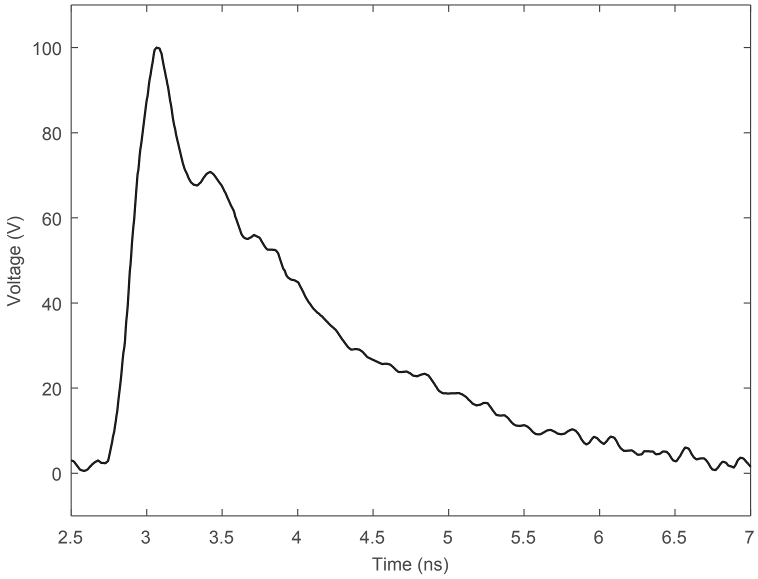

Fig. 5.21 Injected voltage representative of a hyperband IEMI (adapted from [34]).

5.4.2.2 Results

The results for the 10-m LVP line are presented in Fig. 5.22 and Fig. 5.23. They present, respectively, the propagated signals at the far end of the line, and the magnitude of the transfer function. The black-dashed curve corresponds to the calculated signal when no losses are included. If the conductive losses are included (red curve) there is an attenuation of about 12% for the peak amplitude, and an increase in the signal risetime. The attenuation in this case is less than 3dB at the highest frequency.

On the other hand, if only the dielectric losses are considered (blue curve), the peak attenuation is about 40% and a more significant increase is observed for the risetime. The attenuation is more than 30 dB in the GHz range. Finally, the solid black curve shows the results obtained when both losses are included. In this case, the overall peak attenuation is about 50% and the obtained risetime and attenuation are comparable to the values obtained if only dielectric losses are included.

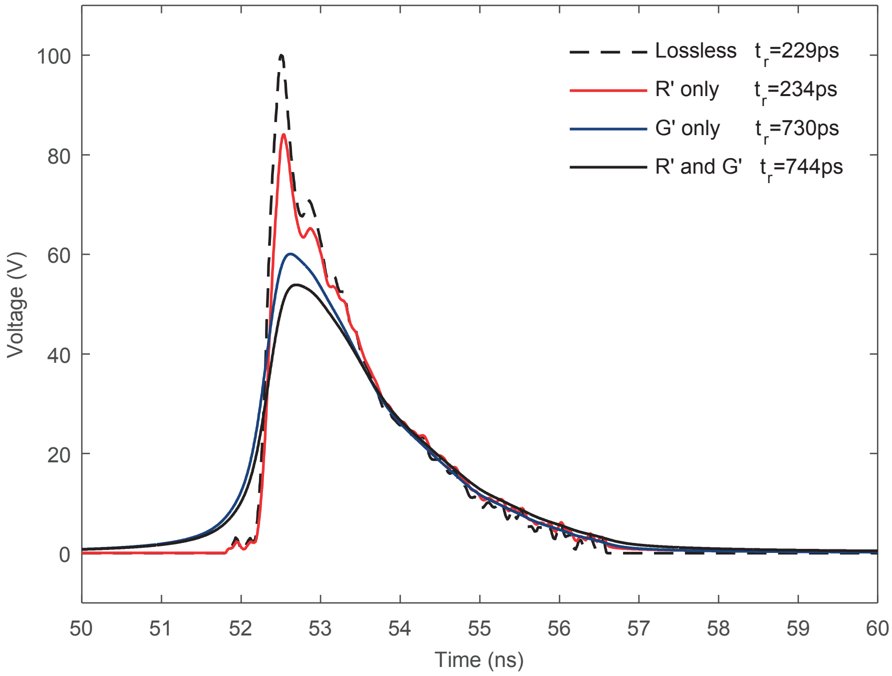

Fig. 5.22 Propagation along a 10-m long LVP line: transmitted signal.

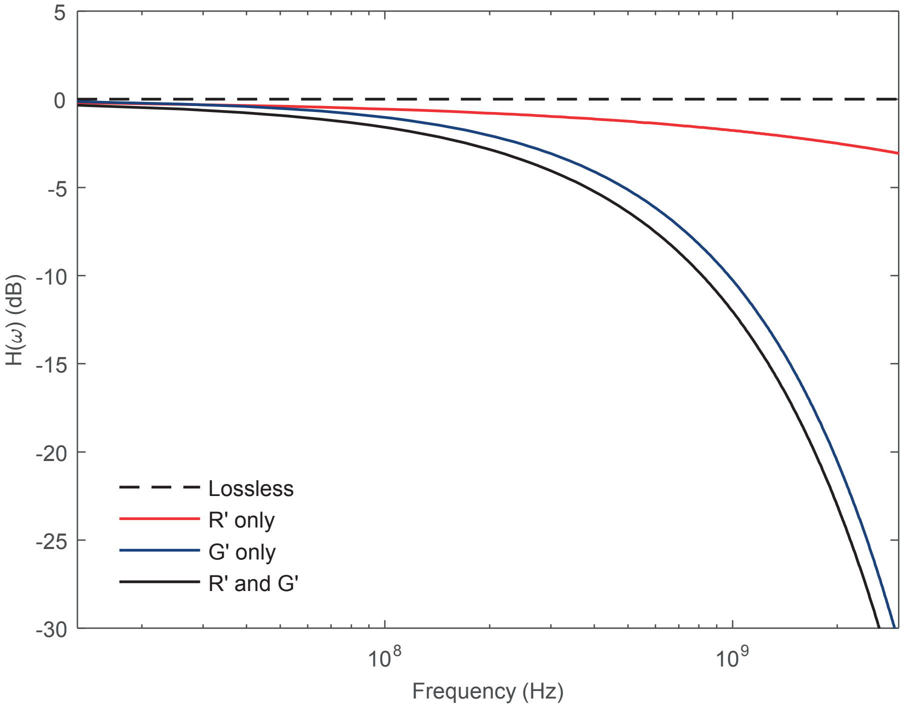

Fig. 5.23 Propagation along a 10-m long LVP line: transfer function.

The simulation results for the 10-m TWP line are shown in Fig. 5.24 and Fig. 5.25. Unlike the case of the LVP line, for which the dielectric losses were predominant, in this case, the conductive losses prevail. This is essentially due to (i) smaller cross section of the wires and (ii) thinner dielectric coating with lower tangent loss for the twisted wires in the network cable in comparison with the power cable. Notice that there is a marginal increase of the risetime, and the attenuation in the GHz range is less than 10 dB.

Finally, the results for the 10-m RFC line are shown in Fig. 5.26 and Fig. 5.27. The performance of this line is similar to the TWP case, with predominant conductive losses due to the small cross section of the inner wire. The effect of the homogeneous padding with dielectric insulator inside the coaxial line can be observed in that the signal arrives 7 to 9 ns later than in the previous cases. Also notice that the dielectric losses are slightly more significant in the GHz range than in the TWP line.

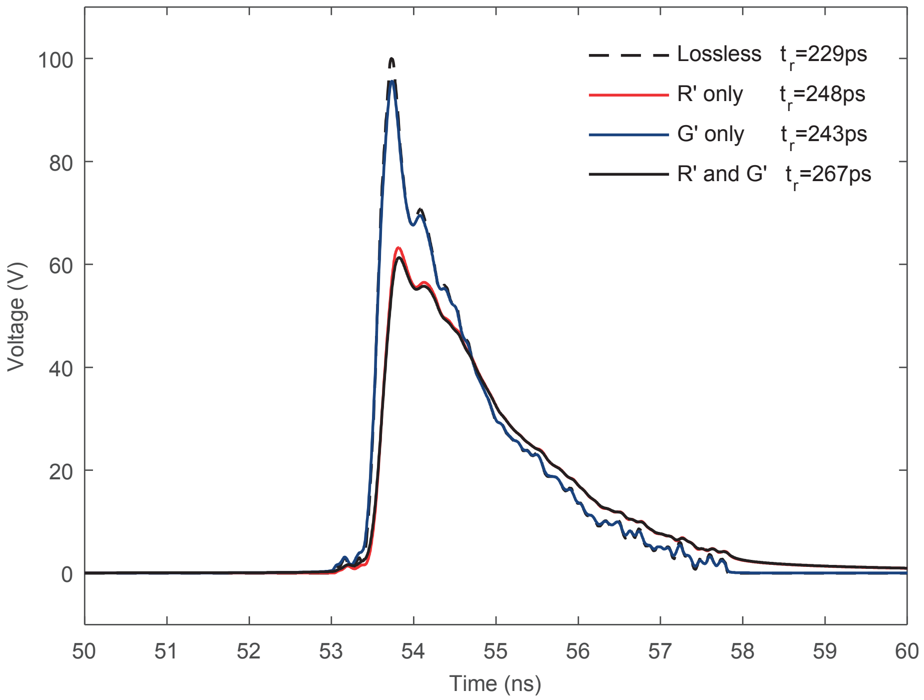

Fig. 5.24 Propagation along a 10-m long TWP line: transmitted signal.

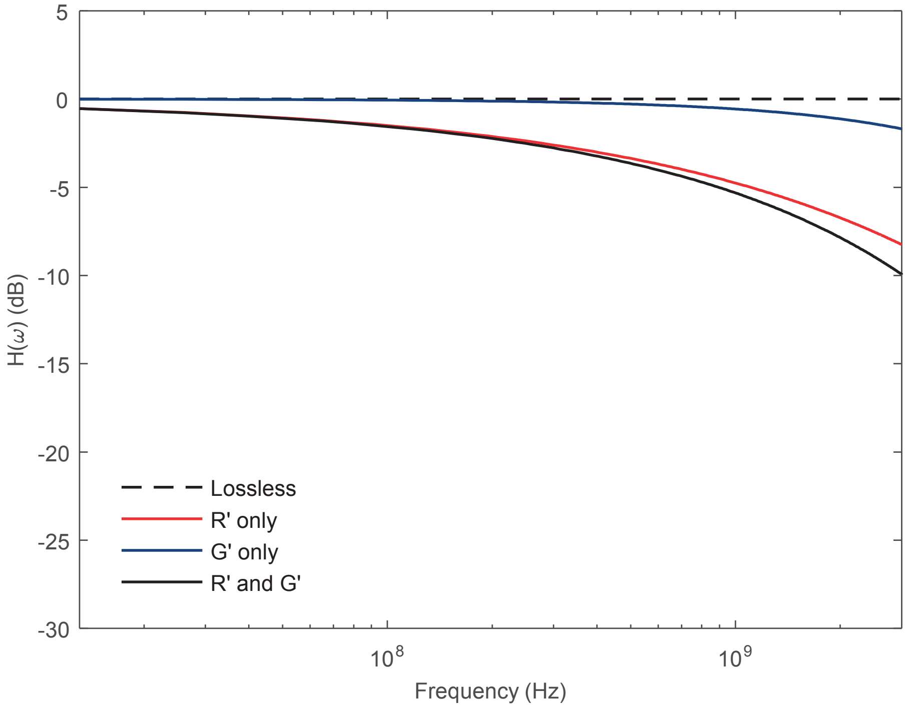

Fig. 5.25 Propagation along a 10-m long TWP line: transfer function.

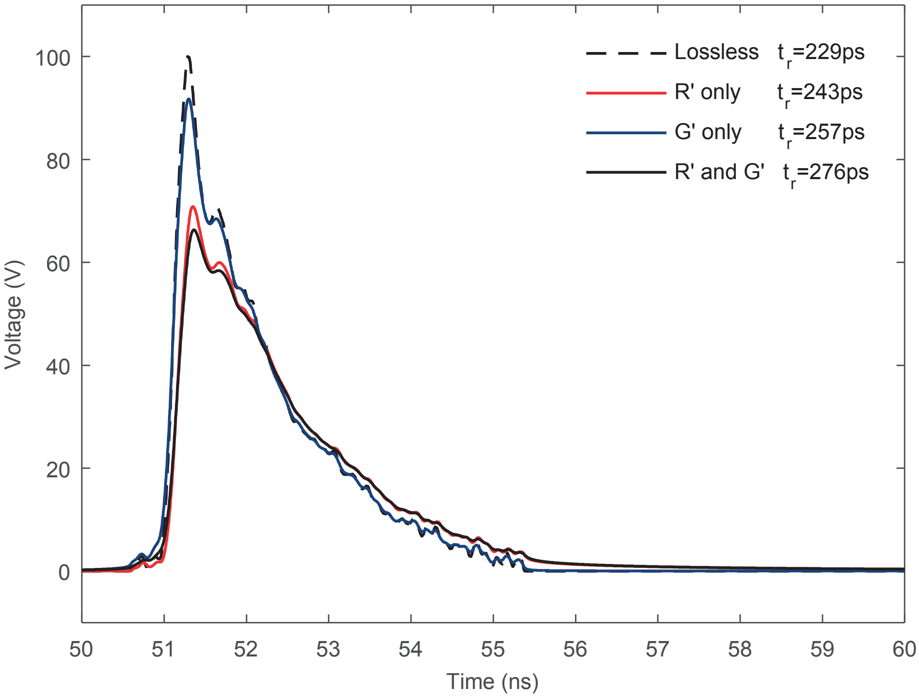

Fig. 5.26 Propagation along a 10-m long RFC line: transmitted signal.

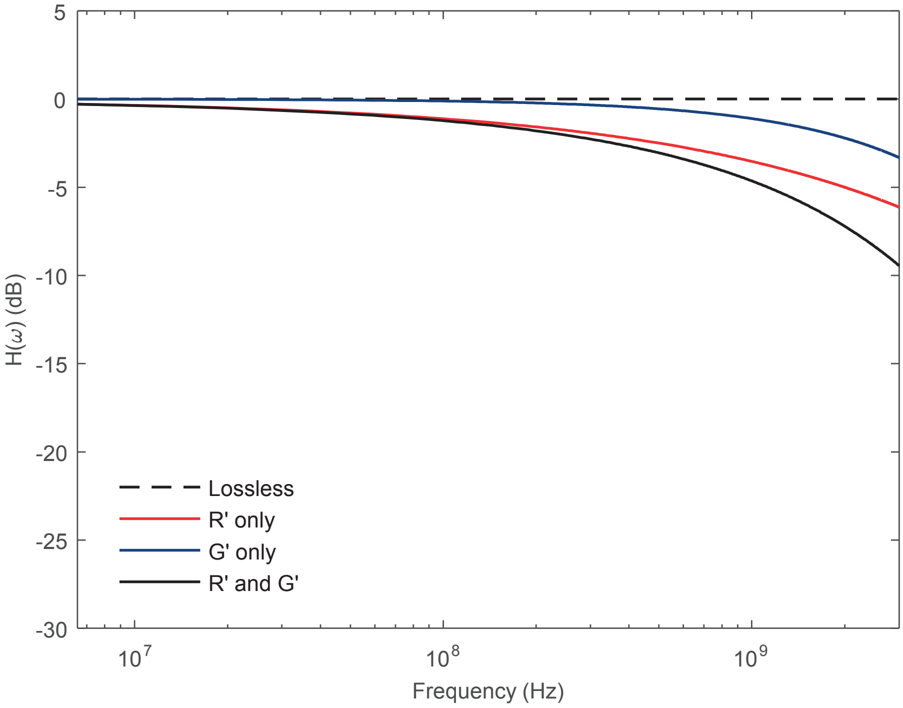

Fig. 5.27 Propagation along a 10-m long RFC line: transfer function.

5.4.3 Discussion

According to the results of the previous section, the differential mode propagation of fast transients can be significantly attenuated by the presence of losses in the transmission lines. One of the effects of thick dielectrics coatings is the increase of the risetime with respect to the original waveform.

Traditional surge protection devices (SPDs) are used to protect from disturbances originated by signals that could be slower than the expected IEMI signals (e.g., those originated from ESD, NEMP, or lightning). Therefore, it is useful to assess the propagation distance at which lossy transmission lines will disperse an IEMI-originated disturbance so that classical SPDs could be used. It is also useful to evaluate the required propagation distance to reduce the disturbance amplitude so that less strong SPDs could be installed (see [80] for further details).

5.5 Conclusions

In this chapter, the applicability of the TL theory in evaluating DM signals in canonical setups of two-wire lines floating above a ground plane was discussed through analysis and simulation. Special attention was given to the possibility of predicting the response of the lines when subjected to waveforms representative of IEMI.

According to the results presented in Section 5.2, two main conclusions can be drawn:

(1) the presence of the ground plane can be disregarded in the calculation of the characteristic impedance of the lines, provided that the height of the wires is larger than about twice the separation distance between them.
(2) The validity of the TL theory for DM induced disturbances is conditioned upon an electrically short distance between the wires, regardless of the distances above the ground plane.

The effects of including conductive and dielectric losses in the analysis of the DM propagation in selected transmission lines was also studied from an analytical point of view. The parameters of several power and communication lines were extracted in order to assess the significance of the conductive and dielectric losses at the expected frequencies of IEMI perturbations. The results show that both dielectric and conductive losses have to be taken into account in order to obtain the total attenuation. However, it has been evidenced that in lines with very small conductor cross-section, it is more likely that the conductive losses will dominate the total attenuation due to the skin effect.

6 Numerical Modeling of the Propagation of IEMI Disturbances in Low Voltage Power Cables

6.1 Introduction

The applicability of TL theory for calculating the propagation of IEMI disturbances in cables representative of real scenarios was previously studied in Chapter 5. This chapter deals with the TL modeling of the propagation of IEMI along LVP networks. Previous studies have experimentally shown the possibility of injecting malicious disturbances in the LVP network [17, 33]. As previously mentioned, in order to estimate the expected voltages and currents at the equipment power plug inputs, EM simulation means have to be used when experiments are not possible. Typical input impedances of commercial equipment obtained by measurement [172, 173] can be included to simulate their connection to the power lines. After calculating the disturbance, the compromise level of the equipment can be estimated after comparing the voltage and current levels to the upset and permanent damage thresholds [7, 11, 174].

In this chapter, the TL modeling of the propagation of high frequency disturbances along the LVP network of the commercial raceway that was already introduced in Chapter 5 is presented. The TL models were implemented using CST Cable Studio [175]. This tool has been previously applied to similar studies and shown to provide accurate results in the analysis of the crosstalk between cables (see e.g., [176]). In order to validate the models, the numerical results were compared against measurements obtained with frequency and time domain techniques. According to the results of Chapter 5, the DM propagation along LVP cables is efficient up to some hundreds of MHz. Therefore, the measurements and the TL models were limited up to a frequency of 200MHz. It is worth noting that, to the best of the Author’s knowledge, the highest frequencies at which propagation effects along power lines have been considered do not exceed a few tens of MHz for Power Line Communication systems (e.g., [177-179]), or 100 MHz for Nuclear Electromagnetic coupling studies (e.g., [180, 181])

The results presented in this chapter are heavily drawn from a previous report by the author and Dr. Kasmi from the Wireless security Lab of the ANSSI [81], and two publications presented at international conferences [81, 82]. In the first part, the experimental setup that was used to measure the propagation along the raceway in the frequency and time domains is introduced. Secondly, the TL modeling procedure and the validation of the simulation tool with a canonical example is presented. Finally, the validation of the raceway models with the experiments is presented and discussed.

This chapter is organized as follows. The experimental setup that was used to measure the transfer functions and the impulse response between the raceway sockets is presented in Section 6.2. The TL model of the LVP cabling of the raceway is presented in Section 6.3. The comparisons between the experimental and simulation results are discussed in Section 6.4. Finally, conclusions are given in 6.5.

6.2 Experimental setup

The experiments were performed along the LVP network of the experimental raceway that was introduced in Chapter 4. For the sake of clarity, some information will be repeated in this section, and further details about the cable connectors will be provided.

Both time-domain and frequency-domain tests were carried out in order to address the propagation along the raceway. The frequency domain tests were carried out by using a VNA. The time domain tests were carried out by using a voltage impulse generator and an oscilloscope.

6.2.1 Test raceway

A schematic diagram representing the test raceway and the LVP circuits is presented in Fig. 4.1. The raceway is composed of 4 triple-power sockets of the SEV 1011 type. The SEV 1011 sockets are the standardized power outlets in Switzerland (see picture in Fig. 6.2). The four power sockets were labeled from left to right as AC1, AC2, AC3, and AC4 respectively.

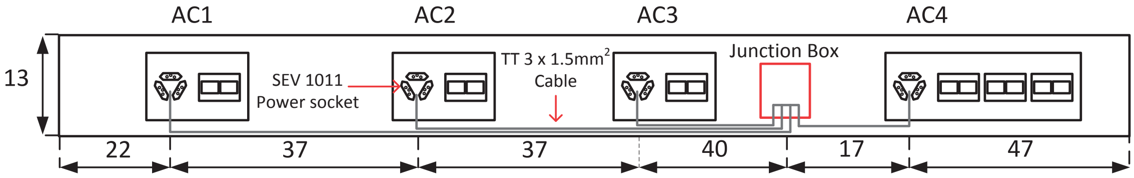

Fig. 6.1 Schematic diagram of the LVP cabling inside the test raceway. Distances are in cm and not to scale.

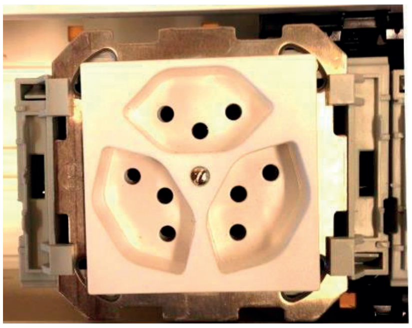

Fig. 6.2 Example of a triple SEV 1011 power socket.

Each of the power sockets are connected to a NEXANS TT 3 x 1.5 mm^2 cable. This type of cable is typically installed in Swiss raceways. The cable has three coated wires that are used for the connection to the Phase, Neutral, and Ground wires of the distribution network, and are tested to withstand a maximum voltage of 1 kV before the dielectric breakdown [182].

The cables are connected in a star configuration; starting at each of the power sockets and ending at a junction box that is schematically shown with a red line in Fig. 4.1. In order to connect to the socket inputs, a vertical extension of 6.2 cm length (not shown in Fig. 4.1) was added to each of the four cables. A picture of the junction box where the arrival and interconnection of the four power cables can be appreciated is presented in Fig. 6.3. Notice that the cables are bent several times in order to make them fit inside. Thus, an additional 18 cm cable length has to be considered at the junction box.

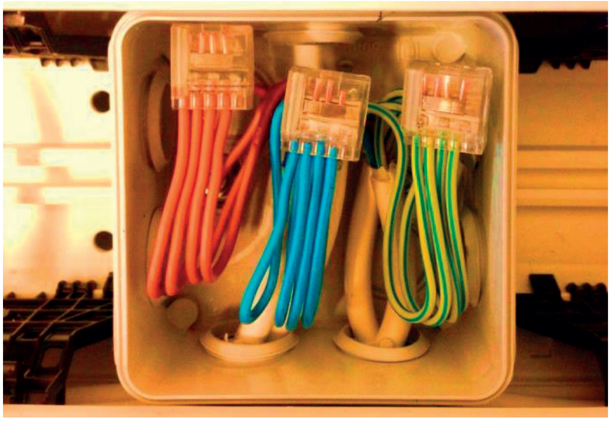

Fig. 6.3 Picture of the junction box containing the four power cables. The phase, neutral and ground conductors of each power cable are interconnected in the box.

The junction box can be alternatively connected to the power grid. Since the study does not require the test of equipment in their on-line state, the cables were left isolated from the power mains.

The tests were carried out at the EMC Lab of EPFL. The raceway was placed inside the semi-anechoic chamber above the metallic ground plane of the room. A picture showing the raceway laying over the ground plane before starting the tests is shown in Fig. 6.4. The plastic walls of the raceway were removed in order to have an easy access to some of the cables during the tests.

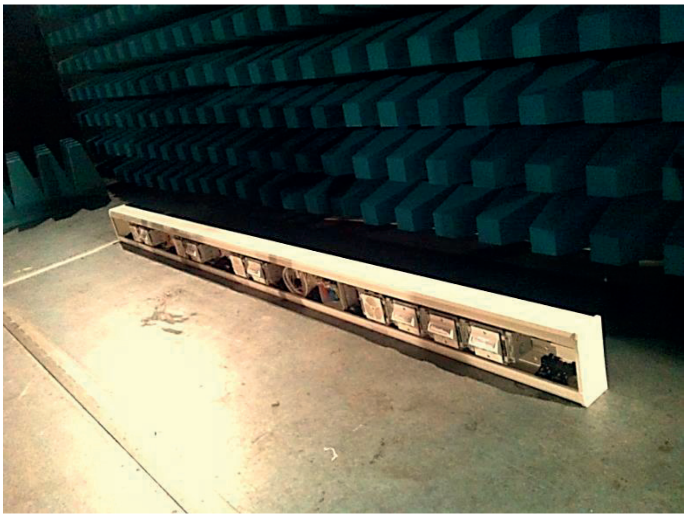

Fig. 6.4 Picture of the raceway laying over the ground plane of the semi-anechoic chamber before starting the tests.

6.2.2 Injection adapters

Two types of adapters enabling the transition from SEV 1011 sockets to BNC connectors were built for injecting and measuring the DM signals in the raceway. A picture showing both types of adapters is presented in Fig. 6.5. The adapters were built by using commercial SEV 1011 connectors, short-length NEXANS cable, and BNC chassis mount connectors. The Phase wire was soldered to the central pin of the BNC connector and the Ground and Neutral wires were soldered together to the BNC chassis. On the other side of the NEXANS cable, each wire was connected to the three pins of the SEV 1011 connector. The ground and neutral pins were short-circuited with pieces of coated 1.5mm^2 copper wires.

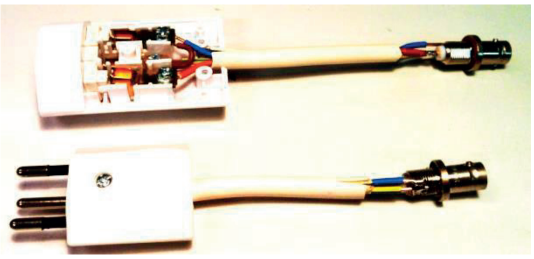

Fig. 6.5 Picture of the SEV 1011 to BNC adapters.

6.2.3 Frequency-domain tests

The magnitudes of the transfer functions between socket AC1 and the other three sockets were measured by using an ANRITSU MS4630B VNA. The schematic diagram of the measurement setup is presented in Fig. 6.6.

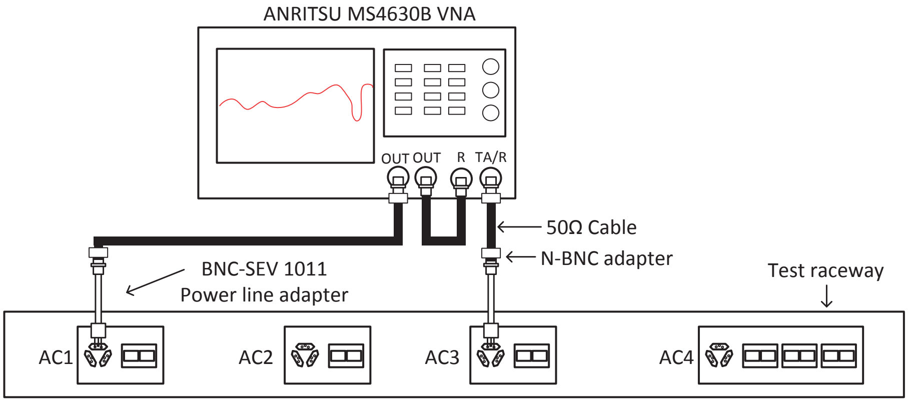

Fig. 6.6 Schematic diagram of the experimental setup for measuring the transfer function among the raceway sockets with a VNA.

The ANRITSU MS4630B VNA provides two identical outputs containing the signal of the local oscillator. One of the outputs was connected to the reference channel R, and the other was injected to AC1 by means of a 50 Ω cable that was connected through an injection adapter. The output of the raceway was connected to the TA/R channel of the VNA by means of another 50 Ω cable connected to the respective adapter. The ratio between the TA/R and R channels was internally calculated by the VNA.

For each of the tests, an average of 50 measurements was recorded. A summary of the configuration of the VNA is reported in Tab. 6.1.

Tab. 6.1 Configuration of the ANRITSU MS4630B for the transfer function measurements

Parameter	Description
Output power level	0 dBm
Number of frequency points	500
Start frequency	1 MHz
Stop Frequency	200 MHz
Resolution Bandwidth (RBW)	20 kHz
Sweep Time	100 ms

6.2.3.1 Reference measurement

In order to correct the calculated transfer function to account for the presence of the measurement cables and adapters, a reference measurement was performed before starting the tests. The schematic diagram of the reference measurement is presented in Fig. 6.7.

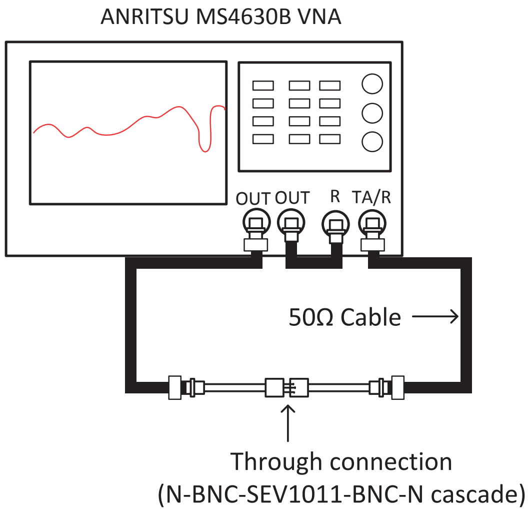

Fig. 6.7 Schematic diagram of the reference measurement setup with the VNA.

Assuming a good match between the adapters and the raceway, the correction of the transfer function can be performed by dividing the original measurement (Fig. 6.6) by the reference measurement (Fig. 6.7). As the frequency starts to increase, the mismatch due to non-uniformities at the adapter-socket transition would require a full two-port calibration of the VNA at the raceway input and output plane. Such calibration was not possible because the calibration kit requires standards connectors.

6.2.4 Time-domain tests

The impulse response between socket AC1 and the other three sockets of the raceway was measured with the aid of a MONTENA PG-45 rectangular voltage generator, a SCHAFFNER DCP 0100 directional coupler, and a Lecroy LC574AL oscilloscope. A schematic diagram of the measurement setup is presented in Fig. 6.8.

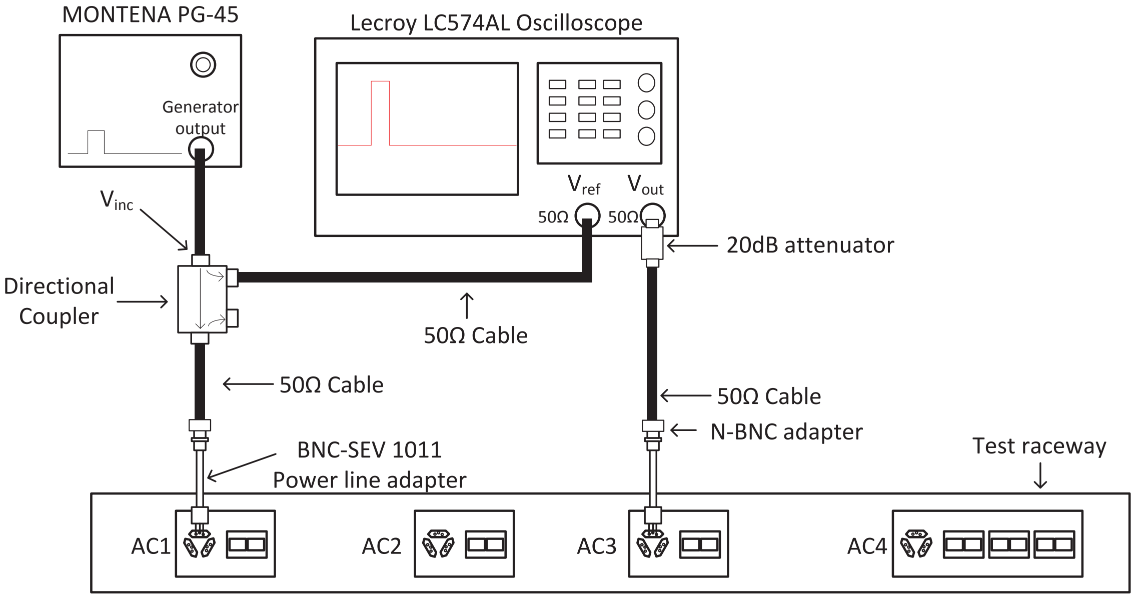

Fig. 6.8 Schematic diagram of the setup for measuring the impulse response among the raceway sockets.

The generator output V_{inc} was injected to the input of the directional coupler. The transmitted signal of the directional coupler was connected to AC1 by using a 50 Ω cable. The output signal from the raceway V_{out} was connected to the oscilloscope through a 50 Ω cable and a 20dB attenuator. On the other hand, in order to trigger the oscilloscope and to obtain a replica of the incident voltage, the forward signal of the directional coupler V_{ref} was connected to a second channel of the oscilloscope through a 50 Ω cable. Notice that the forward signal of the directional coupler is attenuated by about 40dB.

A summary of the configuration of the generator and the oscilloscope is reported in Tab. 6.2.

Tab. 6.2 Configuration of the voltage generator and the oscilloscope for the impulse response measurements

Parameter	Description
Voltage impulse amplitude	33.5 V
Voltage impulse risetime/duration	750ps/30ns
Oscilloscope samples /Sampling rate	1kS/(1GSamples/s)
Oscilloscope Bandwidth	1GHz

6.3 Electromagnetic modeling

6.3.1 Numerical tool: CST Cable Studio

The information provided in this subsection draws heavily from [183].

The TL model of the raceway has been implemented in CST Cable Studio, an EM tool designed for the simulation of cable harnesses. It is based on the TL decomposition of the cable cross-sections into a cascade of circuits that are solved with an enhanced circuit solver that can be optionally coupled with a 3D full wave solver to include the effect of impinging or scattered electromagnetic fields during the simulation. The simulation procedure with CST is as follows.

In a first step, a complex cable harness is divided into a finite number of straight segments. For each segment the program checks for any metallic structure surrounding the cables. The cables' cross sections in combination with additional metallic structures define the segments' cross sections. Secondly, the p.u.l. inductance and capacitance of the segments are calculated with the aid of a static 2D field solver and simplified formulas are used for obtaining the p.u.l. resistance and conductance. Each segment is transformed into an equivalent circuit and finally all circuits are connected together into a single circuit model representing the whole cable harness.

The generated equivalent circuits are valid within a frequency range from DC to a maximum frequency that is defined by the highest frequency at which the cross sections of the harness are electrically small. Additional effects caused by discontinuities like bends or deviations are not considered.

Finally, the electrical model of the cable harness is transferred into the circuit simulation environment in the form of an N-port network. The user is able to define the network loadings (passive/active, linear/non-linear) and calculate its behavior either in time or in frequency domain. The circuit simulation can be optionally coupled with a 3D full wave solver for the calculation of the EM environment around the cable harness and obtain the distributed field sources for considering the field-to-cable coupling. This latter feature is not used in this work since only the propagation effects along the raceway were modeled.

6.3.2 Validation of the numerical tool

Before starting the EM modeling of the complex cablings inside the raceway, the results obtained with the EM simulation tool were validated with measurements performed considering a simpler canonical configuration of a coated wire above a ground plane. In what follows, an explanation of the experimental setup and the modeling procedures for the validation of the numerical tool is presented.

The validation experiment was carried out in the laboratories of the ANSSI. A schematic diagram of the test setup is shown in Fig. 6.9. A coated wire of length L was laid above a metallic ground plane at a height h. A sinusoidal signal generator was applied to one end of the wire under test through an N-type chassis connector. The screen of the chassis connector was screwed to a vertical extension of the ground plane, and its center pin was soldered to the copper wire. The other end of the wire under test was connected to the receptor of a spectrum analyzer in a similar way as it was done for the signal generator. The used wire was a coated copper wire of circular 1.5mm^2 nominal cross section with a 0.5 mm thickness PVC coating.

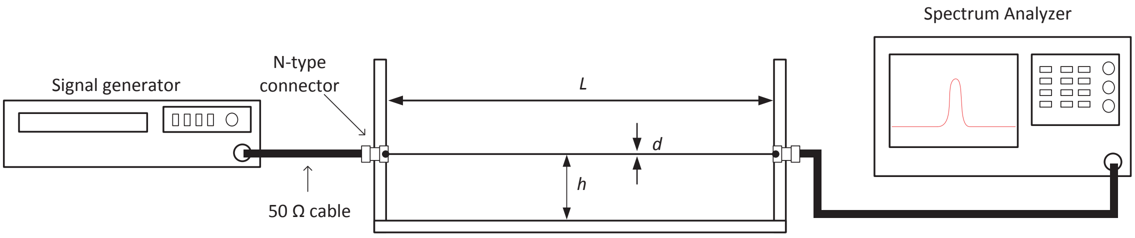

Fig. 6.9 Schematic diagram of the measurement setup of the validation example.

The tests were carried out by injecting a signal to one end of the wire with the signal generator, and simultaneously measuring the amplitude of the signal at the other end with the SA. The voltage transfer function was obtained from 1 to 200 MHz.

A schematic diagram of the simulation setup in CST is presented in Fig. 6.10. The numerical simulations were performed by implementing a transmission line fed by a 1 V /50 Ω generator, and terminated at the other end with a 50 Ω resistance. The output voltage was evaluated across the 50 Ω termination. The transmission line parameters are summarized in Tab. 6.3.

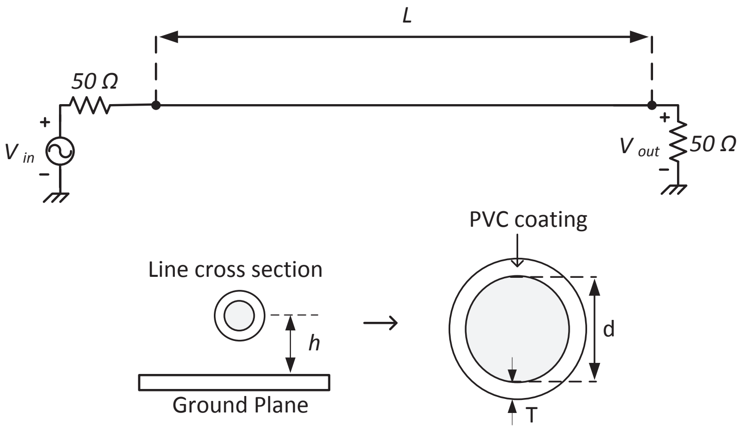

Fig. 6.10 Schematic diagram of the simulation setup of the validation example.

Tab. 6.3 Simulation parameters of the validation example

Parameter	Variable	Value
Line length	L	1 m
Line height	h	35 mm
Wire diameter	d	1.4 mm
Copper conductivity	σ	58 MS/m
PVC coating thickness	T	0.5 mm
PVC relative permittivity	ε_r	3

A comparison of the magnitude of the voltage transfer function obtained with CST and measurements is plotted in Fig. 6.11. There is an excellent agreement between both results. This implies that the transmission line parameters were accurately calculated by the simulation tool. It is worth noting that the agreement between simulation results using a transmission line approach and measurements was expected since in the considered frequency range (up to 200 MHz), the height of the wire remains electrically small.

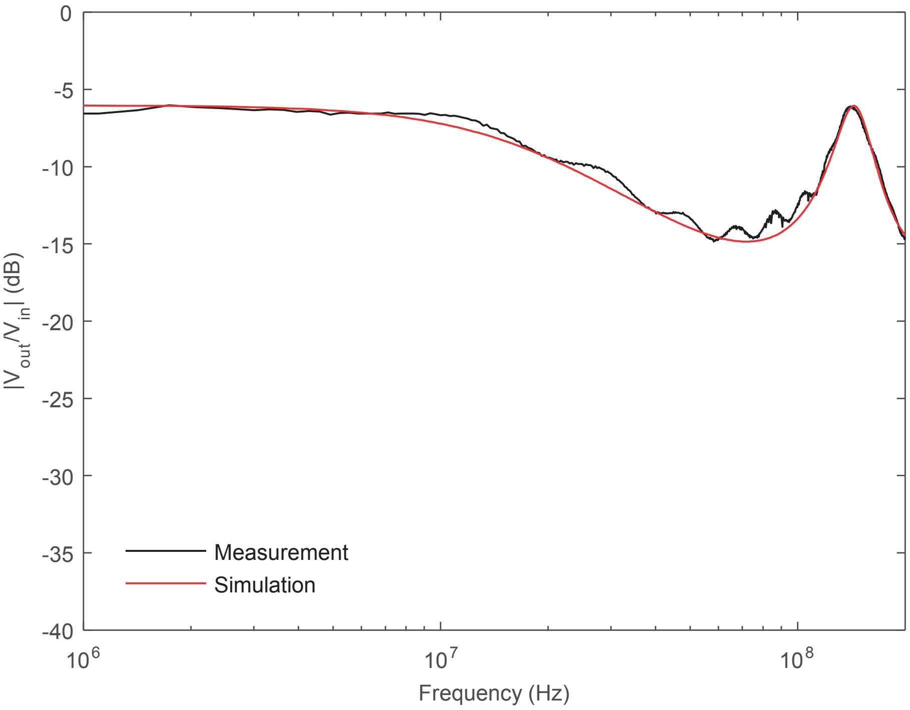

Fig. 6.11 Validation of the simulation tool with a canonical case.

6.3.3 Topological decomposition of the LVP cabling

The topological diagram [56] of the LVP cabling inside the raceway is illustrated in Fig. 6.12 . It is composed of 11 junctions and 10 tubes. The number of junctions and tubes was chosen so that every significant change in the cable cross-sections inside each tube was separately considered. The length of each tube is shown with black arrows. An indication of the number of NEXANS cables running inside each of the tubes is given with gray letters. The junctions labeled as AC1 to AC4 correspond to the power sockets and represent the arrival of the four NEXANS cables. The intermediate tubes connecting junctions N1 to N5 contain the cables that are laying over the bottom of the raceway. The junction box was divided in two separate junctions since 2 tubes were required to model the cable bundles inside the junction box: (i) a tube containing 4 NEXANS cables coming from N4, and (ii) a tube containing the 12 coated cables coming from the 4 NEXANS cables at the Junction Box.

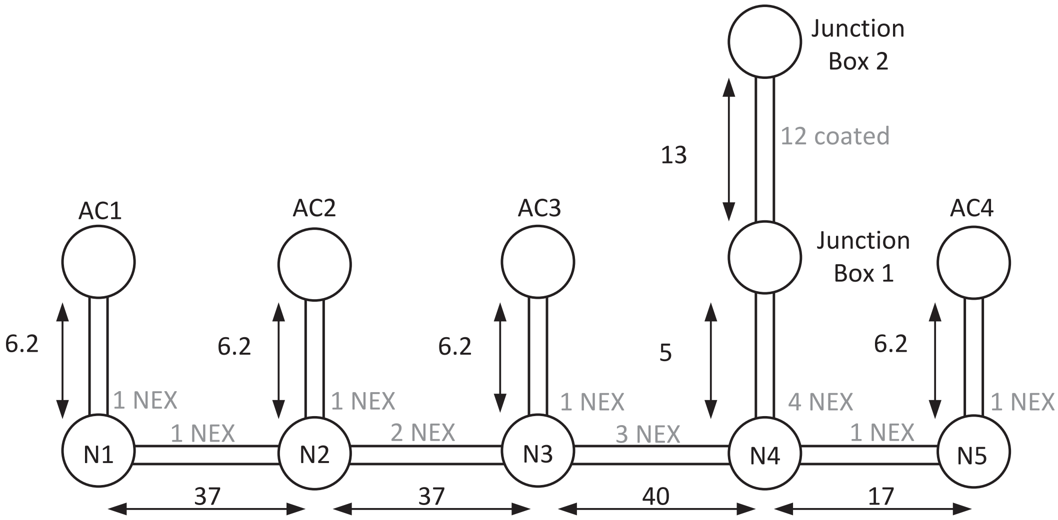

Fig. 6.12 Topology of the test raceway. Distances are in cm and not to scale.

6.3.4 NEXANS cable cross-section

Fig. 6.13 shows the cross section of the NEXANS TT 3 x 1.5 mm^2 cable. According to the manufacturer's datasheet, the wires are made up of copper, the insulation polymer is PVC, and the inner and outer coatings are also made in PVC. The cable diameter is 7.2 mm. Each bare copper wire has a diameter of 1.4 mm and a 0.5 mm PVC coating.

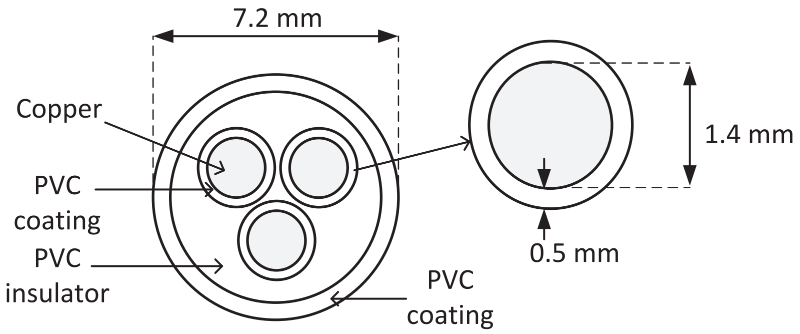

Fig. 6.13 NEXANS cable cross-section.

6.3.5 Raceway simulation model

The fact that the layout of the cables is not uniform inside real buildings (see e.g. Fig. 6.3) requires an approximate representation of the harness cross-sections in the MTL model. The exact reproduction of the real cabling scenario with the numerical tool would require prohibitive efforts since the relative position of each wire among the bundles, and the accurate dielectric parameters of the PVC are unknown.

In a first attempt, the raceway was modeled by using uniform TLs with segments having a fixed cross section along the cable path. The following assumptions were made in the creation of the simulation models with fixed cross sections:

- Since the bottom cable bundles were not running exactly above the ground plane, the effective height of all the cable bundles was set to 35mm with allowed variations in the mm range. The distances were obtained from measurements made to the cables arriving to nodes N1 to N5.
- All the vertical cables were modeled as horizontal straight cables at the same height as the other cables (35 mm).
- The cables inside the junction box were modeled as two tubes containing 4 horizontal NEXANS cables and 12 horizontal coated wires positioned at the same height as the other cables (35 mm)
- The bare wires conductivity was set to copper's conductivity ($\sigma = 5.8 \times 10^7$ S/m)
- After running several tests, the relative dielectric permittivity of the PVC was set to 6 with a loss angle tangent of 0.02.

For filling up the tubes of the topology, five different fixed cross sections were created as schematically shown in Fig. 6.14. The separation distances among the NEXANS cables were also chosen based on measurements made inside the raceway.

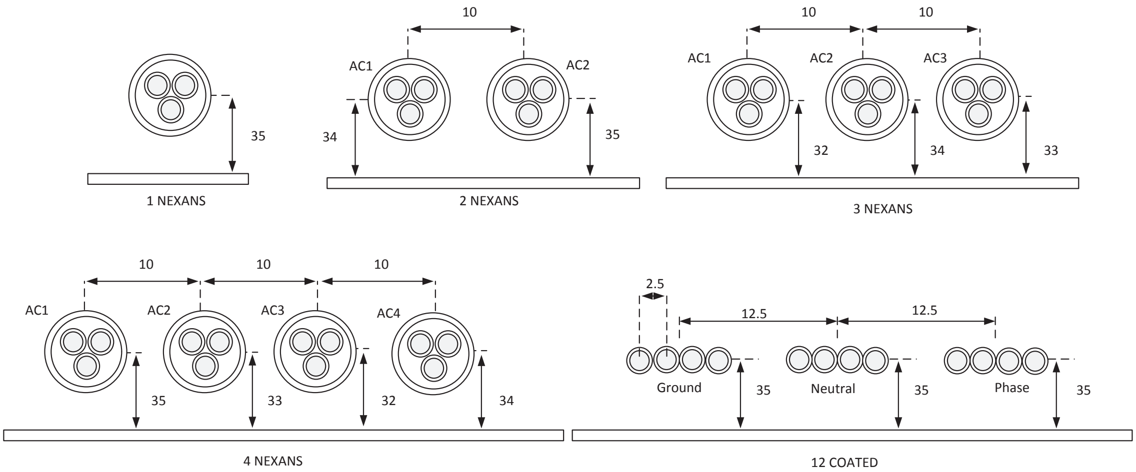

Fig. 6.14 Schematic diagram of the cross-sections. Distances are in mm and not to scale.

In order to better model the propagation along the cables, a second model containing random cross-sections was generated so that the unknown position of all wires was taken into account. It has been shown that by introducing random cross-sections along the cabling, the propagation losses due to the multiple mismatch in the cable paths could be effectively reproduced [109]. The random cross-sections in CST were created by laying the NEXANS cables around a central axis located at the average height of 35mm. Only the same fixed cross-section was used in the tube containing the 12 coated wires.

In order to reproduce the measurements, the simulation setup was chosen as schematically described in Fig. 6.15. A voltage source V_{in} in series with a 50 Ω resistor was connected between the Phase and Neutral wires of the power socket AC1. The Ground wire of AC1 was also connected to the Neutral through a 20nH inductor representing the piece of wire connecting the Ground and Neutral pins of the adapters (see Fig. 6.5). A similar configuration of wires was used to terminate the Phase and Neutral wires at the output socket (AC4 in the case of Fig. 6.15) with a 50Ω resistor.

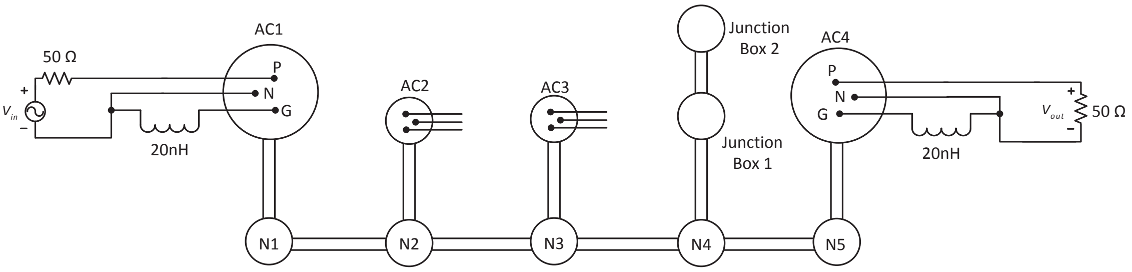

Fig. 6.15 Schematic diagram of the simulation setup of the raceway transfer functions.

The voltage transfer functions were calculated by taking the ratio of the incident voltage in AC1 and the received voltage in the socket under test:

$$H_v = \frac{V_{out}}{V_{in}^{+}} = 2\frac{V_{out}}{V_{in}}, \tag{6.1}$$

where V_{in}^{+} is the incident voltage, V_{in} is the source voltage, and V_{out} is the output voltage measured over the 50Ω resistor (see Fig. 6.15).

For calculating the time-domain response, the above calculated transfer functions were multiplied by the FFT spectrum of the incident voltage that was previously measured by directly connecting the voltage pulse generator to the oscilloscope. Afterwards, a classical IFFT procedure was used to obtain the output waveforms of the sockets.

6.4 Simulation results and experimental validation

6.4.1 Frequency-domain results

In what follows, the transfer functions obtained with the fixed and random cross-section models of the raceway are compared to the measurements obtained with the VNA. The measurement results are plotted with a dashed-black line. The results obtained with the fixed cross sections model are plotted with red lines and those obtained with the random cross section model are plotted with blue lines.

The transfer functions between AC1 and AC2, AC3 and AC4 are plotted in Fig. 6.16, Fig. 6.17, and Fig. 6.18, respectively. Simulations are in fair agreement with the experimental data and reproduce the overall characteristics of the measured transfer functions. There is a better agreement between the curves at low frequencies, even though the predicted resonance frequencies do not always match with the observed ones. This is presumably due to the uncertainty of the cable lengths and dielectric parameters, or the presence of parasitic capacitances at the level of the junction box. Also, the presence of a highly nonuniform cabling in the junction box of the raceway makes it difficult to perform a correct modeling with approximate cross sections.

It can also be noticed that the use of random cross sections in the model provides responses that, in general, are not radically different from those obtained with fixed cross sections. This is certainly due to the fact that the dielectric parameters and the average height above the ground plane were not significantly modified from one simulation to another. In order to better address the sensitivity of the results to each of the model parameters, more elaborate statistical analysis is required, which is beyond the scope of this work. It has been recently suggested [66, 67] that the statistical analysis of the TL predictions can be significantly improved using the extreme value theory, especially when security and safety are under concern.

It has been shown in Chapter 5 that the accuracy of the model in calculating the actual waveform of the disturbance depends on the bandratio of the injected signal. The responses to impulse signals having a large bandratio are generally well reproduced provided the general good accuracy of the TL theory at low frequencies. On the other hand, the TL-predicted response to signals exhibiting a low bandratio is generally less accurate. The accuracy of the method in the prediction of the time domain response of the raceway due to a hyperband injection will be discussed in the following section.

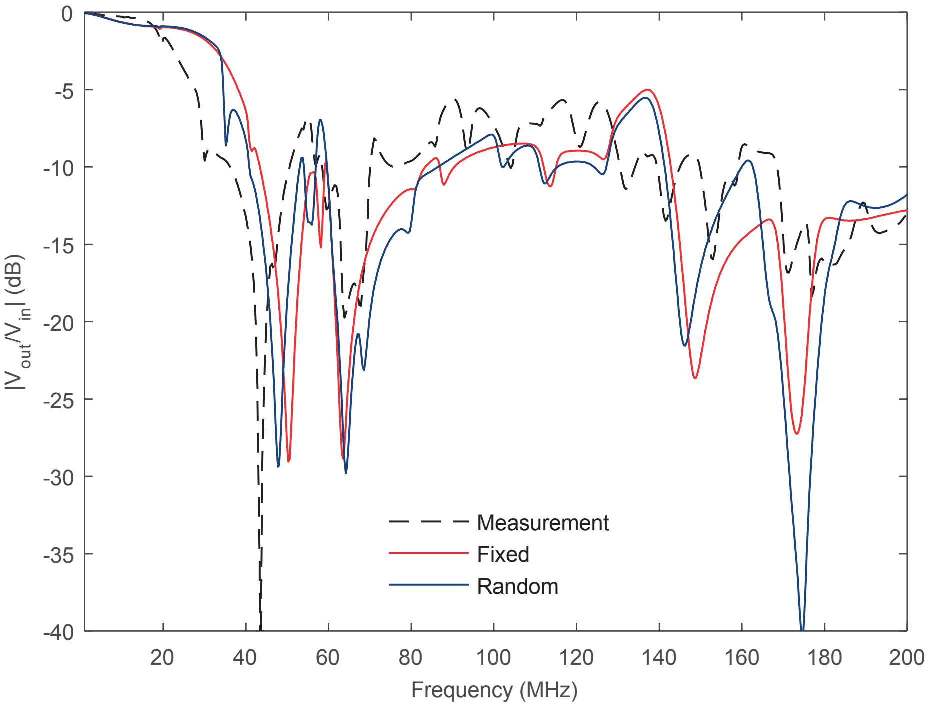

Fig. 6.16 Comparison of the simulation and measurement results for the transfer function between AC1 and AC2.

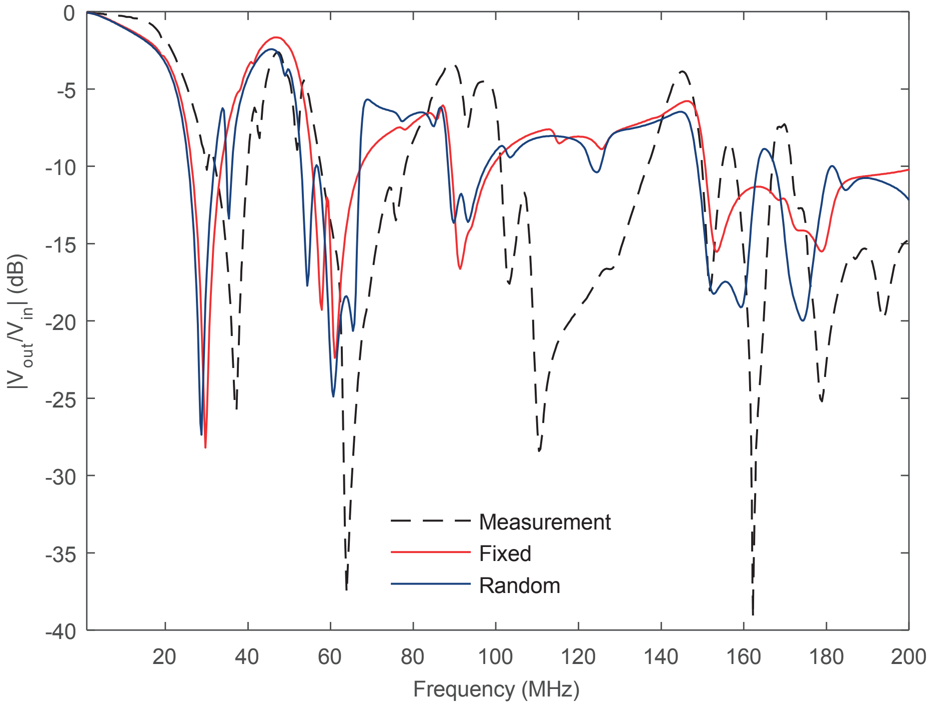

Fig. 6.17 Comparison of the simulation and measurement results for the transfer function between AC1 and AC3.

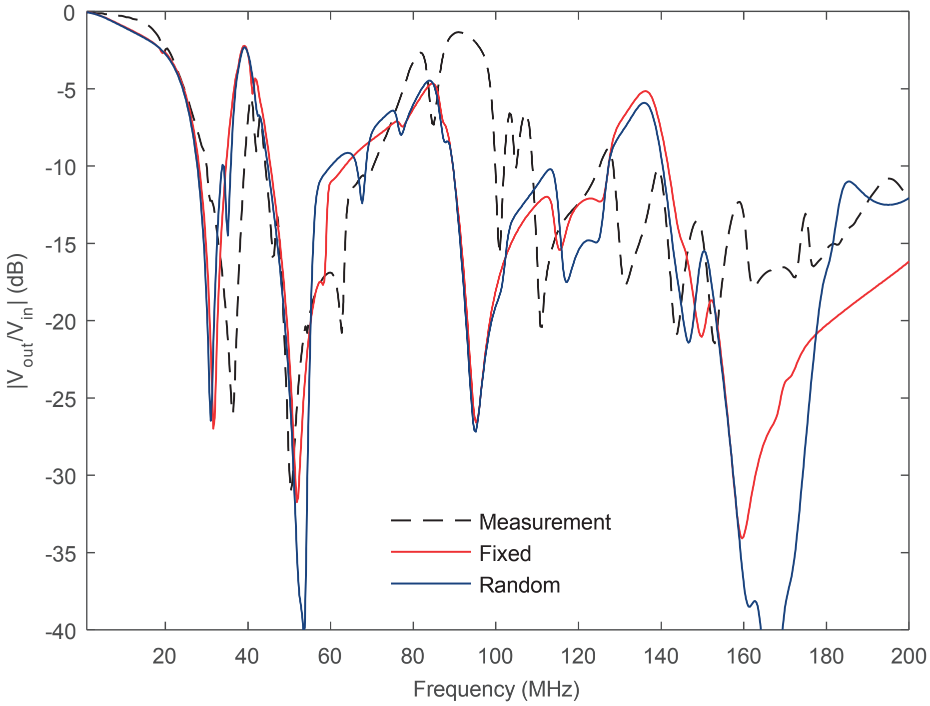

Fig. 6.18 Comparison of the simulation and measurement results for the transfer function between AC1 and AC4.

6.4.2 Time-domain results

In what follows, the impulse responses obtained by convoluting the injected waveform spectra with the transfer functions obtained with the random cross section model are compared with measurement results. The injected signals in AC1 are plotted with a dashed-black line. The outputs of the power socket under study are plotted with red lines. The simulation results are plotted with blue lines.

The impulse response between AC1 and AC2, AC3 and AC4 are plotted in Fig. 6.19, Fig. 6.20, and Fig. 6.21, respectively. In general, it can be seen that simulation results are in very good agreement with the measured results. In particular, the correct delay between the input and the output waveforms shows that the permittivity of the insulators was correctly chosen. Also, the late time response of the model is in good agreement with the measurement results. The small discrepancies found in the early times of the response of Fig. 6.20 and Fig. 6.21 might be attributed to the presence of a highly non-uniform cabling in the junction box of the raceway that are modeled with approximate cross-sections in both models.

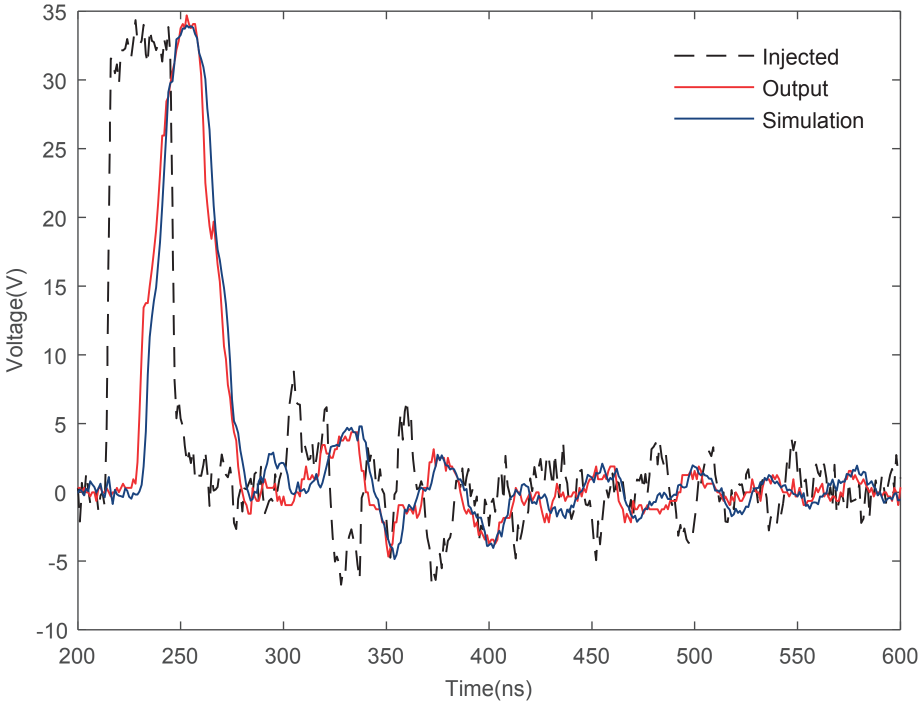

Fig. 6.19 Comparison of the simulation and measurement results for the impulse response between AC1 and AC2.

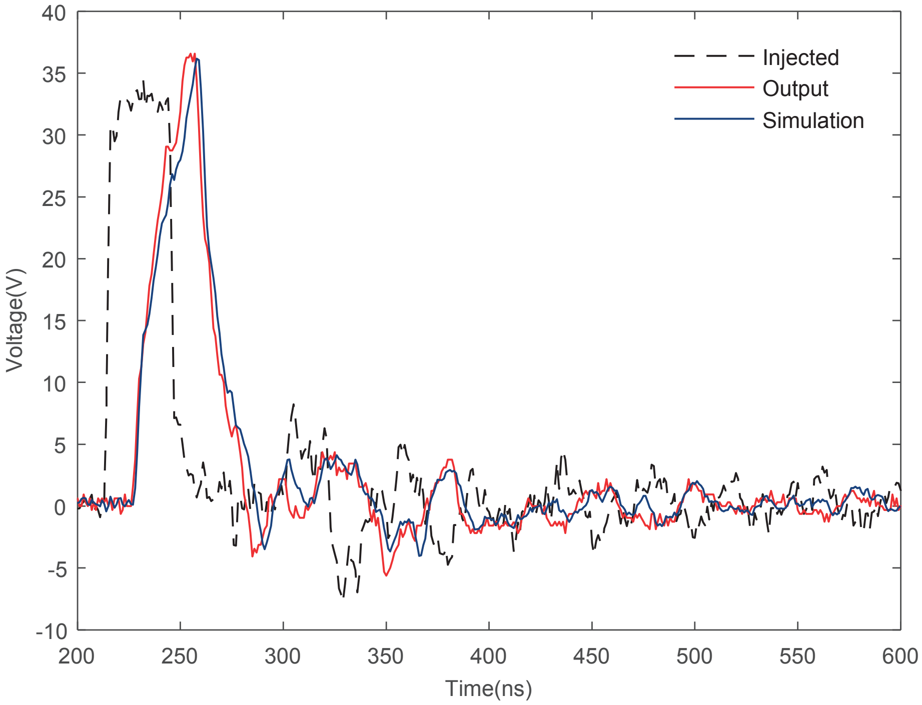

Fig. 6.20 Comparison of the simulation and measurement results for the impulse response between AC1 and AC3.

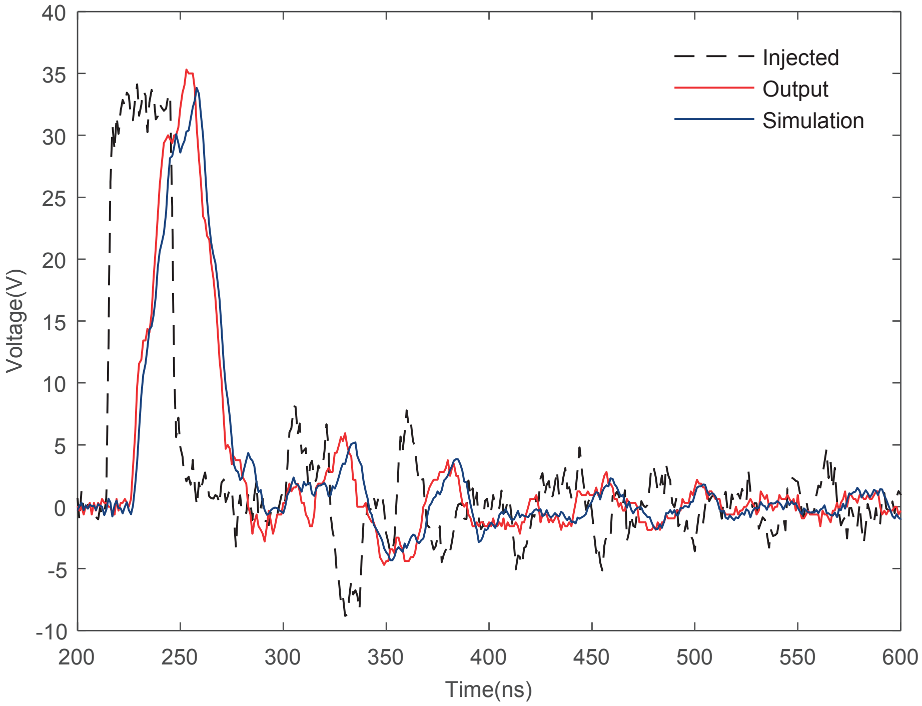

Fig. 6.21 Comparison of the simulation and measurement results for the impulse response between AC1 and AC4.

6.5 Conclusions

In this chapter, we presented a comparison of experimental and simulation results obtained with TL theory on the propagation of high frequency disturbances along the LVP cabling of a commercial raceway. The frequency spectrum of the considered disturbances was representative of IEMI sources. An accurate modeling of the propagation along real cabling scenarios requires a very high degree of knowledge of the simulated topology. Frequently, several input parameters of the models are not precisely known and the related uncertainties may impact the accuracy of results.

It was shown that simulation results are in good agreement with the experimental data and reproduce the overall characteristics of the measured transfer functions. The predicted resonance frequencies of the transfer functions did not always match the experimental observations. This was presumably due to the uncertainty of the cable lengths and dielectric parameters of the PVC. Also, the presence of a highly non-uniform cabling in the junction box of the raceway was difficult to model with approximate cross-sections. However, from the comparison with time domain waveforms, it was concluded that the high frequency discrepancies did not result in significant errors in the evaluation of the impulse responses.

7 Numerical Modeling of the Overall Transfer Impedance of Shielded Cables

7.1 Introduction

The application of TL for calculating the propagation of high frequency fields along unshielded cables like those of the LVP lines was previously presented in Chapter 6. This chapter is devoted to the study of the application and validation of TL theory for the case of shielded harnesses. This Chapter is heavily drawn from [83, 84]. Notice that the experiments performed in [84] were performed with spacecraft cables. However, the conclusions of this work are also applicable to the case of commercial cables in CIs given that the cable cross sections are not very different and that the frequency ranges under study are also within those of IEMI.

The TL theory has been successfully applied to analyze internal and external coupling in shielded cables. Complex harnesses typically include a set of internal cable arrangements that are individually shielded using different technologies (e.g. braided shield or a served wire screens). Depending on the application, the cable harness may also come with overshields that are used to further protect the cables from interferences. The cable arrangements are terminated in multi-pin connectors covered with a backshell that requires the separation of the signal conductors from the shielding conductors, thus reducing the shielding performance if not properly implemented.

The analysis methods of shielded cables with the aid of TL theory were firstly introduced by Vance in [8]. Significant advances were achieved in the subsequent years improving the existing knowledge about braided shields, pigtail cable terminations, and shield discontinuities [1, 2, 9]. Experimental results on the transfer impedance of selected connectors, backshell, and cable shielding mechanisms have enabled a better understanding and generation of guidelines in the selection of appropriate schemes for protecting the critical harnesses [10-13].

In this chapter, we present a review of the use of TL theory to model the overall transfer impedance of shielded cable assemblies. The modeling procedures of cables, shields, and connectors are discussed, and solutions to some practical issues are proposed. The use of the modeling techniques is illustrated by considering a realistic cable assembly for which a comparison of measurement results and simulations are provided.

This chapter is organized as follows. The modeling techniques for cables, shields and connectors are reviewed in Section 7.2. The studied cable assembly and its experimental characterization are presented in Section 7.3. The modeling procedure and the model parameters that were used to generate an equivalent TL structure are explained in Section 7.4. Comparisons between the results obtained with the TL model and measurements are presented in Section 7.5. Finally, concluding remarks are presented in Section 7.6.

7.2 Modeling techniques

In this section, we present an overview of the available techniques for modeling the different components present in a cable harness by using TL theory, taking into account internal conductors, shields, pigtails if necessary, and connectors.

7.2.1 Modeling of the internal conductors

The propagation of currents and voltages along cable bundles can be accurately predicted with the use of TL [46, 47]. Notice that the application of TL theory for the propagation analysis is limited by the validity of the transmission line (TL) theory assumptions (see e.g., [46]). A detailed overview of the methods for obtaining the p.u.l. parameters of multi-conductor geometries can be found in e.g. [88]. As the cable bundles become complex, the use of a numerical 2D tool for the evaluation of the p.u.l. parameters becomes necessary due in particular to inhomogeneities introduced by the presence of lossy dielectric coatings.

7.2.2 Modeling of the shielding screens

The so-called transfer impedance and transfer admittance of the shields [46, 59] are used to model the diffusion of electromagnetic fields through the cable screens and the coupling through its apertures. Many authors have contributed to the analytical calculation of the transfer impedance and transfer admittance of solid and braided shields (see a comprehensive summary in [45, 46]). Schelkunoff derived an analytical expression for the transfer impedance of a solid tubular shield in [184]. Vance [185], Demoulin [45], and Kley [186] presented analytical expressions for the transfer impedance of braided shields that have shown to be accurate up to frequencies of some hundreds of MHz.

Even though analytical expressions are usually preferred due to their simplicity and the possibility of doing parametric studies, the transfer impedance of cable screens can also be measured when little manufacturing information is available [187]. Notice that experimental studies above several hundreds of MHz are rarely available due to the constraints imposed by the propagation phenomena inside the cables that lead to the creation of standing wave patterns. Alternatively, 3D modeling techniques can be used to estimate the transfer impedance but an increased computational cost is required [188].

7.2.3 Modeling of braided shields

A schematic diagram illustrating a typical cable containing two braided-wire shields is shown in Fig. 7.1 [59].

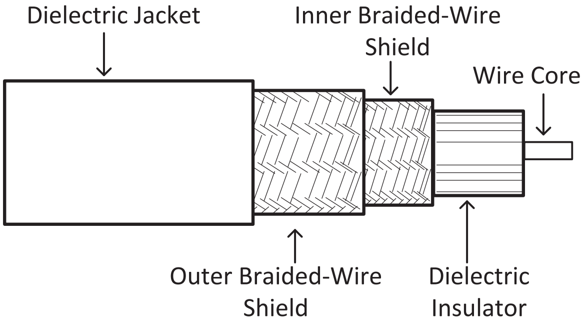

Fig. 7.1 Braided shield wire. Adapted from [59].

The left diagram of Fig. 7.2 shows an unwrapped view of a braided shield of internal radius *a*, and the right diagram shows an enlargement of the weave pattern where additional details of the apertures and the weaving filaments of the shield can be seen.

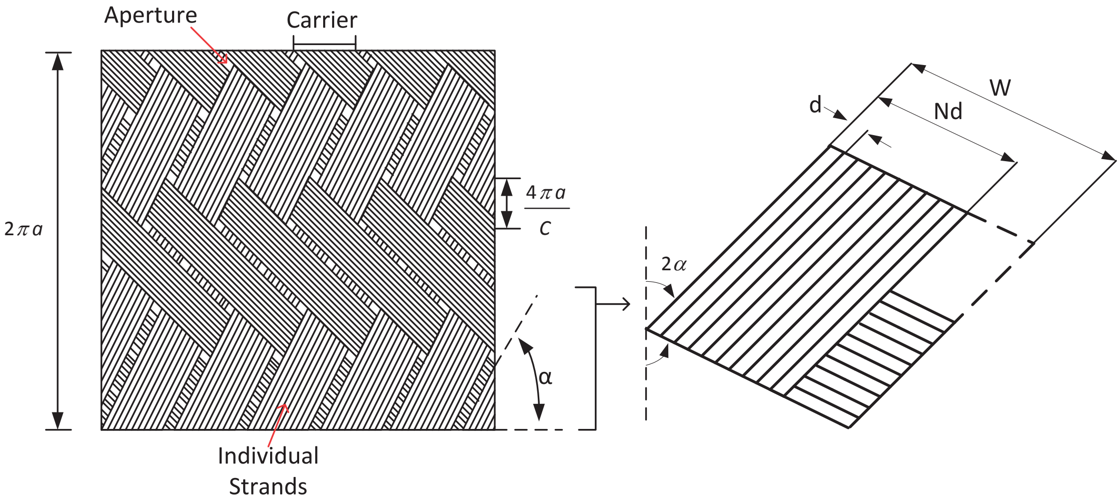

Fig. 7.2 Left: Unwrapped view of a typical braided shield; image adapted from [46]. Right: Enlargement of the weave pattern. Adapted from [59].

The braided shields can be characterized in terms of the inner radius of the shield a, the number of carriers C, the number of filaments N, the filament diameter d, the conductivity of the shield σ, and the weave angle of the shield α. The fill factor F, the coverage factor K and the number of apertures per-unit-length n can be calculated as [46, 59, 189]:

$$\begin{aligned} F &= \frac{NdC}{4\pi a\cos(\alpha)}, \\ K &= 2F - F^2, \\ n &= \frac{C^2\tan(\alpha)}{4\pi\alpha}. \end{aligned} \tag{7.1}$$

The transfer impedance of the braid can be calculated, for example, with the optimized single braided shield model proposed by Kley in [186]. The results provided by this model have been found to be in very good agreement with the performed measurements in this work [83].

On the other hand, the calculation of transfer admittance requires the specification of the p.u.l. capacitance between the braid and the ground return path. Vance has discussed the calculation of the so-called transfer capacitance in [59, 185], but generally this parameter can only be evaluated once the cable harness position has been specified. Thus, this parameter is generally neglected in the simulations. This is the reason why this work focuses in the modeling of transfer impedance of braided shields.

7.2.4 Transfer impedance of single braided shields

7.2.4.1 Vance's model

Vance proposed a model to calculate the transfer impedance of single braided shields that accounts for the effects of diffusion through the metallic shield and magnetic field penetration through its apertures [59]:

$$Z'_t = Z'_d + j\omega L'_a. \tag{7.2}$$

The diffusion term Z'_d is calculated by assuming that the braided-wire shield behaves as a solid tube having a thickness equal to one filament diameter and a modified DC resistance R_o' that accounts for the aperture density in the cross section. The diffusion term is given by:

$$Z'_d = \frac{4}{\pi d^2 NC\sigma\cos(\alpha)}\frac{\gamma d}{\sinh(\gamma d)} = R_0'\frac{\gamma d}{\sinh(\gamma d)}, \tag{7.3}$$

where γ is the complex propagation constant through the sheath approximated by:

$$\gamma \approx (1+j)\sqrt{\frac{\omega\mu\sigma}{2}}. \tag{7.4}$$

The mutual inductance term L'_a is based on the assumption that the braided shield behaves as a thin walled solid tube with elliptical holes of the same density and major and minor axes as the rhombic apertures in the braided-wire shield [59]. This term is given by:

$$\begin{aligned} L'_a &= \frac{\pi\mu_0}{6C}(1-K)^{3/2}\frac{e^2}{E(e)-(1-e^2)K(e)} \quad \text{if} \quad \alpha < 45°, \\ L'_a &= \frac{\pi\mu_0}{6C}(1-K)^{3/2}\frac{e^2/\sqrt{1-e^2}}{K(e)-E(e)} \quad \text{if} \quad \alpha > 45°. \end{aligned} \tag{7.5}$$

The terms $K(e)$ and $E(e)$ in (7.5) denote respectively the complete elliptic integrals of the first and second kind. The eccentricity e of the ellipse is given by:

$$\begin{aligned} e &= \sqrt{1-\tan^2(\alpha)} \quad \text{if} \quad \alpha < 45°, \\ e &= \sqrt{1-\cot^2(\alpha)} \quad \text{if} \quad \alpha > 45°. \end{aligned} \tag{7.6}$$

7.2.4.2 Kley's model

In order to account for the so-called porpoising mechanism (the induction phenomenon due to overlapping of the carriers of the shield), Tyni (see chapter 10 in [46]) and Démoulin (see chapter 6 in [45]) have derived alternative expressions for the transfer impedance. Note that the porpoising effect is more important when the optical coverage is high, because less penetration occurs [46].

Kley proposed an improvement of the transfer impedance model of Tyni by tuning some of the quantities based on several measured cable data up to 200 MHz. In his model, he proposed to calculate the transfer impedance as [186]:

$$Z'_t = Z'_d + j\omega L'_t + (1+j)\omega L'_s . \tag{7.7}$$

The diffusion term Z'_d in Kley´s model is calculated as:

$$Z'_d = R_0'\frac{\gamma d_R}{\sinh(\gamma d_R)}, \tag{7.8}$$

where $d_R = 0.67d / \sqrt{\cos(\alpha)}$.

The inductances L'_t and L'_s are the penetration inductance and the eddy currents inductance, respectively. The penetration inductance L'_t is expressed as the sum of the aperture inductance M'_L and the porpoising inductance M'_G [186]:

$$L'_t = M'_L + M'_G, \tag{7.9}$$

where

$$\begin{aligned} M'_L &= 0.875\frac{\pi\mu_0}{6C}(1-F)^3 e^{-\tau_H}\frac{e^2}{E(e)-(1-e^2)K(e)} \quad \text{if} \quad \alpha < 45°, \\ M'_L &= 0.875\frac{\pi\mu_0}{6C}(1-F)^3 e^{-\tau_H}\frac{e^2/\sqrt{1-e^2}}{K(e)-E(e)} \text{if} \quad \alpha > 45°, \end{aligned} \tag{7.10}$$

and

$$M'_G = -\mu_0\frac{0.11d}{2\pi D_m F_0}\cos(2k_1\alpha). \tag{7.11}$$

The fill factor in Kley's model is defined by using an average shield radius a_m as follows:

$$F = \frac{NCd}{4\pi a_m \cos(\alpha)}, \; a_m = a + 1.25d. \tag{7.12}$$

The magnetic field attenuation factor of the chimney effect in (7.10) is defined as:

$$\tau_H = 9.6F(\frac{K^2 d}{2a_m})^{\frac{1}{3}}. \tag{7.13}$$

The minimal filling factor in (7.11) is:

$$F_0 = F\cos(\alpha), \tag{7.14}$$

and

$$k_1 = \frac{\pi}{4}(\frac{2}{3}F_0 + \frac{\pi}{10})^{-1}. \tag{7.15}$$

The $\omega L'_s$ term in (7.7)was introduced by Démoulin [46] in order to account for the eddy currents in the apertures' walls due to the magnetic field that penetrates the shield. Kley introduced other eddy currents circulating between the inner and outer carriers of the braid that induce a quadrature component $j\omega L'_s$ [46, 186]. If both terms are taken into account, the $(1+j)\omega L'_s$ term in (7.7) is obtained [46].

The eddy currents inductive term can be calculated as:

$$L'_s = \frac{1}{\pi\sigma\delta_s}\left(\frac{1}{D_L}+\frac{1}{D_G}\right), \tag{7.16}$$

with

$$\begin{aligned} D_L^{-1} &= 5\pi F_0^2 \frac{\cos(\alpha)}{a_m}(1-F)e^{-\tau_E}, \\ D_G^{-1} &= -\frac{3.3}{4\pi a_m F_0}\cos(2k_2\alpha), \end{aligned} \tag{7.17}$$

and

$$\tau_E = \frac{\tau_H}{0.8};\; k_2 = \frac{\pi}{4}\left(\frac{2}{3}F_0 + \frac{3}{8}\right)^{-1}. \tag{7.18}$$

7.2.5 Transfer impedance of two-layer braided shields

7.2.5.1 Vance's model

The analysis of two-layer braided shields was made by Vance in [185] by using the per-unit length decomposition shown in Fig. 7.3. He assumed that the external and internal braids are in electrical contact at electrically short spacing along the cable.

The coupling of an external field source would induce the flow of current I_1 along the outer shield external surface that will couple to the outer shield internal surface through its transfer impedance Z'_{t1} and will induce the flow of the internal current I_2. The current I_2 circulates through a mesh composed of the per-unit length series impedance of the outer shield and internal shield Z'_{s1} and Z'_{s2}, respectively, and the per-unit length inductance of the coaxial transmission line formed by the outer shield inner surface and the inner shield outer surface L'_{12}. Finally, the flow of the internal current I_2 will couple through the internal shield transfer impedance Z'_{t2} and will induce the voltage drop E_2 in the inner shield surface.

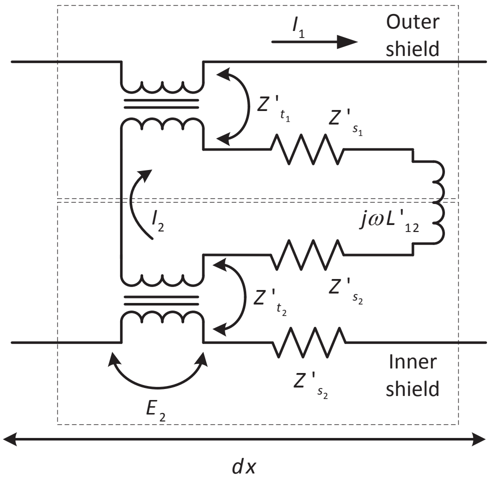

Fig. 7.3 Per-unit length model for analyzing double braid shields. Adapted from [185].

The overall transfer impedance of the double braid line can be calculated from the previous analysis as:

$$Z_T = \frac{E_2}{I_1} = \frac{Z'_{t_1} Z'_{t_2}}{Z'_{s_1} + Z'_{s_2} + j\omega L'_{12}}. \tag{7.19}$$

Vance proposed to calculate the overall transfer impedance by using his model for single braids (see Section 7.2.4.1), resulting in:

$$Z'_T = \frac{R'_{01} R'_{02} \left(\frac{\gamma_1 d_1}{\sinh(\gamma_1 d_1)} + j\omega \frac{L'_{a1}}{R'_{01}} \right) \left(\frac{\gamma_2 d_2}{\sinh(\gamma_2 d_2)} + j\omega \frac{L'_{a2}}{R'_{02}} \right)}{R'_{01} \gamma_1 d_1 \coth(\gamma_1 d_1) + R'_{02} \gamma_2 d_2 \coth(\gamma_2 d_2) + j\omega L'_{12}}, \tag{7.20}$$
$$\text{if } \gamma_s l_s << 1,$$

where subscript 1 applies to the inner shield and 2 to the outer shield, l_s is the spacing between shield-to-shield connections, and γ_s is the complex propagation constant of the shield-to-shield transmission line.

The per-unit-length inductance between the shields can be evaluated using

$$L'_{12} = \frac{\mu_0}{2\pi} \ln(\frac{a_2}{b_1}), \tag{7.21}$$

where a_2 is the inner radius of the outer shield and b_1 is the outer radius of the inner shield.

7.2.5.2 Proposed model

We propose [83] to use (7.19) for estimating the equivalent transfer impedance of a two-layer braided shield and using the optimized single-layer model proposed by Kley for calculating the transfer impedance of the inner and outer braided shields (see Section 7.2.4.2). This model can be referred to as the Vance-Kley model since it uses Vance's approach to estimate the transfer impedance of a double-shield cable, but takes advantage of Kley's model to predict the transfer impedance of each single braid. Putting both models together, the overall transfer impedance reads:

$$Z'_T = \frac{(Z'_{d_1} + j\omega L'_{t_1} + (1+j)\omega L'_{s_1})(Z'_{d_2} + j\omega L'_{t_2} + (1+j)\omega L'_{s_2})}{R'_{01}\gamma_1 d_1 \coth(\gamma_1 d_1) + R'_{02}\gamma_2 d_2 \coth(\gamma_2 d_2) + j\omega L'_{12}}, \quad \text{if } \gamma_s l_s << 1. \tag{7.22}$$

7.2.5.3 Experimental validation

The proposed model was tested by comparing the numerical predictions with experimental results of the transfer impedance of two commercial samples made of silver plated aluminum monofilament wires.

The measurements were performed between 10 kHz and 70 MHz with a triaxial setup (see Fig. 7.4) [187]. Each braided shield was mounted on a calibrated mandrel containing a metallic inner conductor. The resulting coaxial assembly was inserted in a tubular solid tube to conform the triaxial structure where the braided shield and the solid tube conform the outer coaxial. The external and internal coaxial structures were terminated in their characteristic impedances in order to avoid standing wave patterns. An injection probe was used to generate a current flow along the braid and a measurement probe was used to measure the induced current. A spectrum analyzer was used to measure the induced voltage between the innermost conductor and the braid, and therefore, estimate the transfer impedance.

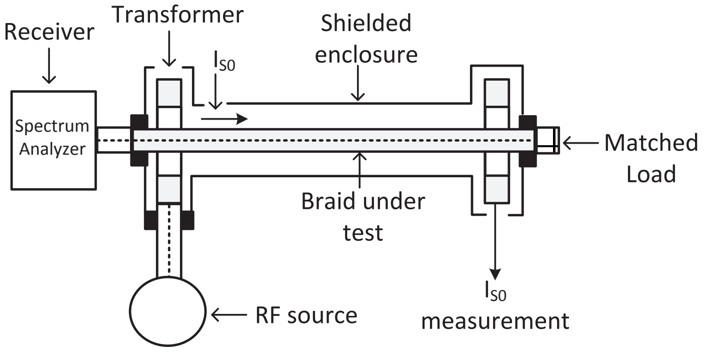

Fig. 7.4 Triaxial setup for measuring transfer impedance of cables by using magnetic current injection with a current transformer. Image adapted from [187].

Regarding the simulation setup, the number of filaments, number of carriers, the filament diameter, and the weave angle of the external and internal braids were included in the datasheets of the samples manufacturer. On the other hand, only the outer diameter of the external braid was available. One of the most difficult-to-measure parameters was the inner and outer diameters of the independent braids, and their separation distance. Also, the conductivity of metal alloys was not provided in the datasheets.

In order to obtain the parameters of the tested braids, the following procedure was used: (i) the number of filaments, number of carriers, filament diameter, and weave angle were obtained from the datasheet nominal values. (ii) The initial conductivity was set to the approximated bulk conductivity of Al: σ = 35 MS/m. The conductivity was corrected to match the DC transfer impedance obtained by measurements. (iii) The external radius of the outer braid was assumed as the nominal ±2mm, and the average thickness of the braids was assumed to be 1.25 times the filament diameter as suggested in [186]. (iv) The separation distance between braids was varied between 50-200µm. (v) The separation distance and the external radius of the outer braid were swept in steps of 10 µm, until a good correspondence was obtained with the model at high frequencies.

In what follows, the results of both models obtained with the parameters optimized for each of the models will be presented. The optimized parameters provide a minimum mean square error between the measurement and the model.

The first sample (sample A), was made of two braids having the same parameters: N=11, C=40 and d=0.2 mm. The weave angles of the inner braid and outer braid were α_1=30°and α_2=40°, respectively. The nominal external diameter of the two-layer braided shield was 22mm and the sample length was 1m.

A summary of the optimized parameters of sample A according to each model is reported in Tab. 7.1. The percentage variations of the conductivity and the external radius with respect to the nominal values are indicated in the last column.

Fig. 7.5 shows a comparison between the results obtained from (i) measurements, (ii) Vance model, and (iii) proposed Vance-Kley model, for sample A. The results of the Vance model are in good agreement with the measurements from about DC to 250 kHz, and beyond 10 MHz or so. On the other hand, the proposed Vance-Kley model shows excellent agreement with the measured data in the whole frequency range.

Tab. 7.1 Optimized Parameters of Sample A

Parameter	Variable	Value	Units	D%
Conductivity	σ	35.2	[MS/m]	0.5
Ext. diameter (Vance)	$2a_m$	20.7	[mm]	-6.1
Sep. distance (Vance)		180	[µm]	
Ext. diameter (Vance-Kley)	$2a_m$	19.9	[mm]	-9.7
Sep. distance (Vance-Kley)		160	[µm]	

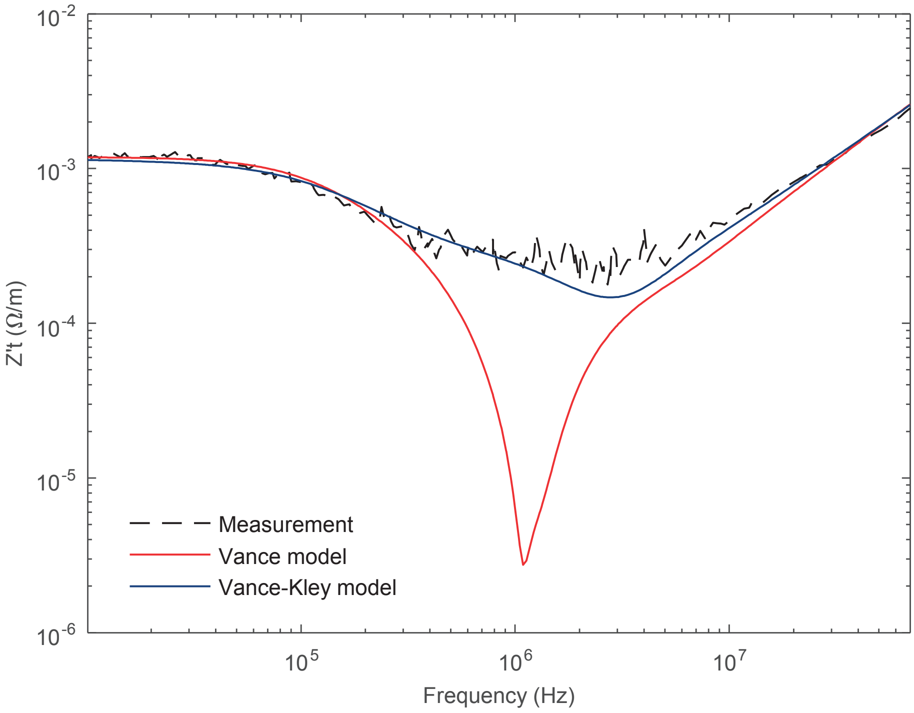

Fig. 7.5 Transfer impedance of Sample A: measurement and simulation results.

The second sample (sample B), was made of two braids having the same parameters: N=14, C=24, and d=0.12 mm. The weave angles of the inner braid and outer braid were α_1=27.5°and α_2=28.7°, respectively. The nominal external diameter of the two-layer braided shield was 10mm and the sample length was 1m.

A summary of the optimized parameters of sample B according to each model is reported in Tab. 7.2.

Fig. 7.6 shows a comparison between the results obtained from (i) measurements, (ii) Vance model, and (iii) Vance-Kley model, for sample B. The results of the Vance model are in good agreement with the measurements from about DC to 800 kHz, and beyond 25MHz, whereas the proposed Vance-Kley model shows excellent agreement in the whole frequency range, as it was observed for Sample A.

Tab. 7.2 Optimized Parameters of Sample B

Parameter	Variable	Value	Units	D%
Conductivity	σ	30.3	[MS/m]	-13.5
Ext. diameter (Vance)	$2a_m$	8.9	[mm]	-11.2
Sep. distance (Vance)		150	[µm]	
Ext. diameter (Vance-Kley)	$2a_m$	9.8	[mm]	-1.8
Sep. distance (Vance-Kley)		170	[µm]	

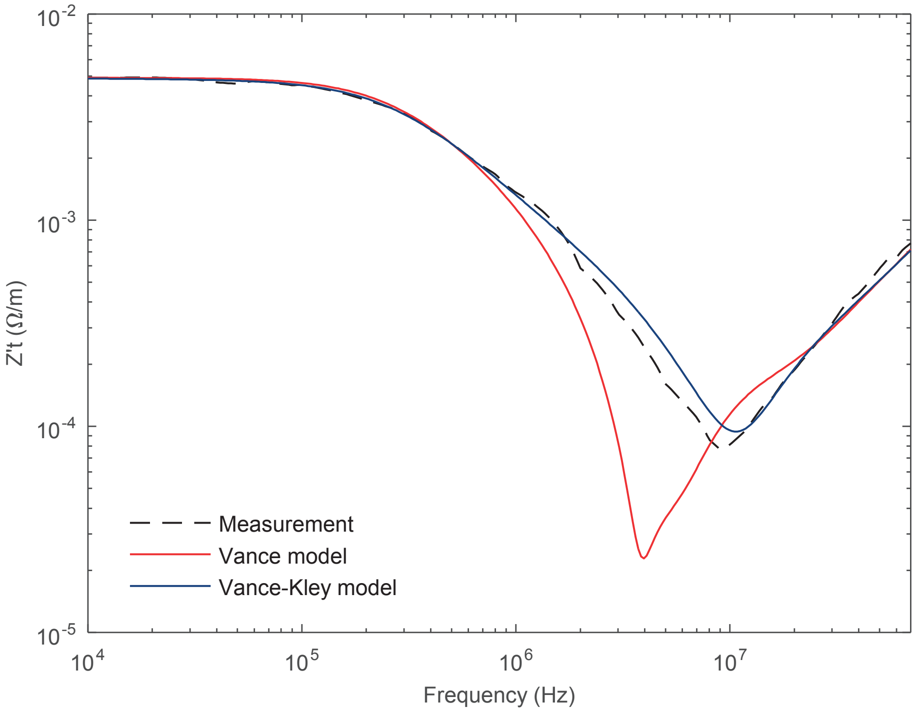

Fig. 7.6 Transfer impedance of Sample B: measurement and simulation results.

7.2.6 Modeling of served wire shields

The term served wire shield refers to a collection of *n* strands that are helically wound around the protected wires. A schematic diagram illustrating the cross-section of a coated pair with a served wire shield is presented in Fig. 7.7. The multiple strands provide with a high optical coverage and also exhibit a low self-inductance, thus working up to relatively high frequencies (some MHz). The term "spiral shield" is also used to refer to the served wire shield.

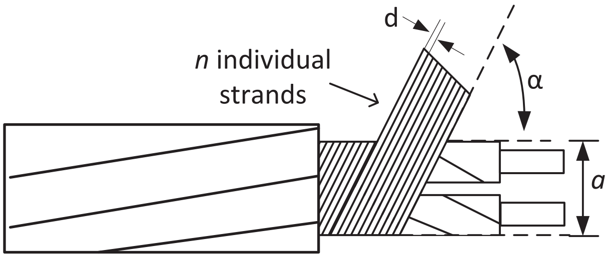

Fig. 7.7 Schematic diagram of the served wire shield.

The served wire shields are specified according to the following parameters [190](See Fig. 7.7): inner radius of the screen *a,* number of strands *n, d*iameter of the strands *d,* conductivity of the strands σ, and the weave angle α.

The calculation of the transfer impedance of the served wire shield has been discussed in a few studies. Tsaliovich [190] derived an approximate formula by considering the decomposition of the total current in the shield in its axial (along the cable) and circular (around the cable) components. According to Tsaliovich, the transfer impedance $Z_{t\alpha}$ of the served wire shield can be estimated as:

$$Z_{t\alpha} = Z_{th} + \left(Z_{sh} + j\omega \frac{\mu_0}{4\pi} \right) \tan^2(\alpha), \tag{7.23}$$

where Z_{th} and Z_{sh} are respectively the transfer and series impedance of a homogeneous tube having conductivity σ, internal diameter *a*, and thickness *d*. These latter can be estimated with the model of Schelkunnof [184].

7.2.7 Modeling of pigtails

A correct layout of cables requires the connection of all the screens to the common current return path (e.g. the metallic backshell of the connectors). The grounding of the shielding screens is generally performed with the use of so-called pigtails that significantly modify the overall immunity responses due to the discontinuities.

Paul presented in [191] a very simple low-frequency model for simulating the presence of pigtails. He used a lumped-parameter solution in which the crosstalk of a shielded cable with pigtail connections is calculated as the superposition of the coupling due to the presence of the shield, and the one due to the two pigtails. As frequency increases, the interaction of the shielded section with the pigtail needs to be considered in the solution. In this case, TL approach may give a more accurate solution since the physical presence of the pigtail wire is included in the MTL matrices. However, notice that a separate section of the unshielded wires has to be added at the ends of the cables.

From a practical point of view, it is very difficult to define the geometry of a pigtail wire since they are generally randomly positioned in the bundles. This gives rise to uncertainties when calculating the MTL impedance and admittance matrices. Therefore, in this study, the pigtails are modeled as lumped inductances of about 1 nH/mm which is a commonly agreed value of the inductance of a piece of wire (see e.g. [139]). The lumped representation of the pigtail is conservative since the mutual inductance between the pigtail and the inner wires are neglected, thus, not providing with capacitive and inductive shielding.

7.2.8 Modeling of the connectors

Connector models should provide with a representation of the resistive and inductive behavior of the conductive backshell, as well as the diffusion of the fields through the connector body, and the penetration through any present aperture.

7.2.8.1 Backshell model

The connector backshells are made up of solid metals or composite materials with no apertures in the cross section (in principle). A good connector from the EMC point of view exhibits 100% optical coverage around the protected wires and it should make a continuous current path to ground when bonded with the cable shields. Thus, connector backshells can be integrated into the TL simulations in the form of a solid shield of a given thickness and an effective conductivity that surrounds the protected wires. The backshell transfer impedance has to be determined through analytical treatment, full wave simulations or experiments.

Typical connectors exhibit circular and rectangular cross-sections. The theoretical expression for the transfer impedance of a solid round tubular shield derived by Schelkunoff [184] can be used as an approximation of the behavior of a rectangular tubular shield with equivalent cross-section.

7.2.8.2 Bonding

The overall shielding quality of the harness is related to the correct bonding of the cable screens to the connector backshell through a low resistance/inductance path and with a good optical coverage (i.e. without leaving any significant aperture). The degradation of the high frequency susceptibility of the harnesses is critically determined by the quality of the connection of the screens to the backshell, and the connection between the backshell to the chassis of the equipment.

The bonding of the backshell to the general chassis of the equipment with screws is included in the simulations by using lumped resistors of some mΩ and inductors of some 10-100 pH.

7.3 Cable assembly under study

7.3.1 Assembly description

The cable assembly under study was composed of a bundle containing 5 AWG26 shielded copper pairs of 950 mm length and terminated in both sides with 37-pins micro-D backshell connectors. Two of the pairs were provided with a braided shield (one for each pair), and 3 pairs were provided with a served wire shield (one for each pair). All the shields were connected to the connector backshell chimney using 20 to 30-mm long pigtails. A picture of the cable assembly is presented in Fig. 7.8. Notice the pigtail connections to the connector backshell with an aluminum wrap around the chimney.

7.3.2 Overall transfer impedance of the cable assembly

In order to evaluate the overall transfer impedance of the assembly, the setup presented in the picture shown in Fig. 7.9 was used. This setup was inspired by the line injection technique for measuring the transfer impedance of braided shields, see e.g. Section 2.4.1.2.2 of [48] or IEC 62153-4-6 [192]. Note that other techniques are available in the literature for the evaluation of the transfer impedance of shielded connector assemblies, e.g. [193-195]. In the used setup, a copper tape was laid above the bundle path in order to create a pseudo micro-strip line that will induce a current flow along all the cable shields. The injection port of a vector network analyzer

(VNA) is connected to the near end of the micro-strip, and a 50 Ω resistor is connected to the far end.

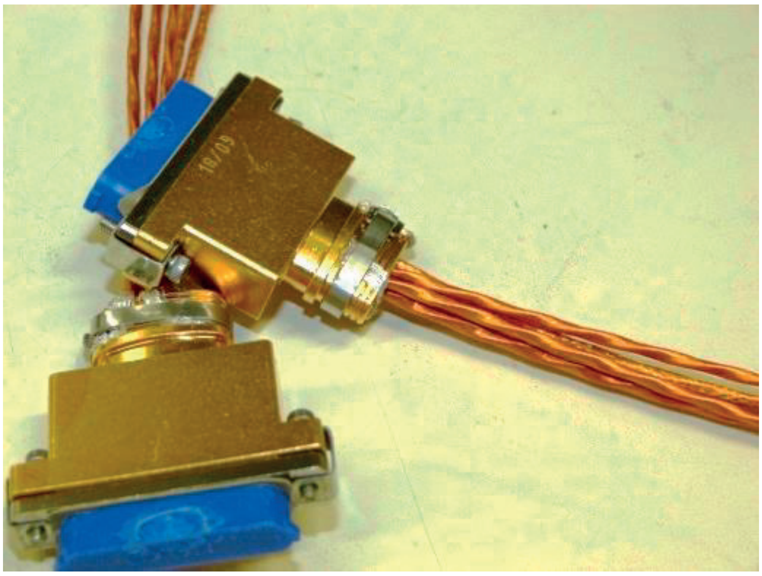

Fig. 7.8 Picture of the cable assembly under study.

A particular wire from the bundle was terminated in 50 Ω at the far end and connected to the measurement port of a VNA at the near end, while the other wires were left floating. Assuming the connector and the shielded pair assembly as a single body, the induced voltage measured by the VNA due to the current injection in the micro-strip provides an indication of the overall transfer impedance of the assembly.

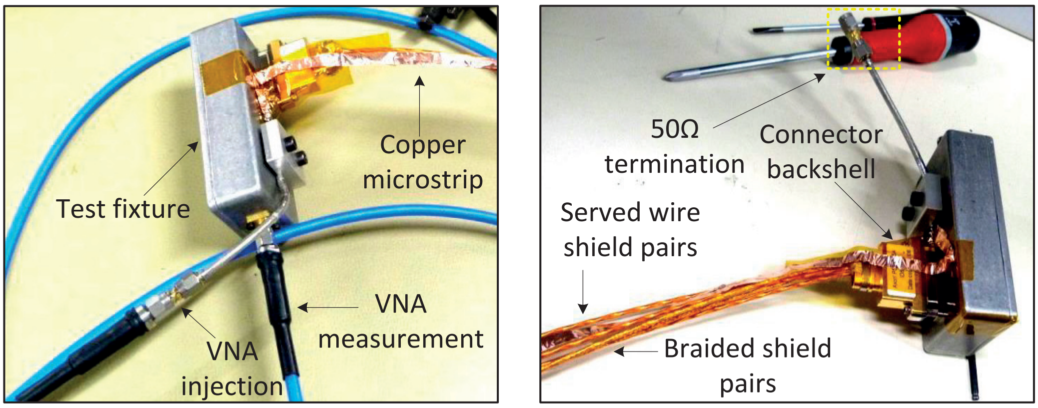

NEAR END **FAR END**

Fig. 7.9 Mictrostrip injection test for measuring the overall shielding performance of the shielded pairs.

In order to assess the influence of the shield type, two different tests were performed. In the first test, the terminated wire was selected from one of the 3 pairs equipped with a served wire shield. In the second test, the terminated wire was selected from one of the 2 pairs with a braided shield. The measurements of the overall transfer impedance for both cases are plotted in Fig. 7.10. Notice that, as expected, a better performance is observed for the pair with the braided shield.

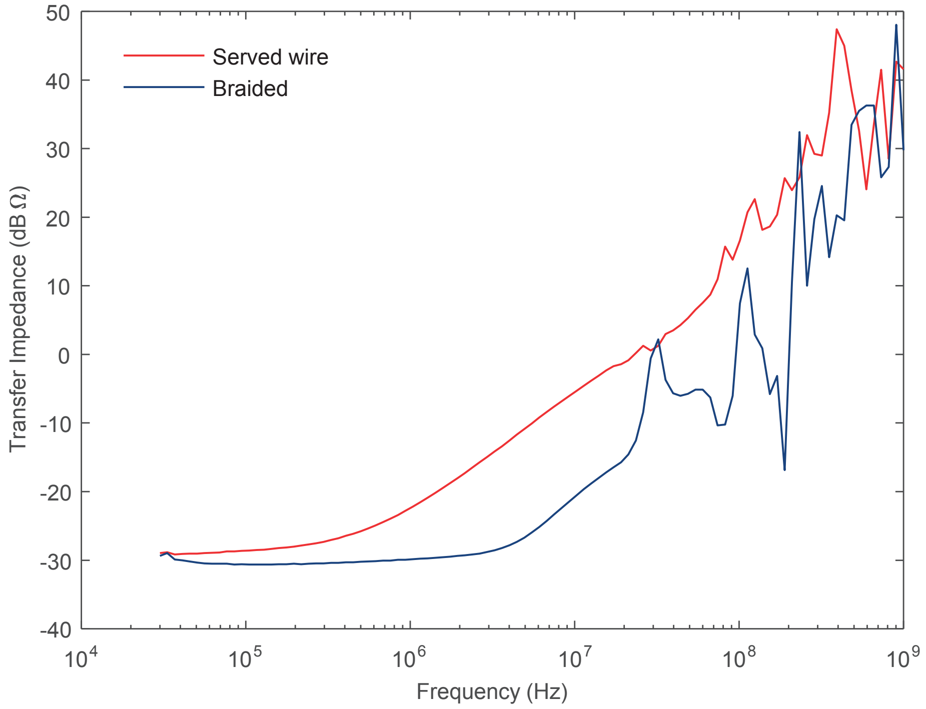

Fig. 7.10 Overall transfer impedance of the cable assembly measured in the served wire shield pair and in the braided shield pair.

7.4 Modeling procedure

In this section, we present the implementation of the TL model of the cable assembly with the aid of the CST Cable Studio (CST-CS) numerical tool. The model attempts to reproduce as accurately as possible the measurement setup used to estimate the overall transfer impedance of the assembly as presented in Fig. 7.9.

7.4.1 General schematic diagram

A schematic diagram showing the model of the measurement setup is presented in Fig. 7.11. The cables are located at a height *h* above a perfectly conducting ground plane. The pigtails are modeled as lumped inductances L_p, and the interconnection between the connector backshell and the ground return path is modeled with a lumped inductance L_{bs}.

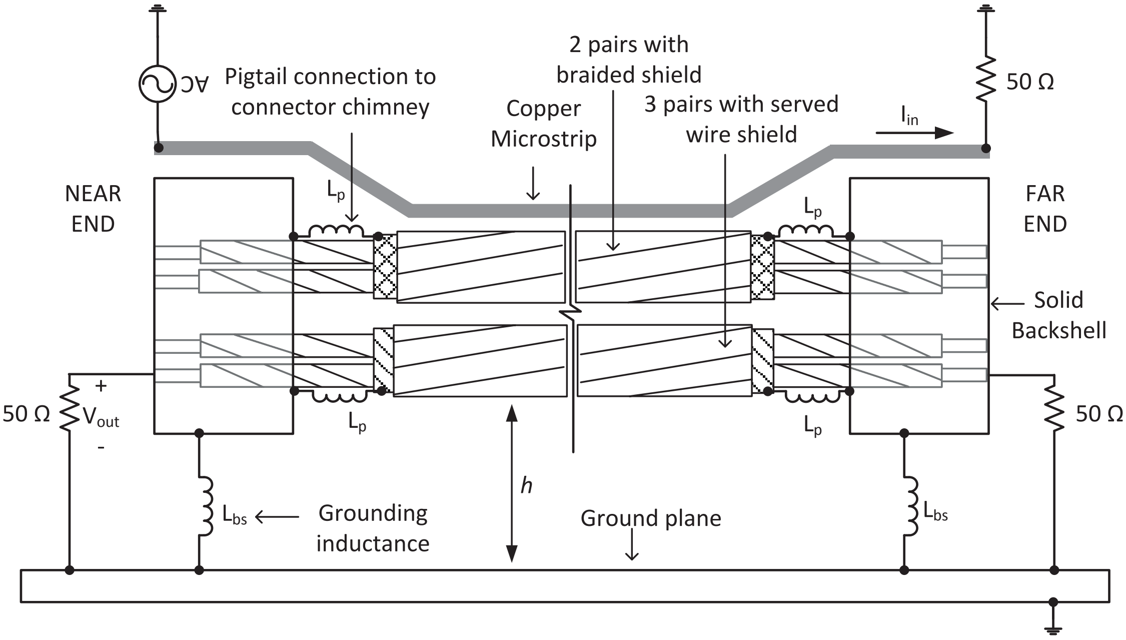

Fig. 7.11 Schematic diagram of the cable assembly model.

7.4.2 Shielded pairs' parameters

The parameters of the cables and shields that were used for creating the cross-sections are given in Tab. 7.4 and Tab. 7.5.Since the exact positions of the cables in the bundle were unknown, a random distribution of the cross-sections was automatically generated around a reference height h = 5cm, that was chosen to approximate the actual position of the whole bundle in the measurement setup.

The transfer impedance of the braided shields were calculated by using Key's model [186] with the CST-CS integrated tool. The transfer impedance of the served-wire shields were calculated by using the approximate formula of Tsaliovich (Equation (7.23)) [190]. Note that the transfer admittance was not considered in this study since for the considered height above ground, its effect is negligible.

The presence of the copper tape above the cable bundle was included in the simulation by adding a rectangular copper cross section. Fig. 7.12 illustrates the randomly distributed cross-sections of the five shielded pairs and the copper tape. The parameters of the copper tape are given in Tab. 7.3.

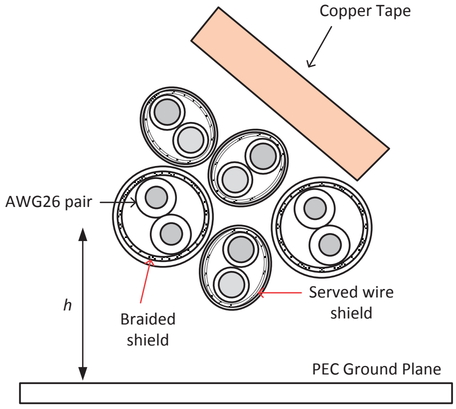

Fig. 7.12 Illustration of the randomly distributed cross sections used for modeling the cable bundle below the copper tape. The dimensions are not to scale.

Tab. 7.3 Summary of the Copper tape dimensions

Parameter	Value	Units
Copper width	5	mm
Copper thickness	1	mm
Copper conductivity	58	MS/m

Tab. 7.4 Parameters of the pairs with braided shield

Parameter	Value	Units
Cores (Inner conductors)		
Number of cores	2	
Core Conductivity (Silver Plated Copper)	13.73	MS/m
Core diameter	0.5	mm
Core insulator rel. permittivity (PTFE)	2.1	
Core insulator tangent loss (PTFE)	1e-6	
Core insulator thickness	0.2	mm
Braided shield		
Number of carriers	16	
Filaments per carrier	6	
Filament diameter	0.071	mm
Inner radius of the braid	0.95	mm
Optical Coverage	86	%
Weave angle	33	°
Conductivity (Silver Plated Copper)	13.73	MS/m
Outer insulator		
Relative permittivity (Kapton)	3.4	
Thickness	0.12	mm

Tab. 7.5 Parameters of the pairs with served wire shield

Parameter	Value	Units
Cores (Inner conductors)		
Number of cores	2	
Core Conductivity (Silver Plated Copper)	13.73	MS/m
Core diameter	0.57	mm
Core insulator rel. permittivity (Kapton)	3.4	
Core insulator thickness	0.24	mm
Served wire		
Number of filaments	56	
Filament diameter	0.079	mm
Inner radius of the shield	0.79	mm
Weave angle	33.5	°
Conductivity (Silver Plated Copper)	13.73	MS/m
Outer insulator		
Relative permittivity (Kapton)	3.4	
Thickness	0.222	mm

7.4.3 Pigtail model

The connection of the cable shields to the backshell chimney were modeled as lumped inductances of different values between 20 to 30 nH depending on the pigtail lengths (20-30 mm).

7.4.4 Backshell model parameters

7.4.4.1 Connector backshell

An isometric view and the side views of the micro-D connector backshell are shown in Fig. 7.13.

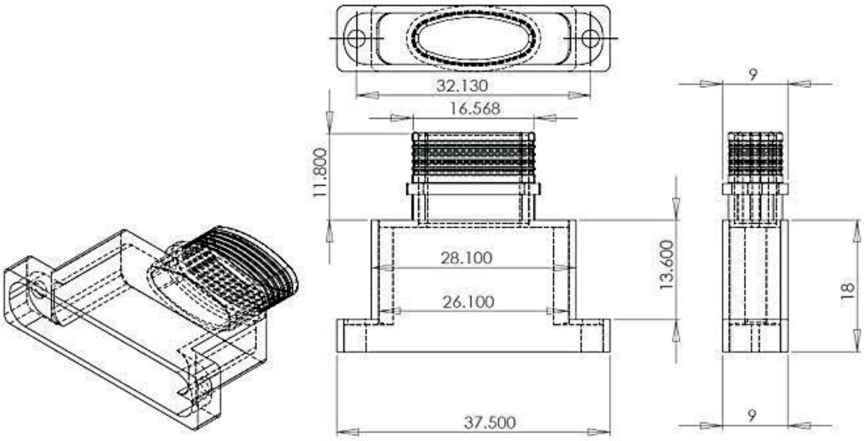

Fig. 7.13 Isometric and side views of the micro D backshell (units in mm).

The volume of the backshell was modeled as the union of two 1-mm thick solid shields of rectangular cross sections located at a height *h* =5cm from the ground plane, that represent the chimney and the body of the backshell, respectively. The rectangular solid shield enclosed the cross-section of the wires of the 5 pairs without the shields. An example of one of the cross-sections used to simulate the connector backshield is schematically shown in Fig. 7.14. The cross sectional parameters are given in Tab. 7.6.

The transfer impedances of the solid shields were calculated using Schelkunoff's formula [184] for the case of a rectangular cross-section [196]. Since the bulk material properties of the backshell were not available from the manufacturer, the conductivity of Aluminum was assumed as 37 MS/m.

Tab. 7.6 Micro-d connector parameters used to generate the rectangular shield cross-section

Parameter	Value	Units
Backshell chimney length	11.8	mm
Backshell chimney cross section	16.56 x 9	mm^2
Backshell body length	13.6	mm
Backshell body cross section	28.1 x 9	mm^2
Backshell thickness	1	mm
Backshell conductivity (Al)	37	MS/m

.1.1.1 Grounding inductance estimation

In order to estimate the value of the grounding inductance L_{bs}, a simplified experiment performed with a very short section of the bundles was performed. A schematic diagram showing the simplified experiment setup is shown in Fig. 7.15.

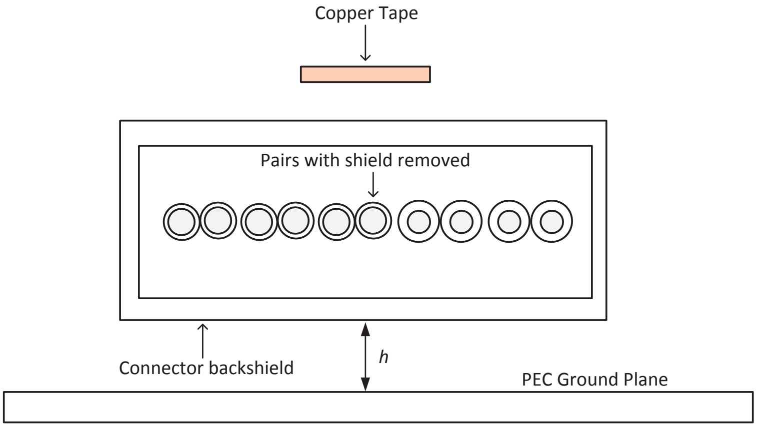

Fig. 7.14 Schematic diagram illustrating the cross section of the connector backshield and the pairs' wires with the shields removed. The dimensions are not to scale.

The five copper pairs were overshielded with an additional braid. At one end, the pairs' wires were connected to the 37-pin micro-D connector. At the other end, one wire of the pairs was short-circuited to the braided overshield, and the current was injected at this point with a signal generator. The other copper wires and their shields were left floating. The overshield was wrapped to the connector backshield chimney using a 360° connection. The shields of the five pairs (2 braided and 3 served wires) were also connected to the chimney through 20 mm long pigtails. Finally, the backshell was connected to the general chassis of the setup by using its mating female micro-D connector (without using RFI gaskets) and was very well secured with the use of two screws.

The injected current was measured with the use of a current transformer, and the induced voltage was measured in the selected wire at the connector level with a spectrum analyzer.

An equivalent TL model of the measurement setup was generated. The pigtails were modeled as lumped inductances of $L_\mathrm{p} = 20$ nH. The lumped inductance L_bs was left as an open parameter in the simulations.

The parameters of the braided overshield that were used for creating the cross-sections are given in Tab. 7.7

Tab. 7.7 Braided overshield parameters

Parameter	Value	Units
Length of the section	124.6	mm
Number of carriers	48	
Filaments per carrier	9	
Filament diameter	0.16	mm
Inner radius of the braid	9.15	mm
Optical Coverage	88.8	%
Weave angle	27.8	°
Conductivity (Silver Plated Copper)	13.73	MS/m

The connector's transfer impedance was measured and calculated for frequencies ranging from 30 kHz to 70 MHz. Three different values for the backshell inductance L_bs were chosen in the model, namely, 10, 50, and 100 pH. A plot of the connector transfer impedance obtained from measurements and simulation are presented in Fig. 7.16.

It can be observed that there is a very good agreement between measurement and simulations at low frequencies. This implies that the selected conductivity values and dimensions of the backshell and the braided overshield reproduce very well the DC resistance of the connector assembly in simulation. The transfer impedance shows an increasing trend as a function of frequency suggesting the presence of a dominant inductive behavior.

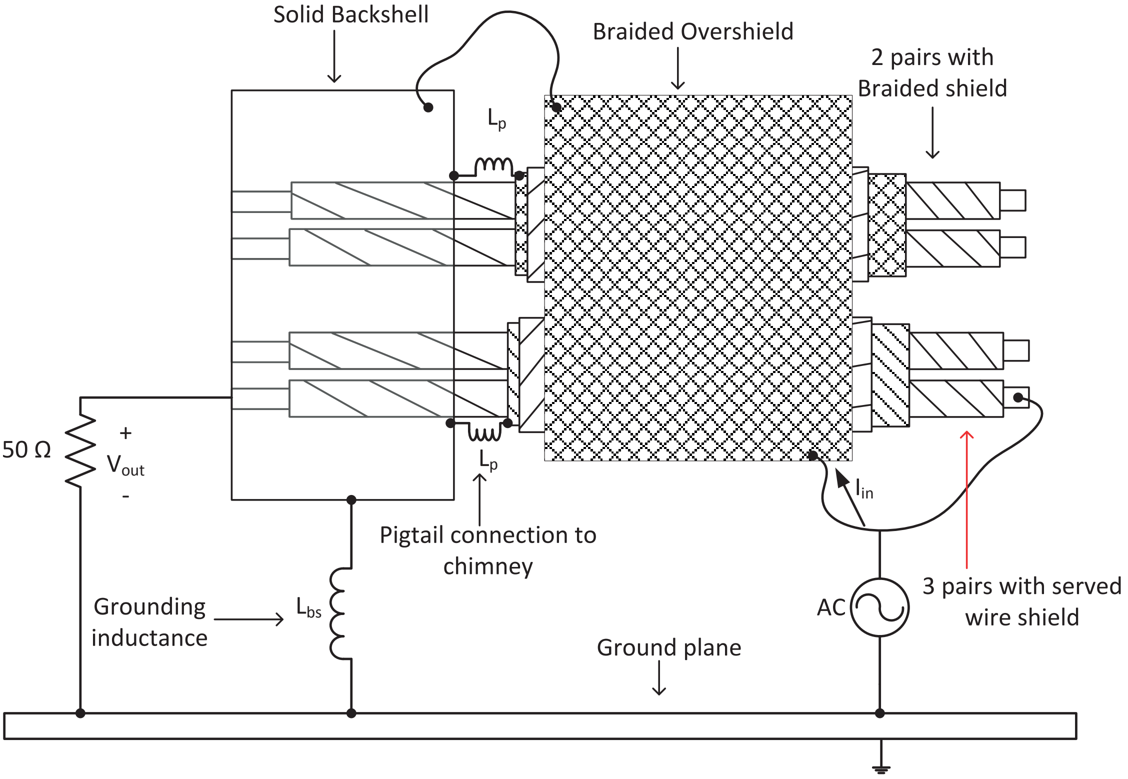

Fig. 7.15 Schematic diagram of the experimental setup for determining the grounding inductance of the connector.

After adding the backshell inductance, the simulation results exhibit a better agreement with the measured data. The curve with L_{bs}=100 pH reproduces well the behavior at the measured low and medium frequencies; the differences in the higher frequency range remain acceptable for engineering purposes.

It is observed that the overall response at high frequencies is very sensitive to the grounding impedance between the connector's surface and the equipment chassis. A very good galvanic contact between male and female connectors is required (for example through the use of RF gaskets)[194]. It is very likely that the inductive behavior of the backshell connection is due to an imperfect mating between the male and female backshells and that the return current is flowing through the securing screws.

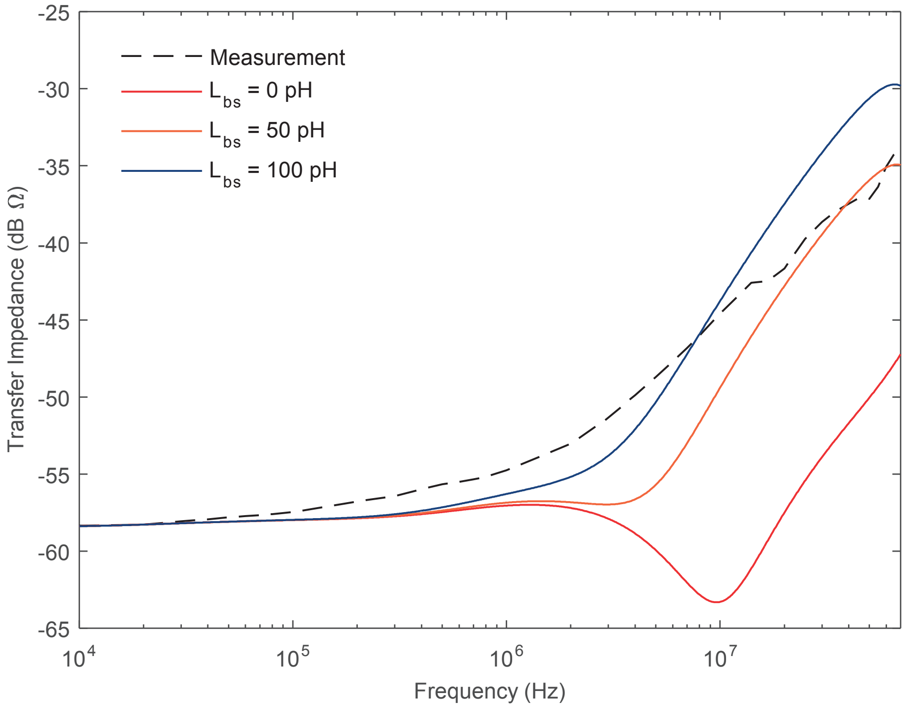

Fig. 7.16 Measurement and simulation results of the connector transfer impedance considering different values for L_{bs} (0, 10, 50, and 100 pH).

7.5 Simulation results for the cable assembly

The overall transfer impedance of the cable assembly was simulated for frequencies ranging from 30 kHz to 500 MHz.

In a first try, the simulation was performed by using a backshell grounding inductance L_{bs}=100 pH. The measurement results and the simulation results obtained for the served wire shielded pair and the braided shield pair are plotted in Fig. 7.17 and Fig. 7.18, respectively.

In both cases, the low frequency transfer impedance predicted by the numerical simulation is about half of the measurement result. Provided that the backshell simulations showed excellent agreement with measurement at low frequencies, the observed discrepancy was identified as due to the contact resistance associated with an imperfect bonding between the shields and the backshell, which was not considered in the model. Therefore, a second set of simulations were performed by adding a series resistance to ground R_{bs}=15mΩ (similar values were reported in [194]), and the low frequency results were improved as it can be seen in the green curves of Fig. 7.17 and Fig. 7.18. The simulation results obtained after adding the backshell resistance are in reasonable agreement with the experimental data.

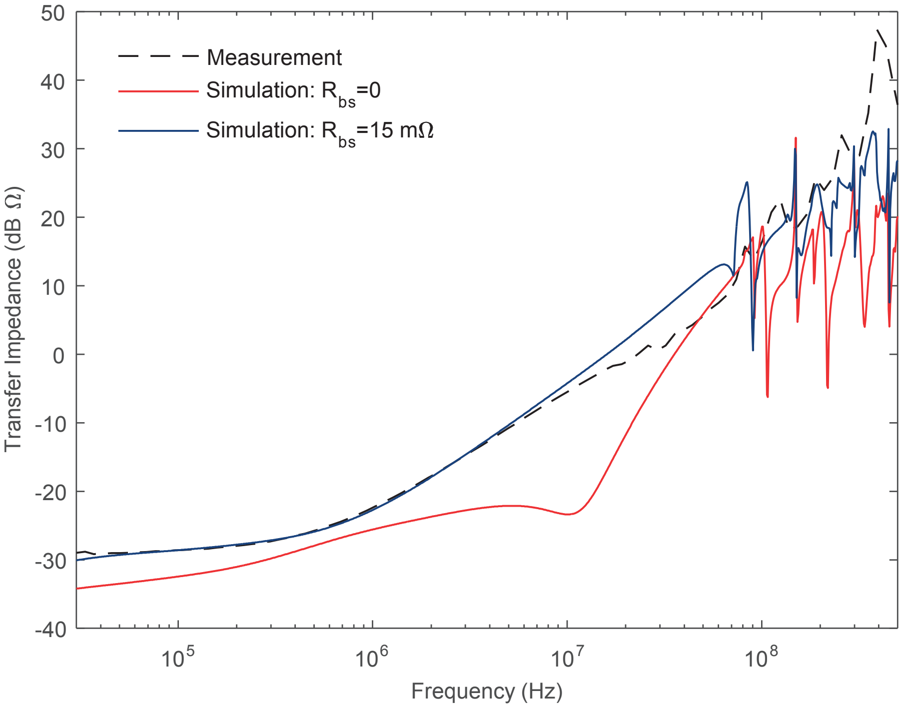

Fig. 7.17 Measurement and simulation of the cable assembly overall transfer impedance obtained in one of the served wire pairs.

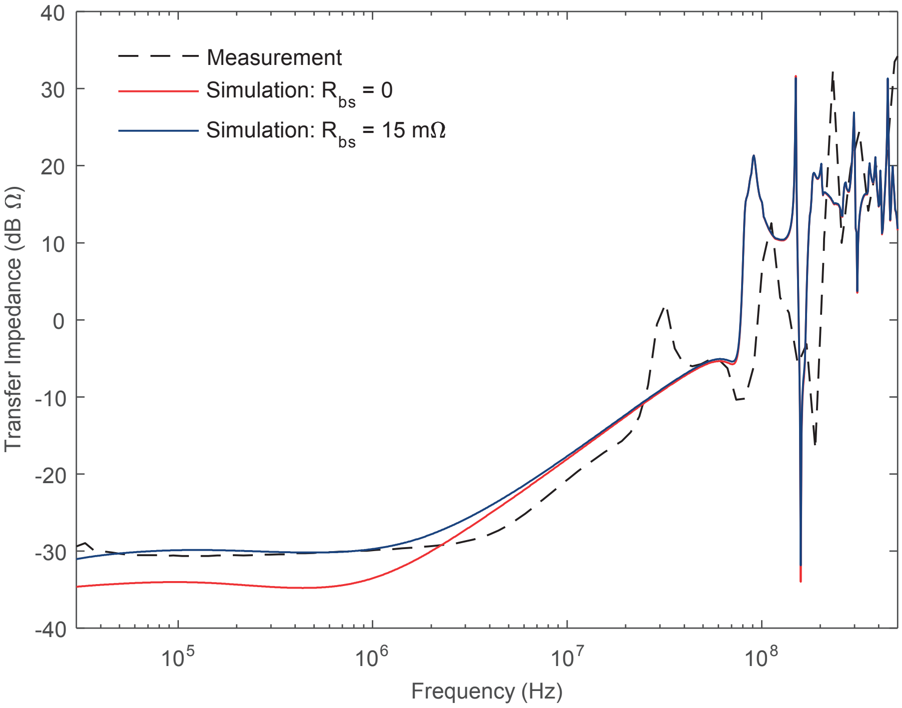

Fig. 7.18 Measurement and simulation of the cable assembly overall transfer impedance obtained in one of the braided shield pairs.

7.6 Conclusions

In this chapter, general considerations for the application of the TL theory for simulating shielded cable assemblies were presented. Some of the practical issues that occur in the modeling process of various components of cable assemblies, namely connectors, pigtails and backshell were discussed.

An improved model for estimating the transfer impedance of a two-layer braided shield was proposed. The proposed model is a combination of the model proposed by Vance for the evaluation of the equivalent transfer impedance of a two-layer braided shield, and the improved Kley model for the transfer impedance of single-layer braided shields. The proposed model has shown to be very accurate in reproducing the measured transfer impedance of two different two-layer braided shielded cables up to 70 MHz.

The overall transfer impedance of the studied cable assembly was used as a figure of merit to evaluate the total shielding provided by the harness. The measurement setup was implemented in CST-CS which uses TL theory to generate a lumped circuit equivalent that is solved to obtain the currents and voltages at the terminations. Some of the parameters of the model were available from the manufacturers' datasheets and others were determined either experimentally or empirically. The position of the cables along the cross section was randomly assigned by the simulation tool.

In general, the obtained simulation results were found to be in reasonable agreement with the experimental data. It was found that the generally overlooked contact impedances between the cable shields and connectors play a significant role, especially at low frequencies. The simulation results also emphasized the importance of the inductance and resistance of the connector backshell interconnection to the equipment chassis.

The presented models could be improved by including a more accurate representation of pigtails as additional wires in the cable cross sections, and the effects due to the transfer capacitance, which at large frequencies may play a significant role.

8 Conclusions

This thesis is a contribution to the assessment of the vulnerability of CIs against IEMI. The performed studies deal with the improvement of the existing methods for the general assessment of the IEMI risks undertaken by CIs, the classification of existing IEMI sources, and the experimental and numerical assessment of the response of commercial cables to IEMI. These studies are important to better understand the compromise of CIs when operating with ICT technologies and to take appropriate corrective and mitigation measures against this new threat that has raised a great deal of attention in the EMC community during the past years.

8.1 General highlights

In Chapter 2, we proposed a qualitative methodology for assessing the risk of CIs against IEMI. The need for a qualitative method for IEMI assessment has been pointed out because a quantitative evaluation of the risk is a very difficult task, given the complexity of CIs. Furthermore, we believe that a qualitative assessment can be better understood by non-EMC experts and allows the intervention of the facilities' staff, who are the main assets of the CIs, and who should be aware of the IEMI threat.

The proposed method is a service-based risk assessment tool that merges the strategies proposed in previous works to infer qualitatively the risk of stopping a service provision with EM means. The method is oriented to assess the business continuity of the utilities and therefore it concentrates only on the equipment involved in the provision of important services, and considers the threats imposed by IEMI sources that are likely to occur given the accessibility constraints of the facility and the availability and transportability of the sources. From a business continuity point of view, the final output of a service-based risk assessment may be less important than all the information about the organizational and IT equipment weaknesses that is gained during the evaluation process.

In Chapter 3, we presented an updated survey and classification of potential IEMI sources that were collected from available literature. The tendencies and characteristics of several conducted and radiated sources were discussed and illustrated in the form of pie charts and bar plots. It was found that potential IEMI conducted sources are more available than radiated sources and they can be regarded as likely to be deployed by malefactors. The radiated sources were found to be still in a development phase and not easily available for purchase. The majority of the radiated sources are transported with vehicles and their typical costs remain high due to the required high technology in their implementation and testing. The physical limitations that constrain the development of current technologies in the generation of faster and stronger HPEM sources have also been reviewed in order to set up an overview of the expected worst case scenario.

In order to study the spectral characteristics of the IEMI sources, we have proposed to represent digitized signals as an expansion of complex exponentials from which their Fourier transform can be calculated analytically. This alternative method facilitates the calculation of the spectral parameters of the signals because the spectra can be calculated at arbitrary frequency points. We have also shown how to decrease the computation time of the bandratio of the signals by using the so-called Blumer index. A summary of the methodology can be found in 8.2Appendix A.

In Chapter 4, a typical electrical and communications raceway including several types of cables found in commercial buildings was built and tested against HPEM transients inside a GTEM cell and low power fields inside a RC. The tests revealed that the LVP cables are the most susceptible compared to TEL or LAN cables. The responses were found to be governed by the configuration of the cable under test in the lower-intermediate frequencies (below 3 GHz). Beyond 3 GHz, the coupling is clearly dominated by the cable terminations (connector imperfections, pigtails, etc.). As expected, the best performance was obtained with the use of shielded twisted pairs.

These experiments improve our understanding of the expected induced voltages and currents in commercial cable systems when exposed to IEMI-like signals. The obtained transfer functions can be used for bounding the disturbance levels in IEMI risk analyses for many types of CIs.

Chapter 5 presents a discussion of the applicability of the TL theory in evaluating DM signals in canonical setups of two-wire lines floating above a ground plane. It was found that the presence of the ground plane can be disregarded in the calculation of the characteristic impedance of the lines, when the height of the wires is larger than about twice the separation distance between them. Also, the results showed that the validity of the TL theory is conditioned upon an electrically short distance between the DM wires, regardless of the distances above the ground plane.

The effects of including conductive and dielectric losses in the analysis of the DM propagation along lines with cross sections representative of commercial cables were also discussed. The results show that both dielectric and conductive losses have to be considered for obtaining accurate attenuation levels. In lines with very small conductor cross-section, it is more likely that the conductive losses will dominate the total attenuation due to the skin effect.

Chapter 6 presents the numerical modeling of the propagation of IEMI disturbances along LVP cables. Even though some of the input parameters of the models are not precisely known, it was shown that simulation results are in good agreement with experimental data obtained in both frequency domain and time domain.

Finally, Chapter 7 was dedicated to the modeling of the so-called overall transfer impedance of complex cable assemblies. The obtained simulation results were found to be in reasonable agreement with the experimental data. It was found that the generally overlooked contact impedances between the cable shields and connectors and the inductance and resistance of the connector backshell interconnection to the equipment chassis play a significant role in the evaluation of the overall transfer impedance. Furthermore, an improved model for estimating the transfer impedance of a two-layer braided shield was also proposed. The proposed model has shown to be very accurate in reproducing the measured transfer impedance of two different two-layer braided shielded cables.

8.2 Future perspectives

The results of this thesis can be readily used for performing IEMI risk analysis of CIs. The systematic application of the service-based risk analysis to existing critical facilities should reveal the technical and organizational shortcomings that should be hardened in order to decrease the risk evaluation of modern CIs.

We have shown the existing limitations on the fabrication of stronger and faster HPEM weapons due to physical constraints. However, the evolution of energy storage technologies and semiconductors could dramatically increase the transportability and availability of IEMI radiated sources and as a consequence the risk evaluation of CIs. Thus, the technical capabilities in the generation of HPEM sources should be continuously monitored.

The majority of the experiments performed in this work were made with reduced-scale cable systems that are representative of real scenarios. However, further experimental evidence at larger scales including the presence of rebar concrete walls and points of entry like window panes or doors are required in order to understand the penetration and diffusion of IEMI fields inside buildings under realistic conditions that are not easily modeled with the existing EM tools.

The final objective of the EM modeling in the framework of IEMI studies is the estimation of the worst case scenarios for the induced voltages, currents, or power at the critical equipment input. Because of all the uncertainties that have been already mentioned, a deterministic solution to this problem turns out to be a challenging task. The presented models could be improved by including a more accurate representation of the cables' dielectrics, terminations such as connectors and pigtails, and the effects due to the transfer admittance, which at large frequencies may play a significant role. A more efficient solution is to create random scenarios in which, variations in parameters such as cable lengths, material properties, and loading could be stochastically included. Once the statistical moments have been calculated, a study of the possible extreme values can be performed in order to predict the worst case results.

Appendix A Selected Waveforms Classification

A.1 Introduction

In this appendix, the adopted procedure to digitize the waveforms extracted from the relevant literature, and the processing steps to produce the *wavecards* containing the time domain and frequency domain parameters of the studied sources in Chapter 3 is presented. Also, a technique for an efficient evaluation of the Fourier transform of the signals and the extraction of their spectral characteristics is introduced. The technique is based on the use of a MPM to expand the time domain waveforms into a series of complex exponentials, whose poles and residues can be used to calculate waveform's Fourier transform analytically. Finally, the use of the so-called Blumer index for improving the time required for estimating the bandratio of a given spectrum is illustrated.

A.2 Selected waveforms parameter extraction

A.2.1 Digitalization of the waveform

The first step in the creation of the *wavecard* is to digitize the reported waveforms. To this aim, a scanner is used to digitize the paper-based documents and a PDF reader for the documents available in electronic format to obtain an image of the waveform. The Engauge digitizer© (free distribution tool) was used to convert the images into numerical vectors to be processed by the main software. It is important to highlight that digitizing a signal from paper does not ensure that the whole spectral attributes of the signal will be correctly reproduced. Nevertheless, a fair approximation of the real measured signal and its properties is expected.

To illustrate the process, an example of a waveform image and its digitized version after using the Engauge digitizer© is presented in Fig. A. 1. The waveform corresponds to the far voltage of the HPEM source reported in [197].

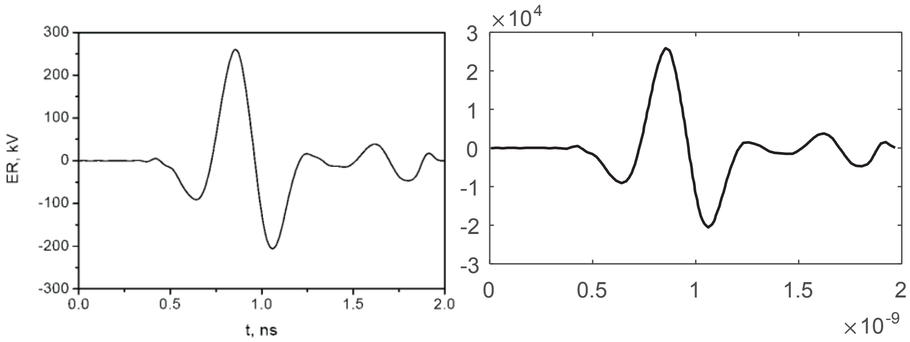

Fig. A. 1 Digitized image (right panel) of the far voltage waveform of the source reported in [197] (left panel).

Since the waveform points provided by the Engauge digitizer© are not sampled with a uniform time step, the whole waveform is interpolated using 1024 points with a uniform time step. Notice that the selected interpolation sampling rate is independent of the sampling rate of the scope that was used to record the waveform.

Once the waveform is digitized, the time-domain attributes of the source can be estimated.

A.2.2 Waveform windowing

It is normal that the digitized signals do not vanish to zero in the late times because of the truncation of the original waveform in the document or because of digitizing errors of the program. Therefore, the signals are windowed with a quasi-rectangular unitary pulse created by using the complementary error function [198]:

$$u_{erfc}(t)=\frac{1}{2}\left(\operatorname{erfc}\left(\frac{t-t_b}{0.55t_r}\right)-\operatorname{erfc}\left(\frac{t-t_a}{0.55t_f}\right)\right), \tag{A.1}$$

where t_a-t_b is the FWHM of the pulse, t_r is the 10-90% risetime of the pulse, and t_f is the 90-10% fall-time of the pulse.

A plot of the erfc window for the case $t_r = t_f = 5$, $t_a = 90$ and $t_b = 10$ is shown in Fig. A. 2

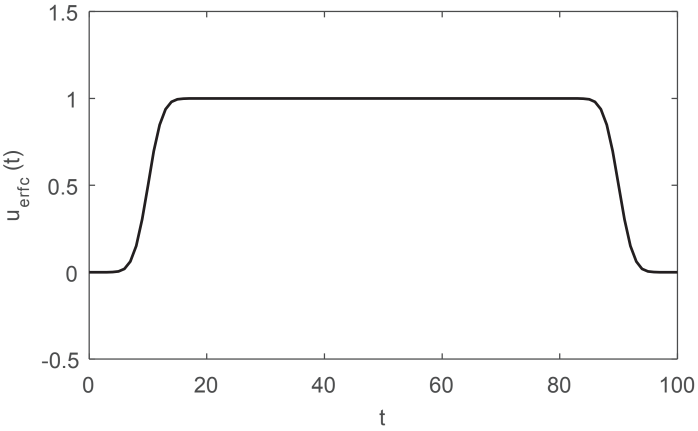

Fig. A. 2 Plot of the u_{erfc} function for $t_r = t_f = 5$, t_a=90 and t_b=10.

To carry out the windowing of the selected waveforms, the time constants in Equation (A.1) are chosen so that the early rise of the window does not modify the early time behavior of the digitized signal. On the other hand, the fall time is also chosen so that the windowed signal smoothly converges to zero in the late times. Notice that the use of the erfc function ensures a smooth transition in the rising and falling edges of the window and, therefore, numerical spectral noise due to discontinuities is reduced.

A.2.3 Zero padding

After windowing the digitized signal, zero padding is performed in order to increase the resolution of the Fourier transformation that is performed in the next step. An example of the windowed version of the waveform in Fig. A. 1 is presented in Fig. A. 3. Note that the effect of the window is unnoticeable and a smooth transition to zero is ensured in the early and late times.

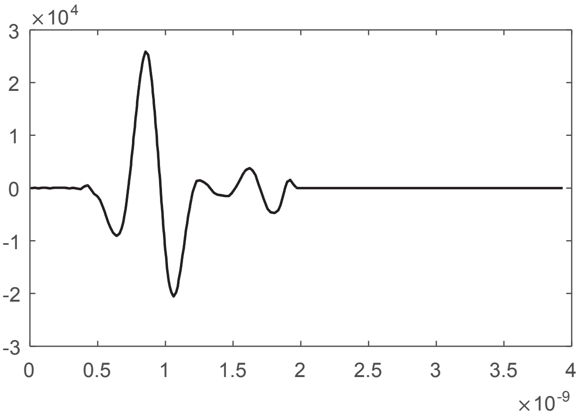

Fig. A. 3 Windowed version of the digitized signal in Fig. A. 1.

A.2.4 Calculation of the signal spectrum

The spectrum of the signal is calculated with an FFT. The resulting spectrum is used to calculate spectral attributes of the signal.

The accuracy of the -3dB bandwidth and, consequently, the quality factor, depend on the frequency resolution of the FFT and, therefore, further zero padding can be used to reduce the frequency step. On the other hand, the estimation of the bandratio becomes time-consuming if the FFT of the spectrum has to be calculated over a large number of frequency points.

The 90% energy bandwidth BW_{90} is iteratively calculated by testing in all the possible frequency points of the discrete spectrum of the signal and, for each pair of tested frequency points, an integration procedure has to be performed. Thus, it is desired to compute BW_{90} from spectra with a reduced number of points, but containing the necessary amount of information for correctly calculating the limits. Notice that traditional sampling schemes with reduced equidistant linear or logarithmic steps may fail to efficiently represent spectra since resonances may be lost.

A.2.5 Alternative method for the estimation of the Fourier transform of the signal

Due to the previously mentioned issues, an alternative method for estimating the frequency spectrum of the waveforms was used in this work. Consider the approximation of the digitized waveform $r(t)$, as the sum of m complex exponentials:

$$r(t) \approx \sum_{i=1}^{m} A_i e^{s_i t} u(t), \tag{A.2}$$

where the residues A_i and the poles s_i are complex numbers and $u(t)$ is the Heaviside function. The exponential nature of the basis functions will ensure the existence of the Fourier transform of $r(t)$ since the real part of the complex poles is negative and, therefore, the signal must vanish at infinite times, i.e.:

$$s_i = \sigma_i + j\omega_i, \sigma_i < 0. \tag{A.3}$$

The Fourier transform of $r(t)$ can be then approximated as:

$$R(\omega) = \Im(r(t)) \approx \Im(\sum_{i=1}^{m} A_i e^{s_i t} u(t)) = \sum_{i=1}^{m} A_i \Im(e^{s_i t} u(t)) = \sum_{i=1}^{m} \frac{-A_i}{s_i - j\omega}. \tag{A.4}$$

Notice that in order to get a good approximation of the original waveform, a sufficient number of poles m has to be chosen.

The interest of this method relies in the fact that if the residues and poles of the original waveform can be retrieved, its Fourier transform can be analytically estimated with the use of

Equation (A.4) at any desired frequency point, and the algorithms for calculating the bandratio can be improved since it is no longer required to sample the spectrum with a regular frequency step.

A.2.5.1 Poles and residues estimation

In order to retrieve the residues and the poles of the signals, we used the MPM in [199]. This technique has been proven to be very efficient in the extraction of the residues and poles of signals containing noise. To choose the number of poles that correctly reproduce the waveform (m), the signal is first expanded into an increased number of complex conjugated pole pairs (typically 25 pairs). It is expected that the poles that contribute most to the expansion of the signal are those having the largest residues. Thus, the retrieved poles are sorted according to a decreasing absolute value of their residues. Then, the number of poles m is chosen to minimize the normalized MSE between the original signal and the m-pole approximated signal [200]:

$$MSE = \frac{\sqrt{\sum_t \left| r(t) - r_{rec}(t) \right|^2}}{\sum_t \left| r(t) \right|}, \tag{A.5}$$

where $r_{rec}(t)$ is the signal reconstructed using Equation (A.2).

Finally, the Fourier transform is calculated analytically using Equation (A.5) at the desired frequency points.

A.2.5.2 Reconstruction example

Fig. A. 4 presents an example of a measured signal and its reconstruction with the MPM. The time domain waveforms are presented in the top panel, and the frequency spectra are shown in the lower panel. The black signal corresponds to the vertical electric field generated by the EPFL switching oscillator connected to a monopole antenna [119]. The waveform plotted with a solid black was reconstructed by using 26 poles resulting in a MSE = 2.3 x 10^{-3}. The spectrum plotted with dashed red lines was calculated by using a FFT of the original waveform and the spectrum in solid black from Equation (A.4).

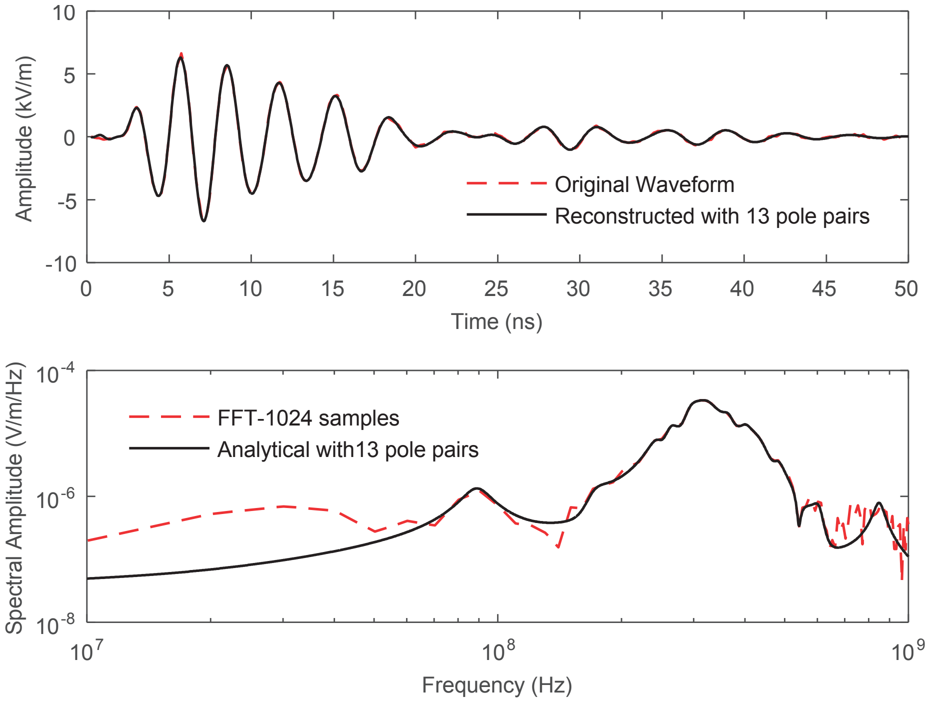

Fig. A. 4 Example of the reconstruction of a measured signal with the MPM (top panel) and the analytical calculation of its Fourier transformation (bottom panel).

Even though the reconstruction of the time domain signal is in very good agreement with the measurement, some differences can be observed in the spectra at low and high frequencies. The advantage of the analytical spectrum is that, since the reconstructed signal must vanish in the late times, it must give a causal Fourier transform. On the other hand, the spectrum calculated with the FFT may contain truncation errors.

A.2.6 Estimation of the bandratio with the aid of the Blumer Index

The calculation of the bandratio *br* and the 90% Bandwidth BW_{90} defined in Chapter 3, are not straightforward. It is required that the spectrum of the signal is calculated in a limited number of frequency points to reduce the algorithm’s calculation time. On the other hand, enough frequency samples are needed so that no spectral information is missing and that the frequency limits f_l and f_h are correctly calculated. If the spectrum contains a reduced number of frequencies, so that the resonances of the signal or important concentrations of energy are missing, the bandratio is not correctly calculated. Thus, a method to evaluate the accuracy of the spectra is needed.

The Blumer index can be used to estimate the accuracy of a measured or numerically calculated spectrum [87]. The index serves as a tool to determine if the information contained in a discrete spectrum is good enough to reproduce a causal signal, or if more frequency samples are required. The Blumer index is derived from the Hilbert transform properties of causal signals and it can be calculated as:

$$B = \left\{ 1 - \frac{\sum_{\omega_{\min}}^{\omega_{\max}} \left| \mathrm{Re}\left\{ R(\omega) \right\} \right|^2 \Delta\omega - \sum_{\omega_{\min}}^{\omega_{\max}} \left| \mathrm{Im}\left\{ R(\omega) \right\} \right|^2 \Delta\omega}{\sum_{\omega_{\min}}^{\omega_{\max}} \left| \mathrm{Re}\left\{ R(\omega) \right\} \right|^2 \Delta\omega + \sum_{\omega_{\min}}^{\omega_{\max}} \left| \mathrm{Im}\left\{ R(\omega) \right\} \right|^2 \Delta\omega} \right\} \times 100\%, \tag{A.6}$$

where $\omega_{\min}$, and $\omega_{\max}$ are the minimum and maximum frequency points in the spectrum, respectively, and $\Delta\omega$ is the frequency step between consecutive frequency points. Notice that for an accurate causal spectrum, the Blumer index is B=100%; since the sum over the real part of the spectrum should be equal to the sum of the imaginary part to satisfy Hilbert transform properties.

To overcome the above-mentioned issues for the estimation of the bandratio of the studied waveforms, the adaptive non-uniform sampling scheme proposed in [87] has been used. In this scheme, in the vicinity of spectral peaks, a large number of data points are sampled. On the other hand, at frequencies where the spectrum changes less rapidly, a lower sampling rate is used. To test the accuracy of the discrete spectral representation of the selected waveform, the Blumer index of the spectrum is evaluated. If the index is below a user-defined threshold (usually around 98-99%), the spectrum is sampled again with an iterative scheme until the threshold is reached. This procedure reduces the errors arising from the under-sampling of the spectrum, and/or from truncation the spectrum at the upper and lower frequency limits. As a consequence, the calculation time of the bandratio is significantly reduced because fewer frequency points need to be tested. Further details in the iterative selection of the frequency points can be found in [87].

To illustrate the use of the adaptive scheme, the Blumer index, and its influence in the estimation of the bandratio of a signal, the spectrum of the waveform presented in Fig. A. 4 was calculated by using the traditional FFT, and the analytical expression in Equation (A.4) with three different (and reduced) numbers of frequency samples: 10, 33, and 106 (see Fig. A. 5). The samples were obtained iteratively with the adaptive scheme with the following Blumer index thresholds: 77%, 97% and 99%, respectively.

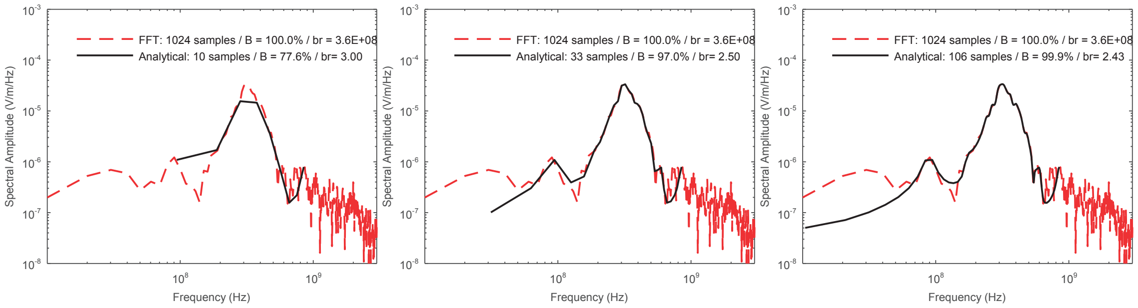

Fig. A. 5 Illustration of the use of the Blumer Index in the calculation of the bandratio.

A summary of the bandratio results obtained with the FFT and the proposed scheme using the Blumer index is reported in Tab. A. 1.

Tab. A. 1 Comparison of the bandratio results obtained with the FFT and the analytical-Blumer index approach

Scheme	Samples	Blumer index	Bandratio
FFT	1024	100%	3.6×10^8
Analytical – Blumer	10	77.6%	3.00
Analytical – Blumer	33	97%	2.50
Analytical – Blumer	106	99%	2.43

Given the damped oscillatory behavior of the waveform, a reduced bandratio is expected. Notice that the bandratio and the resulting BW_{90} estimated from the spectrum obtained with the FFT are not correctly calculated since the frequency-sampling scheme of the FFT is linear and, therefore, very large frequency steps are obtained, and some important resonances are missed. Also due to truncation effects, large energy content is assigned to the low frequency components. In order to reduce the frequency step size, zero padding could be used, but also the number of samples of the FFT would be increased, leading to an increase in the calculation time of the bandratio.

On the other hand, with the adaptive scheme, the bandratio is estimated by using non-equidistant frequencies that are chosen as the frequencies where the majority of the energy is concentrated. The obtained bandratios with the adaptive scheme correspond to a mesoband signal, as expected. Notice that the adaptive scheme already provides a Blumer index of 97% with about 33 samples, and 99% with 106 samples and, therefore the algorithm for estimating the bandratio requires much less time than with an FFT.

Appendix B Parameters of Coaxial and Two-Coated-Wire Lines

B.1 Introduction

In this appendix, the used expressions to calculate the p.u.l. parameters of lossy coaxial and two-coated-wire lines that were used to represent the cross section of typical power and communication lines in Chapter 5, are presented. The p.u.l. resistance and conductance were approximated with analytical formulas for running faster parametric analyses. The constitutive parameters of the dielectrics were approximated with a constant relative permittivity and tangent loss.

B.2 Complex permittivity

The permittivity of a lossy dielectric is a complex number that can be written as:

$$\hat{\varepsilon} = \varepsilon_0 (\varepsilon' - j\varepsilon''), \tag{B.1}$$

where ε_0 is the free space permittivity, and ε' and ε'' account respectively for the polarizability of the medium, and the loss (heat) due to damping of the vibrating dipole moments.

By definition, the tangent loss of a dielectric accounts for the losses due to the conductivity of “free” charges inside the dielectric σ_{dK} and the polarization losses ε'' are related to the displacement currents in the material [171]. In this work we neglected the conduction currents inside the dielectric and therefore:

$$\tan\delta = \frac{\sigma + \omega\varepsilon''}{\omega\varepsilon'} \approx \frac{\varepsilon''}{\varepsilon'}. \tag{B.2}$$

Thus, the complex permittivity of the dielectric materials was expressed as [171]:

$$\hat{\varepsilon} = \varepsilon_0(\varepsilon' - j\varepsilon'') \approx \varepsilon_0\varepsilon'(1 - j\tan\delta) = \varepsilon_0\varepsilon_r(1 - j\tan\delta). \tag{B.3}$$

B.3 Lossy coaxial line

Consider the cross section of a lossy coaxial line as shown in Fig. B. 1. The inner and outer conductors conductivity is σ, and are insulated with a dielectric with a constant relative permittivity ε_r and a tangent loss $\tan\delta$. The inner wire radius is r_w and the coaxial dielectric radius is r_s. The outer conductor thickness is *T*.

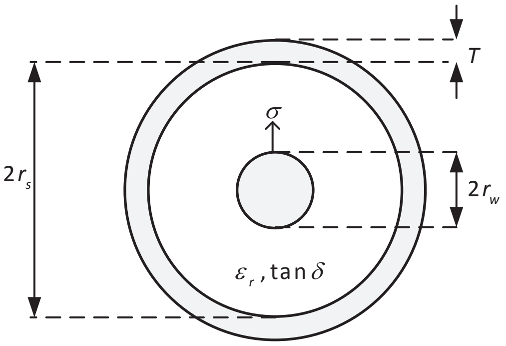

Fig. B. 1 Schematic diagram of the geometry and the constitutive materials of a lossy coaxial line.

The p.u.l. capacitance of the coaxial line in free space can be calculated as [88]:

$$C'_0 = \frac{2\pi\varepsilon_0}{\ln(\frac{r_s}{r_w})}. \tag{B.4}$$

And the p.u.l. inductance can be obtained according to:

$$L' = \frac{\mu_0\varepsilon_0}{C'_0} = \frac{\mu_0}{2\pi}\ln(\frac{r_s}{r_w}). \tag{B.5}$$

Since the coaxial line is filled up with a homogenous medium, the calculation of the p.u.l. capacitance and conductance can be obtained from the free space p.u.l. capacitance C'_0 [88]:

$$\begin{aligned} &C' = \varepsilon_r C'_0, \\ &G = \omega \tan\delta C' = \omega\varepsilon_r \tan\delta C'_0 . \end{aligned} \tag{B.6}$$

Notice that the p.u.l. conductance can be alternatively calculated if the p.u.l. complex capacitance $\hat{C}'$ is calculated with the expression for C' in Equation (B.6) by using the complex permittivity defined in Equation (B.3). In this case, C' and G' will be related to the real and imaginary parts of $\hat{C}'$, respectively:

$$\hat{C}' = C'_R + jC'_I = \varepsilon_r(1 - j\tan\delta)C'_0 = C' - \frac{j}{\omega}G'. \tag{B.7}$$

On the other hand, the self-impedance Z'_1 of the inner conductor can be estimated at low frequencies as [88]:

$$Z'_1 = R'_1 + j\omega L'_1 = \frac{1}{\sigma\pi r^2_w} + j\omega\frac{\mu_0}{8\pi}, \qquad \text{if } r_w < 2\delta_s, \tag{B.8}$$

where $\delta_s = \sqrt{2/(\omega\mu_0\sigma)}$ is the skin depth at the working frequency.

At high frequencies, the self-impedance of the inner wire can be estimated with [88]:

$$Z'_1 = R'_1 + j\omega L'_1 = \frac{1}{2\pi r_w}\sqrt{\frac{j\omega\mu_0}{\sigma}}, \qquad \text{if } r_w > 2\delta_s. \tag{B.9}$$

The self-impedance of the outer coaxial conductor can be estimated with [184]:

$$Z'_2 = \frac{\gamma}{2\pi r_s\sigma}\coth(\gamma T). \tag{B.10}$$

Notice that the inductance in Equation (B.6) neglects the self-inductance of the inner and outer conductors, and Equations (B.8) to (B.10) correct for their presence.

Finally, the overall p.u.l. impedance and admittance of the coaxial line can be estimated as:

$$\begin{aligned} &Z' = Z'_1 + Z'_2 + j\omega L', \\ &Y' = G' + j\omega C'. \end{aligned} \tag{B.11}$$

B.4 Lossy two-coated-wire line

The propagation of DM signals in LVP and/or TWP cables occurs in lines exhibiting cross sections that could be approximated to the one shown in Fig. B. 2. Two wires of radii r_w and conductivity σ are coated with a dielectric characterized by its relative permittivity ε_r and tangent loss $\tan\delta$. The outer radius of the dielectric coating is r_m.

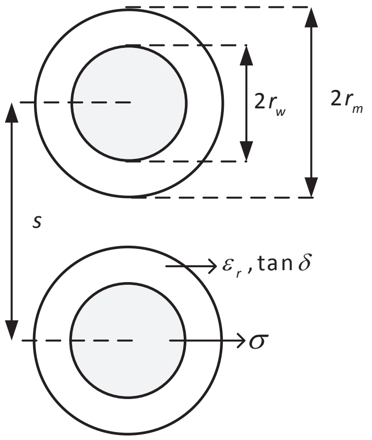

Fig. B. 2 Schematic diagram of the geometry and the constitutive materials of a lossy two-coated-wire line.

The free space p.u.l. capacitance of the line (i.e. with no dielectric coating) can be exactly calculated as [88]:

$$C'_0 = \frac{\pi\varepsilon_0}{\cosh^{-1}(\frac{s}{2r_w})}. \tag{B.12}$$

And the p.u.l. inductance yields:

$$L' = \frac{\mu_0\varepsilon_0}{C'_0}. \tag{B.13}$$

Since the line is immersed inside an inhomogeneous medium, the properties of the p.u.l. capacitance and conductance used in Equation (B.6) do not hold and therefore a numerical method has to be used for calculating the p.u.l. capacitance and conductance.

In what follows, we will present an approximate analytical method for calculating the p.u.l. capacitance and conductance of coated wires by decomposing them into a set of coaxial cables that propagate a TEM mode between their outer conductors. A schematic diagram illustrating the decomposition is shown in Fig. B. 3. The capacitances between the inner conductors and the dielectric coatings C'_c are in series with the capacitance between the two dielectric coatings C'_{tw}. Notice that it has been assumed that the capacitance of the dielectric coatings is the same in both wires.

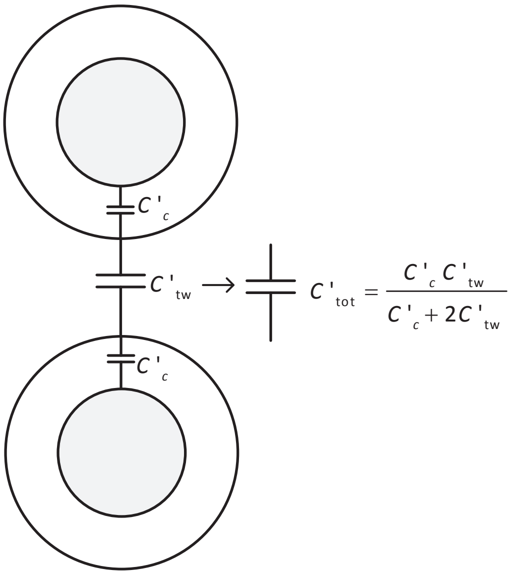

Fig. B. 3 Schematic diagram of the decomposition of a two-coated-wire line.

Therefore, the total p.u.l. capacitance can be calculated as:

$$C'_{tot} = \frac{C'_c C'_{tw}}{C'_c + 2C'_{tw}}. \tag{B.14}$$

The presented analytical approach for calculating the total p.u.l. capacitance has been validated by using reference numerical calculations obtained using the code RIBBON in [88] and the code LAPLACE [201]. The analytical results were found to be in excellent agreement with numerical results.

If the dielectric losses of the coated wires are taken into account, the conductance of the dielectric G'_c needs to be included in the analysis and the circuit in Fig. B. 3 is modified as illustrated in Fig. B. 4. The p.u.l. conductance and the capacitance of the dielectric coatings in parallel can be transformed into an equivalent complex capacitance that will be added in series with the capacitance between the two dielectric coatings.

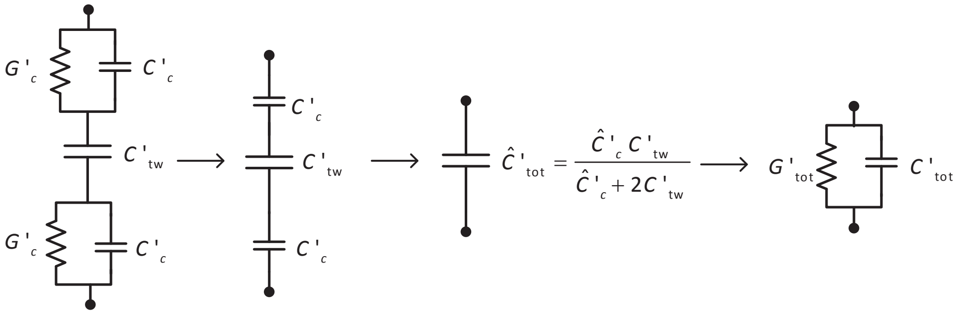

Fig. B. 4 Schematic diagram of the equivalent p.u.l. conductance of a two-coated-wire line.

Finally, the overall complex capacitance can be transformed into an equivalent p.u.l. conductance G'_{tot} and capacitance C'_{tot} by using the relations in Equation (B.7):

$$\begin{aligned} C'_{tot} &= \operatorname{Re}\left\{\hat{C}_{tot}\right\} = \operatorname{Re}\left\{\frac{\hat{C}'_c\, C'_{tw}}{\hat{C}'_c + 2C'_{tw}}\right\}, \\ G'_{tot} &= -\omega \operatorname{Im}\left\{\hat{C}_{tot}\right\} = -\omega \operatorname{Im}\left\{\frac{\hat{C}'_c\, C'_{tw}}{\hat{C}'_c + 2C'_{tw}}\right\}, \end{aligned} \tag{B.15}$$

where

$$\begin{aligned} \hat{C}'_c &= \frac{2\pi\hat{\varepsilon}}{\ln(\frac{r_m}{r_w})} = \frac{2\pi\varepsilon_0\varepsilon_r(1 - j\tan\delta)}{\ln(\frac{r_m}{r_w})}, \\ C'_{tw} &= \frac{\pi\varepsilon_0}{\cosh^{-1}(\frac{s}{2r_m})}. \end{aligned} \tag{B.16}$$

The p.u.l. self impedance of the wires Z'_{w} can be estimated as twice the self-impedance presented in Equations (B.8) and (B.9):

$$\begin{aligned} Z'_{\text{w}} &= R'_{\text{w}} + j\omega L'_{\text{w}} = \frac{2}{\sigma\pi r^2_w} + j\omega\frac{\mu_0}{4\pi}\,, \quad \text{if } r_w < 2\delta_s, \\ Z'_{\text{w}} &= R'_{\text{w}} + j\omega L'_{\text{w}} = \frac{1}{\pi r_w}\sqrt{\frac{j\omega\mu_0}{\sigma}}, \quad \text{if } r_w > 2\delta_s, \end{aligned} \tag{B.17}$$

where $\delta_s = \sqrt{2/(\omega\mu_0\sigma)}$ is the skin depth at the working frequency.

Finally, the overall p.u.l. impedance and admittance of the two-coated-wire line can be estimated as:

$$\begin{aligned} Z' &= Z'_{\text{w}} + j\omega L', \\ Y' &= G_{\text{tot}}' + j\omega C_{\text{tot}}'. \end{aligned} \tag{B.18}$$

References

[1] IEC, "61000-2-13 : Electromagnetic compatibility (EMC) - Part 2-13:Environment – High-power electromagnetic (HPEM)environments –Radiated and conducted," ed: IEC, 2005.

[2] D. V. Giri and F. M. Tesche, "Classification of intentional electromagnetic environments (IEME)," *Electromagnetic Compatibility, IEEE Transactions on,* vol. 46, pp. 322-328, 2004.

[3] D. Watts, "Security and vulnerability in electric power systems," in *35th North American Power Symposium NAPS 2003*, Missouri, 2003, pp. 559-566.

[4] W. Radasky, "Fear of frying electromagnetic weapons threaten our data networks. Here's how to stop them," *Spectrum, IEEE,* vol. 51, pp. 46-51, 2014.

[5] M. Amin, "Toward self-healing energy infrastructure systems," *Computer Applications in Power, IEEE,* vol. 14, pp. 20-28, 2001.

[6] R. Hoad, N. J. Carter, D. Herke, and S. P. Watkins, "Trends in EM susceptibility of IT equipment," *Electromagnetic Compatibility, IEEE Transactions on,* vol. 46, pp. 390-395, 2004.

[7] D. Nitsch, M. Camp, F. Sabath, J. L. ter Haseborg, and H. Garbe, "Susceptibility of some electronic equipment to HPEM threats," *Electromagnetic Compatibility, IEEE Transactions on,* vol. 46, pp. 380-389, 2004.

[8] W. A. Radasky, "18th International Zurich symposium on Electromagnetic Compatibility-Tutorial in EMI," ed. Munich, Germany, 2007.

[9] X. Jianfeng, Y. Wen-Yan, M. Jun-Fa, and L. W. J. Li, "Thermal Transient Response of GaAs FETs Under Intentional Electromagnetic Interference (IEMI)," *Electromagnetic Compatibility, IEEE Transactions on,* vol. 50, pp. 340-346, 2008.

[10] F. Sabath, "Classification of electromagnetic effects at system level," in *Electromagnetic Compatibility - EMC Europe, 2008 International Symposium on*, 2008, pp. 1-5.

[11] F. Brauer, F. Sabath, and J. L. ter Haseborg, "Susceptibility of IT network systems to interferences by HPEM," in *Electromagnetic Compatibility, 2009. EMC 2009. IEEE International Symposium on*, 2009, pp. 237-242.

[12] D. Mansson, R. Thottappillil, M. Backstrom, and O. Lunden, "Vulnerability of European Rail Traffic Management System to Radiated Intentional EMI," *Electromagnetic Compatibility, IEEE Transactions on,* vol. 50, pp. 101-109, 2008.

[13] D. Mansson, R. Thottappillil, T. Nilsson, O. Lunden, and M. Backstrom, "Susceptibility of Civilian GPS Receivers to Electromagnetic Radiation," *Electromagnetic Compatibility, IEEE Transactions on,* vol. 50, pp. 434-437, 2008.

[14] R. Thottappillil, D. Mansson, and M. Backstrom, "Response of electrified railway facilities to intentional electromagnetic interference: Review of research at Uppsala University," in *Electromagnetic Compatibility and 19th International Zurich Symposium on Electromagnetic Compatibility, 2008. APEMC 2008. Asia-Pacific Symposium on*, 2008, pp. 291-294.

[15] (2005, December 2005) Electric system vulnerabilities: the crucial role of ICT in recent blackouts. *Electra*. 6-17.

[16] M. W. Wik, W. A. Radasky, and R. L. Gardner, "Intentional Electromagnetic Interference (EMI) -- What is the Threat and What Can We Do About It?," in *15th International Wroclaw Symposium and Exhibition on EMC*, Wroclaw, Poland, 2000, pp. 896-897.

[17] Y. V. Parfenov, L. N. Zdoukhov, W. A. Radasky, and M. Ianoz, "Conducted IEMI threats for commercial buildings," *Electromagnetic Compatibility, IEEE Transactions on,* vol. 46, pp. 404-411, 2004.

[18] F. Sabath, "What can be learned from documented Intentional Electromagnetic Interference (IEMI) attacks?," in *General Assembly and Scientific Symposium, 2011 XXXth URSI*, 2011, pp. 1-4.

[19] C. E. Baum, "Reminiscences of High-Power Electromagnetics," *Electromagnetic Compatibility, IEEE Transactions on,* vol. 49, pp. 211-218, 2007.

[20] D. V. Giri, *High-power electromagnetic radiators : nonlethal weapons and other applications*. Cambridge, MA: Harvard University Press, 2004.

[21] URSI, "Resolution of criminal activities using electromagnetic tools," International Radio Scientific Union, Toronto, Canada1999.

[22] "Special Issue on high-power electromagnetics (HPEM) and intentional electromagnetic interference (IEMI), ," *Electromagnetic Compatibility, IEEE Transactions on,* August 2004.

[23] "Proceedings of AMEREM’2006 (American Electromagnetics)," in *AMEREM’2006 (American Electromagnetics),* Albuquerque, 2006.

[24] W. A. Radasky and M. Backstrom, "Brief historical review and bibliography for Intentional Electromagnetic Interference (IEMI)," in *General Assembly and Scientific Symposium (URSI GASS), 2014 XXXIth URSI*, 2014, pp. 1-4.

[25] L. L. Siniy, V. E. Fortov, Y. V. Parfenov, and L. N. Zdoukhov, "Russian research of intentional electromagnetic disturbances over the past ten years," in *AMEREM’2006 (American Electromagnetics)*, Albuquerque, 2006, p. 403.

[26] D. R. Wilton, D. J. Riley, D. R. Jackson, F. M. Tesche, and V. Jandhyala, "Modeling EMI in Complex and Electrically Large Systems," in *AMEREM'2006 (American Electromagnetics)*, Albuquerque, 2006, p. 404.

[27] R. Montano, M. Backstrom, D. Mansson, and R. Thottappillil, "On the response and immunity of electric power infrastructures against IEMI -Current Swedish initiatives," in *Electromagnetic Compatibility and 19th International Zurich Symposium on Electromagnetic Compatibility, 2008. APEMC 2008. Asia-Pacific Symposium on*, 2008, pp. 510-513.

[28] D. Mansson, M. Backstrom, and R. Thottappillil, "Intentional EMI against critical infrastructures, a discussion on mitigation philosophy," in *Electromagnetic Compatibility (APEMC), 2010 Asia-Pacific Symposium on*, 2010, pp. 134-137.

[29] D. Mansson, R. Thottappillil, and M. Backstrom, "Methodology for Classifying Facilities With Respect to Intentional EMI," *Electromagnetic Compatibility, IEEE Transactions on,* vol. 51, pp. 46-52, 2009.

[30] J. Foster, E. Gjelde, W. R. Graham, R. J. Hermann, H. M. Kluepfel, G. R. L. Lawson*, et al.*, "Report of the Commission to Assess the Threat to the United States from Electromagnetic Pulse (EMP) Attack," Critical National Infrastructures2008.

[31] W. A. Radasky and E. Savage, "Intentional Electromagnetic Interference (IEMI) and Its Impact on the U.S. Power Grid (Meta-R-323)," Metatech Corporation, Goleta, California2010.

[32] IEC, "61000-1-5 :Electromagnetic compatibility (EMC) –Part 1-5: General –High power electromagnetic (HPEM) effects on civil systems Reference," ed: IEC, 2004.

[33] D. Mansson, R. Thottappillil, and M. Backstrom, "Propagation of UWB Transients in Low-Voltage Power Installation Networks," *Electromagnetic Compatibility, IEEE Transactions on,* vol. 50, pp. 619-629, 2008.

[34] D. Mansson, T. Nilsson, R. Thottappillil, and M. Backstrom, "Propagation of UWB Transients in Low-Voltage Installation Power Cables," *Electromagnetic Compatibility, IEEE Transactions on,* vol. 49, pp. 585-592, 2007.

[35] J. H. Hagmann, S. Dickmann, and S. Potthast, "Application and propagation of transient pulses on power supply networks," in *EMC Europe 2011 York*, 2011, pp. 7-12.

[36] E. Genender, H. Garbe, and F. Sabath, "Probabilistic Risk Analysis Technique of Intentional Electromagnetic Interference at System Level," *Electromagnetic Compatibility, IEEE Transactions on,* vol. 56, pp. 200-207, 2014.

[37] S. van de Beek and F. Leferink, "Current intentional EMI studies in Europe with a focus on STRUCTURES," in *Electromagnetic Compatibility, Tokyo (EMC'14/Tokyo), 2014 International Symposium on*, 2014, pp. 402-405.

[38] S. van de Beek, J. Dawson, I. Flintoft, F. Leferink, N. Mora, F. Rachidi*, et al.* (2014) Overview of the European project STRUCTURES. *Electromagnetic Compatibility Magazine, IEEE*. 70-79.

[39] O. H. Arnesen and R. Hoad, "Overview of the European project HIPOW," *Electromagnetic Compatibility Magazine, IEEE,* vol. 3, pp. 64-67, 2014.

[40] V. Deniau, "Overview of the European project security of railways in Europe against Electromagnetic Attacks (SECRET)," *Electromagnetic Compatibility Magazine, IEEE,* vol. 3, pp. 80-85, 2014.

[41] S. van de Beek, J. Dawson, I. Flintoft, F. Leferink, N. Mora, F. Rachidi*, et al.*, "Overview of the European Project STRUCTURES," *IEEE EMC Magazine,* 2015.

[42] N. Mora, G. Lugrin, F. Rachidi, I. Junqua, J. P. Parmantier, S. Tkachenko*, et al.*, "On the validity limits of the transmission line theory in evaluating differential-mode signals along a two-wire line above a ground plane," in *Electromagnetic Compatibility (EMC), 2015 IEEE International Symposium on*, 2015, pp. 797-800.

[43] P. Ängskog and B. Oakes, "Maintaining Functional Safety under an Intentional Electromagnetic Interference (IEMI) Attack," in *TAMSEC 2013, National Symposium on Technology and Methodology for Security and Crisis Management, 13-14 November 2013, Stockholm, Sweden*, 2013, pp. 44-44.

[44] P. Angskog, M. Backstrom, and B. Vallhagen, "Measurement of radio signal propagation through window panes and energy saving windows," in *Electromagnetic Compatibility (EMC), 2015 IEEE International Symposium on*, 2015, pp. 74-79.

[45] P. Degauque and J. Hamelin, *Compatibilite electromagnetique : bruits et perturbations radioelectriques*. Paris: Dunod, 1990.

[46] F. M. Tesche, M. V. Ianoz, and T. Karlsson, *EMC analysis methods and computational models*. New York: Wiley, 1997.

[47] C. R. Paul, *Introduction to electromagnetic compatibility*. Hoboken, NJ: Wiley, 2006.

[48] P. Degauque and A. Zeddam, *Compatibilite electromagnetique: des concepts de base aux applications*: Hermes science publ., 2007.

[49] K. S. H. Lee, *EMP interaction : principles, techniques, and reference data a handbook of technology from the EMP interaction notes*. Washington, D.C.: Hemisphere Pub. Corp., 1986.

[50] J. P. Parmantier, M. Ridel, S. Bertuol, I. Junqua, C. Giraudon, C. Girard*, et al.*, "Modelling of HIRF coupling on complex cable architectures," in *Electromagnetics in Advanced Applications (ICEAA), 2011 International Conference on*, 2011, pp. 219-222.

[51] A. R. Ruddle, "The EU framework V project GEMCAR: guidelines for electromagnetic compatibility modeling for automotive requirements," presented at the 15th Int. Zurich EMC Symp., Zurich, Switzerland, 2003.

[52] L. Paletta, J. P. Parmantier, F. Issac, P. Dumas, and J. C. Alliot, "Susceptibility analysis of wiring in a complex system combining a 3-D solver and a transmission-line network simulation," *Electromagnetic Compatibility, IEEE Transactions on,* vol. 44, pp. 309-317, 2002.

[53] J. P. Parmantier, "Numerical coupling models for complex systems and results," *Electromagnetic Compatibility, IEEE Transactions on,* vol. 46, pp. 359-367, 2004.

[54] W. A. Radasky and E. Savage, "Intentional Electromagnetic Interference (IEMI) and Its Impact on the U.S. Power Grid " Metatech Corporation2010.

[55] C. E. Baum, "Electromagnetic Topology: A Formal Approach to the Analysis and Design of Complex Electronic Systems," *Interaction Note 0400,* Sep 1980.

[56] J. P. Parmantier, J. C. Alliot, G. Labaune, and P. Degauque, "Electromagnetic Coupling on Complex Systems: Topological Approach," *Interaction Note 0488,* May 1990.

[57] F. Rachidi and S. V. Tkachenko, *Electromagnetic field interaction with transmission lines from classical theory to HF radiation effects*. Southampton: WIT, 2008.

[58] C. E. Baum, T. K. Liu, and F. M. Tesche, "On the Analysis of General Multi-conductor Transmission - Line Networks," *Interaction Notes,* vol. 350, Nov 1978.

[59] E. F. Vance, *Coupling to shielded cables / Edward F. Vance*. New York :: Wiley, 1978.

[60] S. Tkatchenko, F. Rachidi, and M. Ianoz, "High-frequency electromagnetic field coupling to long terminated lines," *Electromagnetic Compatibility, IEEE Transactions on,* vol. 43, pp. 117-129, 2001.

[61] G. Lugrin, N. Mora, F. Rachidi, S. Tkachenko, M. Rubinstein, and R. Cherkaoui, "High-Frequency Electromagnetic Coupling to Long Loaded Multiconductor Transmission Lines," in *European Electromagnetics International Symposium EUROEM 2012*, Toulouse, France, 2012.

[62] G. Lugrin, S. V. Tkachenko, F. Rachidi, M. Rubinstein, and R. Cherkaoui, "High-Frequency Electromagnetic Coupling to Multiconductor Transmission Lines of Finite Length," *Electromagnetic Compatibility, IEEE Transactions on,* vol. 57, pp. 1714-1723, 2015.

[63] C. Christopoulos, "Dealing with complexity in EMC modelling," in *General Assembly and Scientific Symposium, 2011 XXXth URSI*, 2011, pp. 1-4.

[64] F. M. Tesche, "Methodology and Models for Estimating HPM Responses Conducted into Protective Enclosure," *Interaction Notes,* vol. 518, August 1996.

[65] F. Paladian, P. Bonnet, and S. Lallechere, "Modeling complex systems for EMC applications by considering uncertainties," in *General Assembly and Scientific Symposium, 2011 XXXth URSI*, 2011, pp. 1-4.

[66] C. Kasmi, M. Darces, M. Hélier, and E. Prouff, "Modélisation des valeurs extrêmes des courants induits par des interférences électromagnétiques," *18èmes Journées Nationales Microondes,* 2013.

[67] C. Kasmi, M. Hélier, M. Darces, and E. Prouff. (2013, Generalised Pareto distribution for extreme value modelling in electromagnetic compatibility. *Electronics Letters 49(5),* 334-335.

[68] I. Junqua, J.-P. Parmantier, and F. Issac, "A Network Formulation of the Power Balance Method for High-Frequency Coupling," *Electromagnetics,* vol. 25, pp. 603-622, 2005/10/01 2005.

[69] D. A. Hill, "Plane wave integral representation for fields in reverberation chambers," *Electromagnetic Compatibility, IEEE Transactions on,* vol. 40, pp. 209-217, 1998.

[70] I. Junqua, J. P. Parmantier, F. Issac, and W. Quenum, "Application of Electromagnetic Topology and Power Balance concepts to Radio Frequency Couplings into Buildings," *Interaction Notes,* vol. 625, October 2014 2014.

[71] R. Hoad and W. Radasky, "Overview of HPEM Standards Produced by IEC SC 77C," in *ASIA ELECTROMAGNETICS - ASIAEM 2015*, Jeju Island, South Korea, 2015.

[72] M. G. Backstrom and K. G. Lovstrand, "Susceptibility of electronic systems to high-power microwaves: summary of test experience," *Electromagnetic Compatibility, IEEE Transactions on,* vol. 46, pp. 396-403, 2004.

[73] IEC, "61000-5-9 : Electromagnetic compatibility (EMC) –Part 5-9: Installation and mitigation guidelines – System-level susceptibility assessments for HEMP and HPEM," ed: IEC, 2009.

[74] IEC, "61000-4-36: Electromagnetic compatibility (EMC) –Part 4-36: Testing and measurement techniques – IEMI immunity test methods for equipment and systems," ed: IEC, 2014.

[75] IEEE, "IEEE P1642: Recommended Practice for Protecting Public Accessible Computer Systems from Intentional EMI," ed. New York: IEEE, 2015.

[76] CIGRE, *600 : Protection of High Voltage Power Network Control Electronics Against Intentional Electromagnetic Interference (IEMI)*: CIGRE WG C4.206, 2014.

[77] N. Mora, G. Lugrin, R. Cherkaoui, F. Rachidi, and M. Rubinstein, "On the vulnerability Analysis against IEMI," in *European Electromagnetics International Symposium EUROEM 2012*, Toulouse, France, 2012.

[78] N. Mora, F. Vega, G. Lugrin, F. Rachidi, and M. Rubinstein, "STUDY AND CLASSIFICATION OF POTENTIAL IEMI SOURCES," *SYSTEM DESIGN AND ASSESSMENT NOTES,* vol. 41, 2014.

[79] N. Mora, I. D. Flintoft, L. Dawson, J. F. Dawson, F. Rachidi, M. Rubinstein*, et al.*, "Experimental Characterization of the Response of an Electrical and Communication Raceway to IEMI," *Electromagnetic Compatibility, IEEE Transactions on,* vol. PP, pp. 1-12, 2016.

[80] N. Mora, G. Lugrin, and F. Rachidi, "Study of the Propagation of IEMI Signals Along Power and Communication Lines," *Interaction Notes,* 2015 2015.

[81] N. Mora, C. Kasmi, F. Rachidi, M. Darces, and M. Helier, "Modeling of the propagation along low voltage power networks for IEMI studies," in *Electromagnetics in Advanced Applications (ICEAA), 2013 International Conference on*, 2013, pp. 436-439.

[82] N. Mora, C. Kasmi, F. Rachidi, M. Darces, M. Hélier, and M. Rubinstein, "Analysis of the Propagation of High Frequency Disturbances along Low-Voltage Test Raceway," presented at the American Electromagnetics International Symposium (AMEREM), Albuquerque, New Mexico, USA, 2014.

[83] N. Mora, F. Rachidi, P. Pelissou, and A. Junge, "An Improved Formula for the Transfer Impedance of Two-Layer Braided Cable Shields," *Electromagnetic Compatibility, IEEE Transactions on,* vol. PP, pp. 1-4, 2015.

[84] N. Mora, F. Rachidi, A. Junge, and P. Pelissou, "Numerical Simulation of the Overall Transfer Impedance of Shielded Spacecraft Harness Cable Assemblies," *IEEE Transactions on Electromagnetic Compatibility,* vol. IN PRESS, 2015.

[85] W. A. Radasky, C. E. Baum, and M. W. Wik, "Introduction to the special issue on high-power electromagnetics (HPEM) and intentional electromagnetic interference (IEMI)," *Electromagnetic Compatibility, IEEE Transactions on,* vol. 46, pp. 314-321, 2004.

[86] IEC, "61000-4-35 :Electromagnetic compatibility (EMC) –Part 4-35: Testing and measurement techniques – HPEM simulator compendium," ed: IEC, 2009.

[87] A. Rubinstein, "Simulation of electrically large structures in EMC studies - application to automotive EMC," Swiss Federal Institute of Technology -EPFL, 2004.

[88] C. R. Paul, *Analysis of multiconductor transmission lines*. Hoboken, N.J.: Wiley-Interscience : IEEE Press, 2008.

[89] ITU, "K.81- High-power electromagnetic immunity guide for telecommunication systems," ed, 2009.

[90] F. M. Tesche, "Methodology to Estimate the Vulnerability of Electrical Systems to HPEM Environments," Armasuisse, Spiez, Switzerland Contract 4500317796, NEMP Technical Support 2006, ARAMIS No. AR/R-3210/046-02, 2006.

[91] E. Genender, A. Kreth, D. Zamow, H. Garbe, and S. Potthast, "Combination of the failure probability with a random angle of incidence of the radiated interference," in *General Assembly and Scientific Symposium, 2011 XXXth URSI*, 2011, pp. 1-4.

[92] F. M. Tesche, "Transformer Responses to Fast Transient Excitations," The Defense Procurement Agency of the Federal Department of Defense, Civil Protection and Sports, NEMP Laboratory2002.

[93] F. M. Tesche, "Methods of Estimating Equipment Failure from High Power Electromagnetic Excitations," The Defense Procurement Agency of the Federal Department of Defense, Civil Protection and Sports, HPE Laboratory2005.

[94] E. Genender, S. Fisahn, H. Garbe, and S. Potthast, "On the Use of Probabilistic Risk Analysis for IEMI," in *2010 American Electromagnetics Conference, AMEREM 2010*, Ottawa, 2010.

[95] E. Genender, M. Mleczko, O. Doring, H. Garbe, and S. Potthast, "Fault tree analysis for system modeling in case of intentional EMI," *Adv. Radio Sci.,* vol. 9, pp. 297-302, 2011.

[96] F. Sabath and H. Garbe, "Risk potential of radiated HPEM environments," in *Electromagnetic Compatibility, 2009. EMC 2009. IEEE International Symposium on*, 2009, pp. 226-231.

[97] R. Hoad, "Information Security and Electromagnetic Attack – A Vulnerability Often Overlooked ", ed. University of Plymouth, United Kingdom, 2008.

[98] R. K. Nana, S. Dickmann, B. Schetelig, J. Keghie, and F. Sabath, "EMT based methodology for the vulnerability analysis of complex systems to IEMI," in *Proc. IEEE Int. Symp. Electromagnetic Compatibility EMC 2009*, ed, 2009, pp. 243-248.

[99] G. Lugrin, N. Mora, F. Rachidi, M. Rubinstein, and R. Cherkaoui, "Report on the characterization of potential IEMI threats against power systems," Swiss Federal Institute of Technology-EPFL, University of Applied Sciences Yverdon2012.

[100] N. Mora, F. Vega, G. Lugrin, F. Rachidi, and M. Rubinstein, "Study and Classification of Potential IEMI Sources," *System Design and Assessment Notes, Note 41,* 2014.

[101] Y. V. Parfenov, W. A. Radasky, B. A. Titov, and L. N. Zdoukhov, "The method for evaluating the probability of failures of digital devices under the influence of short

electromagnetic pulses," in *Electromagnetic Compatibility (APEMC), 2012 Asia-Pacific Symposium on*, 2012, pp. 353-356.

[102] S. Bazzoli, "Caractérisation et Simulation de la Susceptibilité des Circuits Intégrés face aux Risques d'Inductions engendrées par des Micro-ondes de Forte Puissance," DOCTEUR en ELECTRONIQUE, L'UNIVERSITE des SCIENCES et TECHNOLOGIE de LILLE, 2005.

[103] J. Delsing, J. Ekman, J. Johansson, S. Sundberg, M. Backstrom, and T. Nilsson, "Susceptibility of sensor networks to intentional electromagnetic interference," in *Proc. 17th Int. Zurich Symp. Electromagnetic Compatibility EMC-Zurich 2006*, ed, 2006, pp. 172-175.

[104] D. V. Giri, "Documented Electromagnetic Effects (EME)," in *EUROEM 2008*, Lausanne, Switzerland, 2008.

[105] L. Palisek and L. Suchy, "High Power Microwave effects on computer networks," in *EMC Europe 2011 York*, 2011, pp. 18-21.

[106] F. Brauer, S. Fahlbusch, J. L. ter Haseborg, and S. Potthast, "Investigation of Hardening Measures for IT Equipment against Radiated and Conducted IEMI," *Electromagnetic Compatibility, IEEE Transactions on,* vol. 54, pp. 1055-1065, 2012.

[107] L. Sauvage, S. Guilley, J. Danger, N. Homma, and Y. Hayashi, "A fault model for conducted intentional electromagnetic interferences," in *Electromagnetic Compatibility (EMC), 2012 IEEE International Symposium on*, 2012, pp. 788-793.

[108] V. G. J.P. Parmantier, F. Issac I. Jungua Y. Daudy and J. M. Lagarde, "An Application of the Electromagnetic Topology Theory on the Test-Bed Aircraft, EMPTAC," *Interaction Note 0506,* 16 Nov 1993.

[109] V. G. J.P. Parmantier, F. Issac L. Paletta I. Junqua Y. Daudy J.M. Lagarde, "ETE III: Application of the Electromagnetic Topology Theory on the Emptac," *Interaction Note 0527,* May 1997.

[110] I. Junqua, J. Parmantier, and M. Ridel, "Modeling of high frequency coupling inside oversized structures by asymptotic and PWB methods," in *Electromagnetics in Advanced Applications (ICEAA), 2011 International Conference on*, 2011, pp. 68-71.

[111] W. A. Radasky and E. Savage, "High-Frequency Protection Concepts for the Electric Power Grid William Radasky(Meta-R-324)," Metatech Corporation, Goleta, California2010.

[112] I. Junqua, J. P. Parmantier, and P. Degauque, "Field-to-Wire Coupling in an Electrically Large Cavity: A Semianalytic Solution," *Electromagnetic Compatibility, IEEE Transactions on,* vol. 52, pp. 1034-1040, 2010.

[113] C. Kasmi, M. Darces, and M. Hélier, "Statistical analysis of a spurious signal level in a low voltage PLC network," in *Electromagnetic Compatibility (EMC EUROPE), 2012 International Symposium on*, 2012, pp. 1-5.

[114] F. M. Tesche, "CW Test Manual," *Measurement Notes,* vol. 64, 2013.

[115] E. B. Savage, J. L. Gilbert, and W. A. Radasky, "Expedient Building Shielding Measurement Method for HEMP Assessments," *Electromagnetic Compatibility, IEEE Transactions on,* vol. 55, pp. 508-517, 2013.

[116] C. E. Baum, "A time-domain view of choice of transient excitation waveforms for enhanced response of electronic systems," presented at the International Conference Electromagnetics Advanced Applications (ICEAA 2001), 2001.

[117] W. D. Prather, C. E. Baum, R. J. Torres, F. Sabath, and D. Nitsch, "Survey of worldwide high-power wideband capabilities," *Electromagnetic Compatibility, IEEE Transactions on,* vol. 46, pp. 335-344, 2004.

[118] M. Armanious, "DESIGN AND ANALYSIS OF A HIGH POWER MODERATE BAND RADIATOR USING A SWITCHED OSCILLATOR," DOCTOR OF PHILOSOPHY, COLLEGE OF OPTICAL SCIENCES, THE UNIVERSITY OF ARIZONA, 2010.

[119] F. Vega, "Analytical Methods for the Study and Design of Integrated Switched Oscillators and Antennas for Mesoband Radiation," DOCTEUR ÈS SCIENCES, FACULTÉ DES SCIENCES ET TECHNIQUES DE L'INGÉNIEUR, ÉCOLE POLYTECHNIQUE FÉDÉRALE DE LAUSANNE, 2013.

[120] D. V. Giri, F. M. Tesche, M. D. Abdalla, M. C. Skipper, and M. Nyffeler, "Switched Oscillators and Their Integration into Helical Antennas," *Circuit and Electromagnetic System Design Notes,* vol. 58, 2009.

[121] D. V. Giri, F. M. Tesche, M. D. Abdalla, M. C. Skipper, and M. Nyffeler, "Switched Oscillators and Their Integration Into Helical Antennas," *Plasma Science, IEEE Transactions on,* vol. 38, pp. 1411-1426, 2010.

[122] D. V. Giri, "Helical antennas energized by transient marx generators," in *High Power Microwave Defense & Security Workshop*, Saint-Louis, France, 2011.

[123] D. V. Giri, "Classification of Intentional EMI based on bandwidth," presented at the AMEREM 2002, Annapolis, 2002.

[124] O. H. Arnesen, E. Krogager, M. Backstrom, S. Bo-Sande, J. Godo, S. Harkonen*, et al.*, "HIGH POWER MICROWAVE EFFECTS ON CIVILIAN EQUIPMENT," presented at the URSI General Assembly, New Delhi, 2005.

[125] F. Sabath, "Effects of documented HPEM attacks on systems. Course HPE 201-2011: High-Power Electromagnetics Course - Effects," ed. Schloss Noer, Germany, 2011.

[126] C. E. Baum, W. L. Baker, W. D. Prather, J. M. Lehr, J. P. O'Loughlin, D. V. Giri*, et al.*, "JOLT: A Highly Directive, Very Intensive, Impulse-Like Radiator," *Sensor and Simulation 0480,* November 2003.

[127] C. E. Baum, W. L. Baker, W. D. Prather, J. M. Lehr, J. P. O'Loughlin, D. V. Giri*, et al.*, "JOLT: a highly directive, very intensive, impulse-like radiator," *Proceedings of the IEEE,* vol. 92, pp. 1096-1109, 2004.

[128] P. Delmote, J. P. Duperoux, F. Bieth, and S. Pinguet, "UWB HPM at ISL: The GIMLI project and other applications," in *High Power Microwave Defense & Security Workshop*, Saint-Louis, France, 2011.

[129] D. V. Giri, H. Lackner, I. D. Smith, D. W. Morton, C. E. Baum, J. R. Marek*, et al.*, "Design, fabrication, and testing of a paraboloidal reflector antenna and pulser system for impulse-like waveforms," *Plasma Science, IEEE Transactions on,* vol. 25, pp. 318-326, 1997.

[130] J. Benford, E. Schamiloglu, and J. A. Swegle, *High power microwaves*. New York [u.a.]: Taylor & Francis, 2007.

[131] E. Nasser, *Fundamental of Gaseous Ionization and Plasma Electronics*: Wiley Interscience, 1971.

[132] G. Schaefer, M. Kristiansen, and A. H. Guenther, *Gas discharge closing switches*. New York, N.Y: Plenum Press, 1991.

[133] J. C. Martin, "Nanosecond pulse techniques," *Proceedings of the IEEE,* vol. 80, pp. 934-945, 1992.

[134] J. C. Martin, T. H. Martin, A. H. Guenther, and M. Kristiansen, *J.C. Martin on pulsed power*. New York: Plenum Press, 1996.

[135] V. Carboni, H. Lackner, D. V. Giri, and J. M. Lehr, "The Breakdown Fields and Risetimes of Select Gases Under Conditions of Fast Charging (~20 ns and less) and High Pressures (20-100 atmospheres)," *Switching Notes,* vol. 32, 2002.

[136] R. J. Barker and E. Schamiloglu, *High-power microwave sources and technologies*. New York, NY: IEEE Press, 2001.

[137] S. T. Pai and Q. Zhang, *Introduction to high power pulse technology*. Singapore [u.a.]: World Scientific, 1995.

[138] D. V. Giri, "Personal Communication," N. Mora, Ed., ed, 2012.

[139] J. M. Lehr, C. E. Baum, W. D. Prather, and F. J. Agee, "Fundamental Physical considerations for ultrafast spark gap switching," *Switching Notes,* vol. 28, 1997.

[140] M. Armanious, J. S. Tyo, M. C. Skipper, M. D. Abdalla, W. D. Prather, and J. E. Lawrance, "Interaction Between Geometric Parameters and Output Waveforms in High-Power Quarter-Wave Oscillators," *Plasma Science, IEEE Transactions on,* vol. 38, pp. 1124-1131, 2010.

[141] M. Armanious, J. S. Tyo, M. C. Skipper, M. D. Abdalla, W. D. Prather, and G. Gruen, "Electrostatic field management and electrodynamic modeling of switched quarter-wave oscillators," *Dielectrics and Electrical Insulation, IEEE Transactions on,* vol. 18, pp. 1054-1065, 2011.

[142] DIEHL, "Product Catalog - HPEM Case: Non-Lethal Effector Systems for the Protection of Persons and Buildings," D. B. Defence, Ed., ed: Diehl.com, 2011.

[143] C. D. Taylor and D. V. Giri, *High-power microwave systems and effects*. [Washington]: Taylor and Francis, 1994.

[144] M. Kreitlow, H. Garbe, and F. Sabath, "Influence of software effects on the susceptibility of Ethernet connections," in *Electromagnetic Compatibility (EMC), 2014 IEEE International Symposium on*, 2014, pp. 544-548.

[145] S. A. Pignari and G. Spadacini, "Plane-Wave Coupling to a Twisted-Wire Pair Above Ground," *Electromagnetic Compatibility, IEEE Transactions on,* vol. 53, pp. 508-523, 2011.

[146] F. Rachidi, "A Review of Field-to-Transmission Line Coupling Models With Special Emphasis to Lightning-Induced Voltages on Overhead Lines," *Electromagnetic Compatibility, IEEE Transactions on,* vol. 54, pp. 898-911, 2012.

[147] M. Magdowski, S. V. Tkachenko, and R. Vick, "Coupling of Stochastic Electromagnetic Fields to a Transmission Line in a Reverberation Chamber," *Electromagnetic Compatibility, IEEE Transactions on,* vol. 53, pp. 308-317, 2011.

[148] G. Spadacini and S. A. Pignari, "Numerical Assessment of Radiated Susceptibility of Twisted-Wire Pairs With Random Nonuniform Twisting," *Electromagnetic Compatibility, IEEE Transactions on,* vol. 55, pp. 956-964, 2013.

[149] C. E. Baum, "Aspects of Random-Lay Multiconductor Cable Propagation Which Are Not Statistical," *Interaction Notes,* vol. 595, 2004.

[150] S. Silfverskiold, M. Backstrom, and J. Loren, "Microwave field-to-wire coupling measurements in anechoic and reverberation chambers," *Electromagnetic Compatibility, IEEE Transactions on,* vol. 44, pp. 222-232, 2002.

[151] R. B. Armenta and C. D. Sarris, "Efficient Evaluation of the Terminal Response of a Twisted-Wire Pair Excited by a Plane-Wave Electromagnetic Field," *Electromagnetic Compatibility, IEEE Transactions on,* vol. 49, pp. 698-707, 2007.

[152] R. B. Armenta and C. D. Sarris, "Modeling the Terminal Response of a Bundle of Twisted-Wire Pairs Excited by a Plane Wave," *Electromagnetic Compatibility, IEEE Transactions on,* vol. 49, pp. 901-913, 2007.

[153] M. Magdowski and R. Vick, "Simulation of the stochastic electromagnetic field coupling to an unshielded twisted pair of wires," in *Electromagnetic Compatibility (EMC), 2013 IEEE International Symposium on*, 2013, pp. 33-37.

[154] M. Magdowski, J. Ladbury, C. Holloway, and R. Vick, "Measurement of the stochastic electromagnetic field coupling to an unshielded twisted pair cable," in *Electromagnetic Compatibility (EMC Europe), 2014 International Symposium on*, 2014, pp. 659-664.

[155] G. Spadacini, S. A. Pignari, and F. Marliani, "Experimental measurement of the response of a twisted-wire pair exposed to a plane-wave field," in *Electromagnetic Compatibility (EMC), 2011 IEEE International Symposium on*, 2011, pp. 828-833.

[156] F. Grassi, G. Spadacini, and S. A. Pignari, "The Concept of Weak Imbalance and Its Role in the Emissions and Immunity of Differential Lines," *Electromagnetic Compatibility, IEEE Transactions on,* vol. 55, pp. 1346-1349, 2013.

[157] G. Spadacini, F. Grassi, and S. A. Pignari, "On the combined effect of random nonuniformity and deformation of twisting on the radiated immunity of twisted-wire pairs," in *Electromagnetic Compatibility (EMC), 2013 IEEE International Symposium on*, 2013, pp. 489-493.

[158] C. Jullien, P. Besnier, M. Dunand, and I. Junqua, "Advanced Modeling of Crosstalk Between an Unshielded Twisted Pair Cable and an Unshielded Wire Above a Ground Plane," *Electromagnetic Compatibility, IEEE Transactions on,* vol. 55, pp. 183-194, 2013.

[159] C. Jullien, "Contribution à l’analyse et à la modélisation des couplages électromagnétiques au sein de torons de câbles à grand nombre de liaisons – Application aux câblages aéronautiques," Docteur de l'INSA de Rennes, Electronique et Télécommunications, Institut National des Sciences Appliquées de Rennes, Rennes, 2013.

[160] M. Backstrom, T. Nilsson, and B. Vallhagen, "Guideline for HPM protection and verification based on the method of power balance," in *Electromagnetic Compatibility (EMC Europe), 2014 International Symposium on*, 2014, pp. 128-133.

[161] D. V. Giri and M. Nyffeler, "Pulse Adaptor for GTEM-3750 " presented at the 2011 Armasuisse HPE Workshop, Thun, Switzerland, 2011.

[162] A. C. Marvin, G. Esposito, J. F. Dawson, I. D. Flintoft, L. Dawson, J. A. K. Everard*, et al.*, "A wide-band hybrid antenna for use in reverberation chambers," in *Electromagnetic Compatibility (EMC), 2013 IEEE International Symposium on*, 2013, pp. 222-226.

[163] IEC, "61000-4-21: Electromagnetic compatibility (EMC) - Part 4-21: Testing and measurement techniques - Reverberation chamber test methods," ed: IEC, 2011.

[164] J. G. Kostas and B. Boverie, "Statistical model for a mode-stirred chamber," *Electromagnetic Compatibility, IEEE Transactions on,* vol. 33, pp. 366-370, 1991.

[165] L. Musso, V. Berat, F. Canavero, and B. Démoulin, "A plane wave monte carlo simulation method for reverberation chambers," in *Int. Symp. Electromagn. Compat. EMC Europe 2002*, Sorrento, Italy, 2002, pp. 45-50.

[166] R. Rambousky, A. Bausen, L. O. Fichte, and F. Sabath, "HPEM susceptibility testing using a special infrastructure facility," in *Future Security 2013*, Berlin, 2013.

[167] Y. V. Parfenov, W. A. Radasky, B. A. Titov, and L. N. Zdoukhov, "Some features of the pulse electrical disturbances influence on digital devices functioning," in *General Assembly and Scientific Symposium (URSI GASS), 2014 XXXIth URSI*, 2014, pp. 1-4.

[168] D. Poljak, F. Rachidi, and S. V. Tkachenko, "Generalized Form of Telegrapher's Equations for the Electromagnetic Field Coupling to Finite-Length Lines Above a Lossy Ground," *Electromagnetic Compatibility, IEEE Transactions on,* vol. 49, pp. 689-697, 2007.

[169] F. M. Tesche, "Comparison of the transmission line and scattering models for computing the HEMP response of overhead cables," *Electromagnetic Compatibility, IEEE Transactions on,* vol. 34, pp. 93-99, 1992.

[170] G. Burke, "Numerical Electromagnetic Code - NEC-4. Method of Moments. Part II: Program Description - Theory," 1992.

[171] D. M. Pozar, *Microwave Engineering*. Hoboken, NJ: Wiley, 2012.

[172] C. Kasmi, M. Darces, and M. Hélier, "HF Input Impedance Measurement Based On A De-embedding Technique," in *EUROEM 2012*, Toulouse, France, 2012, pp. 1-5.

[173] N. Mora, M. J. Salvatierra, C. Romero, F. Rachidi, and M. Rubinstein, "Critical Equipment Input Impedance Measurement for IEMI Calculations," in *IEEE EMC 2013 Symposium*, Denver, USA, 2013.

[174] W. A. Radasky, "Electromagnetic Pulse: Effects on the U.S. Power Grid," Metatech Corporation, Goleta, California2011.

[175] CST. (2015). *CST EM Studio*. Available: https://www.cst.com/Products/CSTEMS

[176] N. Mora, F. Rachidi, P. Pelissou, and A. Junge, "Cable crosstalk analysis and simulation: A comparison between low frequency circuit approach and transmission line theory," in *Aerospace EMC, 2012 Proceedings ESA Workshop on*, 2012, pp. 1-6.

[177] P. Degauque, P. Laly, V. Degardin, and M. Lienard, "Power line communication and compromising radiated emission," in *Software, Telecommunications and Computer Networks (SoftCOM), 2010 International Conference on*, 2010, pp. 88-91.

[178] S. Bertuol, I. Junqua, V. Degardin, P. Degauque, M. Lienard, M. Dunand*, et al.*, "Numerical assessment of propagation channel characteristics for future application of power line communication in aircraft," in *EMC Europe 2011 York*, 2011, pp. 506-511.

[179] V. Degardin, I. Junqua, M. Lienard, P. Degauque, S. Bertuol, J. Genoulaz*, et al.*, "Predicted performances of power line communication in aircraft," in *Aerospace EMC, 2012 Proceedings ESA Workshop on*, 2012, pp. 1-4.

[180] F. M. Tesche and P. R. Barnes, "A Multiconductor Model for Determining the Response of Power Transmission and Distribution Lines to a High Altitude Electromagnetic Pulse (HEMP)," *Power Engineering Review, IEEE,* vol. 9, pp. 82-82, 1989.

[181] D. V. Giri and W. D. Prather, "High-Altitude Electromagnetic Pulse (HEMP) Risetime Evolution of Technology and Standards Exclusively for E1 Environment," *Electromagnetic Compatibility, IEEE Transactions on,* vol. 55, pp. 484-491, 2013.

[182] NEXANS, "Cable TT : Non armoured PVC, one or multi-conductors building cables," ed: NEXANS, 2012.

[183] CST, "CST CABLE STUDIO - Online Help," CST, Ed., ed, 2012.

[184] S. A. Schelkunoff, "The Electromagnetic Theory of Coaxial Transmission Lines and Cylindrical Shields," *Bell System Technical Journal,* vol. 13, pp. 532-579, 1934.

[185] E. F. Vance, "Shielding Effectiveness of Braided Wire Shields," *Interaction Notes,* vol. 172, 1974.

[186] T. Kley, "Optimized single-braided cable shields," *Electromagnetic Compatibility, IEEE Transactions on,* vol. 35, pp. 1-9, 1993.

[187] B. Démoulin and L. Koné, "Shielded Cables Transfer Impedance Measurement," *IEEE EMC Society Newsletter,* vol. Fall 2010, pp. 38-45, 2010.

[188] R. Otin, J. Verpoorte, and H. Schippers, "Finite Element Model for the Computation of the Transfer Impedance of Cable Shields," *Electromagnetic Compatibility, IEEE Transactions on,* vol. 53, pp. 950-958, 2011.

[189] E. F. Vance, "Shielding Effectiveness of Braided-Wire Shields," *Electromagnetic Compatibility, IEEE Transactions on,* vol. EMC-17, pp. 71-77, 1975.

[190] A. B. Tsaliovich, *Cable shielding for electromagnetic compatibility*. New York [u.a.]: Chapman and Hall, 1995.

[191] C. R. Paul, "Effect of Pigtails on Crosstalk to Braided-Shield Cables," *Electromagnetic Compatibility, IEEE Transactions on,* vol. EMC-22, pp. 161-172, 1980.

[192] IEC, "IEC 62153-4-6: Metallic communication cable test methods - Part 4-6: Electromagnetic compatibility (EMC) - Surface transfer impedance - Line injection method," ed: IEC, 2006.

[193] S. Dunwoody and E. Vanderheyden, "Transfer impedance testing of multi-conductor shielded connectors of arbitrary cross-section," in *Electromagnetic Compatibility, 1990. Symposium Record., 1990 IEEE International Symposium on*, 1990, pp. 581-585.

[194] L. O. Hoeft, M. T. Montoya, and J. S. Hofstra, "Electromagnetic coupling into rectangular rack-and-panel connectors," in *Electromagnetic Compatibility, 1995. Symposium Record., 1995 IEEE International Symposium on*, 1995, pp. 475-479.

[195] L. O. Hoeft, J. L. Knighten, and M. Ahmad, "Measured surface transfer impedance of multi-pin Micro-D Subminiature and LFH^{TM} connector assemblies at frequencies up to 1 GHz," in *Electromagnetic Compatibility, 1999 IEEE International Symposium on*, 1999, pp. 577-582 vol.2.

[196] L. O. Hoeft and J. S. Hofstra, "Measured electromagnetic shielding performance of commonly used cables and connectors," *Electromagnetic Compatibility, IEEE Transactions on,* vol. 30, pp. 260-275, 1988.

[197] A. M. Efremov, V. I. Koshelev, B. M. Kovalchuk, V. V. Plisko, and K. N. Sukchushin, "High-Power Sources of Ultrawideband Radiation with Subnanosecond Pulse Length," presented at the 14th International Symposium on High Current Electronics, Tomsk, Russia, 2006.

[198] F. Vega, "DESIGN OF A HIGH POWER ULTRA WIDEBAND SYSTEM USING A FAST IMPULSE CURRENT GENERATOR," Doctor of Philosophy, Electrical and Electronics Engineering Department, National University of Colombia, 2011.

[199] Y. Hua and T. K. Sarkar, "Matrix pencil method for estimating parameters of exponentially damped/undamped sinusoids in noise," *Acoustics, Speech and Signal Processing, IEEE Transactions on,* vol. 38, pp. 814-824, 1990.

[200] J. Chauveau, N. de Beaucoudrey, and J. Saillard, "Selection of Contributing Natural Poles for the Characterization of Perfectly Conducting Targets in Resonance Region," *Antennas and Propagation, IEEE Transactions on,* vol. 55, pp. 2610-2617, 2007.

[201] J. P. Parmantier, S. Bertuol, and I. Junqua, "CRIPTE : Code de réseaux de lignes de transmission multiconducteur - USER'S GUIDE – Version 5.1," ONERA/DEMR/T-N119/10 - CRIPTE 5.1 2010.

CURRICULUM VITAE

Nicolas MORA PARRA

Date of Birth : 28th May 1985

Nationality : Colombian

Email: nicolas.mora@epfl.ch

Education

2011–2016	Ph.D. in Electrical Engineering, Swiss Federal Institute of Technology (EPFL), Lausanne, Switzerland.
2007–2009	Master of Science in Electrical Engineering - major in High Voltage Engineering, National University of Colombia, Bogota, Colombia
2001–2006	Bachelor of Science in Electronics Engineering, National University of Colombia, Bogota, Colombia

Professional Experiences

2015 - present	R & D Engineer, Montena Technology, Rossens, Switzerland.
2009 - 2015	Research Assistant, EMC Lab, Swiss Federal Institute of Technology (EPFL), Lausanne, Switzerland.
2007-2011	Research Assistant, EMC Lab, National University of Colombia, Bogota, Colombia
2008	Lecturer, Antennas and propagation course, Javeriana University, Bogota, Colombia
2004-2005	Engineering Assistant, Digesa SARL, Bogota, Colombia

Distinctions

2016	Distinguished Reviewer, IEEE Transactions on EMC
2015	Young Scientist Award, Summa Foundation
2015	Distinguished Reviewer, IEEE Transactions on EMC
2011	Frank Gunther Award, Radio Club of America
2011	Young Scientist Award, URSI
2009-2010	Research Scholarship, Swiss Confederation
2009	Honor prize for Cum Laude M. Sc. thesis, National University of Colombia

Languages

Spanish :	Mother tongue
English :	Fluent
French :	Fluent

PUBLICATIONS LIST

Publications related to this thesis

Peer-reviewed journals:

1. Mora, N., et al., *Study and Classification of Potential IEMI Sources.* System Design and Assessment Notes, Note 41, 2014.
2. Mora, N., G. Lugrin, and F. Rachidi, *Study of the Propagation of IEMI Signals Along Power and Communication Lines.* Interaction Notes, 2015(IN 627).
3. Mora, N., et al., *An Improved Formula for the Transfer Impedance of Two-Layer Braided Cable Shields.* Electromagnetic Compatibility, IEEE Transactions on, 2015. **57**(3): p. 607-610.
4. Mora, N., et al., *Numerical Simulation of the Overall Transfer Impedance of Shielded Spacecraft Harness Cable Assemblies.* Electromagnetic Compatibility, IEEE Transactions on, 2015. **57**(4): p. 894-902.
5. Mora, N., et al., *Experimental Characterization of the Response of an Electrical and Communication Raceway to IEMI.* IEEE Transactions on Electromagnetic Compatibility, 2016. **58**(2): p. 494-505.

Conference proceedings

6. Mora, N., et al. *On the vulnerability Analysis against IEMI.* in *European Electromagnetics International Symposium EUROEM 2012*. 2012. Toulouse, France.
7. Mora, N., et al. *Cable crosstalk analysis and simulation: A comparison between low frequency circuit approach and transmission line theory*. in *Aerospace EMC, 2012 Proceedings ESA Workshop on*. 2012.
8. Lugrin, G., et al. *Overview of IEMI conducted and radiated sources: Characteristics and trends*. in *Electromagnetic Compatibility (EMC EUROPE), 2013 International Symposium on*. 2013.
9. Mora, N., et al. *Modeling of the propagation along low voltage power networks for IEMI studies*. in *Electromagnetics in Advanced Applications (ICEAA), 2013 International Conference on*. 2013.
10. Mora, N., et al., *Analysis of the Propagation of High Frequency Disturbances along Low-Voltage Test Raceway*, in *American Electromagnetics International Symposium (AMEREM)*2014: Albuquerque, New Mexico, USA.
11. Mora, N., et al. *MTL modeling of spacecraft harness cable assemblies*. in *Electromagnetic Compatibility (EMC), 2014 IEEE International Symposium on*. 2014.

12. Mora, N., et al., *Response of an Electrical and Communication Raceway to HPEM Transient Field Illumination*, in *American Electromagnetics International Symposium (AMEREM)*2014: Albuquerque, New Mexico, USA.
13. Mora, N., et al. *On the validity limits of the transmission line theory in evaluating differential-mode signals along a two-wire line above a ground plane.* in *Electromagnetic Compatibility (EMC), 2015 IEEE International Symposium on*. 2015.
14. Van de Beek, S., et al., *The European Project STRUCTURES: Challenges and Results*, in *Joint IEEE International Symposium on EMC and EMC Europe*2015: Dresden, Germany.

Magazines

15. Lugrin, G., et al., *La vulnérabilité des réseaux électriques en cas d'attaques électromagnétiques: Caractéristiques des sources d'interférences intentionnelles*, in *Bulletin AES (No.5)*2013.
16. van de Beek, S., et al., *Overview of the European project STRUCTURES*, in *Electromagnetic Compatibility Magazine, IEEE*2014. p. 70-79.
17. Lugrin, G., et al., *Protection contre les interférences électromagnétiques intentionnelles. Peut-on utiliser les techniques classiques de la CEM ?*, in *Bulletin Electrosuisse*2015. p. 38-41.

Other publications

Peer-reviewed journals:

18. Vega, F., et al., *Design, Realization and Experimental Test of a Coaxial Exponential Transmission Line Adaptor for a Half Impulse Radiating Antenna.* Sensor and Simulation Notes, 2011. **556**.
19. Mora, N., F. Rachidi, and M. Rubinstein, *Application of the time reversal of electromagnetic fields to locate lightning discharges.* Atmospheric Research, 2012. **117**: p. 78-85.
20. Romero, C., et al., *Measurement of Lightning Currents Using a Combination of Rogowski Coils and B-Dot Sensors.* Journal of Lightning Research, 2012. **4**(1): p. 71-77.
21. Vega, F., et al., *Method for the Analysis and Design of Coaxial Switched Oscillators Using Chain Parameters.* Sensor and Simulation Notes, 2012. **561**.
22. Pantoja, J.J., et al., *On the Electromagnetic Susceptibility of Hot Wire-Based Electroexplosive Devices to RF Sources.* Electromagnetic Compatibility, IEEE Transactions on, 2013. **55**(4): p. 754-763.

23. Shoory, A., et al., *Application of the Cascaded Transmission Line Theory of Paul and McKnight to the Evaluation of NEXT and FEXT in Twisted Wire Pair Bundles.* Electromagnetic Compatibility, IEEE Transactions on, 2013. **55**(4): p. 648-656.

24. Vega, F., et al., *Design, Realization, and Experimental Test of a Coaxial Exponential Transmission Line Adaptor for a Half-Impulse Radiating Antenna.* Plasma Science, IEEE Transactions on, 2013. **41**(1): p. 173-181.

25. Cavka, D., N. Mora, and F. Rachidi, *A Comparison of Frequency-Dependent Soil Models: Application to the Analysis of Grounding Systems.* Electromagnetic Compatibility, IEEE Transactions on, 2014. **56**(1): p. 177-187.

26. Lugrin, G., et al., *On the Location of Lightning Discharges Using Time Reversal of Electromagnetic Fields.* Electromagnetic Compatibility, IEEE Transactions on, 2014. **56**(1): p. 149-158.

Conference proceedings

27. Mora, N., I. Jaramillo, and E. Barrera. *Diseño de Módulos GPIB de propósito especial con celdas Estándar*. in *XIII Iberchip Workshop*. 2007. Lima, Peru.

28. Roman, F., et al. *Radiating broad-band pulse generator with corona charging mechanism*. in *EUROEM 2008*. 2008. Lausanne, Switzerland.

29. Santamaria, F., et al. *Application of the IEEE Std 299-1997 "Standard Method for Measuring the Effectiveness of Electromagnetic Shielding Enclosures"*. in *EUROEM 2008*. 2008. Lausanne, Switzerland.

30. Mora, N., F. Roman, and F. Vega. *Application of Electrical Coronas in Fast Impulse Generation*. in *CREES 2009*. 2009. Barranquilla, Colombia.

31. Mora, N., et al. *Corona Charged Subnanosecond Impulse Generator*. in *Electromagnetic Compatibility, 2009 20th International Zurich Symposium on*. 2009.

32. Vega, F., et al. *Design and construction of a corona charged high power impulse generator*. in *Pulsed Power Conference, 2009. PPC '09. IEEE*. 2009.

33. Vega, F., et al. *Design and simulation of an electromagnetic lens for a half impulse radiating antenna*. in *Electromagnetics in Advanced Applications, 2009. ICEAA '09. International Conference on*. 2009.

34. Mora, N., F. Rachidi, and A. Rubinstein. *Locating Lightning using Time Reversal of Electromagnetic Fields*. in *30th International Conference on Lightning Protection, ICLP 2010*. 2010. Cagliari, Italy.

35. Mora, N., et al. *Application of high power electromagnetics to human safety*. in *EPFL - UNESCO Chair International Scientific Conference on Technologies for Development*. 2010. Lausanne, Switzerland.

36. Romero, C., et al. *Measurement Of Lightning Currents Using A Combination Of Rogowski Coils And B-Dot Sensors*. in *30th International Conference on Lightning Protection, ICLP 2010*. 2010. Cagliari, Italy.

37. Vega, F., et al. *Design, Construction And Test Of A Half Impulse Radiating Antenna*. in *American Electromagnetics (AMEREM) 2010 Conference* 2010. Ottawa, Canada.

38. Vega, F., et al. *Time-domain analysis of an electromagnetic lens for a Half Impulse Radiating Antenna*. in *Electromagnetic Compatibility (APEMC), 2010 Asia-Pacific Symposium on*. 2010.

39. Mora, N., et al. *Improving the Electromagnetic Shielding of Composite Materials using Metallic Nanoparticles*. in *International Wokshop on Applications Prospects of Nanostructured Metamaterials*. 2011. Lausanne, Switzerland.

40. Mora, N., T. Mordiabou, and F. Rachidi. *Design and simulation of a tem sensor for electric field impulse measurements*. in *CST European User Conference*. 2011. Freising, Germany.

41. Mora, N., et al. *Modeling of the electromagnetic coupling to electro-explosive devices*. in *General Assembly and Scientific Symposium, 2011 XXXth URSI*. 2011.

42. Mora, N., et al. *Response of canonical ports to a high power electromagnetic excitation*. in *Electromagnetics in Advanced Applications (ICEAA), 2011 International Conference on*. 2011. Torino, Italy.

43. Vega, F., et al. *Design and simulation of a coaxial exponential transmission line for a Half Impulse Radiating Antenna*. in *General Assembly and Scientific Symposium, 2011 XXXth URSI*. 2011.

44. Vega, F., et al. *Design and optimization of mesoband radiators using chain parameters*. in *Electromagnetics in Advanced Applications (ICEAA), 2011 International Conference on*. 2011. Torino, Italy.

45. Dadras, M.M., et al. *Polymer Matrix Composites with Nickel Nanoparticles for Electromagnetic Shielding Applications*. in *15th European Microscopy Congress*. 2012. Manchester, UK.

46. Lugrin, G., et al. *Localisation de la Foudre par Retournement Temporel*. in *16e Colloque International sur la Compatibilité Electromagnétique,*. 2012. Rouen.

47. Lugrin, G., et al. *On the use of the Time Reversal of Electromagnetic fields to locate lightning discharges*. in *Lightning Protection (ICLP), 2012 International Conference on*. 2012.

48. Lugrin, G., et al. *High-Frequency Electromagnetic Coupling to Long Loaded Multiconductor Transmission Lines*. in *European Electromagnetics International Symposium EUROEM 2012*. 2012. Toulouse, France.

49. Mora, N., M.M. Dadras, and F. Rachidi. *Electromagnetic Shielding using Nanoparticles Embedded in Polymer Matrix Composites*. in *4th International Conference "Smart Materials Structures Systems" CIMTEC*. 2012. Motecatini, Italy.

50. Cavka, D., et al. *On the application of frequency dependent soil models to the transient analysis of grounding electrodes*. in *Electromagnetic Compatibility (EMC EUROPE), 2013 International Symposium on*. 2013.

51. Mora, N., et al. *Critical Equipment Input Impedance Measurement for IEMI Calculations*. in *IEEE EMC 2013 Symposium*. 2013. Denver, USA.

52. Vega, F., et al. *Design of a switched oscillator for IEMI susceptibility testing*. in *Electromagnetic Compatibility (EMC), 2013 IEEE International Symposium on*. 2013.

53. Bertholet, P., et al., *Design and Realization of a High-Voltage Adapter for the Testing of Surge Protective Devices against Intentional Electromagnetic Interferences*, in

*American Electromagnetics International Symposium (AMEREM)*2014: Albuquerque, New Mexico, USA.

54. Junge, A., et al., *Electromagnetic Interference Control Techniques for Spacecraft Harness*, in *2014 International Symposium on Electromagnetic Compatibility*2014: Tokyo.
55. Kasmi, C., et al., *Analyse multi-niveaux des effets induits par des interférences électromagnétiques*, in *17e Colloque International et Exposition sur la Compatibilité Electromagnétique*2014: Clermont-Ferrand, France.
56. Recordon, D., et al. *A comparator-based technique for identification of intentional electromagnetic interference attacks*. in *Electromagnetic Compatibility (EMC Europe), 2014 International Symposium on*. 2014.
57. Vega, F., N. Mora, and F. Rachidi, *Numerical Calculation of the Fields on the Aperture Plane of an Impulse Radiation Antenna*, in *American Electromagnetics International Symposium (AMEREM)*2014: Albuquerque, New Mexico, USA.
58. Daout, B., et al., *Analysis of the Induced Electromagnetic Field in the Surroundings of a NEMP Simulator*, in *Asia Electromagnetics International Symsposium (ASIAEM)*2015: Jeju, Republic of Korea.
59. Lugrin, G., et al., *Test of Surge Protective Devices to Mitigate Intentional Electromagnetic Interferences (IEMI)*, in *Asia Electromagnetics International Symsposium (ASIAEM)*2015: Jeju, Republic of Korea,.
60. Lugrin, G., et al., *On the Applicability of the Transmission Line Theory for the Analysis of Common-Mode IEMI-Induced Signals*, in *Asia Electromagnetics International Symsposium (ASIAEM)*2015: Jeju, Republic of Korea.
61. Mora, N., et al., *Effect of the Penetration through a Concrete Wall on the Propagation of Common Mode IEMI Signals*, in *Asia Electromagnetics International Symsposium (ASIAEM)*2015: Jeju, Republic of Korea.
62. Mora, N., et al., *Analysis and Modeling of Epoxy/MWCNT Composites*, in *15th International Conference on Electromagnetics in Advanced Applications ICEAA*2015: Torino, Italy.
63. Runke, S., et al., *Evaluation of The Electric-Field Transfer Functions Between IEMI Sources and Banking IT Equipment*, in *Joint IEEE International Symposium on EMC and EMC Europe*2015: Dresden, Germany.
64. Smorgonskiy, A., et al., *Measurements of Transient Grounding Impedance of a Wind Turbine at Mont-Crosin Wind Park*, in *2015 Asia Pacific International Symposium on Electromagnetic Compatibility*2015: Taipei, Taiwan.

Supervised master thesis

65. Lugrin, G., *Localisation de la foudre par retournement temporel*, in *Institute of Electrical Engineering* 2011, Swiss Fedearl Insitute of Technology (EPFL): Lausanne, Switzerland.

66. Elouali, L., *Numerical study of the target identification with natural resonances extraction*, in *Institute of Electrical Engineering* 2012, Swiss Fedearl Insitute of Technology (EPFL): Lausanne, Switzerland.

67. Uribe, M., *Design of a measurement setup for the evaluation of the soil parameters*, in *Institute of Electrical Engineering* 2012, Swiss Fedearl Insitute of Technology (EPFL): Lausanne, Switzerland.

68. Salvatierra, M.J., *Characterization of the input impedance of electronic equipment at radio frequencies*, in *Institute of Electrical Engineering* 2013, Swiss Fedearl Insitute of Technology (EPFL): Lausanne, Switzerland.